SAPIENZA
UNIVERSITÀ DI ROMA

Modeling and Numerical Simulation of Solid Rocket Motors Internal Ballistics

a Dissertation submitted to the Doctoral Committee of
Tecnologia Aeronautica e Spaziale
of the
Sapienza Università di Roma
in partial fulfillment of the requirements for the
degree of Doctor of Philosophy

Candidate
Ing. Enrico Cavallini

Tutor
Prof. Maurizio Di Giacinto

Dipartimento di Meccanica e Aeronautica
Sapienza Università di Roma
Via Eudossiana 18, 00184 Rome, Italy

XXII Ciclo
Academic Year 2008/2009

Dipartimento di Ingegneria Aerospaziale e Astronautica
Sapienza Università di Roma
Via Eudossiana 18, 00184, Rome, Italy

Abstract

In the design and development of solid propellant rocket motors, the use of numerical tools able to simulate, predict and reconstruct the behavior of a given motor in all its operative conditions is particularly important in order to decrease all the planning times and costs.

This work is devoted to present an approach to the numerical simulation of SRM internal ballistic during the entire combustion time (ignition transient, quasi steady state and tail-off) by means of a Q1D unsteady numerical simulation model, named SPINBALL (Solid Propellant rocket motor INternal BALListic).

SPINBALL comes out from the updating and further development of the numerical, mathematical and physical models of the SPIT model (Solid Propellant rocket motor Ignition Transient), that allows to extend the numerical simulation of the SRM internal ballistic, from the ignition transient, to quasi steady state and tail-off.

SPINBALL core model is a quasi-1D unsteady gasdynamics model of the internal ballistic, with source terms that take into account the contribution to the bore flowfield conditions due to the igniter, the grain propellant and thermal protections. The flow is assumed as a non-reacting mixture of perfect gases with space and time varying thermophysical properties (standard thermodynamics approach). The governing equations are discretized by a Godunov-type scheme, first or second order in space and time. The use of a such approach allows to consider the addition into the chamber due to both ablation phenomena from thermal protections and combustion reactions from the grain propellant, but even to take into account the equilibrium point of the grain propellant exothermic reactions, as function of the local pressure and the variation from that nominal condition, through the combustion efficiency.

This main model is completed by several sub-models, in order to describe all the driving phenomena that lead the internal ballistic for the entire combustion time: an igniter model, an heat transfer model for convection and radiation, propellant ignition criterion, a cavity model to account submergence and slot regions, a grain combustion model with the pressure term (APN model) and the erosive term (Lenoir-Robillard model with the modifications due to Lawrence and Beddini). Some of them coming from the SPIT model.

Focusing on the driving phenomena that characterize the internal ballistic over the ignition transient, it is known that, during quasi steady state and tail-off, the motor bore flowfield conditions are led mainly by the grain burning surface evolution in time and the possible nozzle throat area ablation phenomena.

The grain burning surface evolution model is a 3D numerical grain regression model (named GREG) based on a full matrix level set approach, on both rectangular and cylindrical structured grids, that gives to the gasdynamical model the evolution in time of port area, wet perimeter and burn perimeter along the motor axis and in the submergence zone. The numerical scheme for the numerical integration of the Level Set equation is built from the strong link between Hamilton-Jacobi equations and conservation laws and it is a first or second order (minmod flux limiter and Heun's method) in time and space time marching scheme based of an exact Riemann solver. The use of a 3D model is mandatory to carry out the grain burnback analysis in the case of general and complex 3D grain shapes, as finocyl grains, whatever bore flowfield dimensional model (0D or Q1D) is adopted. GREG module can handle 3D complex geometries directly from CAD tools, building up its initial condition as a narrow signed distance function from STL (stereolithography) files of the grain propellant and the thermal protections and insulation shapes by a completely automatic procedure. The grain burning rate can be variable, both in

space and time. The use of grain propellant shape symmetries is exploited with the setting up of mirroring, or periodic boundary conditions, reducing the computational costs. The evaluation of the grain geometrical parameter, as areas, volumes and perimeters, is made with a robust second order regularization of the Dirac Delta and Heaviside functions to avoid the typical problems related with the use of the standard regularization techniques.

While potentially GREG module can be completely coupled with the Q1D unsteady flowfield model, in this work, we will consider a decoupling between the grain burnback model and the flowfield model, in order to reduce the computational cost required. GREG model is, hence, used as a pre-processor that generates tables of pre-evaluated grain geometrical properties for a constant burning rate in time and space. During the numerical simulation, these tables of port area, wet perimeter and burning perimeter are then interpolated using the local increment of the web variable, defined by the local grain burning rate, coming from APN and LR models.

The final objective is, hence, to develop an analysis/simulation capability of SRM internal ballistic for the entire combustion time, with simplified physical models, in order to reduce the computational cost required, but ensuring, in the meanwhile, an accuracy of the simulation greater than the one usually given by 0D quasi steady models. In this framework, the comparison between the results obtained with a 0D quasi steady chamber model and SPINBALL will be made and the effects of the increased detail level of the internal ballistic simulation on the overall prediction capability will be discussed for three SRMs: Zefiro 23 second stage of the new European launcher VEGA and two military motors, NAWC n. 6 and 13, on which there are different work in literature, and all motor data are available. Comparisons with the experimental data and with other codes results will be also made.

Publications

Some of the contents and of the results of this doctoral research activity appeared in the following publications ([112; 111; 113; 119]):

Numerical Simulation of the SRM Combustion Surface Evolution with Time
Enrico Cavallini and Bernardo Favini Internal Report for ESA-ESRIN, Frascati, Italy, January 2008.

An Ignition-to-Burn out Analysis of Internal Ballistic in Solid Rocket Motors
Maurizio Di Giacinto, Enrico Cavallini, Bernardo Favini and Ferruccio Serraglia
Space Propulsion 2008 - International Symposium on Propulsion for Space Transportation, 5 - 9 May 2008, Heraklion, Crete, Greece.

An Ignition-to-Burn Out Analysis of SRM Internal Ballistic and Performances
Maurizio Di Giacinto, Bernardo Favini, Enrico Cavallini and Ferruccio Serraglia
AIAA-2008-5141
44th AIAA/ASME/SAE/ASEE Joint Propulsion Conference and Exhibit, Hartford, CT, July 21-23, 2008.

SRM Internal Ballistic Numerical Simulation by SPINBALL Model
Enrico Cavallini, Bernardo Favini, Maurizio Di Giacinto and Ferruccio Serraglia
AIAA-2009-5512
45th AIAA/ASME/SAE/ASEE Joint Propulsion Conference and Exhibit, Denver, Colorado, Aug. 2-5, 2009.

Contents

List of Figures

List of Tables

Acronyms

BC Boundary Condition

CAD Computer Aided Design

CEA computer program for calculation of complex Chemical Equilibrium compositions and Applications

CFD Computational Fluid Dynamics

CFL Courant Friedrichs Lewy

CT Combustion Time

DMA Department of Mechanics and Aeronautics

ENO Essentially Non Oscillatory

EO Engquist Osher

ESA European Space Agency

FM Full Matrix

FOM Face Offsetting Method

GREG Grain REGression model

LR Lenoir Robillard

HJ Hamilton-Jacobi

HEP Head End Pressure

HPC High Performances Computer

IC Initial Condition

IT Ignition Transient

LF Lax Friedrichs

LLF Local Lax Friedrichs

LLLF Local Local Lax Friedrichs

LS Level Set

LSM Level Set Method

MUG Multidimensional Unsteady Gasdynamics

NAWCWD Naval Air Warefare Weapons Division

NB Narrow Banding

ODE Ordinary Differential Equation

OOP Object Oriented Programming

OS Osher-Sethian

PDE Partial Differential Equation

Q1D Quasi 1D

QSS Quasi Steady State

RF Roe Fix

SDF Signed Distance Function

SFT Static Firing Test

SPINBALL Solid Propellant rocket motor Internal Ballistics

SPIT Solid Propellant rocket motor Ignition Transient

SPP Solid propellant rocket motor Performance Program

SPqR Space Propulsion quasi Research

SRM Solid Rocket Motor

STL StereoLithography

TO Tail Off

TP Thermal Protection

TVB Total Variation Bounded

TVD Total Variation Decreasing

VEGA Veicolo Europeo di Generazione Avanzata

VOF Volume of Fluid

WENO Weighted Essentially Non Oscillatory

Z23 Zefiro 23

ZN Zeldovich-Novozhilov

List of Symbols

α	empirical coefficient of the cavity model
α	semi-empirical LR model
$\bar{v}_{inj}$	igniter jets average axial velocity
Δt	time discretization
Δx	spatial discretization
δ	Dirac Delta function
$\dot{m}$	mass flow rate
$\dot{m}_{ig}$	igniter mass flow rate
$\dot{m}_s$	cavity source term mass flow rate
ϵ	smearing parameter for Dirac Delta and Heaviside regularization
η_{c_F}	nozzle efficiency
$\Gamma(\gamma)$	Vandekerkoven function
Γ	grain surface
γ	specific heat ratio
$\hat{n}$	normal versor
$\hbar, H$	Heaviside function
$\mathcal{M}$	combustion products molecular weight
μ	dynamic viscosity
Ω	domain of interest
ϕ	Level Set function
ρ	density
ρ_{ig}	igniter gases density
ρ_{in}	pressurizing gas density
ρ_p	grain propellant density
σ_p	burning rate temperature coefficient
θ	arclength
$\tilde{P}_b$	consistent burning perimeter
$\tilde{F}$	experimental thrust
$\tilde{p}$	experimental pressure
$\vec{x}$	$= [\theta, r, z]^T$ position vector in cylindrical coordinates
$\vec{x}$	$= [x, y, z]^T$ position vector
a	parameter of the APN burning rate law
A_p	port area
A_t	nozzle throat area
C	generic specific heat
c	mass concentration
$c^\star$	characteristic velocity
c_F	thrust coefficient
c_f	friction term for the momentum equation
c_p	specific heat at constant pressure
c_v	specific heat at constant volume
C_{pr}	grain propellant specific heat at constant volume
D_h	hydraulic diameter
E	total internal energy per unit mass
F, f	fluxes
g	metric radius
H	Hamiltonian
h	HUMP parameter (scale factor included)
h_c	convective heat transfer coefficient
H_f	grain combustion products enthalpy per unit mass
H_{ig}	igniter enthalpy per unit mass
H_s	cavity source term enthalpy per unit mass
i, j, k	spatial indices
K	curvature

k_p	grain propellant conductivity
k_{ab}	ablation calibration constant
m	mass
M_p	propellant mass
n	parameter of the APN burning rate law
n	time index
P	generic point in a 3D space
p	pressure
P_b	burning perimeter
P_w	wet perimeter
Q	chemical heat release
r_b	burning rate
r_{b_e}	erosive burning rate
ref	reference status index
s	curvilinear abscissa
S_b	burning surface
S_w	wet surface
SDF	Signed Distance Function
t	time
t_b	burn-out time
T_f	combustion products temperature
T_i	grain initial temperature
T_s	grain surface temperature
T_{ia}	grain initial apparent temperature
u	axial velocity
U, u	conservative variable
V	velocity
V	volume
V_b	bore volume
V_g	grain volume
w, web	web variable
x	axial motor abscissa or generic abscissa
α_p	thermal diffusivity
$\eta_{c^\star}$	combustion efficiency
$c^\star$	characteristic velocity

1

Introduction

In this introductory chapter a brief description of Solid Rocket Motors (SRMs) is presented, with the definition and characterization of the main driving phenomena of the SRM internal ballistics operative phases. Hence, the importance of SRM internal ballistics models for the prediction, reconstruction and analysis in SRM design and development is discussed. Later on, the state of the art of the internal ballistics model and grain burning surface evolution model is presented. Finally, a brief overview of the structure of this dissertation is shown.

1.1 Solid Rocket Motors

We can define "Propulsion System" a system able to achieve a prefixed state of motion: the system must be able to determine the thrust (propulsive force) in one or more its features (intensity, direction, verso and duration). All existing at present propulsion systems are based on the action-reaction principle: generating a variation of the propulsive flow momentum, it is achieved a momentum variation of the propulsion system itself. If part or all the propulsive fluid is stored into the propulsion system the system is referred as "jet engine"; this broad definition of jet engines includes air-breathing engines like turbojets, turbofans, ramjets, pulse jets and pump-jets and nor-air-breathing engines like rockets. A rocket engine is a jet engine that takes all its propulsive mass from within propulsion system itself.

Rocket engines can be classified according to the type of energy conversion from primary energy to kinetic energy:

- Thermal Rocket enthalpic energy is converted to kinetic energy by a thermodynamic transformation.
- Electric Rocket electric energy is converted to kinetic energy by the application of electrostatic or electromagnetic fields to electrical charged particles.
- Nuclear Rocket nuclear energy is converted to kinetic energy by the discharge of fast moving particles (nuclear reaction products).

This thesis is focused only on the first type, the thermal rockets. More in depth there is large variety of thermal rockets; we are interested in the chemical thermal rocket: the thermal energy is obtained by the exothermic reactions that characterized combustion processes of rocket propellants; the thermal energy is then transformed into kinetic energy by the propulsive nozzle.

At the present, the chemical thermal rocket engines constitute the motors of modern launch vehicles. The word "launcher" means space vehicle, constituted by one or more propulsive stages, able to give suitable velocity to its payload (in order to put the payload into the designed orbit).

Among the different propellants of chemical thermal rockets we can distinguish between solid propellants, liquid propellants and hybrid propellants. The Solid Rocket Motor type is conceptually very simple: the oxidizer and combustive agent are mixed together in a single "propellant

solid grain"; this propellants grain cannot burn itself: it has to be ignited by an external source of energy, that are the igniter hot jets.

The simplest and well-known expression of the thrust, scope of this propulsion system, is given by equation 1.1

$$T = \dot{m}_j u_j + (p_j - p_a) A_j \tag{1.1}$$

where $\dot{m}_j$ is the exhaust gas mass flow, u_j is the actual jet velocity at nozzle exit plane, p_j is the static pressure at nozzle exit plane, p_a is the ambient (or atmospheric) pressure and A_j is the flow area at nozzle exit plane. The simplicity of this expression can cover up the fact that the thrust is made up by the integral of the pressure over the combustion chamber walls. Using the segmentation technique it is possible to develop very large SRM joining different segments together: this technique allow the development of very high thrust SRM. In rocketry specific impulse is defined as the change in momentum per unit weight-on-Earth of the propellant $I_{sp} = \frac{u_j}{g_0}$ where g_0 is the acceleration at the Earth's surface.

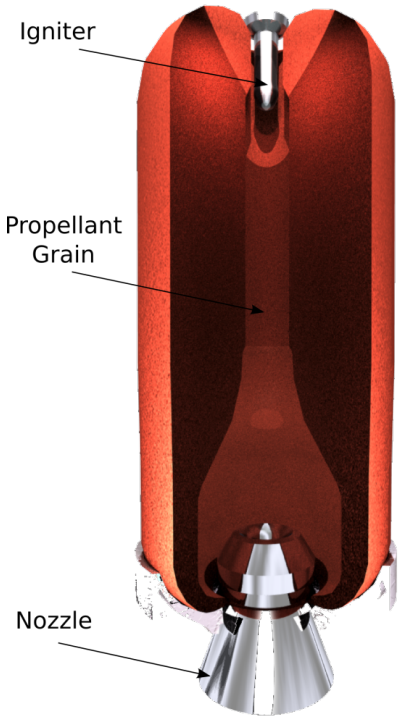

Figure 1.1: Generic SRM Scheme

The grain shape influences the behaviour of the thrust: because the mass flow rate and pressure of the gas generated by grain combustion depends on the grain surface itself (and on nozzle throat). This fact explains why the SRMs grain shapes are often very complex with the presence of three-dimensional regions, allowing the suitable thrust curve required for the mission. The typical three-dimensional regions are, in fact, "star-shaped" or "finocyl" (finocyl stands for fins on cylinder), but the variety of grain propellant shapes is quite wider.

The presented dissertation is focused on SRMs, and in particular on the modelling and numerical simulation of the SRM internal ballistics. A simple scheme of a generic SRM is shown in figure 1.1.

1.2 Solid Rocket Motors Internal Ballistics

The SRMs internal ballistics studies the internal flowfield conditions inside a solid propellant rocket motor during all its operative conditions, from motor start-up to burn-out, that completely characterize and define motor behaviour, performance and its mission capabilities.

The overall Combustion Time (CT) of a given SRM can be separated into three main different temporal phases, each of them characterized by different driving phenomena. Considering the relation between thrust and time, or the same, pressure and time (fig. 1.2), the SRM internal ballistics can be separated into the fol lowing different phases: Ignition Transient (IT), Quasi Steady State (QSS) and Tail Off (TO), that will be briefly discussed.

1. Ignition Transient

After the electric delay of the igniter, the impingement of the igniter jets on the propellant surface causes, as result, the grain propellant ignition, with possible acoustic mode excitement due to the interaction between the jets and the bore chamber geometry. After that, so called "induction interval", the flame spreading triggers the ignition of the entire grain propellant surface, causing a greater and greater mass addition from the propellant and consequent chamber pressure increasing. During this period so called "flame spreading interval", there are also two events that, typically, affect the internal ballistics: the igniter stops to produce mass in the bore and the nozzle throat seal rupture occurs. Moreover, a

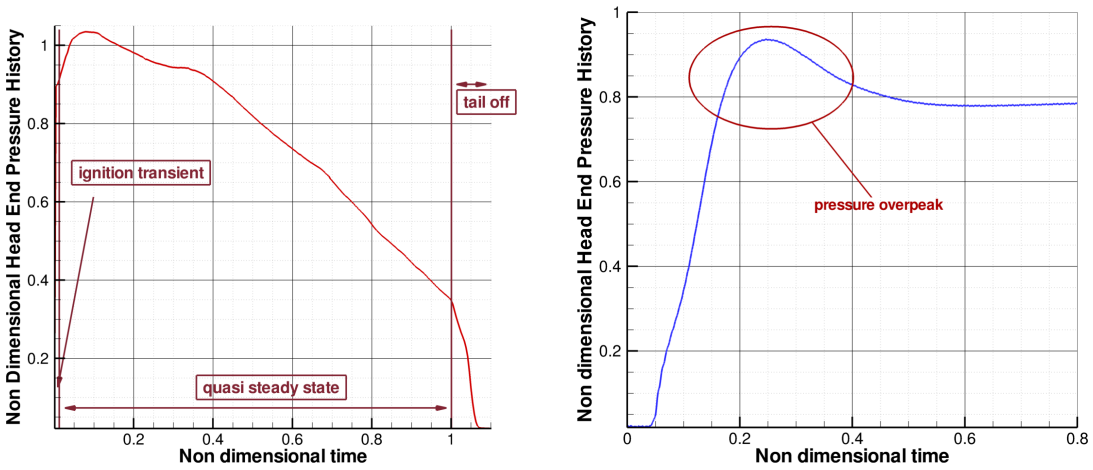

(a) Whole operative life

(b) Ignition Transient

Figure 1.2: Head-end pressure time history

pressure overpeak due to the erosive contribution (related to igniter gases high tangential velocities respect to the grain surface) to the burning rate, as enhancing mechanism of the grain propellant combustion process, and to the igniter inlet mass flow rate in the bore is often exhibited. Finally, after that the burning surface is completely ignited, the chamber filling and quasi steady state conditions are reached in the SRM chamber.

As a consequence, a model able to describe correctly the IT must necessarily account the strongly unsteadiness of the aforementioned phenomena (with possible relevant multidimensional effects related to the igniter jets[115]) in terms of fluid dynamics (acoustics and gasdynamics phenomena), heating and the mixing of gases into the bore (pressurizing gas, igniter gas products and grain combustion products). While, instead, during this operative phase can be totally neglected the grain geometry variation due to combustion, so that the bore geometry can be considered fixed at its initial configuration.

2. Quasi Steady State

In this subsequent operative phase the internal ballistics is mainly led by the grain mass addition and its variation in time due to grain combustion and burning surface recession and evolution in time. However, even the nozzle throat geometry variations could not, in general terms, be totally neglected. These phenomena, in fact, acting as passive thermal control of the nozzle structure, are due to the erosion-ablation phenomena to which the convergent zone, and the throat section are mainly subjected and occur in particular for SRMs with long combustion time (more that some seconds) In a very secondarily manner, the ablation phenomena interest also the inner parts of the chamber, which are discovered during the grain propellant combustion and, consequently, exposed to the chamber hot gases. In facts, the SRM metallic or composite casing structure is completely covered inwards by ablative materials, acting as passive thermal control system.

During this phase, moreover, acoustics instability phenomena can cause low level, but sustained, pressure and thrust oscillations [43] in the chamber due to the vortex shedding related mainly to a shear layer instability. These phenomena arise as an acoustic longitudinal mode excitation, that can occur depending mainly on the grain shape and its evolution and on the flow velocity, as a typical hydrodynamic instability.

In order to describe all these phenomena, even because of the possible presence of vortex shedding, a completely unsteady chamber dimensional (not oD) model is necessarily required.

Another possible instability phenomenon, which a smaller number of SRMs can be prone to during their operative functioning, is instead the combustion instability. Its basic mechanism is related to a bulk-mode instability[72] due to the possible coupling between the combustion of the solid propellant and the bulk-mode filling and emptying of the motor chamber. Thus, depending also on the pressure regime in the bore, the perturbations in the chamber produce fluctuations in the combustion processes and so in the propellant burning rate. This can produce itself pressure fluctuations through the gas flow inlet in the chamber, with a possible coupled mechanism.

Hence, assuming to neglect the modeling of instability phenomena (the aeroacoustics or the combustion one), even simple approaches given by quasi steady 0D models, can be, not much accurate, but sufficient in the description of the motor behaviour, only if the total pressure drops along the motor axis and the erosive burning are negligible, or limited. In fact, the significant grain geometry evolution time scales are much larger than the time scales of the fluid dynamics. Otherwise, when erosive burning and/or total pressure drops become important, at least Q1D models becomes mandatory. Moreover, the grain and nozzle geometry evolution must be imperatively accounted, as they both lead the bore flowfield conditions (the second with an effect that differs from motor to motor and negligible in certain motor configurations). While the presence of a gas mixture in the motor bore, coming from grain combustion and thermal protection ablation reactions, is essentially negligible in its effects on the internal ballistics. And hence, the inlet mass flow rate due to ablation phenomena occurring on the nozzle and case ablative surfaces can be totally neglected.

3. Tail Off

As the grain burning surface recedes and decreases in time, larger and larger parts of the liner and the case Thermal Protections (TPs) are exposed to the action of the chamber hot gases. Consequently, they are heated and because of ablative phenomena and begin to add ablation products in the chamber, in a way that is more and more important, dependently on the motor configuration. As the grain combustion products mass addition into the chamber becomes smaller and smaller, a rapid decrease of the chamber pressure occurs, with possible combustion fluctuations and sliver generation.

The tail-off phase, hence, is characterized by unsteady events, related to the chamber pressure decrease in time, mixing of gases coming from the residual grain propellant combustion and case thermal protections ablation. Hence, they need to be described correctly by an accurate burning surface evolution evaluation. While the less important effect of TPs mass addition due to ablative phenomena can be neglected, if not necessary for TPs dimensioning.

1.3 Internal Ballistics Prediction and Analysis in SRM Design and Development

The design and development phase of a Solid Rocket Motor is typically defined by numerous parametric studies conducted in order to optimize the motor design. Firstly technological and then political and commercial problems influence the possible configurations investigated and define constraints for the optimization problem.

Hence, once the optimum configuration is selected, detailed analyses examine critically the design configuration: propellant, grain design and motor configuration, in order to predict the full-scale motor performance. This target is obtained by using a combination of theoretical performance prediction methods and models with the help of the numerical simulation of the internal ballistics and motor performance. However, these prediction methods must be validated with the performance data obtained from subscale motor tests, or from previous firings on the full-scale motor, or from similar design SRMs. Performance prediction methods and models must account, identify and possibly qualitatively evaluate the non-ideal conditions within a

SRM that could define a lower than theoretical performance, by means of know-how assumptions on similar SRMs configurations. The full-scale motor behaviour is then experienced by means of subscale and SFTs for the full-scale configuration, which validate and/or define the distance between the designed/predicted and real performance, helping in the tuning of the non-ideal parameters, when the real SRM behaviour is adequately predicted by the simulation models. The incorrect or insufficient consideration for the differences between the theoretical or the subscale motor behaviour and the resulting real performance of the full-scale SRM can result in costly redesign and schedule slippage, or totally compromise the SRM mission objectives and/or the motor reliability[11].

Hence, in the design and development of Solid Rocket Motors, the increase of internal ballistics prediction capabilities can improve the SRM reliability and reduce, in the meanwhile, the design and development costs, related to experimental activities (especially Static Firing Tests (SFTs)). Both these targets require an accurate numerical simulation and the consequent physical understanding of the main and complex interacting internal ballistics driving phenomena, that characterize SRM performance and its mission capabilities, for the entire combustion time. In the meanwhile, the availability of reliable and accurate SRM models can help in the prediction of the in-flight real motor behaviour and performance, that can not be simply extrapolated by the use of the SFT-configuration experimental data, because of the different motor set-up (e.g. typically the truncation of the nozzle in the SFT with respect to the in-flight motor configuration for second or third solid stages).

However, these needs have to face two competitive features. By one part they must have the ability to represent in a detailed manner the main physical phenomena. But by the other, these models need to have in their numerical representation reduced computational times, to allow their use in the study of the SRM design options modifications impact in the mission profile, as result of parametric analyses, beyond their employ in the SRM internal ballistics and performance prediction and reconstruction.

In particular, this last constraint limits in a relevant way, the possibility to use fully dimensional 3D models of the flowfield in the combustion chamber, because their high computational cost for the typical combustion time of a SRM[1]. Their use is hence relegated to the accurate numerical simulation of the bore flowfield conditions for limited time intervals of the entire combustion time (i.e. the pre-ignition transient [115; 102; 97; 117; 116], or for some defined configurations during the quasi steady state [109; 110; 118]).

In the meanwhile, the use of 2D models for the SRM internal ballistics is strongly restricted to a certain class of simple motor configurations, since typically all recent configurations are characterized by finocyl, or 3D star shaped grains, or complex 3D geometries. Hence, it is possible to state that these kind of models are still computational expensive to simulate the entire combustion time, with respect to the considered relevant approximations of the 3D motor real geometry.

Moreover, in both 2D or 3D bore chamber models, some not trivial difficulties related to the accounting of the moving boundaries, due to grain propellant regression, that must be faced in the numerical simulation over the IT.

For the aforementioned reasons, a good compromise between the stated needs for the numerical simulation of the whole combustion time, can be, therefore, the use of Quasi 1D (Q1D) unsteady flowfield models. In fact, these chamber models have shown to be able to yield, if equipped with different sub-models, accurate predictions and descriptions of the motor IT [66; 76; 75; 70; 67; 103; 84; 91; 97]. In the meanwhile, they ensure an increasing of the modeling capabilities with respect to 0D models, largely adopted for the numerical simulation of the quasi steady state and tail off.

By the point of view of the grain burnback analysis, which studies the evolution of the grain propellant burning surface during time, instead, in general terms, all high performaces SRMs

1 for the pre-ignition transient, $\approx$ 0.1 s, 3D models requires 1K $\div$ 1M hours on parallel High Performances Computers (HPCs)

involve the choice of complex 3D grain geometries to fulfill mission requirements. Thus, simplified 0D, 1D or 2D regression models introduces representations of the grain surface, which are unacceptable for the accuracy obtained. Hence, complete 3D models are required, for whatever internal ballistics model and dimensional representation is chosen for the modeling of the bore flowfield conditions.

In fact, only limited and particular cases involve simple grain geometries, like axisymmetric grains or 2D grain, for which analytical or phase-based methods can be used (discussed briefly in 1.5).

1.4 Internal Ballistics Models Overview

1.4.1 0D Quasi Steady Flowfield Models

A simple but useful modelling of the internal ballistic is represented by the so called zero dimensional models or lumped parameter, volume-filling models [80]. Among many present in literature [9; 6; 7] we will consider the one due to Salita [51]. It is based on considering a spatially constant time dependent value of the flowfield properties in the bore, so that the thermodynamics properties of the gas are represented by total values. Under the hypothesis that the combustion phenomena happens completely in a very thin zone near the ignited grain surface, the gases in the bore can be treated as non reactive perfect gas.

These models historically were built to describe the behavior of a SRM during the Ignition Transient. In order to accomplish this target, they need an empirical specification of an ignition delay time and a flame spreading time [9; 6; 7], or some semi empirical tuning parameters to simulate the igniter. Because of this simple chamber model, in general terms, they become quite inaccurate for boosters with large length-to-diameter ratios and very low port area-to-throat area, where large total and static pressure drops must be accounted.

Considering, in particular, this kind of models for the QSS modeling, under the simplified assumptions that:

- the nozzle flow is a choked adiabatic expansion
- the flowfield characteristic time is far less than the burning surface evolution characteristic time
- hence, the evolution of the thermodynamics properties of the gases in chamber can be seen as an evolution of quasi steady states

it is possible to obtain from the mass balance, the evolution with time of the chamber pressure (assuming for the burning rate the De Veille - Saint Robert expression), given in the classical equation for the ballisticians 1.2.

$$p_c(t) = \left[\rho_p \, a(T_i, \sigma_p) \, c^* \frac{S_b(t)}{A_t(t)}\right]^{\frac{1}{1-n}} \tag{1.2}$$

This expression can be used both in the direct numerical simulation of the quasi steady state and tail-off phases. But, its use can be also extended for post firing test (or instrumental flight) analyses, considering the introduction of some non-ideal behaviour parameters of the the SRM (as will be explained in details in H, page b) if coupled with:

- a chemical equilibrium model able to compute the value of the c^* parameter
- a *grain burnback analysis* model that gives the evolution in time of the burning surface S_b
- a nozzle thermal protections ablation/erosion prediction model able to compute the evolution in time of the throat area

1.4.2 Quasi 1D Unsteady Flowfield Models

In order to accomplish a more accurate analysis of modern solid boosters internal ballistic, featuring high length-to-diameter ratios and low port area-to-throat area ratios, unsteady one-dimensional models are required. These class of chamber flowfield models exploit the major dimension of the bore (along the motor axis) and describe the flowfield properties as dependent on the spatial position along the motor axis and time [80; 12; 70; 111; 113].

We assume, then, that all chemical reactions occur in a very thin region near the propellant surface, so that the combustion products enter in the main stream with zero axial momentum, and considering the products as a perfect gas (or as a mixture of perfect gases). Thus, the equations that describe the internal ballistic are the mass, momentum and energy conservation equation written for a channel with area variations and sources terms, representing the mass and energy addition from burning grain and igniter and the friction terms (as shown in equation 1.3).

$$\begin{cases} \dfrac{\partial(\rho A_p)}{\partial t} + \dfrac{\partial(\rho u A_p)}{\partial x} = r_b P_b \rho_p + \dfrac{\dot{m}_s A_p}{V} + \dfrac{\dot{m}_{ig} A_p}{V} \\ \dfrac{\partial(\rho u A_p)}{\partial t} + \dfrac{\partial\left[\left(\rho u^2 + p\right) A_p\right]}{\partial x} - p\dfrac{\partial A_p}{\partial x} = \dfrac{\dot{m}_{ig} A_p \bar{v}_{inj}}{V} + \dfrac{1}{2}\rho u^2 c_F P_w \\ \dfrac{\partial(\rho E A_p)}{\partial t} + \dfrac{\partial\left[(\rho E + p)\, u A_p\right]}{\partial x} = r_b P_b \rho_p h_f + \dfrac{\dot{m}_{ig} A_p H_{ig}}{V} + \dfrac{\dot{m}_s A_p H_s}{V} \end{cases} \tag{1.3}$$

In order to describe all the aforementioned driving events that affect the internal ballistic, during all the operative phases of a given motor (IT, QSS & TO), the model must necessarily be completed with some other sub-models:

- igniter model
- ignition criterion
- heat transfer model: conduction in the solid propellant, convection and radiation
- slots and submergence model
- burning rate model
- grain burnback model giving port area, burning perimeter and wet perimeter along the motor axis in time
- liner, nozzle and case thermal protections ablation/erosion models

1.4.3 2D-3D Unsteady Flowfield Models

A general and even more complex modelling of a SRM combustion chamber considers the Euler or Navier-Stokes equations written for a completely 2D-3D unsteady flow. These kind of modelling could be very accurate in the description of the propagative phenomena and igniter jets that characterize the pre-ignition transient [103; 97; 115] and Ignition Transient, or the two-phases flowfield features in the motor during some selected time instants during Quasi Steady State[109; 118; 110]. On the other side, they are computationally very expensive, as they requires 1K ÷ 1M simulation hours on parallel high performance computers for a typical pre-ignition transient simulation. Moreover the accuracy of the results during the IT, in terms of head-end pressure time history prediction, can be achieved even with Q1D models (that instead have 10^3 seconds of computational cost). Certainly, they become completely mandatory for the accurate study of the jet features and of the flowfield conditions that occurs in the chamber during this very unsteady phase.

Instead, the numerical simulation of the two-phases flowfield features during QSS requires about the same computational time 1K ÷ 1M hours on parallel high performance computers, for achieving a steady state solution. Thus, all the resultant modelling accuracy of the motor internal ballistics simulation can be not necessary during the entire SRM combustion time, respect to the

required computational cost. Moreover, considering the complete simulation of the internal ballistic over the IT, during QSS and TO some not trivial problems must be faced:

- as the grain burning surface recedes in time, the flowfield computational domain changes (the same problems are present to account the nozzle and case thermal protection and liner consumption) and new bore volume must be accounted in the flowfield solver
- a strong and complex coupling between the mesh of the grain burnback solver and the main stream computational grid must be present

Hence, all these problems and peculiarities related to the 3D unsteady models of the bore chamber strongly reduce their use in the numerical simulations of SRM internal ballistic over IT.

1.5 SRM Internal Ballistics Analysis and Prediction: State of the Art

At the present state of the art many different numerical tools are present in the literature to simulate the internal ballistics of a given SRM. They have different degrees of accuracy, bore chamber dimensional models and, often, prediction abilities restricted to temporal bounded operating intervals (IT, QSS and TO), related to the sub-models connected to the gasdynamics model. Typically, 3D unsteady models of the internal ballistics are considered for the simulation of the Ignition Transient and for the two-phase and/or vortex shedding effects during particular instants in the Quasi Steady State. Instead, the use of 2D models is quite restricted, because of the typical grain configuration is 3D and 2D/axisymmetric configurations are quite limited in their use for SRM applications, as discussed before. Moreover, while Q1D unsteady models are potentially to be considered for the entire combustion time, in literature are present applications only for the IT or for the QSS and TO. While the use of unsteady or steady 0D model is restricted only to the operational phases subsequent to the Ignition Transient.

Unfortunately, the list can not be a complete outline of the existing internal ballistics codes. In fact, basically almost all the industries yielding SRM have own-made proprietary models which are covered by industrial secret. While some other numerical tools are adaptation of commercial tool tailored for the SRM numerical simulation. However, the internal ballistics models, classified by means of the internal ballistics phases modeled, are:

- for the Ignition Transient: SPIT [76], KUO [12], MUG [103; 97], ROCSTAR [86; 87];
- for the Quasi Steady State: PIBALL [73], SPP [77], ROCBALLIST [108], ROCSTAR;
- for the Tail Off: PIBALL, SPP, ROCBALLIST and ROCSTAR

The aforementioned internal ballistics numerical simulation models can be even classified by their dimensional modeling type of the bore chamber flowfield: 0D quasi steady or unsteady models (PIBALL, SPP , ROCBALLIST 0-D); Q1D unsteady models (SPIT, KUO, ROCBALLIST 1-D); 2D-3D unsteady models (MUG, ROCSTAR).

Hence, typically for the analysis, study and prediction of SRMs internal ballistics are used different numerical models for the Ignition Transient and for the subsequent operative phases: unsteady 3D, 2D or Q1D models for the former phase and, instead, in order to limit the computational time required, 0D unsteady or quasi steady models for the subsequent ones.

Concerning, instead, the grain burning surface evolution analysis, which is the main driving phenomena for the QSS and TO, there are a variety of ways to numerically and/or analytically represent the geometrical evolution of a 2D or 3D surface. The most popular one is certainly the Solid propellant rocket motor Performance Program (SPP)[77; 29], which describes the grain burning surface evolution by an analytical approach for 2D, axisymmetric and 3D geometries [29]. Because of complexity and lengthy computational requirements in setting up 3D shapes, users are encouraged to use 2D geometry rather that the 3D method, whenever possible. The 2D

grain geometry design consists of defining several planar cross sections of the grain propellant, with lines and arcs and the program assumes a linear transference of the port area, burning surface between the defined sections[29]. The surface evolution is simply made for linear segments using the normal to the line and arcs by adjusting the radius, assuming a spatially constant burning rate. The axisymmetric grain design method is similar to 2D and assumes differently a rotation around the motor axis. The geometrical properties are still evaluated using closed-form analytical methods. The 3D geometry uses a combination of nine analytical shapes to define, as intersection of them, the initial grain design: sphere, torus, plane, cylinder, cone, spheroid, hyperbolic torus, elliptical torus and parabolic torus. The method of analysis consists of mapping the 3D surface to a 2D plane and checking several boundary conditions such as other burning surfaces, insulation, or user-defined dummy boundaries [29].

Another different way is represented by phase-based methods (with a numerical layering technique). When possible and appropriate, grid-based geometry methods can be replaced by analytical methods, in order to reduce computational time required, hence, many analytical methods have been developed for several simple and complex cross-sectional geometries using numerical layering techniques [83; 78]. These methods describe the evolution of simple and complex 2D grain shapes by means of their division in time periods, or phases, within which the surface properties (port area, burn perimeter and wet perimeter) can be defined by a single set of equations in closed form.

Another completely general method is represented by the Level Set Method (LSM) [31], for which some recent interest has been considered for the grain burnback analysis [95; 98] and which will be analyzed in a deepened manner in the chapter 3, page 32. Briefly, the level set method embeds the interface as the zero level of a level set grid function defined on the domain of interest in order to track the motion of the grain burning surface. The evolution of the level zero is obtained evolving all the level set of the grid function, which is mathematically defined by an initial value Partial Differential Equation (PDE) that is an Hamilton-Jacobi (HJ) equation. This hyperbolic PDE is solved using entropy-satisfying schemes borrowed from the solution of the hyperbolic conservation laws, which select the correct vanishing viscosity solution. The level set method allows, in its general formulation, an easy evaluation of the motion of complex and topology varying interfaces, with simple computation of the front curvatures and normal direction.

A recent Lagrangian method is represented by the Face Offsetting Method (FOM)[104], based on a generalized Huygens' principle. This method operates directly on a Lagrangian surface mesh, without requiring an Eulerian volume mesh. Unlike traditional Lagrangian methods, which move each vertex directly along an approximate normal or user-specified direction, the face offsetting method propagates faces and then reconstructs vertexes through an eigenvalue analysis. Locally at each vertex the motion of the interface is solved along the normal and tangential directions of the interface itself simultaneously, in order to make a vertexes redistribution, to maintain and/or improve the mesh quality, as the front enlarges during its motion.

An important remark is that the last two methods (LSM and FOM) can be used for constant or space and time variable burning rate grain burnback analyses, as they perform a completely general approach for solving the moving boundary problem. While the others can be used only for spatially constant burning rate grain surface evolution evaluations.

1.6 Motivations

The doctoral reseach presented wants to be a step on the numerical modeling and consequent physical understanding on the SRM internal ballistics phenomena for the entire combustion time, which define the SRM performance and consequently its mission capabilities. Accurate

SRM performance models and prediction capabilities may, in fact, reduce the huge experimental costs necessary for SRMs design and development.

The approach considered is to use reduced models for the complex interacting physical and chemical phenomena that affect the combustion chamber conditions of a Solid Rocket Motor, rather than direct, unfeasible, prime principle approaches. In fact, several key physical phenomena are not still well understood. With the current state of the art of the numerical simulation tools for the internal ballistics, indeed, even nominal performance prediction is still not possible in many cases, because of the too simplified internal ballistics simulation models considered up to now. As a matter of fact, in the open literature it is difficult to find Q1D studies of the SRM internal ballistics for the entire combustion time, from motor start up to burn out which, as the one that will be proposed in this work. At the present computational power available, in fact, these models are the only way to perform numerical simulation for the whole combustion time. Thus, the numerical simulation of the SRM internal ballistics is typically focused on the QSS phase and the TO phase with the use of simple 0D quasi steady or, at the most, unsteady models. But these models are not able to describe some key phenomena, that may strongly affect the SRM behaviour.

The objective proposed must certainly face the problem of the study of the 3D grain surface evolution in time, due to the grain regression, defined by its combustion. In fact, these phenomena principally lead the SRM internal flowfield conditions during Quasi Steady State and Tail Off. This last achievement certainly opens a wider scenario in terms of more complex internal ballistics simulations, which can be done in order to have a better understanding of some time-limited phenomena that can affects the SRM behaviour.

The final objective of this work is, hence, to develop and present a Q1D SRM internal ballistics numerical simulation tool, coupled with a 3D grain burnback simulation model. The internal ballistics model is able to perform SRMs internal flowfield conditions simulations and analyses, predictions and reconstructions of the SRM behaviour, for the whole combustion time of a given SRM.

1.7 Structure of the Work

The present Ph. D. Dissertation is organized, excluding this introductory chapter, as following:

- Part I: SRM Internal Ballistics Models and Numerical Simulation: it describes the internal ballistics mathematical, physical and numerical models, necessary to describe all the main driving phenomena of the SRM combustion chamber flowfield conditions.
  - Chapter 2: SPINBALL Model: it presents the Solid Propellant rocket motor Internal Ballistics, by a physical, mathematical and numerical point of view. It considers the background work status and the developments carried on during this thesis work, in order to make the numerical simulation of the internal ballistics for the SRM ignition to burn out.
  - Chapter 3: GREG Model: this chapter deals with the problem of evaluating the evolution of the grain burning surface during time. It illustrates the main requirements that must be fulfilled by the technique chosen and the mathematical properties of the problem of tracking interfaces and in particular, the application to the grain burning surface evolution. A brief review of the state of the art in grain burnback models is also made, and the technique developed during this work is presented, remarking the main advantages and drawbacks. In particular, the techniques developed to describe the complex 3D grain propellant shape and to evaluated the grain geometrical properties during its evolution in time are extensively discussed.
  - Chapter 4: SPINBALL/GREG Coupling: it describes the way in which the grain burnback model and the internal ballistics model have been coupled in this thesis work, considering the potential possible coupling ways, with their limits of application and possible consequences on the computed internal ballistics solution.

- Part II: Results : this part shows and analyzes the results on this research activity provided by the models described in the Part I.
  - Chapter 5: GREG Validation: it draws out the test cases performed for the validation of the grain burnback model, starting from some literature test cases, a test for the accuracy of the numerical scheme chosen and the ones made for the validation of the technique for the evaluation of the grain geometrical properties.
  - Chapter 6: GREG Results: this chapter is dedicated to the analysis of the results obtained by the grain burnback model for the study of the 3D evolution of the grain burning surface in time for three SRMs.
  - Chapter 7: SPINBALL Results: it describes the analysis of SRMs internal ballistics numerical simulations of three SRMs, yielded with the numerical tool devised in this thesis work.
- Conclusions : it presents the conclusions of the work performed.

Part I

SRM Internal Ballistics Models and Numerical Simulation

2

SPINBALL Model

In this chapter the physical, mathematical and numerical models of the Solid Propellant rocket motor Internal Ballistics (SPINBALL) model for the internal ballistics numerical simulation of the entire combustion time, from motor start-up to burn out, are presented.

The attention will be particularly focused on the models which describe the driving phenomena over the IT: the gasdynamical model, the cavity model and the burning rate models, partially developed during this thesis work. The other sub-models that are part of the SPINBALL model, as heritage of the Solid Propellant rocket motor Ignition Transient (SPIT) model, will not be discussed. But they will be briefly mentioned for completeness and clarity in the following section 2.3, page 25, as they are not fundamental parts of this thesis work. Detailed descriptions of these sub-models can be, however, found in the works [80; 76; 75; 66; 67]. In fact, the SPINBALL model, devoted to the numerical simulation of the entire SRM combustion time, is an evolution of the existing SPIT model, which is instead tailored to the numerical simulation of only the IT.

The grain burning surface evolution model is not directly embedded in the SPINBALL model. It will be discussed in the chapter 3, page 32. While the possible integration and coupling ways of the gasdynamical models of SPINBALL and the grain burnback analysis model will be analyzed and described in the chapter 4, page 79.

2.1 Gasdynamical Model

The phenomenological description of the internal ballistics flowfield features during the overall combustion time, divided into Ignition Transient, Quasi Steady State and Tail Off, made in paragraph 1.2, page 2, points out the main modelling capabilities, that the gasdynamical model must describe.

The presence of different gases (igniter, pressurant gas and grain combustion products) is particular important for the description of the IT phenomena, together with the ability of the gasdynamics to capture strong unsteady and discontinuous flowfield features. In fact, both the propagation velocity of the pressure waves and of the contact discontinuity and their energy content can be altered, if the mixture nature of the bore gases is not taken properly into account.

In the same time, the possibility to consider the variations with the pressure of the grain combustion products mixture thermophysical properties, and the ones due to the non-ideality of the grain combustion processes, can be important during all the QSS and TO, since the flowfield pressure condition may have a wide range of variation from the reaching of QSS conditions to the motor burn-out. Moreover, the gasdynamical model formulation must take into account the bore geometrical variations due to the grain burning surface evolution in time and, in case of the nozzle geometrical evolution, due to relevant ablation phenomena of the nozzle Thermal Protections surface.

The SPINBALL gasdynamical unsteady Q1D model is based on the assumption of an Eulerian unsteady flowfield model with mass, momentum and energy addition and geometry evolution

in space and time. The SRM geometry is represented in the Q1D view of the problem with the converging and diverging part of the nozzle, while the cross sectional area does not account for the possbile presence of grain slots, floaters channels and submergence regions. The effect on the Q1D flowfield conditions are represented as source terms in the Q1D mass and energy equations (see paragraph 2.1.2, page 18). The thermophysical properties of the bore mixture are considered variable in both space and time during the numerical simulation, with a mixture thermodynamics standard model, as described in the following. The assumption of a one-phase (gas only) mixture of non-reacting perfect gases is also made, assuming that all the grain combustion chemical reaction occur in an ideal thin layer on the grain propellant surface. The mass addition of the grain propellant and from the slots, floaters or submergence regions is considered with zero axial momentum, while the igniter jets effects on the momentum equation are taken into account with an igniter sub-model.

Unlike the gasdynamical formulation used in SPIT, named 3-gases formulation, where there are considered three mass conservation equations, one for each single species of the mixture (igniter combustion products, pressurizing gas and propellant combustion products), and the problem is focused on the concentration transport of species, in SPINBALL the point of view is quite different. In the 3-gases model, in fact, the thermophysical characteristics of the mixture is given by a weight average of the thermophysical parameters of the single species, assumed to be spatial and time constant, with weights, the concentrations of the single species present in the generic cell, at the considered time . Hence, the thermophysical characteristics of the bore added gases are considered constant too.

Focusing again on the SPINBALL gasdynamical model formulation and assuming the previous hypothesis, the conservation equations for an compressible mixture of gases is are a set of differential equations composed by: six mass conservation equations for each mixture component, one momentum conservation equation and one energy conservation equation for the gases mixture present in the bore (see equation 2.1); closed by perfect gases equation.

$$\begin{cases} \dfrac{\partial\left(\rho_i A_p\right)}{\partial t}+\dfrac{\partial\left(\rho_i u A_p\right)}{\partial x}=r_b P_b \rho_p+\dfrac{\dot{m}_s A_p}{V}+\dfrac{\dot{m}_{ig} A_p}{V} & \text{for } i=1,\ldots,6 \\ \dfrac{\partial\left(\rho u A_p\right)}{\partial t}+\dfrac{\partial\left[\left(\rho u^2+p\right) A_p\right]}{\partial x}-p\dfrac{\partial A_p}{\partial x}=\dfrac{\dot{m}_{ig} A_p \bar{v}_{inj}}{V}+\dfrac{1}{2}\rho u^2 c_f & \\ \dfrac{\partial\left(\rho E A_p\right)}{\partial t}+\dfrac{\partial\left[\left(\rho E+p\right) u A_p\right]}{\partial x}=r_b P_b \rho_p H_f+\dfrac{\dot{m}_{ig} A_p H_{ig}}{V}+\dfrac{\dot{m}_s A_p H_s}{V} & \end{cases} \tag{2.1}$$

Equation 2.1 is a system of hyperbolic Partial Differential Equations, characterized by strongly non-linear source terms, for which the following remarks are given:

- the source terms including $\dot{m}_s$ are non zero in the flow regions nearby the grain slots, floaters or submergence zone
- the source terms accounting the mass, momentum and energy due to the igniter $\dot{m}_{ig}$ are non-zero only in the its control volume, defined by the igniter and impingement region sub-models
- the source terms due to grain propellant combustion products inlet are non-zero when the propellant is ignited (which is defined by an ignition criterion)
- the friction term in the momentum equation are non-zero only in the nozzle and on the propellant surface when it is not still ignited

The formulation considered in SPINBALL, named infinite-gases formulation, is not interested in the spatial and time evolution in the chamber of the single mixture gas (igniter, pressurant or

propellant combustion products), as the one in SPIT does. In fact, it makes an evaluation of the mixture properties present in each cell, space and time variables, considering the mass fluxes of the mixture coming from adjacent cells, located at the left and right of the considered one, and from the sources terms from the grain combustion reactions, the igniter and the cavity model. Thus, the thermophysical properties of the mixture in a generic cell is given by a weigh average of the gases mixture coming from left-right cells and source terms, with coefficients defined by concentrations of each mixture present in the cell at considered time marching step.

In fact, really the implementation of the six mass conservation equations in equation 2.1 hides the so called infinite gases formulation for the mixture gas components, as will be explained in the following.

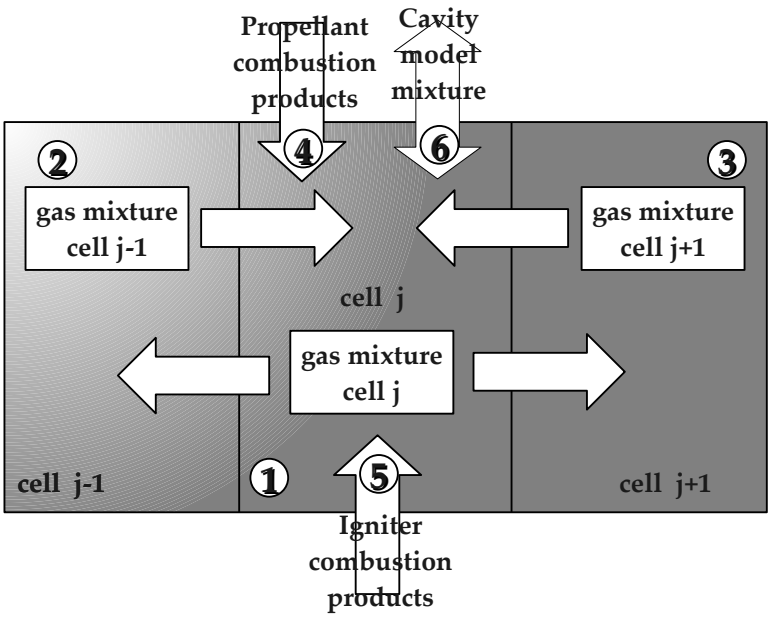

Figure 2.1: SPINBALL infinite-gases model

Naming with the indices illustrated in figure 2.1, respectively:

- 1 for the generic (j)-th cell
- 2 for the $(j-1)$-th cell
- 3 for the $(j+1)$-th cell
- 4 for the propellant combustion products gases
- 5 for the igniter combustion products gases
- 6 for the cavity exchanging mixture gases

we have the six mass conservation equation shown in equation 2.2, where the sources terms are generically indicated with the symbol $\dot{\rho}$.

$$\frac{\partial(\rho_i A_p)}{\partial t} + \frac{\partial(\rho_i u A_p)}{\partial x} = \dot{\rho}_i \qquad \text{for } i = 1,\dots,6 \tag{2.2}$$

The global mass equation written in 2.1, is simply obtained by equation 2.2, considering equation 2.3.

$$\rho = \sum_{i=1}^{6} \rho_i \tag{2.3}$$

In order to understand how the mixture formulation is able to deal with thermophysical properties variable in space and time, we consider the equation for the mass conservation in a discretized manner. Thus, the single equation for the i-th gas of the mixture can be discretized in a conservative fashion integrating in space over the meshgrid cell and over time in the timestep (as made in paragraph 3.4.1, page 44), as shown in equation 2.4 .

$$(\rho_i A_p)_j^{n+1} = (\rho_i A_p)_j^n - \frac{\Delta t}{\Delta x}\left[(\rho_i u A_p)_{j+\frac{1}{2}} - (\rho_i u A_p)_{j+\frac{1}{2}}\right] + (\dot{\rho}_i)_j^n \qquad \forall i = 1,\dots,6 \tag{2.4}$$

For every timestep, it is supposed that the system is constituted by six gases, of which three purely advected and the other three purely added to the main flow. The initial condition for every timestep is that, focusing the attention on the j-th cell, it is defined only by the gas mixture 1, while the left and right cells, respectively by mixtures gases 3 and 2. Now, considering the following simplification due to the nomenclature used for the indices and given the interface velocity values for the solution of the Riemann problem (see paragraph 2.4.1, page 30), we have that:

1. generic (j)-th cell

$$\rho_1^n = \begin{cases} \rho_j^n & \text{for } x_{j-\frac{1}{2}} \leqslant x \leqslant x_{j+\frac{1}{2}} \\ 0 & \text{otherwise} \end{cases}$$

$$\dot{\rho}_1 = 0 \quad \forall x$$

$$(\rho_1 u A_p)_{j+\frac{1}{2}}^n = \begin{cases} 0 & \text{if } u_{j+\frac{1}{2}}^n < 0 \\ (\rho u A_p)_{j+\frac{1}{2}}{}^n & \text{if } u_{j+\frac{1}{2}}^n > 0 \end{cases} \tag{2.5}$$

$$(\rho_1 u A_p)_{j-\frac{1}{2}}^n = \begin{cases} 0 & \text{if } u_{j-\frac{1}{2}}^n > 0 \\ (\rho u A_p)_{j-\frac{1}{2}}{}^n & \text{if } u_{j-\frac{1}{2}}^n < 0 \end{cases}$$

2. generic $(j-1)$-th cell

$$\rho_2^n = \begin{cases} \rho_{j-1}^n & \text{for } x_{j-\frac{3}{2}} \leqslant x \leqslant x_{j-\frac{1}{2}} \\ 0 & \text{otherwise} \end{cases}$$

$$\dot{\rho}_2 = 0 \quad \forall x$$

$$(\rho_2 u A_p)_{j+\frac{1}{2}} = 0 \quad \forall j \, \forall n \tag{2.6}$$

$$(\rho_2 u A_p)_{j-\frac{1}{2}}^n = \begin{cases} 0 & \text{if } u_{j-\frac{1}{2}}^n < 0 \\ (\rho u A_p)_{j-\frac{1}{2}}^n \Longrightarrow (\rho_2 u A_p)_j^{n+1} = 0 & \text{if } u_{j-\frac{1}{2}}^n > 0 \end{cases}$$

3. generic $(j+1)$-th cell

$$\begin{aligned}
&\rho_3^n = \begin{cases} \rho_{j+1}^n & \text{for } x_{j+\frac{1}{2}} \leqslant x \leqslant x_{j+\frac{3}{2}} \\ 0 & \text{otherwise} \end{cases} \\
&\dot{\rho}_3 = 0 \quad \forall x \\
&(\rho_3 u A_p)_{j+\frac{1}{2}}^n = \begin{cases} 0 & \text{if } u_{j+\frac{1}{2}}^n > 0 \\ (\rho u A_p)_{j+\frac{1}{2}}^n \Longrightarrow (\rho_3 u A_p)_j^{n+1} = 0 & \text{if } u_{j-\frac{1}{2}}^n < 0 \end{cases} \\
&(\rho_3 u A_p)_{j-\frac{1}{2}}^n = 0 \quad \forall j \, \forall n
\end{aligned} \tag{2.7}$$

4. propellant combustion products gases source term (depending on the grain ignition and presence [1])

$$\begin{aligned}
&\rho_4^n = 0 \quad \forall j \, \forall n \\
&\dot{\rho}_4 \neq 0 \; \dot{\rho}_4 = \rho_p \, (r_b P_b)_j^n \, \Delta x \quad \forall x \\
&(\rho_4 u A_p)_{j+\frac{1}{2}}^n = 0 \quad \forall j \, \forall n \\
&(\rho_4 u A_p)_{j-\frac{1}{2}}^n = 0 \quad \forall j \, \forall n
\end{aligned} \tag{2.8}$$

5. igniter combustion products gases source term (depending on the igniter and impingement region model[1])

$$\begin{aligned}
&\rho_5^n = 0 \quad \forall j \, \forall n \\
&\dot{\rho}_5 \neq 0 \quad \forall x \\
&(\rho_5 u A_p)_{j+\frac{1}{2}}^n = 0 \quad \forall j \, \forall n \\
&(\rho_5 u A_p)_{j-\frac{1}{2}}^n = 0 \quad \forall j \, \forall n
\end{aligned} \tag{2.9}$$

6. cavity exchanging mixture gases source term (depending on the cavity presence[1])

$$\begin{aligned}
&\rho_6^n = 0 \quad \forall j \, \forall n \\
&\dot{\rho}_6 \neq 0 \quad \forall x \\
&(\rho_6 u A_p)_{j+\frac{1}{2}}^n = 0 \quad \forall j \, \forall n \\
&(\rho_6 u A_p)_{j-\frac{1}{2}}^n = 0 \quad \forall j \, \forall n
\end{aligned} \tag{2.10}$$

Once evaluated the density partials values at the next timestep, we use equation 2.3 to update the overall mixture density and we evaluate the new concentrations of gases present in the generic cell by equation 2.11.

$$c_{i_j}^{n+1} = \frac{\rho_{i_j}^{n+1}}{\rho_j^{n+1}} \tag{2.11}$$

Then we evaluate the new thermophysical properties of the mixture of gases present in the generic cell, as defined by equation 2.12, the gas mixture constant and the generic specific heat (at constant pressure or volume) and then all the derived quantities.

1 see reference [80] for more details

$$
\begin{aligned}
R_j^{n+1} &= \sum_{i=1}^{6} {c_i}_j^{n+1} R_i^n = \sum_{i=1}^{6} \frac{{\rho_i}_j^{n+1} R_i^n}{\rho_j^{n+1}} \\
C_j^{n+1} &= \sum_{i=1}^{6} {c_i}_j^{n+1} C_i^n = \sum_{i=1}^{6} \frac{{\rho_i}_j^{n+1} C_i^n}{\rho_j^{n+1}} \\
\mu_j^{n+1} &= \sum_{i=1}^{6} {c_i}_j^{n+1} \mu_i^n = \sum_{i=1}^{6} \frac{{\rho_i}_j^{n+1} \mu_i^n}{\rho_j^{n+1}}
\end{aligned}
\tag{2.12}
$$

At last, we set the condition for the new iteration.

Thus, this approach allows to consider the presence in the bore of a non-reactive mixture of perfect gases with thermophysical properties variable in space and time, as the thermophysical properties of the source terms can be variable and the mixture content and thermophysical properties in each cell is update at every timestep. Consequently, it makes possible to evaluate the variations with pressure of the thermophysical characteristics of added gases from grain burning processes, supposing that the chemical equilibrium is reached. But even, through combustion efficiency, the non-ideal equilibrium point of chemical burning reactions, that brings a variation from ideal conditions of the source terms properties. Moreover, this approach allows to consider, in potential, also the low but present mass addition into the bore caused by the casing Thermal Protections consumption due to ablation phenomena, related to their discovering and chamber hot gases exposure, as the grain is consumed during time, if a suitable model is introduced. The grain combustion products thermophysical properties, in fact, as well as the combustion products enthalpy, are evaluated depending on local pressure value, taking into account the combustion efficiency, through the access to chemical equilibrium tables, generated starting from the known grain propellant composition by chemical equilibrium models [38; 44].

2.1.1 Initial and Boundary Conditions

As the Solid Propellant rocket motor Internal Ballistics model considers the numerical simulation of the internal ballistics for the entire combustion time, the Initial Condition (IC) are very simple to be imposed, since they are the physical and geometrical conditions of the SRM at motor start-up. Hence, the geometrical Q1D configuration of the motor is set up starting from the grain, nozzle and igniter geometrical data. While the other initial conditions are only related to the initial state of the pressurizing gas, that typically has a pressure slightly higher that the atmospheric pressure in order to preserve the chamber inner environment.

For what concern the BC, wall Boundary Conditions (BCs) are initially assumed at both the head-end and the nozzle throat, in order to simulate the typical presence of the nozzle seal, which scope is to protect to combustion chamber environment from the atmospheric or external agents. When a prescribed differential pressure is reached (which is typically a design parameter of the nozzle seal), the nozzle diaphragm is removed and the external pressure value is defined at the nozzle exit section. Then, supersonic outflow BC is imposed with an extrapolation of the solution from the inner flowfield, since for all typical SRM configurations, immediately after the nozzle seal rupture, sonic conditions at the nozzle throat are reached.

2.1.2 Cavity Model

The evaluation of the evolution for the cavities, so that slots, floaters and submergence region, is obtained by means of the conservation equations volume averaging over the cavity, based on the experimental and theoretical evidence that these regions are characterized by small flow velocities with typical generation of flow recirculating zones. The resultant model, so called oD model of the cavity, is defined by the mass and energy equations that bring to a system of two Ordinary Differential Equations (ODEs). This model is an adaptation of the one implemented

in the SPIT model (see Ref. [80]), to take into account the formulation with thermophysical properties variable.

For simplicity we consider a cavity whose length is exactly equal to one meshgrid cell defined by the chamber discretization by the Q1D flowfield model, as represented in figure 2.2.

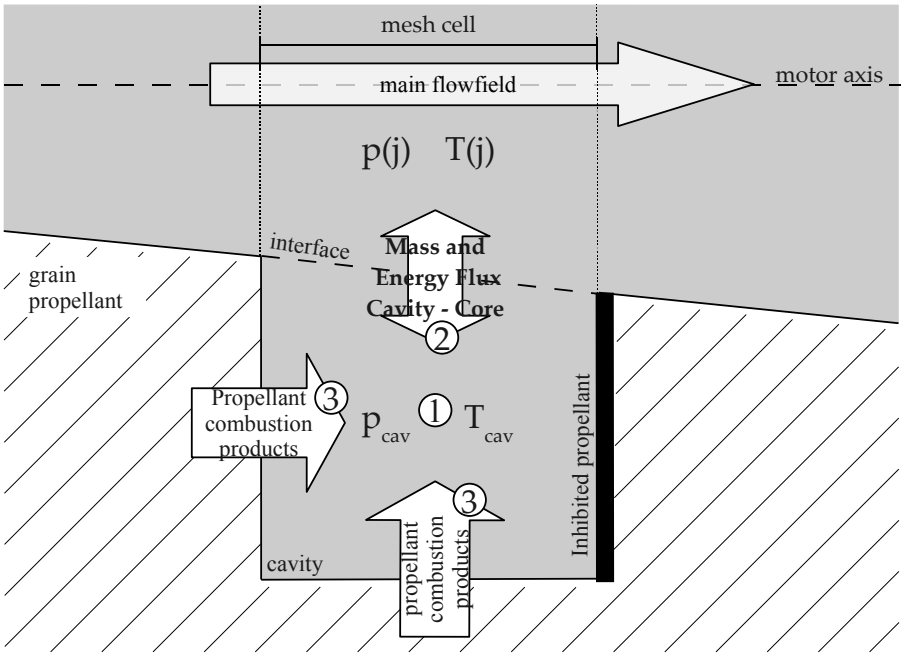

Figure 2.2: Cavity model sketch

Knowing the core flowfield conditions in the cell j-th of the Q1D computational mesh at a given timestep n, we call the thermodynamics cavity fluid state with p^n_{cav}, T^n_{cav} and ρ^n_{cav}. Note that in a consistent manner with the infinite-gases formulation of the mixture in the combustion chamber, we consider the mixture properties of the cavity known at timestep n, indicated with index 1 (see figure 2.2). We have to evaluate the evolution of the cavity thermodynamics state and mixture thermophysical properties at the next timestep $n+1$ and the energy and mass exchanging with the bore indicated with index 2 (which is seen by the infinite-gases formulation of the Q1D gasdynamics model as source term 6). Moreover, the propellant combustion products gas inlet is known, active if the grain propellant inside the cavity is ignited otherwise zero, and named with index 3. In this manner, in fact, as for the given formulation of the Q1D unsteady Euler equations, we can take into account the variation with pressure and combustion efficiency of the thermophysical properties of the grain propellant combustion products. Hence, at the generic given timestep in the cavity, we have only the mixture of gases indicated with index 1.

The coupling between the flowfield evolution along the chamber and the state evolution inside the cavity is given by the evaluation of the mass and energy exchange, as a function of the pressure jump at their interface. Since conservation equations are averaged on the cavity volume, the amount of the mass exchange is calibrated, in order to obtain a delay corresponding to a finite mass transfer velocity, as in real conditions.

The pressure inside the cavity at the next timestep is, hence, evaluated by equation 2.13, where α is the calibration coefficient to tune the finite mass and energy transfer velocity.

$$p^{n+1}_{cav} = p^n_{cav} - \alpha \left(p^n_{cav} - p\,(j)^n \right) \tag{2.13}$$

Once we have an evaluation of the pressure inside the cavity, we can obtain also the variation of the cavity enthalpy from timestep n to $n+1$, as defined by equation 2.14, where the single terms are also expressed respectively, H^n_{cav} the cavity enthalpy at the timestep n, H^n_{pr} the enthalpy

inlet by grain propellant combustion products and H_{cav}^{n+1} the cavity enthalpy at the timestep $n+1$.

$$\begin{aligned}
\Delta H_{cav} &= -\left(H_{cav}^{n} + H_{pr} - H_{cav}^{n+1}\right) \\
H_{cav}^{n} &= c_{p_{cav}}^{n} \cdot m_{cav}^{n} \cdot T_{cav}^{n} \\
H_{pr}^{n} &= r_b^n \cdot S_b^n \rho_p \cdot \Delta t \cdot T_f^n \\
H_{cav}^{n+1} &= c_{p_{cav}}^{n} \cdot p_{cav}^{n+1} \frac{V_{cav}^{n}}{R_{cav}^{n}}
\end{aligned} \tag{2.14}$$

Now, by the sign of the ΔH_{cav}, it is possible to obtain the direction of the flow across the ideal interface cavity-core due to the Q1D modelling of the combustion chamber.

- if $\Delta H_{cav} > 0$
  We have a mass and energy spillage from the chamber to the cavity, and the updating of the total mass of the gas mixtures 1, 2 and 3 is given in equations 2.15, 2.16 and 2.17.

$$\Delta m_{cav_1} = 0 \tag{2.15}$$

$$\Delta m_{cav_2} = \frac{\Delta H_{cav}}{c_p(j)\, T(j)} \tag{2.16}$$

$$\Delta m_{cav_3} = r_b^n S_b^n \rho_p \cdot \Delta t \tag{2.17}$$

- if $\Delta H_{cav} < 0$
  We have, as opposite, a mass spillage from the cavity to the chamber, and this time, the updating of the total mass of the gas mixtures 1, 2 and 3 is given in equations 2.18, 2.19 and 2.20.

$$\Delta m_{cav_1} = \frac{\Delta H_{cav}}{c_{p_{cav}}^{n} T_{cav}^{n}} \tag{2.18}$$

$$\Delta m_{cav_2} = 0 \tag{2.19}$$

$$\Delta m_{cav_3} = r_b^n S_b^n \rho_p \cdot \Delta t \tag{2.20}$$

Hence, the single mixture of gases total masses in the chamber can be updated together with the cavity total mass, density and temperature, and the new concentrations for the cavity mixture components evaluated (see equations 2.21, 2.22, 2.23, 2.24 and 2.25)

$$m_{cav_i}^{n+1} = m_{cav_i}^{n} + \Delta m_{cav_i} \quad \text{for } i = 1, \ldots, 3 \tag{2.21}$$

$$m_{cav}^{n+1} = \sum_{i=1}^{3} m_{cav_i}^{n+1} \tag{2.22}$$

$$\rho_{cav}^{n+1} = \frac{m_{cav}^{n+1}}{V_{cav}^{n}} \tag{2.23}$$

$$T_{cav}^{n+1} = \frac{p_{cav}^{n+1}}{R_{cav}^{n+1} \cdot \rho_{cav}^{n+1}} \tag{2.24}$$

$$c_{cav_i}^{n+1} = \frac{m_{cav_i}^{n+1}}{m_{cav}^{n+1}} \tag{2.25}$$

Thus, by the concentrations, it is possible to evaluate the mixture thermophysical properties, as given by equation 2.12, and for all the derived quantities.

Hence, the mass source term for the cavity interaction with the Q1D flowfield representation is given by equation 2.16 or equation 2.18, depending on the sign of H_{cav} and shown in equations 2.26 and 2.27. While the energy source term is given directly by equation 2.14 divided by the term $\Delta x \Delta t$.

$$\dot{m}_s = \frac{\Delta H_{cav}}{c_{p_{cav}} T_{cav} \cdot \Delta x \Delta t} \quad \text{if} \quad \Delta H_{cav} < 0 \tag{2.26}$$

$$\dot{m}_s = \frac{\Delta H_{cav}}{c_p(j)\, T(j) \cdot \Delta x \Delta t} \quad \text{if} \quad \Delta H_{cav} > 0 \tag{2.27}$$

At last, the cavity properties are rearranged in order to give the initial formulation of the mixture present in the cavity for the next timestep (so all the cavity gas is represented by the index 1).

2.2 Burning Rate Model

The combustion phenomena and mechanisms of solid propellants are quite complex and dependent on many local fluid dynamics, chemical and thermal conditions to which the combustion process occurs. Hence, far from deepened studies on combustion processes [53; 61; 63; 24; 37], many propellant grain combustion model used for internal ballistics numerical simulations are simplification of these dependencies, retaining the main ones. Focusing the attention on the macroscopic results of the combustion phenomena given by the grain propellant regression rate, so called grain burning rate. The grain burning rate can be defined as the the grain regression distance per unit of time, perpendicular pointwise to the grain burning surface. In particular, a wide assumption is to not consider at all the complex physical and chemical processes occurring at the propellant surface nearby the combustion region, assuming in the chamber a non reacting mixture of perfect gases, given by the grain combustion products at the chemical equilibrium. Hence, the models for the grain burning rate, as the most important effect for the internal ballistics, are typically given by semi-empirical expressions, where some experimental investigations parameters must be evaluated and imposed for the grain propellant considered. Thus, the overall grain burning rate can be seen as the superposition of different effects, related to different and separated phenomena that can describe the combustion processes. So the burning rate can be split into three separated components: the quasi steady term, related to motor pressurization, a non-linear unsteady term, dependent mainly on the pressurization rate and the erosive contribution, related primarily to the crossflow flowfield velocity.

In Q1D models for the SRM internal ballistics simulation, the efforts of a more accurate internal ballistics model than 0D ones, can account for effects related to the erosive burning, that 0D model can not describe at all. While the other two terms can be potentially modeled by both the internal ballistics models.

The burning rate model adopted in SPINBALL, partial heritage of the SPIT model, is based on the classical assumption that all the chemical reactions are very fast and occur in an ideal thin layer, located at the surface of the solid propellant. The total burning rate is assumed as the sum of a term dependent on the pressure, given by the classical APN expression, and an erosive term dependent on the gas flow rate, with the classical formulation due to Lenoir Robillard (LR)[4] (with the corrections due to Lawrence[10] and Beddini[15]), which will be discussed in the following. A separated section is, instead, briefly dedicated to the dynamic burning, based on the Zeldovich-Novozhilov (ZN) model, which is not yet implemented in the

internal ballistics model, since in some discussed results in the chapter 7, page 130, it will help the understanding of the yielded achievements, in comparison with the published ones.

2.2.1 Quasi-Steady Burning Rate

The most utilized quasi-steady pressure dependent model to predict solid propellant burning rate is the so called APN model, which is a semi-empirical model. The APN model considers the grain burning rate quasi-steady term as dependent on the mean local pressure, as given by equation 2.28, named De-Vieille Saint Robert law.

$$r_b = a \left(\frac{p}{p_{ref}} \right)^n \tag{2.28}$$

Two semi-empirical parameters are introduced a and n which main dependencies are expressed in equation 2.29 for a given propellant.

$$\begin{cases} a = a(p, T_i) = a_{ref} e^{\sigma_p (T_i - T_{ref})} \\ \\ n = n(p) \end{cases} \tag{2.29}$$

Typically, the a and n empirical coefficients are considered constant for wide pressure ranges, and are experimentally evaluated in given pressure ranges, by means of the Crawford Bomb or the BARIA testing. The introduced modeling for the grain initial temperature T_i dependence of the a parameter, defines the propellant temperature sensitivity, as related to σ_p coefficient, that must be evaluated experimentally too, together with the a_{ref} parameter at a reference temperature T_{ref}.

2.2.2 Erosive Burning Contribution

The erosive burning effects become important in SRMs with high gas crossflow velocities and can strongly affect the SRM internal ballistics and performances. They define, in fact, an increase on the quasi-steady burning rate, especially during the IT and also in the first part of the QSS, for certain SRM configurations. This typically occurs in SRM with large length-to-diameter ratio and low port area-to-throat area ratio and grain designed with star-aft configurations. Moreover, the occurrence of relevant erosive burning can define in unpredicted pressurization of the combustion chamber and unequal web consumption of the propellant. These effects can heavily modify the combustion surface evolution in time and result in a early exposure to hot gases of parts of the motor case.

The erosive burning mechanism is believed to be caused by the increase in the gas to solid heat feedback and by the turbulence enhanced mixing and reaction of the oxidizer or fuel rich gases pyrolyzed from composite propellants [22; 24].

The erosive burning mechanism is quite complicated and, hence, many correlation theoretical-experimental activities have been carried out in order to have a deep understanding of the phenomenon [94; 48]. Notwithstanding, a very simple and successfull used model for the erosive burning is the Lenoir Robillard model [4], that considers the main cause of the effects related to an additional heat flux to the propellant.

The model assumes a splitting of the heat transfer to the grain propellant from the flame zone into two separate independent mechanisms. The first is the heat transfer from the primary burning zone, that depends only on the pressure local value (that can be modelled in term of contribution to the burning rate with the APN model). The second one is due to the combustion gases flowing over the surface and is only related, as stated before, to the crossflow velocities. Since, these two mechanisms are assumed to be independent, the two burning rate terms are additive 2.30 [108].

$$r_b = r_{b_p} + r_{b_e} \tag{2.30}$$

The erosive term for the LR model can, hence, following [4], be expressed by the equation 2.31, where the α parameter can be assigned from empirical data or evaluated with equation 2.32.

$$r_{b_e} = \alpha \frac{(\rho u)^{0.8}}{L^{0.2}} e^{-\frac{\beta r_b \rho_p}{\rho u}} \tag{2.31}$$

$$\alpha = 0.0288 C_p \mu^{0.2} Pr^{-2/3} \frac{1}{\rho_p C_{pr}} \frac{T_f - T_s}{T_s - T_i} \tag{2.32}$$

The equations 2.31 and 2.32 allow to evaluate the erosive burning contribution using only the empirical value of the β parameter. This parameter accordingly to [4] is assumed to be 53; while instead Lawrence et al. [10] use different values of this parameter to fit the experimental data.

However, it is known that for large scale SRM, the LR model overpredict the erosive burning term [10; 15]. In particular, the overprediction has been attributed to the use of the distance from the SRM head end for evaluating the Reynolds number characteristic length L in equation 2.31. Hence, Lawrence et al. proposed a slight modification of the original Lenoir Robillard model, that was found to be more accurate for large-scale SRMs. This modification replaced the axial distance L with the hydraulic diameter D_h, as expressed in equation 2.33.

$$r_{b_e} = \alpha \frac{(\rho u)^{0.8}}{D_h^{0.2}} e^{-\frac{\beta r_b \rho_p}{\rho u}} \tag{2.33}$$

Where the expression of the hydraulic diameter is given in the equation 2.34, using the wet perimeter and the port area.

$$D_h = \frac{4 A_p}{P_w} \tag{2.34}$$

A further improvement of the LR model is given by Beddini [15], in order to retain the original LR model and further improve the model ability to predict the erosive burning effects on large SRMs. It considers, again, the substitution of the L length with an empirical fitted function, dependent on the hydraulic diameter, given in the equation 2.35.

$$f(D_h) = 0.90 + 0.189 D_h \left[1 + 0.043 D_h \left(1 + 0.023 D_h\right)\right] \tag{2.35}$$

2.2.3 Dynamic Burning Rate

The dynamic burning rate term represents a correction to the quasi-steady burning rate model, in order to account the effects of non-steady combustion processes, due in particular to unsteady phenomena occurring in the combustion chamber. Hence, the effects of the dynamic burning must be expected to affect only transient phenomena of the SRM internal ballistics, thus: the propellant ignition and initial pressurization during the IT, the tail off phase and possible motor pulsing related to motor acoustic instability.

A very simple, but in the meantime, smart model to describe the non-quasi-steady burning rate term in represented by the Zeldovich-Novozhilov model for the dynamic burning. It provides a simple way to represent the conductive heat feedback from the surface to the gas phase [63], that modify in some manner the grain propellant combustion processes.

In the steady state, or the quasi steady state burning laws for the grain propellant, we have that, in the assumption that the condensed phase is transformed into gaseous products in an infinitely thin layer, the grain burning rate and the surface temperature of the grain burning surface are known as functions (theoretically by flame models or experimentally) of the pressure and the initial grain temperature (equation 2.36).

$$\begin{cases} r_b = r_b\left(p, T_i\right) \\ \\ T_s = T_s\left(p, T_i\right) \end{cases} \tag{2.36}$$

We consider now the 1D steady heat equation with a moving interface, expressed by 2.37 with the required BCs.

$$\begin{cases} \rho_p r_b \dfrac{dT}{dx} = k_p \dfrac{d^2T}{dx^2} \\ \\ T\left(-\infty\right) = T_i \\ \\ T\left(0\right) = T_s \\ \\ \left.\dfrac{dT}{dx}\right|_{x=0^-} = \dfrac{k_g \left.\dfrac{dT}{dx}\right|_{x=0^+} + \rho_p r_b Q}{\alpha_p} \end{cases} \tag{2.37}$$

The equation 2.37 has an analytic solution in terms of temperature profile and heat flux at the interface $x = 0$, as given by equation 2.38.

$$\begin{cases} T\left(x\right) = T_i + \left(T_s - T_i\right) e^{\frac{r_b x}{\alpha_p}} \\ \\ \left.\dfrac{dT}{dx}\right|_{x=0^+} = \dfrac{r_b}{\alpha_p}\left(T_s - T_i\right) \end{cases} \tag{2.38}$$

Assuming that is not possible to use steady-state relations 2.36 directly in the theory of non-steady burning, the key point of the ZN model is the following. The instantaneous state of the gas-phase chemical reaction zone and the thin condensed phase in which chemical reactions occurs, by no means depend on the temperature profile far from these regions [45]. Hence, to consider the unsteady process it occurs to introduce, instead of the dependence on T_i, some other parameters of the condensed phase, that directly affects the combustion regions. This parameter is identified in the surface heat flux. Therefore, the Zeldovich-Novozhilov model assumes and consists of using the steady burning laws and the integral energy equations to transform the steady burning laws into a from valid for the non-steady burning [108], by modifying just the dependence from the T_i parameter.

In the unsteady case, in fact, the heat equation with the unsteady term brings to the integral expression given in equation 2.39 (by a simply integration over the condensed phase region).

$$\frac{\partial}{\partial t}\int_{-\infty}^{0} T\left(x\right) dx + r_b\left(T_s - T_i\right) = \alpha_p \left.\frac{dT}{dx}\right|_{x=0^+} \tag{2.39}$$

We rearrange the equation 2.39 in a form similar to the expression of the heat flux in the quasi-steady case, as expressed by equation 2.38, as this is the leading parameters of the phenomena. Hence, in order to account the non-steady regime in the combustion processes, we introduce a modification of the parameter grain initial temperature T_i (see equation 2.40), with the introduction of an initial apparent temperature of the grain propellant, T_{ia}. This quantity accounts for the unsteady energy accumulation in the condensed-phase region, due to the heat feedback, to the surface, from the gas phase.

$$T_{ia} = T_i - \frac{1}{r_b}\frac{\partial}{\partial t}\int_{-\infty}^{0} T\left(x\right) dx \tag{2.40}$$

As stated before, in fact, the instantaneous state quick response of the grain combustion is defined by the pressure and the temperature gradient at the interface of the condensed phase, without setting a limit on the type of burning regime (steady or non-steady). Therefore, the dependencies expressed for the steady burning are still valid for the unsteady burning regimes

with a correction on the T_i parameter, as expressed in equation 2.41. This correction, in fact, accounts for the variation in the unsteady regimes of the surface heat flux in the condensed phase.

$$\begin{cases} r_b = r_b\left(p, T_{ia}\right) = r_b\left(p, T_i - \dfrac{1}{r_b}\dfrac{\partial}{\partial t}\displaystyle\int_{-\infty}^{0} T\left(x\right) dx\right) \\ \\ T_s = T_s\left(p, T_{ia}\right) = T_s\left(p, T_i - \dfrac{1}{r_b}\dfrac{\partial}{\partial t}\displaystyle\int_{-\infty}^{0} T\left(x\right) dx\right) \end{cases} \tag{2.41}$$

Hence, in order to evaluate T_{ia}, we must solve the 1D Fourier unsteady equation in a moving boundary, with given and imposed IC and BCs and couple the two timesteps of the Fourier equation of the gasdynamical solver. When the dynamic model converges to quasi-steady state, the Fourier equation solution can be avoided at all in the numerical algorithm, as the dynamic burning effects are negligible in quasi steady regimes.

In particular, in [108] the APN law modification is made with the expression given in equation 2.42.

$$r_b = \mathrm{APN} \cdot \left(\frac{T_s - T_i}{T_s - T_{ia}}\right) \tag{2.42}$$

We stress the reader that this model is not yet implemented in the SPINBALL model. However, it is described for reasons of clarity and completeness, with respect to the results that will be discussed in the chapter 7, page 130.

2.3 SPIT Heritage Sub-models

The sub-models able to describe the IT phenomena will not discussed in this thesis. But as part of the SPIT, and consequently with some small algorithmic differences present in the SPINBALL model, they will be here briefly discussed (for more details see [80; 76; 75; 66; 67]):

- an Ignition Criterion for the solid propellant based on a temperature pressure dependent of combustion phenomena activation;
- an Igniter Model to simulate the presence of the igniter, its configuration, its operative conditions and its interaction with the chamber environment, as it has a strong impact on the ignition sequence, and consequently on the chamber pressure time history, during the IT;
- a Heat Transfer Model between the propellant grain and the combustion chamber gases, by convection and radiation, where local convective heat coefficients are evaluated with different models, depending on the chamber region (impingement region or standard region);
- a Conduction Heat Transfer Model into the solid grain propellant to characterize the propellant surface heating, and hence, ignition.

2.4 Numerical Integration Technique

The numerical discretization method to discretize the PDE system 2.1 of the Q1D unsteady flowfield model is a finite volume Godunov scheme first or second order (Essentially Non Oscillatory (ENO) scheme) accurate, coupled with an exact Riemann solver. In particular, the exact Riemann solver is modified to take into account the presence in the chamber of a mixture of different gases (see paragraph 2.4.1, page 30). The main characteristics of this method

are the robustness and the capability to deal with flowfield affected by propagation phenomena with strong discontinuities and source terms. The former becomes very important in order to adequately represent the strong unsteady and complex interacting propagation phenomena that occur during the Ignition Transient. While the latter is necessary in order to have a robust numerical method, for integrating the Q1D Euler equations, with the time and space variable source terms, even with wide variations, due during all the Quasi Steady State and the Tail Off to the grain propellant combustion processes.

Obviously, the accuracy in describing the shape, strength and the propagation velocity of the flow discontinuities during the IT is related to the spatial and time resolution adopted. In the same manner, the accurate description of the grain geometrical evolution is defined by a proper representation of the SRM flowfield conditions. Over the IT they are affected by the bore geometry due, mainly, to grain recession in time, whose accuracy is certainly related to the spatial grid resolution and not to time resolution (the flowfield characteristics times are much smaller than the geometrical variations characteristics time). Notwithstanding in this operative phase, the numerical simulation must properly describe the flowfield phenomena related to SRM natural frequencies (acoustic and/or combustion instabilities), which can, in a such manner potentially be analyzed and studied. In every case, both phenomena must be accurately represented in principle, in order to obtain and accurate numerical simulation of the internal ballistics for the entire combustion time, with the former constraints more stringent than the latter.

For motor lengths ranging from 5 to 40 meters, a reliable simulation can be obtained with a number of cells ranging from 100 to 1000 [80]. In fact, considering a wave propagation velocity inside the combustion chamber ranging from about 300 to 1700 meters per second, about 25000 timesteps are needed for the numerical simulation of 1 second, and such spatial and temporal discretization can accurately describe unsteady phenomena and the SRM natural frequencies along the longitudinal axis (from 5 to 200 hertz).

The fundamental features of the Godunov methods relies on the fact that the discretization of the conservation equations is obtained directly from their mathematical properties of the integrated PDEs. In such a manner, even in problems with strong discontinuities the entropy satisfying weak solution of the starting PDEs is naturally selected. In fact, Godunov schemes can be considered as a generalization of the characteristics based methods for problem with discontinuities.

Without lack of generality, consider the Euler conservation equation written on a uniform grid, as expressed in equation 2.43, where the conservative variables and fluxes are given respectively by equations 2.44 and 2.45.

$$\begin{cases} \dfrac{\partial U}{\partial t} + \dfrac{\partial F(U)}{\partial x} = 0 \\ \\ U(0,x) = U_0(x) \end{cases} \tag{2.43}$$

$$U = \begin{bmatrix} \rho \\ \rho u \\ \rho E \end{bmatrix} \tag{2.44}$$

$$F = \begin{bmatrix} \rho u \\ \rho u^2 + p \\ \rho u H \end{bmatrix} \tag{2.45}$$

This system, closed by proper Boundary Conditions, is a PDEs system, non-linear, unsteady and hyperbolic, as the eigenvalues of the Jacobian matrix are all real (see equation 2.46).

$$A(U) = \frac{\partial F}{\partial U} \tag{2.46}$$

Now, integrating the starting PDE system in a generic space and time domain $\left[x_{j-\frac{1}{2}}; x_{j+\frac{1}{2}}\right] \times [0; \Delta t]$, with some algebra we have the expression given by equation 2.47.

$$\int_{x_{i-1/2}}^{x_{i+1/2}} U(x,t+\Delta t)\,dx - \int_{x_{i-1/2}}^{x_{i+1/2}} U(x,t)\,dx + \int_{t}^{t+\Delta t} \left[F\left(x_{i+1/2},t\right) - F\left(x_{i-1/2},t\right)\right] dt = 0 \quad (2.47)$$

Introducing the average of the conservative variables vector in the generic x domain $\left[x_{j-\frac{1}{2}}; x_{j+\frac{1}{2}}\right]$ (equation 2.48), we have that the starting system of PDEs has a natural discretized time marching solution given by equation 2.49, which evaluates the average of the solution in a given domain, if one assume a proper relation for the time integration domain and the spatial integration domain, which guarantee that the interface fluxes does not change in the time integration interval.

$$U_j^n = \overline{U}_j(t) = \frac{1}{\Delta x}\int_{x_{j-1/2}}^{x_{j+1/2}} U(x,t)\,dx \quad (2.48)$$

$$U_j^{n+1} = U_j^n - \frac{\Delta t}{\Delta x}\left[F_{j+1/2}^n - F_{j-1/2}^n\right] \quad (2.49)$$

Hence, the basic idea is to discretize the space support x by means of N finite volumes of width Δx (in general not uniform), see figure 2.3. Through this discretization we can find an approximation $\widetilde{U}(x,t)$ of the exact solution $U(x,t)$ by projecting the exact solution over the discretized grid, as expressed by equation 2.51, where $\overline{U}_i(t)$ is the average of the exact solution at time t over the cell j-th and $I_j(x)$ is the "projector" of the exact solution over the cell j-th, equation 2.50.

$$I_j(x) = \begin{cases} 1 & \forall x \in \left[\ x_{j-1/2} \quad x_{j+1/2}\ \right] \\ 0 & otherwise \end{cases} \quad (2.50)$$

$$\widetilde{U}(t,x) = \sum_{i=1}^{N} \overline{U}_i(t)\cdot I_i(x) \quad (2.51)$$

Analysing the time marching discrete solution of the starting problem, equation 2.49, we can recognize the 3 steps that constitute the finite volume Godunov schemes:

1. Reconstruction of the variables at the cell interfaces.
2. local Evolution of the solution at the cell interfaces (to find interface fluxes).
3. time Integration of the cell average variables (via equation 2.49).

Reconstruction In the reconstruction step a certain distribution of the variables in the cell must be provided. This distribution is used in the second step to evaluate the discontinue values of the solution at the interface in a given timestep.

In the finite volume scheme proposed by Godunov [5] the distribution of the solution in the cell was considered as constant (figure 2.4a), so that the solution itself is represented by a piecewise constant function. This reconstruction is simplest and it corresponds directly to only project the solution on the discretized grid, by the projector operator (see equation 2.50). So if a constant reconstruction is adopted there no other calculations are necessary: the reconstruction is directly the U_j^n approximation. Using this kind of reconstruction the method is first order accurate in space.

For a higher reconstruction accuracy its order must be increased. If a linear piecewise reconstruction (figure 2.4b) is used for the variables, a second order accuracy in space is reached. In this kind of reconstruction a slope in each cell must be provided. In particular the slope of the linear cell reconstruction is selected with respect to the average value of the cell U_j and of the contiguous cell U_{j-1} and U_{j+1}. Since the linear cell reconstruction can originate spurious non physical oscillations, known as Gibbs phenomenon [2], and thus an unstable computed solution,

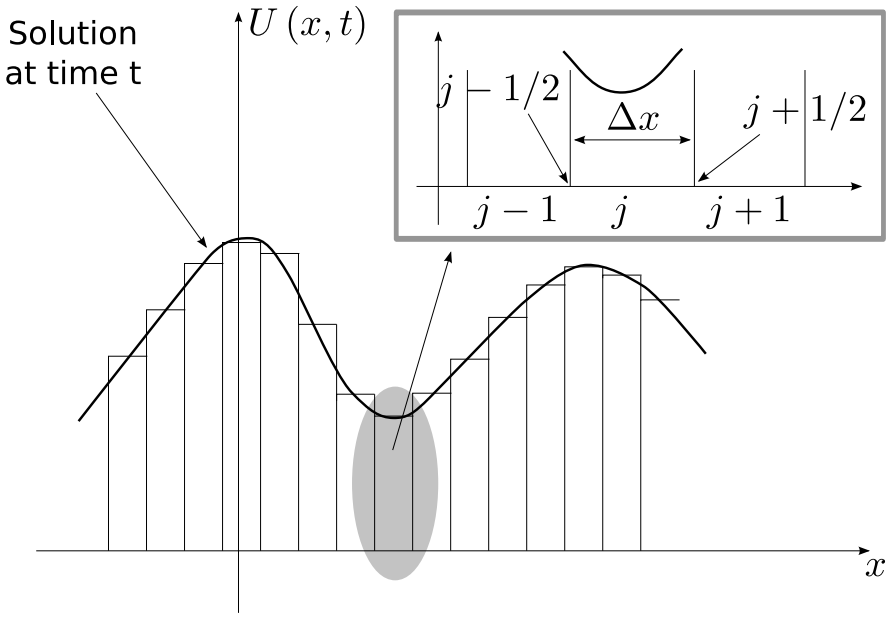

Figure 2.3: Approximation of the $U(x,t)$ Solution at time t

a slope limiter must be used in order to ensure the stability of the numerical scheme, so Total Variation Decreasing (TVD) condition.

In order to avoid the generation of non physical oscillations the slope into each cell must be compared themselves. It is useful to define the parameter r of equation 2.52, which shows directly if the slope reconstruction is generating spurious oscillation of the reconstructed solution.

$$r = \frac{U_j - U_{j-1}}{U_{j+1} - U_j} \tag{2.52}$$

In fact, if $r < 1$ the slope into the cell must be properly modified (figure 2.5).

Hence, with a linear reconstruction of the conservative variables, we can simply express the value of the discontinuous (left and right) reconstructed solution at the interface $j + 1/2$, as in equation 2.53, where the σ variables introduce is expressed in equation 2.54.

$$\begin{aligned} U^L_{j+1/2} &= U_j + \sigma_j \frac{\Delta x}{2} \\ U^R_{j+1/2} &= U_{j+1} - \sigma_{j+1} \frac{\Delta x}{2} \end{aligned} \tag{2.53}$$

$$\begin{aligned} \sigma_j &= \frac{U_{j+1} - U_j}{\Delta x} \varphi(r_j) \\ \sigma_{i+1} &= \frac{U_{j+2} - U_{j+1}}{\Delta x} \varphi(r_{j+1}) \end{aligned} \tag{2.54}$$

The function $\varphi(r_i)$ is the slope limiter that must be provided.

There are a lot of different slope limiters, among these the MinMod Limiter is considered (see equation 2.55).

$$\varphi(r) = \max[0, \min(|r|, 1)] \tag{2.55}$$

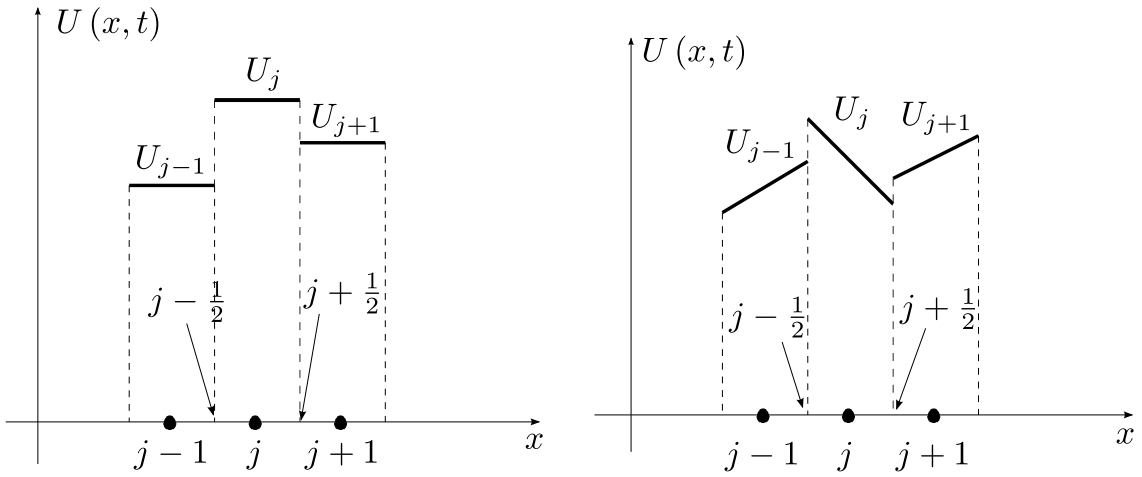

(a) Piecewise Constant Reconstruction

(b) Piecewise Linear Reconstruction

Figure 2.4: Some Types of Reconstruction Algorithms

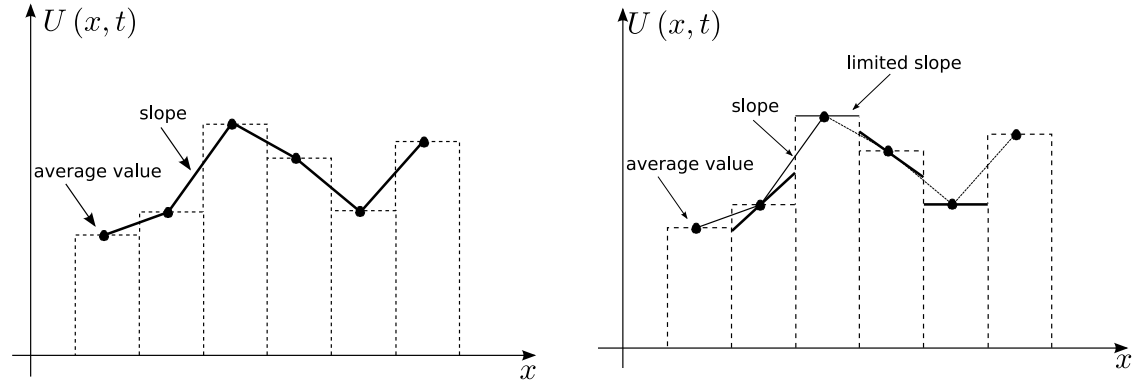

(a) Piecewise Linear Reconstruction without Slope Limiter

(b) Piecewise Linear Reconstruction with Slope Limiter

Figure 2.5: Reconstruction Algorithms with and without Slope Limiter

Evolution In the local evolution step the vector of fluxes must be evaluated at the interfaces. In fact, the reconstruction step has provided two values of the solution at the same interface $x_{j+1/2}$: $U^R_{j+1/2}$ of the solution reconstruction in the cell $j+1$ at the space abscissa $x_{j+1/2^-}$ and the value $U^L_{j+1/2}$, reconstruction in the cell j at the space abscissa $x_{j+1/2^+}$. These two values constitute a Riemann Problem. The value of interface Eulerian fluxes $F_{j+1/2}(t)$ is determined by the local evolution of this discontinuity and, hence, in order to evaluate the fluxes at the interfaces, a Riemann Problem must be solved, as illustrated in paragraph 2.4.1, page 30.

Integration If the solution of the Riemann Problem is constant between time t^n (initial time of the Riemann Problem) and time $t^n + \Delta t$, the fluxes computed in the evolution step are also constant in this time interval; so the equation 2.49 is operative and gives a time marching expression to compute the problem solution in time, giving the integration step.

All these 3 steps must be repeated for each cell and for the necessary timestep.

As announced before, during the reconstruction step, in order to guarantee the stability of this numerical algorithm the time step Δt must be related in some physical manner to the spatial discretization of the problem. From each interface Riemann problem, three waves are generated, hence, evaluating the time step Δt must ensure that the waves originated from one interface do

not reach the contiguous interfaces, otherwise the interface fluxes solution is no more constant (into the assumed Δt).

Imposing this condition, we obtain the so called Courant Friedrichs Lewy (CFL) condition, naming with λ_{max} the fastest wave speed originated by the Riemann Problem, the time step Δt must satisfy the CFL condition given in equation 2.56.

$$\Delta t^n \leqslant \frac{\Delta x}{\lambda^n_{max}} \tag{2.56}$$

For the Q1D PDE system, describing the SRM internal ballistics the discretized version, equation 2.1, is given in equation 2.57, where generically the source terms have been indicated with the symbol S, the i index is considered for $i = 1, \ldots, 6$ and the implementation algorithm given in equations 2.5, 2.6, 2.7, 2.8, 2.9 and 2.10 has to be considered to take into account the formulation with thermophysical properties variable in space and time.

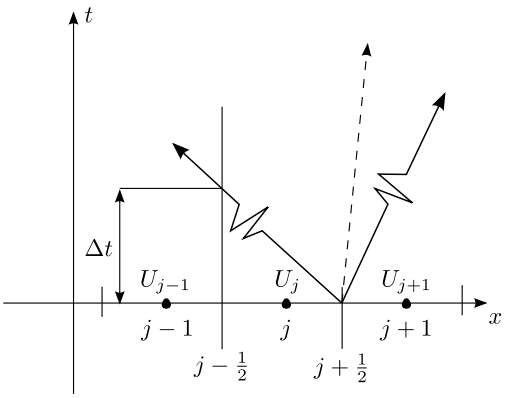

Figure 2.6: Evaluation of the Time Step Δt: CFL Condition

$$\left\{ \begin{array}{c} \rho_i A_p \\ \rho u A_p \\ \rho E A_p \end{array} \right\}_j^{n+1} = \left\{ \begin{array}{c} \rho_i A_p \\ \rho u A_p \\ \rho E A_p \end{array} \right\}_j^{n} +$$

$$-\frac{\Delta t^n}{\Delta x} \left\{ \begin{array}{c} (\rho_i u A_p)^n_{j+\frac{1}{2}} - (\rho_i u A_p)^n_{j-\frac{1}{2}} \\ \left[\left(\rho u^2 + p\right) A_p\right]^n_{j+\frac{1}{2}} - \left[\left(\rho u^2 + p\right) A_p\right]^n_{j-\frac{1}{2}} + p^n_j \left(A^n_{j+\frac{1}{2}} - A^n_{j-\frac{1}{2}}\right) \\ (\rho u H A_p)^n_{j+\frac{1}{2}} - (\rho u H A_p)^n_{j-\frac{1}{2}} \end{array} \right\} + \tag{2.57}$$

$$+ \left\{ \begin{array}{c} S^n_1 \\ S^n_2 \\ S^n_3 \end{array} \right\}$$

2.4.1 Riemann Problem for Mixture of Gas

The exact Riemann solver has been necessarily formulated, in order to account the discontinuities arising from the solution of the Riemann Problem for different gases. In fact, with both the SPIT gasdynamics model and the SPINBALL one, the adjacent cells contain gases with different thermophysical properties, the former due to the mixture of the three gases (pressurant, igniter gases and grain combustion products), while the latter related to the formulation for mixture of gases with thermophysical properties variable in space and time. Hence, for every Riemann Problem that must be solved for the Evolution step in the Godunov finite volume schemes, we have that the state left and right at each interface are characterized by different specific heat ratio, gas constant, molecular weight, and so on.

Assuming that, at a given time (or timestep) in the Godunov algorithm, we focus the attention on the left and right side of the generic cell interface, we know the fluid dynamics field of these two interface values by means of the Reconstruction step, that we called state 1 and 4 (see figure 2.7).

Now, the quantities given by equations 2.58, 2.59, 2.60, 2.61 can be evaluated. Where a_1 and a_4 represent the speed of sound of the left right states respectively, γ is the value of the specific heat ratio of the gas mixture crossing the interface.

$$R_2 I = u_1 \left(\frac{2}{\gamma_1 - 1} \right) a_1 \tag{2.58}$$

$$R_1 IV = u_4 \left(\frac{2}{\gamma_4 - 1} \right) a_4 \tag{2.59}$$

$$\beta = \frac{\gamma - 1}{2\gamma} \tag{2.60}$$

$$Z = \left(\frac{\gamma_1 - 1}{\gamma_4 - 1} \right) \left(\frac{a_4}{a_1} \right) \left(\frac{p_1}{p_4} \right)^{\beta} \tag{2.61}$$

This last can be evaluated considering the initial values of the pressure of the left right states, as expressed by equation 2.62.

$$\gamma = \begin{cases} \gamma_1 & \text{if } p_1 > p_4 \\ \gamma_4 & \text{if } p_1 < p_4 \end{cases} \tag{2.62}$$

The standard iterative algorithm for the exact solution of the standard Riemann problem can now be used, adopting as iteration variable the velocity of the intermediate states (2 and 3) [58]. For every interaction, the left-side and right-side waves are evaluated separately, verifying if they are shock waves or rarefaction waves and hence utilizing the Rankine-Hugoniot or the isentropic relations[58], across states $1-2$ and $4-3$, until convergence is reached. The left-side solution gives the status 2 ($p_2, \rho_2, u_2, \gamma_2$), while the right-side solution gives the status 3 ($p_3, \rho_3, u_3, \gamma_3$). The iterative procedure is triggered by an initial guess for the velocity of the intermediate states, as expressed by equation 2.63.

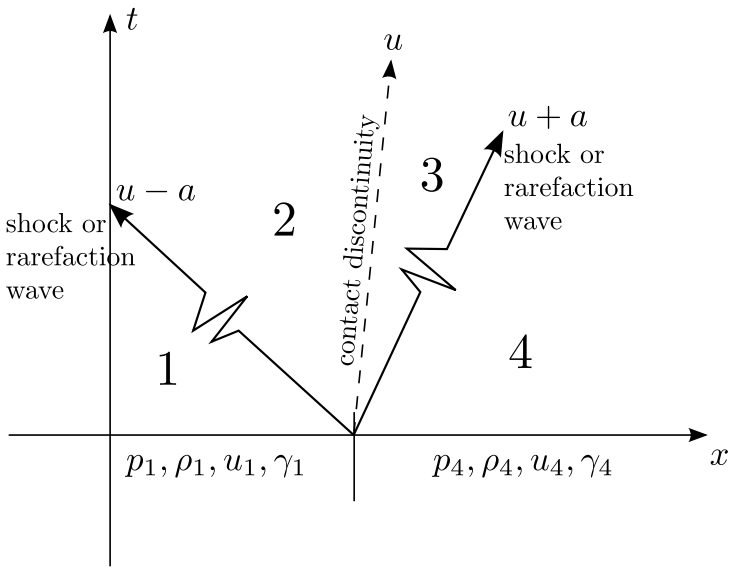

Figure 2.7: Riemann Problem for a mixture of gases

$$u^0 = \frac{Z \cdot R_2 I + R_1 IV}{1 + Z} \tag{2.63}$$

Once the iterative solution of the problem is found, under a convergence condition related to the satisfying of the equality $p_2 = p_3$, with a given tolerance, the direction of the flow across the interface is known, together with all the interface state flowfield properties, which allow to evaluate the interface fluxes. Hence, by the information of the interface velocity, the correct information for the gas mixture evolution inside each cell is provided. Hence, its thermophysical properties are evaluated, as given in the paragraph 2.1, page 13, where the SPINBALL gasdynamical model is presented.

3

GREG Model

This chapter is devoted to present a grain regression numerical model developed under this thesis work, based on the Level Set Method, named Grain REGression model (GREG). A first part will introduce the needs for the internal ballistics numerical simulation of the study of the grain burning surface evolution and the requirements the technique for the grain regression must fulfill. An introductory part will consider the more general problem than the grain burning surface evolution problem, of tracking of a general whatever complex surface subjected to a general motion field, in order to understand the geometrical and mathematical properties of the problem that must be faced. Then, a brief analysis of the Lagrangian and the Eulerian solution approach will be pointed out, remarking the main advantages and drawbacks of the techniques considered. Hence, the description of the Level Set Method by a mathematical and numerical point of view will be made, with the problem formulation specialized for the grain regression problem. In the following, the description of the technique for building the Initial Condition and to define the Boundary Conditions of the LSM will be made, with particular attention to the grain burnback problem. Thus, a brief analysis of the Narrow Band Methods and of the Extension of the Velocity off the interface will be considered, to give a larger perspective of the LSM applied to the grain propellant evolution problem. At last, a detailed description of the techniques for the extraction of the integral properties of the 3D grain surface from its Level Set representation will be considered. These techniques, in fact, are necessary for the coupling of the grain regression model with the SRM internal ballistics models, in particular, 0D and Q1D models.

3.1 Grain Burnback analysis to go over Ignition Transient

Focusing on the problem of the evolution of the grain burning surface with time, so called grain burnback analysis, the following remark are due:

- for the whole ignition transient it is possible to obtain an accurate prediction of experimental measurements neglecting the evolution of the grain burning surface and of the geometry inside the bore. In fact, the grain geometry is approximately fixed to its initial shape during this phase. Thus, as stated before, during the ignition transient, the chamber volume variations and grain burning surface regression with time and space is a secondary phenomena, that does not affect directly the SRM start-up. These statements find their proof in different works that considered for the numerical simulation of different motors start-up, a fixed geometry approach [103; 101; 97; 96; 90; 91; 84; 76; 75; 66; 67; 74; 80]
- in the operative phases subsequent to ignition transient, the quasi steady state and tail off, instead, the driving events of the internal ballistics and of the flowfield conditions of the motor bore are led by the grain recession in time. By one part through the modulation of the injected burning mass flow rate and by the other through the geometrical variations of the chamber free space.

A secondary role, however in general not negligible on the internal ballistics and on the motor overall performances is given by the liner, case and, especially, the nozzle thermal protections consumption. These cause a geometrical variation, especially of the nozzle throat area, but even a further mass addition with thermophysical properties different from the grain combustion products, in the main core flowfield. All these phenomena must necessarily be accounted in the modelling of the SRM internal ballistics.

The grain burnback analysis is defined as the study of the grain burning surface evolution with time. Hence, it has to provide to the chamber flowfield solver all the geometrical parameters necessary to solve the internal ballistics for each time, whose shall be constrained to the dimensional characteristics of the chosen flowfield model (0D, Q1D, 2D, or 3D).

Whatever is the assumed combustion model, the grain propellant surface motion is determined by the knowledge of regression speed along the pointwise normal direction. As discussed in the paragraph 2.2, page 21, the value of the burning rate, that is defined as the motion of the burning surface along its normal direction is constituted by a pressure dependent term, an erosive term and a dynamic burning term [22; 24; 61; 37].

Hence, the grain burnback analysis can be formulated into a more general problem of moving a general given interface (the solid propellant surface) with the particular constraint given by the case, or better the Thermal Protections inner surface, under a normally directed motion field.

Moreover, it is important to underline that, since all recent and practical SRMs grain configurations (Ariane4 Solid Boosters, Ariane5 Solid Boosters, Zefiro9, Zefiro23 & P80FW) have completely 3D complex shapes (finocyl or 3D star shaped grains), independently from the aforementioned internal ballistics flow model, the grain burnback analysis must be necessarily three-dimensional.

3.1.1 The grain burning surface evolution: method requirements

A grain burnback analysis technique must, hence, fulfill and have the following features:

- capable in treating the motion of complex 3D geometries, such as completely 3D star shaped grains or finocyl grains, with possible simple input of such 3D complex geometries;
- the ability in dealing with topology variations to describe particular grain shapes, like multi-perforated grains or modular cartridge-loaded grains;
- accurate in the reconstruction of the normal direction of the front during its motion, because the front moves exactly along this direction;
- an accurate evaluation of the grain and bore surface geometrical properties of a "ballistic interest": areas, surfaces and perimeters;
- a simple extension to High Order Schemes of the numerical solution for the motion equation, in order to increase the accuracy of results;
- the ability in treating the presence of a sort of boundary condition for the grain motion, exploited by the case boundary, or better, the liner and case TPs;
- a simple coupling with 0D and Q1D internal ballistics gasdynamics models, especially for the second ones in terms of meshes coupling and data exchanging.

3.2 Interfaces Tracking Problem

In order to appreciate the main properties of the problem of moving a general given interface, consider as case problem [31; 28], the motion under a general normal oriented velocity field, dependent eventually from the front local curvature K, V of a closed curve Γ in $\Re^2$. The interface

is parametrized by a curvilinear abscissa $s \in [0; S]$, such that the interior of the curve is on the left of the direction of increasing s.

Let:

$$\vec{x}(s,t) = [x(s,t); y(s,t)] \tag{3.1}$$

we have that, being the curve closed

$$\vec{x}(s=0,t) = \vec{x}(s=S,t) \qquad \forall t \tag{3.2}$$

The motion equation of the front can be written down for the case under analysis in the following manner, calling with $\hat{n}$ the pointwise normal vector of the front:

$$\hat{n}(s,t) \cdot \frac{d\vec{x}}{dt} = V(K) \tag{3.3}$$

Written in terms of $\vec{x}(s,t) = [x(s,t); y(s,t)]$, we have:

$$\begin{cases} \dfrac{\partial x}{\partial t} = V(K) \dfrac{\frac{\partial y}{\partial s}}{\sqrt{\frac{\partial x}{\partial s}^2 + \frac{\partial y}{\partial s}^2}} \\ \dfrac{\partial y}{\partial t} = -V(K) \dfrac{\frac{\partial x}{\partial s}}{\sqrt{\frac{\partial x}{\partial s}^2 + \frac{\partial y}{\partial s}^2}} \end{cases} \tag{3.4}$$

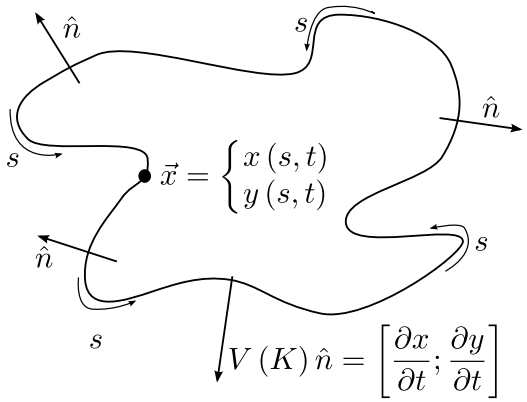

Figure 3.1: A Propagating Curve

with the Initial Condition:

$$\vec{x}(s,0) = \Gamma \quad \forall s \in [0; S] \tag{3.5}$$

and where K is the curvature of the front given by:

$$K = \frac{\frac{\partial^2 y}{\partial s^2}\frac{\partial x}{\partial s} - \frac{\partial^2 x}{\partial s^2}\frac{\partial y}{\partial s}}{\left(\frac{\partial x}{\partial s}^2 + \frac{\partial y}{\partial s}^2\right)^{3/2}} \tag{3.6}$$

A powerful formulation of the problem can be obtained considering now, the motion equation written down in a different set. Following [28] and calling with θ the arc length and $g(s,t)$ the metric, we have that the problem (see equations 3.3,3.4) can be formulated by the following equations too:

$$\begin{cases} \dfrac{\partial g}{\partial t} = \theta_s \, V(K) \\ \dfrac{\partial \theta}{\partial t} = -\dfrac{1}{g}\dfrac{\partial}{\partial s}\left[V(K)\right] \end{cases} \tag{3.7}$$

in which the following relations are valid:

$$\frac{\partial \theta}{\partial s} = \tan^{-1}\left(\frac{\frac{\partial y}{\partial s}}{\frac{\partial x}{\partial s}}\right) \qquad K = \frac{\frac{\partial \theta}{\partial s}}{g} \tag{3.8}$$

Now, using equation 3.7, it is possible to obtain the following equation for the evolution of the front curvature:

$$\frac{\partial K}{\partial t} = -\frac{\partial}{\partial s}\left[\frac{\partial V(K)}{\partial s}\frac{1}{g}\right]\frac{1}{g} - K^2 V(K) \tag{3.9}$$

In the case that $V(K) = 1 - \epsilon K$, it is simplified as:

$$\frac{\partial K}{\partial t} = \epsilon \frac{\partial^2 K}{\partial s^2} + \epsilon K^3 - K^2 \tag{3.10}$$

This equation is a reaction-diffusion equation, in which the following terms can be interpretable as follow:

- $\epsilon K^3 - K^2$: is the reaction term which, as will be clear later on, can cause the solution blow-up
- $\epsilon \frac{\partial^2 K}{\partial s^2}$: is the diffusion term, which instead smooths the solution

again, if $\epsilon = 0$, the resulting equation has the following solution:

$$K(s,t) = \frac{K(s,t=0)}{1 + tK(s,t=0)} \tag{3.11}$$

that means that the solution in terms of curvature becomes infinite (blow-up) in a finite time

$$t_{blow-up} = -\min\left(\frac{1}{K(s,t=0)}\right) \tag{3.12}$$

anywhere the front curvature is initially negative (concave). This can be simply interpreted considering the advection nature of the problem along the front normal direction. Exactly, if the front is locally concave as initial condition, it brings to the formation of a corner, where the interface is no longer differentiable, and the signals propagation direction falls into the corner itself (shock formation).

This is strictly analogous to what happens in the Burgers equation (with the dissipative term present $\epsilon > 0$):

$$\frac{\partial u}{\partial t} + u\frac{\partial u}{\partial x} = \epsilon \frac{\partial^2 u}{\partial x^2} \tag{3.13}$$

when the numerical viscosity $\epsilon \to 0$ (Riemann equation), and the solution creates shocks due to characteristics directions intersection. In fact, the solution behavior of the equation 3.4 can be summarized as follows:

- with $\epsilon = 0$ the characteristic directions of the equation 3.13 are lines in the plane $x - t$ along which u is constant. If the initial data is $u_{x_0} < 0$ the characteristics intersect at

  $$t = \min\left(-\frac{1}{u_{x_0}}\right) \tag{3.14}$$

  and a shock develops;
- with $\epsilon > 0$ the viscous term (diffusive term) on the right side, diffuses the steepening front, consequently the shock is smeared out and the solution remains smooth.

Hence, the case of motion of a given interface with a normal directed motion velocity (independent from its curvature), and the case of the Riemann equation 3.13 have similar mathematical features and properties. In order to build-up the solution after the solution blowing-up, that is possible in both cases, an entropy condition (that for the Riemann equation is that the characteristics go into shock as time advance [56]) is necessary, for selecting the physically relevant weak solution.

3.2.1 Lagrangian formulation & Lagrangian Front Tracking Techniques

Consider again the problem of moving a given front Γ under a known velocity field $\vec{V}(\vec{x}) = \langle u, v, w \rangle$. The straightest way to accomplish that target is to consider the *Lagrangian* formulation of the interface evolution, defined by the ODE 3.15:

$$\frac{d\vec{x}}{dt} = V(K)\,\hat{n}(\vec{x}) \tag{3.15}$$

Since the interface Γ is analytically defined by an infinite number of points, the numerical integration of equation 3.15 needs to follow the evolution of a proper discrete parametrization of the interface Γ. Hence, segments in 2D front problems and triangles (more often used) in 3D spatial dimensions problems. These techniques are called *Marker particles* or *Nodal* or *String Methods*.

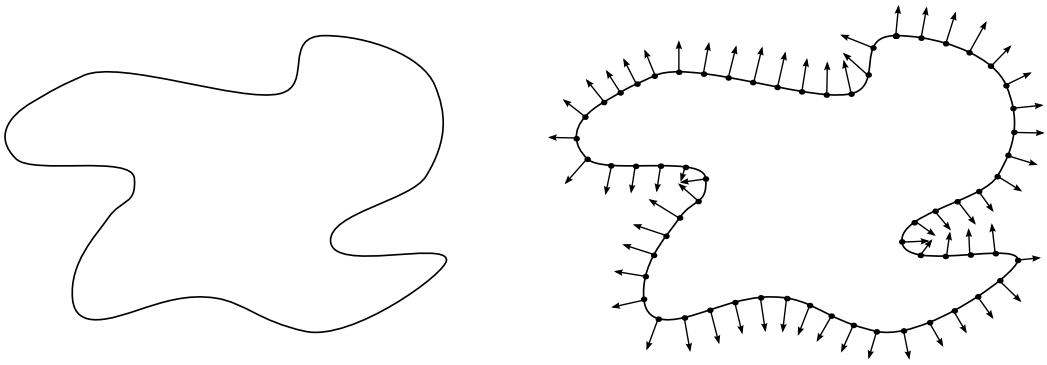

(a) Front to be evolved

(b) Marker Particles on the Boundary

Figure 3.2: Marker Particles Method

The numerical integration of the motion equation 3.4 is made, hence, using a finite number of front points as solution points (or markers), which without less of generality, can be considered as equally spaced respect to the curvilinear abscissa. These techniques in every case will face the following problems:

- the evolution of zones of the front where the curvature is negative (the front is locally concave), evolving will cause a shock formation, as shown in the paragraph 3.2, page 33. This brings to a markers approaching an each other, as the arc length between markers decreases. As a consequence, the stability of the numerical method sets a timestep bound more stringent, in such a manner, that it becomes excessively small and impractical;
- other zones in which the curvature is positive (the front is locally convex), as the time increases, bring the markers to move far apart each other, making a very poor numerical reconstruction of the front
- the front topological changes are difficulty handled naturally, as the introduction of an entropy condition is required. As an example, if the front is made on several parts that merge together, it is difficult to decide which marker has to be deleted and which remains alive.

Typically the remedies of such problems can be (with the exception of the last one in the previous list, which will be discussed in the following):

- a smoothing of the speed function V, so that all markers remain far enough to allow reasonable timesteps for the numerical technique;

- a periodic "regridding" of the markers along the front, according, for example, to the arc length, in order to avoid that markers stay too far, or to close each other;
- the introduction of some filtering techniques, maintaining a practical stable timestep, to remove oscillations in the particles position evolution

Unfortunately, all these techniques used in practice, are not appealing [59]. In fact, they alter in a not obvious way the starting motion equation 3.15, introducing a smoothing process and, practically, sacrificing interesting front properties, such front sharpening and curvature to make the simulation alive.

This situation becomes even more critical in the case that the front velocity V is not a function of the curvature K. In fact, where the front is locally concave, as seen before, during its evolution, it forms sharp corners and an entropy condition is required to build the solution beyond the corner generation (this situation is similar to the characteristics intersection occurring in a shock formation for the Riemann equation). However, the necessary entropy condition is not included in the Lagrangian formulation. Hence, the marker particles methods bring to the formation of a so called swallow-tail solution. To prevent that kind of problems ad-hoc *de-looping* techniques are necessary to introduce the required entropy condition while the front is moving. Even if such algorithms are quite simple to be developed in 2D problems, because of their complexity, are totally prohibitive in 3D ones (code can break down in complex situations).

3.2.2 Eulerian formulation & Eulerian Front Tracking Techniques

A completely different approach to solve the problem of moving a general closed boundary Γ, under a given motion field $\vec{V}$ (that could be even depend on the local properties of the front itself, as normal and curvature), is the *Eulerian* approach.
This kind of approach, in its different formulations, considers the interface embedded in one more dimension space, in which the front moves. The front is, hence, represented by a proper grid function $\phi(\vec{x}, t)$, that assumes a different meaning for the two main Eulerian formulations:

- Volume of Fluid (VOF) Techniques / Cell Method / Method of partial fractions
- Level Set Method

Volume of Fluid(VOF)/Cells Methods

The VOF technique is based on a grid function $\phi(\vec{x}, t)$ given by the volume fraction of "matter" inside the front, included in each cell. In this way the boundary itself is located as a discontinuity, by all the cells that have a volume fraction between 0 and 1. In the same time all the cell completely inside the front have a cell volume given by 1; while all the cells outside are defined by a ϕ value of 0. In a such manner, we can say that, in terms of representation of the grid function, the front itself is captured (as the approach is Eulerian) as a discontinuity (numerically smeared out) (see fig. 3.3). Hence, these techniques suffer for all the problems related to make a reconstruction of the discontinuity, starting from the cells volume representation. In particular, with these techniques it is difficult to control the artificial spreading of the interface due to numerical diffusion, related just to the reconstruction of the interface from its volume representation.

In fact, many different approximation techniques are used in literature to reconstruct the boundary from the cell fractions.

The original one is known as the SLIC algorithm (Simple Line Interface Calculation) [13], even if many elaborate ones have been developed to include pitch slopes and curved surfaces [17] [27] [39] [36]. These techniques are known under many names, such as the "cell method" or "method of partial fractions". In order to move the interface, the cell fractions need to be updated under the velocity field given by $\vec{V}$, solving directly the advection equation of the front, in a such manner that depends on the chosen reconstruction of the front. In their SLIC algorithm [13],

(a) Mathematical Model (b) Numerical Model

Figure 3.3: VOF Interface Representation

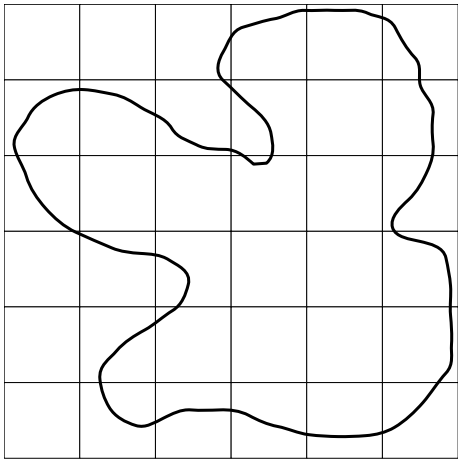

0.0	0.0	0.1	0.8	0.9	0.15
0.6	0.7	0.05	0.95	1.0	0.65
0.7	1.0	0.98	0.96	1.0	0.4
0.05	0.3	0.9	1.0	1.0	0.65
1.0	0.35	0.98	1.0	1.0	0.94
0.0	0.4	0.45	0.65	0.75	0.35

(a) Front & Grid (b) Volume fractions

Figure 3.4: VOF - Volume of Fluid

Noh and Woodward have considered a methodology in which the updating of each cell fraction is made through sweeps along each coordinate direction (see fig. 3.5), by means of a local reconstruction of the front and exchange of "matter" between the cell under consideration and the neighbor cells.

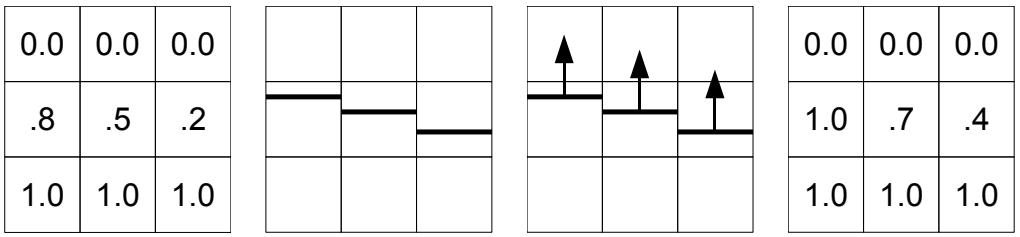

0.0	0.0	0.0
.8	.5	.2
1.0	1.0	1.0

0.0	0.0	0.0
1.0	.7	.4
1.0	1.0	1.0

(a) Volume Fractions (b) Reconstructed Front (c) Front Advection (d) New Volume Fractions

Figure 3.5: SLIC - Advection Algorithm: Sweep in the $\uparrow$ Direction with $V = 0.2$

Hence, the original SLIC algorithm was designed to compute the motion of a given interface under a given general velocity field $\vec{V}$, in a independent manner of the local properties of the front itself.

A modification of this algorithm, proposed by Chorin [16; 26] instead, is able to compute the interface motion even in the case of velocity field pointwise normally directed. In fact, in this case, as seen for the marker particles methods, corners and cusps of the front may be generated and in such cases an entropy condition must be invoked to select the physically relevant weak solution. Chorin considered this by means of the use of the Huygens' principle, in a proper

formulation consistent to the VOF approach, seeing each spot on the front as a point source. Thus, the new position of the boundary is built-up making the envelope of influence of all these sources. Using a sufficient number of cells to approximate this source point, that correspond to sufficient number of directions in the computational grid, as will be clear in the following, a natural selection of the entropy condition occurs and the correct weak solution is so selected.

In its implementation of the Huygens' principle, Chorin considered all the angles given by all the neighbor cells of a given cell (8 cells in 2D problems, 26 in 3D ones):

$$\alpha_l = \frac{(l-1)2\pi}{L} \qquad l = 1, \dots, L \tag{3.16}$$

Thus, he considers the upgrading of the grid function in the cell i-th j-th (2D problem, without less of generality) given by:

$$\phi_{ij}^{n+1} = \max_{\forall l} \phi_{ij}^{n}\Big|_l \tag{3.17}$$

where $\phi_{ij}^{n}\Big|_l$ are the volume fraction in the cell i-th j-th at step $(n+1)$-th, when cell volume is moved in the l-th direction with a motion field

$$\vec{V} = V\,[\cos\alpha_l; \sin\alpha_l] \tag{3.18}$$

As $L \to \infty$ and the mesh size goes to zero, this algorithm corresponds to draw a disk of a unit radius from each spot. Thus, making the envelope it is possible to define the new position of the front in the VOF representation of the problem.

In the case that $V(K)$, it is enough obvious that the maximum allowable curvature is limited by one cell width resolution of the front. In a such case, moreover, a method for determining the curvature of the front, starting from cells volume fractions and based on the fitting osculating circle, was developed by Chorin [27].

This technique, in its Eulerian nature, avoids many of the Lagrangian problems previously underlined and, hence, has the following important advantages:

- it is unchanged in several dimensions, especially in complex three-dimensions problems;
- the topological changes of the front are handled naturally. In particular the front can break and merge, without the need of ad-hoc techniques to face that situations, on the contrary to Lagrangian approach;
- in addition to that, in the case of motion along the front normal direction, a numerical procedure based on the application of the Huygens' principle applies in order to select the correct weak solution (even if quite inaccurate).

In the meantime, there are some evident drawbacks:

- such techniques are inaccurate, since the approximation of the front through volume fractions is quite crude and a large number of cells is required to obtain reasonable results;
- the evolution under complex speed motion fields is problematic (results are noticeably dependent on the underlying orientation of the grid) and it become worse in the presence of directional velocity fields (such as those arising from not-convex laws);
- the calculation of the intrinsic geometric properties of the front, such as curvature and normal direction, may be inaccurate;
- the calculation of the other geometrical properties of the boundary such as surfaces and perimeters are difficult to perform directly and are strongly dependent by the reconstruction technique considered for the front (instead, volume calculation is straightforwardly made by the sum of the grid function in the entire domain);

- a considerable work may be required to develop higher order versions of such techniques;
- in higher dimensions, accurate calculations of the mean and Gaussian curvatures are difficult to perform, especially at saddle points.

Level Set Method

Another *Eulerian* formulation of the interface motion, different from the VOF is the so called Level Set approach. It considers again the introduction of a grid function, but with a completely different representation of the front respect to VOF techniques. In this method, in fact, the grid function is an implicit function $\phi(\vec{x}, t)$ that represents the interface to be evolved Γ, with its zero level for every time.

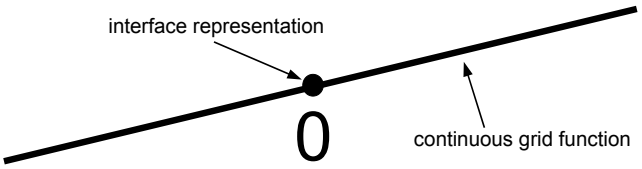

Figure 3.6: Level Set Interface Representation

Consequently, all the problems related to the reconstruction of the interface from its discretized value do not stand, as the front is not more seen as a discontinuity, as the VOF does, rather as a level of a continuous grid function. As matter of fact, no spreading out of the front due to its numerical representation stands. While as the numerical grid is refined a greater and greater accuracy of the front representation is obtained.

Considering now, the Level zero of the grid function:

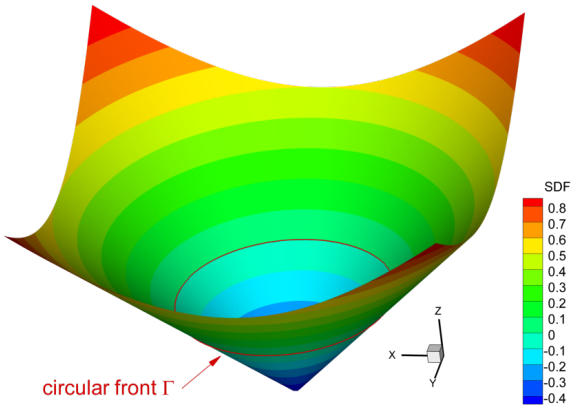

Figure 3.7: Level Set of a Circular Front

$$\phi(\vec{x}(t), t) = 0 \tag{3.19}$$

$$\vec{x} \; : \; \phi(\vec{x}, t = 0) = 0 \quad \Longleftrightarrow \quad \vec{x} \in \Gamma \tag{3.20}$$

Differencing equation 3.20 in time:

$$\frac{\partial \phi}{\partial t} + \sum \phi_{x_i} \frac{\partial x_i}{\partial t} = 0 \tag{3.21}$$

$$\frac{\partial \phi}{\partial t} + \vec{V} \cdot \vec{\nabla} \phi = 0 \tag{3.22}$$

The equation 3.22 properly stands the Eulerian formulation of the problem, as an advection problem of the continuous grid function ϕ, under the motion field $\vec{V}$. It is referred in literature as *level set equation*, introduced by Osher and Sethian [59] [79], but it is also popular in combustion applications as the *G-equation*, due to Markstein [8; 1].

In addition to the above mentioned features related to its *Eulerian* approach (see paragraph 3.2.2, 37), the use of the Level Set Method in solving the problem of moving a general given closed surface has the following relevant properties:

- it relies on viscosity solution of the associated partial differential equations in order to guarantee that the unique, entropy satisfying weak solution is obtained;
- in the numerical solving of the equation 3.22, it can be seen as an hyperbolic system of equations for partial derivatives of the ϕ function. It is, hence, possible to use numerical schemes considered for numerical solution of Euler equations and borrow them in a quite straightforward manner;
- the intrinsic geometric properties of the front are easily evaluated, such as the normal and the curvature of Γ, using the mathematical properties of implicit functions;
- even if following the evolution in time of all the level set of ϕ is much computational time and space consuming, efficient methods have been developed in order to limiting the attention only on the zero level set of interest ([42; 57; 59], see paragraph 3.9, 61);
- the evaluation of other geometric properties of the boundary in its evolution in time, such as volumes, areas, surfaces and perimeters can be easily made directly with or without the need of a previous reconstruction of the level of interest (the zero one, or everyone other), from the grid function (see paragraph 3.11, 66).

In the evolution of the level set function $\phi(\vec{x}, t)$ solving the equation 3.22, it could be interesting to underline that: *the velocity field effects on the interface motion is strictly related only to the normal component of it, because of the term $\vec{\nabla}\phi$ is for each point $\vec{x}$ defined normal to $\phi(\vec{x}, t)$.*

In fact, writing $\vec{V}$ by normal and tangential component respect to the level set function ϕ, we have:

$$\vec{V} = V_n \hat{n} + V_t \hat{\tau} \tag{3.23}$$

since:

$$\hat{n} = \frac{\vec{\nabla}\phi}{\left|\vec{\nabla}\phi\right|} \qquad \hat{n} \cdot \hat{\tau} = 0 \tag{3.24}$$

by some calculations:

$$\frac{\partial \phi}{\partial t} + (V_n \hat{n} + V_t \hat{\tau}) \cdot \vec{\nabla}\phi = 0 \tag{3.25}$$

$$\frac{\partial \phi}{\partial t} + V_n \frac{\vec{\nabla}\phi}{\left|\vec{\nabla}\phi\right|} \cdot \vec{\nabla}\phi = 0 \tag{3.26}$$

$$\frac{\partial \phi}{\partial t} + V_n \left|\vec{\nabla}\phi\right| = 0 \tag{3.27}$$

This last equation is still known, as equation 3.22, as the *level set* equation. Here V_n represents, in general terms, the normal component of the velocity field. The equation 3.22 is part of the HJ equations class.

As in this dissertation, it is of interest the motion of interfaces under an internal generated motion field, defined along the normal of the front at each point $\vec{x}$, the equation 3.27 will be referred in the following as the *Level Set Equation*. Finally, hence, it can be expressed as:

$$\frac{\partial \phi}{\partial t} + V\left|\vec{\nabla}\phi\right| = 0 \tag{3.28}$$

considering V the value of the velocity field at each point $\vec{x}$.

For its generality and for all the relevant features related to the Level Set technique with respect to the application of this tracking interface method to the grain burnback analysis, the Level Set Method has been chosen to be implemented for the numerical simulation of grain burning surfaces evolution. Hence, in the following paragraphs, it will be extensively analyzed in terms of mathematical properties, numerical schemes for the integration of the LS equation and the technique for evaluating grain geometrical properties from the LS front representation.

3.3 Level Set Equation Mathematical Properties

3.3.1 Mathematical properties of the LS Equation

The level set equation introduced in equation 3.28 is a partial differential equation, first order in time and space. Ignoring cases for which $V = V\left(\phi_{x_i x_j}\right) \quad \forall i, j = 1 \dots 3$, depending for example by mean curvature, we consider only cases where almost $\vec{V} = V\hat{n}$ with $V = V(\vec{x}, t)$. As said before, the level set equation 3.29 can be seen in the class of *HJ equations*, in the sense:

$$\phi_t + V\left|\vec{\nabla}\phi\right| = 0 \qquad\qquad \phi_t + H(\phi_x, \phi_y, \phi_z) = 0 \tag{3.29}$$

where:

$$H(x, y, z, \phi_x, \phi_y, \phi_z, t) = V\left|\vec{\nabla}\phi\right| \tag{3.30}$$

defining with H the Hamiltonian.

The previous equation 3.29 is also called *eikonal equation* for the characteristic term after the temporal derivative and is a first order Hamilton-Jacobi type equation. Its solution is known to have the following properties:

- starting from a continuous and differentiable initial condition, the solution itself remains always continuous for all time;
- however the solution can loose its differentiability (as if the $\vec{\nabla}\phi$ falls into a shock formation with a solution blow-up);
- in such cases, it is still possible to produce Lipschitz continuous solutions, but these "generalized solution" are not unique;
- hence, it is required an entropy condition to select the vanishing viscosity solution.

It is possible, in fact, to prove [19] that the Huygens' principle is nothing less than an approximation of the eikonal equation, in which a natural satisfaction of the entropy condition occurs.

These remarks are very important in order to develop numerical schemes to discretize the equation 3.28, since first order Hamilton-Jacobi equations are strictly related to conservation laws (Euler equations for compressible flows, such as an example). Therefore, the numerical schemes for the level set equation are taken from that ones largely adopted in the computational solutions of the conservation laws.

3.3.2 Connection between HJ equations and conservation laws

Consider a one dimensional scalar conservation law 3.31, in which u is the conserved quantity and $F(u)$ the flux function:

$$u_t + [F(u)]_x = 0 \tag{3.31}$$

and a general one-dimensional HJ equation ($\phi = \phi(x,t)$)

$$\phi_t + H(\phi_x) = 0 \tag{3.32}$$

Differencing 3.32 along x, and naming $u = \phi_x$ we have:

$$(\phi_x)_t + [H(\phi_x)]_x = 0 \qquad \Longrightarrow \qquad u_t + [H(u)]_x = 0 \tag{3.33}$$

Hence, a comparison between equations 3.31, 3.32 and 3.33 shows a direct correlation between one dimensional level set equation and a general conservation law [59], in particular: *the solution of a conservation law is the derivative of the solution of the first order Hamilton-Jacobi one dimensional equation*. In a converse reasoning: *the solution of the Hamilton-Jacobi equation is the integral of the solution of a conservation law, where the flux function coincides with the Hamiltonian*. This remark allows to point out the following useful facts:

- since the conservation law 3.31 admits from initial smooth conditions, discontinuous solutions, and the integral of a discontinuity is a kink (discontinuity of the first derivative), solutions of the Hamilton-Jacobi equations can develop kinks even if initial conditions are smooth (as seen already in paragraph 3.2, page 33, for the general properties of the problem);
- the solutions of the HJ equations can not be discontinuous, since the derivative of that kind of solution would be a delta function. Thus, the solutions of the equation 3.32 are generally continuous;
- moreover, since the conservation laws can admit not unique solutions, an entropy-condition is necessary to pick out the correct physically relevant viscosity vanishing solution, even for the HJ equation 3.32. Hence, the numerical schemes used to solve it must account in some manner an entropy condition to select the right weak solution.

The pointed out correlation between HJ equations and conservation laws can be exploited even in multiple dimensions, as will be shown in the following.

Starting from:

$$\phi_t + H\left(\vec{\nabla}\phi\right) = 0 \qquad \left(H\left(\vec{\nabla}\phi\right) = H(\phi_x, \phi_y, \phi_z)\right) \tag{3.34}$$

applying gradient:

$$\vec{\nabla}\left(\frac{\partial \phi}{\partial t}\right) + \vec{\nabla}\left(H\left(\vec{\nabla}\phi\right)\right) = 0 \tag{3.35}$$

now, by chain rules, we have:

$$\vec{\nabla}\left(H\left(\vec{\nabla}\phi\right)\right) = \underline{\underline{I}} \cdot \vec{\nabla}\left(H\left(\vec{\nabla}\phi\right)\right) = \underbrace{H\left(\vec{\nabla}\phi\right)\ \vec{\nabla}\cdot\underline{\underline{I}}}_{=0} + \underline{\underline{I}} \cdot \vec{\nabla}\left(H\left(\vec{\nabla}\phi\right)\right) = \vec{\nabla}\cdot\left(H\left(\vec{\nabla}\phi\right)\underline{\underline{I}}\right) \tag{3.36}$$

It is, hence, possible to write the equation 3.34 in a familiar manner, similar to the conservation laws:

$$\left(\vec{\nabla}\phi\right)_t + \vec{\nabla}\cdot\left(H\left(\vec{\nabla}\phi\right)\underline{\underline{I}}\right) = 0 \tag{3.37}$$

In fact, naming with $\vec{U} = \vec{\nabla}\phi$, it is simple to write the equation 3.37 with a structure similar to Euler conservation laws for inviscid fluid motion [55], expressed in the *conservative form* (*divergence form*):

$$\vec{U}_t + \vec{\nabla} \cdot \underline{\underline{F}}\left(\vec{U}\right) = 0 \tag{3.38}$$

where $\underline{\underline{F}}\left(\vec{U}\right) = [f; g; h]^T$ is, in the correlation with the HJ equation, expressed by:

$$\underline{\underline{F}}\left(\vec{\nabla}\phi\right) = H\left(\vec{\nabla}\phi\right)\underline{\underline{I}} \tag{3.39}$$

Now, with some mathematical passages, it is also possible to consider the *quasi linear form* of the gradient equation of the ϕ level set function 3.37, or that is the same for the equation 3.38. This gives us information about the characteristic velocities (through the eigenvalues of the F, G and H matrix) and the conserved quantities (through the corresponding eigenvectors) along each coordinate direction:

$$\begin{aligned} \vec{\nabla} \cdot \underline{\underline{F}}\left(\vec{U}\right) &= \vec{\nabla} \cdot \left[\vec{f}; \vec{g}; \vec{h}\right] = \frac{\partial\left[\vec{f}; \vec{g}; \vec{h}\right]}{\partial \vec{U}}^T \cdot \vec{\nabla}\vec{U} = \underline{\underline{\vec{A}}}\left(\vec{U}\right) \cdot \vec{\nabla}\vec{U} = \\ &= \left[\underline{\underline{F}}\left(\vec{U}\right); \underline{\underline{G}}\left(\vec{U}\right); \underline{\underline{H}}\left(\vec{U}\right)\right]^T \cdot \vec{\nabla}\vec{U} = \\ &= \underline{\underline{F}}\left(\vec{U}\right) \cdot \vec{U_x} + \underline{\underline{G}}\left(\vec{U}\right) \cdot \vec{U_y} + \underline{\underline{C}}\left(\vec{U}\right) \cdot \vec{U_z} \end{aligned} \tag{3.40}$$

where:

$$\underline{\underline{F}}\left(\vec{U}\right) = \frac{\partial \vec{f}}{\partial \vec{U}} \quad ; \quad \underline{\underline{G}}\left(\vec{U}\right) = \frac{\partial \vec{g}}{\partial \vec{U}} \quad ; \quad \underline{\underline{H}}\left(\vec{U}\right) = \frac{\partial \vec{h}}{\partial \vec{U}} \tag{3.41}$$

so that:

$$\vec{U}_t + \underline{\underline{F}}\left(\vec{U}\right) \cdot \vec{U_x} + \underline{\underline{G}}\left(\vec{U}\right) \cdot \vec{U_y} + \underline{\underline{H}}\left(\vec{U}\right) \cdot \vec{U_z} = 0 \tag{3.42}$$

or the equivalent formulation, in terms of the stated correlation *conservation laws - gradient of HJ level set equation*:

$$\left(\vec{\nabla}\phi\right)_t + \underline{\underline{F}}\left(\vec{\nabla}\phi\right) \cdot \left(\vec{\nabla}\phi\right)_x + \underline{\underline{G}}\left(\vec{\nabla}\phi\right) \cdot \left(\vec{\nabla}\phi\right)_y + \underline{\underline{H}}\left(\vec{\nabla}\phi\right) \cdot \left(\vec{\nabla}\phi\right)_z = 0 \tag{3.43}$$

Therefore, even in the case of multi-dimensional problems, a relation between the Hamilton-Jacobi equations and the conservation laws is still valid, as well as all the mentioned remarks made on the solution characteristics and the numerical scheme. Thus, it is still possible *to think the HJ as the conservation law "integrated once"* .
This connection is particularly important because makes possible to build up numerical schemes to solve the HJ equations, directly borrowed from the ones used for conservations laws, in particular, as shown afterwards, because of the direct relation in the 1D case.

3.4 Level Set Equation Numerical Integration

3.4.1 Level Set Equation: building up the numerical scheme

1-D HJ equations

As shown in the paragraph 3.3.2, page 43, a strict relation between the one dimensional level set equation 3.32 (as being part of the first order Hamilton-Jacobi class of equations) and the one dimensional conservation laws 3.31 stands. This theoretical circumstance is very important in building up the numerical schemes that allows to discretize the PDE 3.28:

$$\phi_t + H(\phi_x) = 0 \qquad \Longrightarrow \qquad \phi_t + V|\phi_x| = 0 \quad \left(\phi_t + V\sqrt{\phi_x^2} = 0\right) \tag{3.44}$$

In fact, all robust numerical schemes largely developed and successfully used to numerically solve the conservation laws can be considered to evaluate the second term of equation 3.44, as we will see in the following.

Starting again from a scalar conservation law equation in *conservative form*

$$u_t + [F(u)]_x = 0 \qquad \left((\phi_x)_t + [H(\phi_x)]_x = 0 \quad \Longrightarrow \quad F(u) = H(\phi_x) \right) \tag{3.45}$$

there is a very straightforward way to build a numerical method that picks out the physically relevant solution of the problem: the method considered must be, as the differential equation that it numerically solves, in the *conservation form*:

$$U_j^{n+1} = U_j^n - \frac{k}{h}\left[\tilde{F}\left(U_{j-p}^n, U_{j-p+1}^n, \cdots, U_{j+q}^n\right) - \tilde{F}\left(U_{j-p-1}^n, U_{j-p}^n, \cdots, U_{j+q-1}^n\right)\right] \tag{3.46}$$

where let U be some "numerical version of the quantity" u, $\tilde{F}$ the numerical flux function of $p+q+1$ arguments, k and h respectively timestep and mesh width, while j, n denote respectively the generic mesh node and time step number. This generalized expression can be simply considered in the case $p = 0$ and $q = 1$, so the numerical flux function depends only on two variables and takes form:

$$U_j^{n+1} = U_j^n - \frac{k}{h}\left[\tilde{F}\left(U_j^n, U_{j+1}^n\right) - \tilde{F}\left(U_{j-1}^n, U_j^n\right)\right] \tag{3.47}$$

The formulation 3.47, in fact, is a very natural manner to approximate the starting differential equation, if U_j^n is seen as the cell average of the conserved quantity u over the j-th mesh cell:

$$U_j^n = \bar{u}_j^n = \int_{x_{j-1/2}}^{x_{j+1/2}} u(x, t_n)\, dx \tag{3.48}$$

targeting the attention on the integral form of the conservation law:

$$\int_{x_{j-1/2}}^{x_{j+1/2}} \int_{t_n}^{t_{n+1}} (u_t + [F(u)]_x)\, dt\, dx = 0 \tag{3.49}$$

$$\int_{x_{j-1/2}}^{x_{j+1/2}} u(x, t_{n+1})\, dx = \int_{x_{j-1/2}}^{x_{j+1/2}} u(x, t_n)\, dx - \left[\int_{t_n}^{t_{n+1}} F\left(u\left(x_{j+1/2}, t\right)\right) dt - \int_{t_n}^{t_{n+1}} F\left(u\left(x_{j-1/2}, t\right)\right) dt\right] \tag{3.50}$$

and, hence

$$\bar{u}_j^{n+1} = \bar{u}_j^n - \frac{1}{h}\left[\int_{t_n}^{t_{n+1}} F\left(u\left(x_{j+1/2}, t\right)\right) dt - \int_{t_n}^{t_{n+1}} F\left(u\left(x_{j-1/2}, t\right)\right) dt\right] \tag{3.51}$$

Comparing now, the equations 3.51 and 3.47, it is easy to see that it is possible to relate the numerical flux function with the average of the analytical one over the time step $[t_n\,;\, t_{n+1}]$:

$$\tilde{F}\left(U_j, U_{j+1}\right) \approx \frac{1}{k} \int_{t_n}^{t_{n+1}} F\left(u\left(x_{j+1/2}, t\right)\right) dt \tag{3.52}$$

Moreover, if a relation between the characteristic velocities (which carry signals along the field), the timestep k and the mesh width h is considered, such that the state of the conserved quantity at the cell interface $x_{j-1/2}, t$ is not changing during the time $[t_n\,;\, t_{n+1}]$, we have also:

$$\tilde{F}\left(U_j, U_{j+1}\right) \approx F\left(u\left(x_{j+1/2}, t\right)\right) \tag{3.53}$$

The relation 3.53 is an important and straightforward connection between the numerical flux function and the analytical one, in order to build up numerical schemes for the Level Set equation.

In fact, a numerical scheme in the *conservative form* (equation 3.47) is related, as shown, to the integral formulation of the conservation law 3.45, that is satisfied by any *weak solution* of the starting PDE. What is missing now is to prove that the numerical scheme converges to the vanishing viscosity weak solution. Moreover, building up the numerical solution of the conservation law 3.45, the numerical flux function $\tilde{F}$ of the conservative form must be *consistent* to the analytical one, in a way such that in the case of constant flow, the function $\tilde{F}$ reduces to F. So that:

$$\tilde{F}\left(u, u\right) = F\left(u\right) \qquad \forall u = \text{const} \in \Re \tag{3.54}$$

Hence, in the case of a *consistent* and *conservation form*, the confidence of the solution of a such numerical method and it is relation to a weak solution (that can not be unique) of the correspondent conservation law is guaranteed by the Lax and Wendroff theorem [56]. Finally, the prove that a numerical scheme converges to the vanishing viscosity solution and not to a non-physical (non-entropy satisfying) weak solution, is guaranteed if the numerical scheme further to be *consistent* and in a *conservation form*, is *monotone* too. That is to say mathematically that $\tilde{F}\left(U_j^n, U_{j+1}^n\right)$ is a not decreasing function of its arguments [56].

The numerical Hamiltonian can be, thereby, expressed by an exact or an approximate Riemann solver (Engquist-Osher, or Osher-Sethian, or Lax-Friederichs flux with its local version LF, SLF, LLF, RF) [18] [5], with whatever temporal (multistep Runke-Kutta) and spatial (ENO, WENO) accuracy order [59; 79; 35].

Multi-D HJ equations

In one dimensional problems, we pointed out that the numerical schemes for the HJ equations (and hence the Level Set (LS) equation) are merely adaptations of the well-known ones for the conservation laws 3.31. Instead, in several dimensions problems, in spite of the relation between Hamilton-Jacobi equation 3.34 and the conservation laws 3.38 (written for $\vec{\nabla}\phi$) is still effective, the building of numerical schemes is not directly borrowed from the ones developed for multidimensional conservation laws for the numerical Hamiltonian building-up. This consideration is due because of the difficulty to see, in multiple dimensions, the correlation between the analytical Hamiltonian $H\left(\vec{\nabla}\phi\right)$ and the numerical one, in some integral form of the related conservation laws , since the relation between ϕ and $\vec{U} = \vec{\nabla}\phi$ is not simply a straightforward integral operator.

$$\begin{array}{ccccc} \phi_t + H\left(\vec{\nabla}\phi\right) = 0 & \overset{\vec{U}=\vec{\nabla}\phi}{\Longleftrightarrow} & \vec{U}_t + \vec{\nabla}\cdot\underline{\underline{F}}\left(\vec{U}\right) = 0 \\ & \Downarrow & \\ H\left(\vec{\nabla}\phi\right) & \overset{?}{\Longleftrightarrow} & \tilde{H}\left(\vec{\nabla}\phi\right) \end{array} \tag{3.55}$$

Fortunately for the multidimensional case, Crandall and Lions [20; 21] have shown that it is still possible to build a discrete approximation of the general first order Hamilton-Jacobi PDE 3.34, with explicit marching schemes. These scheme have the form (for a two dimensional problem, without any loss of generality for several dimensions):

$$\phi_{j\,k}^{n+1} = G\left(\phi_{j-p\;k-r}^n \cdots, \phi_{j+q+1\;k+s+1}^n\right) \tag{3.56}$$

which gives a computed solution with some relation in terms of "convergence", with the vanishing viscosity solution of the starting Hamilton-Jacobi equation. Let, in fact, consider the following theorems and definitions, following references [20; 21].

Definition A numerical method

$$\phi_{j\,k}^{n+1} = G\left(\phi_{j-p\;k-r}^{n} \cdots, \phi_{j+q+1\;k+s+1}^{n}\right) \tag{3.57}$$

for problems of the form:

$$\begin{cases} \phi_t + H\left(\vec{\nabla}\phi\right) = 0 \\ \phi\left(\vec{x}, t = 0\right) = \phi_0\left(\vec{x}\right) \end{cases} \tag{3.58}$$

has a *differenced form*, if exists some function $\tilde{H}$ such that:

$$G\left(\phi_{j-p\;k-r}^{n} \cdots, \phi_{j+q+1\;k+s+1}^{n}\right) = \phi_{j\,k}^{n} - \Delta t^{n} \quad \tilde{H}\left(\frac{\Delta_+^x}{\Delta x}\phi_{j-p\;k-r}^{n}, \cdots, \frac{\Delta_+^x}{\Delta x}\phi_{j+q+1\;k+s+1}^{n}; \frac{\Delta_+^y}{\Delta y}\phi_{j-p\;k-r}^{n}, \cdots, \frac{\Delta_+^y}{\Delta y}\phi_{j+q+1\;k+s+1}^{n}\right) \tag{3.59}$$

where:

$$\Delta_\pm^x \phi_{i\,j} = \pm\left(\phi_{i\pm1\,j} - \phi_{i\,j}\right) \quad ; \quad \Delta_\pm^y \phi_{i\,j} = \pm\left(\phi_{i\,j\pm1} - \phi_{i\,j}\right) \tag{3.60}$$

Definition A numerical scheme in *differenced form* is consistent if:

$$\tilde{H}\left(a \cdots a; b \cdots b\right) = H\left(a, b\right) \qquad \forall a, b \in \Re \tag{3.61}$$

Definition An explicit marching scheme in the form 3.56 or in its differenced form 3.59 is *monotone* if

$$G\left(\phi_{j-p\;k-r}^{n} \cdots, \phi_{j+q+1\;k+s+1}^{n}\right) \tag{3.62}$$

is a nondecreasing function of each argument, as long as the discrete derivatives along x and y are bounded.

Theorem 3.4.1. *Given a time marching numerical scheme*

$$G\left(\phi_{j-p\;k-r}^{n} \cdots, \phi_{j+q+1\;k+s+1}^{n}\right) \tag{3.63}$$

with a differenced form, consistent and monotone ; let u *be the viscosity solution of the Hamilton-Jacobi equation type 3.58, then there is a constant* c *(depending only on* $\sup|u_0|$, $\tilde{H}$ *and* $N\,\Delta t^n$*) such that:*

$$\left|\phi_{j\,k}^{n} - u\left(x_j, y_k, n\Delta t^n\right)\right| \leqslant c\left(\sqrt{\Delta t^n}\right) \tag{3.64}$$

for $0 \leqslant n \leqslant N$ *and* $\forall j, k$.
Note that theorem is still valid in the case of general Hamiltonian $H\left(\vec{x}, t, \phi, \vec{\nabla}\phi\right)$.

Hence, an important remark that can now be underlined in terms of the confidence of the numerical solutions for the first order Hamilton-Jacobi in multidimensional problems is the follow:

- as mentioned before, for monodimensional Hamilton-Jacobi equations type, it is possible to prove the convergence to the vanishing viscosity weak solution of a conservative, consistent and monotone numerical scheme for equation 3.44;

- passing to multidimensional problems 3.34 that statement, proved for monodimensional ones, is still valid. In fact the last statement of the theorem 3.4.1 says proper that the limit, as $\Delta t \to 0$, of the numerical solution evaluated with a differenced form (like conservative form for conservation law), consistent and monotone is the vanishing viscosity solution (or that is the same: entropy satisfying solution), with a rate of convergence $O\left(\sqrt{\Delta t}\right)$.

This fact allows to build convergent numerical schemes for several dimensional Hamilton-Jacobi equations with the same techniques devised for the one dimensional type one, with the sole complication due to multidimensional aspects, as will be shown in the following.

Some remarks on the use of the 1D RP for the multi-D problem

The LS equation for the multi-D case and its solution by means of the use of 1D Riemann problems along each coordinate direction allows to make some remarks if the starting problem is seen as an advection problem.

The Level Set equation can, in fact, be written down explicitly in its *quasi linear formulation* for a 2D problem without less of generality (remember that the LS equation for an internally generated motion field, pointwise normal to the interface, does not admit a conservative formulation, that instead its "derivative version" has got):

$$\phi_t + V\frac{\phi_{x_1}}{\sqrt{\phi_{x_1}^2 + \phi_{x_2}^2}} \cdot \phi_{x_1} + V\frac{\phi_{x_2}}{\sqrt{\phi_{x_1}^2 + \phi_{x_2}^2}} \cdot \phi_{x_2} = 0 \tag{3.65}$$

In other terms, considering the expressions of the normal components and its relation with the ϕ function

$$\phi_t + V\, n_{x_1} \cdot \phi_{x_1} + V\, n_{x_2} \cdot \phi_{x_2} = 0 \tag{3.66}$$

that can be interpreted just in terms of an advection problem:

- the characteristic direction along a given coordinate axis is given just by the local normal correspondent component value
- numerically, the decision about the stencil "upwind" direction can be done by a *reconstruction* of the local normal value

As a consequence, the use of 1D Riemann problems coupled with an unsplit technique [120] allows to consider the multidimensional nature of the problem to build up a numerical approximation of the Hamiltonian term

$$V\left|\vec{\nabla}\phi\right| = V\sqrt{\phi_{x_1}^2 + \phi_{x_2}^2} \cong V\sqrt{\phi_{x_1}^*\big|_{j\,k}^2 + \phi_{x_2}^*\big|_{j\,k}^2} \tag{3.67}$$

(where $\phi_{x_1}^*\big|_{j\,k}^2$, $\phi_{x_2}^*\big|_{j\,k}^2$ are the solutions of 1D Riemann along x_1 and x_2 axis)

In particular, this allows exactly (see figure 3.8) to make a "decision" about the local value of the normal component along the correspondent axis, and select properly the right expression for the upwind derivative. This happens except for the case of transonic expansion, where the normal component is set to zero as an ambiguity of the normal stands on the correspondent 1D problem along the chosen coordinate direction.

3.4.2 Level Set Equation: Numerical Scheme

Focusing now the attention on the mentioned numerical schemes applied to the Level Set equation for an internally generated field of motion along the normal direction given by the 3.28, it is now straightforward to consider the formulation of numerical schemes for the one-dimension

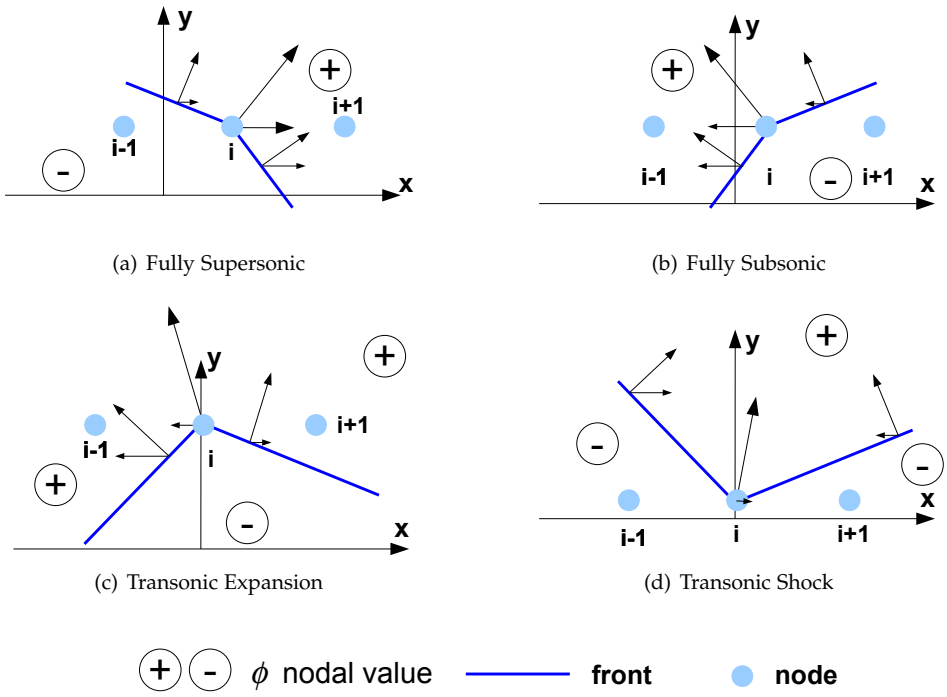

Figure 3.8: Meaning of the Solution of the Riemann Problems

and several dimensions level set equation with the desired order of spatial and time accuracy [31].
In particular, considering the case of one space and time first and second order accuracy numerical schemes, we have the following numerical time marching expressions.

One dimensional Level Set Equation

- Space and Time First Order Scheme

  For the one dimensional Level Set equation, it is immediately possible to write down the following *space and time first order numerical scheme*. Pointing with V the motion velocity, under the hypothesis for it to be convex (concave) in $u = \phi_x$ (in order to have a convex (concave) Hamiltonian) [1] for the exact Riemann solver, we have:

$$\begin{aligned}\phi_j^{n+1} &= \phi_j^n - \Delta t^n \left\{ \max\left(V_j^n, 0\right) \sqrt{\max\left(\max\left(D^{-x}\phi_j^n, 0\right)^2, \min\left(D^{+x}\phi_j^n, 0\right)^2\right)} + \right. \\ &\left. + \min\left(V_j^n, 0\right) \sqrt{\max\left(\min\left(D^{-x}\phi_j^n, 0\right)^2, \max\left(D^{+x}\phi_j^n, 0\right)^2\right)} \right\}\end{aligned} \tag{3.68}$$

  where:

$$D^{-x}\phi_j^n = \frac{\Delta_x^- \phi_j^n}{\Delta x} = \frac{\phi_j^n - \phi_{j-1}^n}{\Delta x} \quad ; \quad D^{+x}\phi_j^n = \frac{\Delta_x^+ \phi_j^n}{\Delta x} = \frac{\phi_{j+1}^n - \phi_j^n}{\Delta x} \tag{3.69}$$

  are the numerical derivatives of the Level Set function along the x direction.

[1] a function f of one variable x and twice differentiable is convex (concave) if: $\frac{d^2 f}{dx^2} > 0 \ (< 0) \quad \forall x$

The numerical scheme 3.68 is monotone under the CFL condition:

$$\Delta t^n \leqslant \frac{\Delta x}{\max(\left|V_j^n\right|)} \tag{3.70}$$

- Space and Time Second Order Scheme

  If again the front motion velocity V is convex (concave), a second order in time and space numerical scheme can be obtained considering: an ENO scheme for the building of the numerical Hamiltonian, coupled with the exact Riemann solver and the Heun's method for the time derivative. Rearranging the expression of the numerical Hamiltonian as follows:

$$\begin{aligned}\tilde{H}\left(V_j^n, D^{-x}\phi_j^n, D^{+x}\phi_j^n\right) &= \left\{\max\left(V_j^n, 0\right)\sqrt{\max\left(\max\left(D^{-x}\phi_j^n, 0\right)^2, \min\left(D^{+x}\phi_j^n, 0\right)^2\right)} + \right. \\ &\left. + \min\left(V_j^n, 0\right)\sqrt{\max\left(\min\left(D^{-x}\phi_j^n, 0\right)^2, \max\left(D^{+x}\phi_j^n, 0\right)^2\right)}\right\}\end{aligned} \tag{3.71}$$

  Its second order approximation by a second order ENO scheme is simply obtained substituting the numerical derivatives expressions with their second order approximations:

$$\begin{aligned}D^{-x}\phi_j^n\Big|_{II} &= D^{-x}\phi_j^n + \frac{\Delta x}{2}\text{MINMOD}\left(D^{-x-x}\phi_j^n\,,\, D^{-x+x}\phi_j^n\right) \\ D^{+x}\phi_j^n\Big|_{II} &= D^{+x}\phi_j^n - \frac{\Delta x}{2}\text{MINMOD}\left(D^{+x+x}\phi_j^n\,,\, D^{+x-x}\phi_j^n\right)\end{aligned} \tag{3.72}$$

  where the following symbolic notation is introduced:

$$\begin{aligned}D^{-x-x}\phi_j^n &= \frac{D^{-x}\phi_j^n - D^{-x}\phi_{j-1}^n}{2\Delta x} = \frac{\phi_j^n - 2\phi_{j-1}^n + \phi_{j-2}^n}{2\Delta x^2} \\ D^{+x-x}\phi_j^n = D^{-x+x}\phi_j^n &= \frac{D^{+x}\phi_j^n - D^{-x}\phi_j^n}{2\Delta x} = \frac{\phi_{j+1}^n - 2\phi_j^n + \phi_{j-1}^n}{2\Delta x^2} \\ D^{+x+x}\phi_j^n &= \frac{D^{+x}\phi_{j+1}^n - D^{+x}\phi_j^n}{2\Delta x} = \frac{\phi_{j+2}^n - 2\phi_{j+1}^n + \phi_j^n}{2\Delta x^2}\end{aligned} \tag{3.73}$$

$$\text{MINMOD}(a,b) = \begin{cases} \text{if} \quad a\cdot b \geqslant 0 & \begin{cases} a & \text{if} \quad |a| \leqslant |b| \\ b & \text{if} \quad |a| > |b| \end{cases} \\ \text{if} \quad a\cdot b < 0 & 0 \end{cases} \tag{3.74}$$

  So that the resultant time marching expression of the numerical scheme is given by

$$\phi_j^{n+1} = \phi_j^n - \Delta t^n \frac{1}{2}\left[\tilde{H}\left(V_j^n, D^{-x}\phi_j^n\Big|_{II}, D^{+x}\phi_j^n\Big|_{II}\right) + \tilde{H}\left(V_j^n, D^{-x}\phi_j^{n+1}\Big|_{II}, D^{+x}\phi_j^{n+1}\Big|_{II}\right)\right] \tag{3.75}$$

  where the solution of the predictor step is given by

$$\phi_j^{n+1} = \phi_j^n - \Delta t^n\,\tilde{H}\left(V_j^n, D^{-x}\phi_j^n\Big|_{II}, D^{+x}\phi_j^n\Big|_{II}\right) \tag{3.76}$$

  and the CFL condition is expressed by equation 3.70.

Multi dimensional Level Set Equation

Without less of generality, we will consider to illustrate the multidimensional case, only the case of a 2D problem in Cartesian uniform rectangular coordinates, as the case in cylindrical coordinates will be discussed in the paragraph 3.4.2, page 52.

- Space and Time First Order Scheme

  Considering the case of V convex (concave) in $u = \phi_x$; $v = \phi_y$ (so that it gives a convex (concave) Hamiltonian) [2], in order to build-up a numerical scheme for a multi-D problem, starting from the one-dimensional problem, the step is short. In fact, using an exact Riemann solver for the spatial term and a one-step Runke-Kutta scheme, we have:

$$\begin{aligned}\phi_{jk}^{n+1} = \phi_{jk}^{n} - \Delta t^{n} \Big\{ & \max\left(V_{jk}^{n}, 0\right)\left[\max\left(\max\left(D^{-x}\phi_{jk}^{n}, 0\right)^{2}, \min\left(D^{+x}\phi_{jk}^{n}, 0\right)^{2}\right) + \right. \\ & \left. + \max\left(\max\left(D^{-y}\phi_{jk}^{n}, 0\right)^{2}, \min\left(D^{+y}\phi_{jk}^{n}, 0\right)^{2}\right)\right]^{\frac{1}{2}} + \\ & + \min\left(V_{jk}^{n}, 0\right)\left[\max\left(\min\left(D^{-x}\phi_{jk}^{n}, 0\right)^{2}, \max\left(D^{+x}\phi_{jk}^{n}, 0\right)^{2}\right) + \right. \\ & \left. + \max\left(\min\left(D^{-y}\phi_{jk}^{n}, 0\right)^{2}, \max\left(D^{+y}\phi_{jk}^{n}, 0\right)^{2}\right)\right]^{\frac{1}{2}} \Big\}\end{aligned} \tag{3.77}$$

  where

$$\begin{aligned} D^{-x}\phi_{jk}^{n} &= \frac{\Delta_x^{-}\phi_{jk}^{n}}{\Delta x} = \frac{\phi_{jk}^{n} - \phi_{j-1\,k}^{n}}{\Delta x} \quad ; \quad D^{+x}\phi_{jk}^{n} = \frac{\Delta_x^{+}\phi_{j}^{n}}{\Delta x} = \frac{\phi_{j+1\,k}^{n} - \phi_{jk}^{n}}{\Delta x} \\ D^{-y}\phi_{jk}^{n} &= \frac{\Delta_y^{-}\phi_{jk}^{n}}{\Delta y} = \frac{\phi_{jk}^{n} - \phi_{jk-1}^{n}}{\Delta y} \quad ; \quad D^{+y}\phi_{jk}^{n} = \frac{\Delta_y^{+}\phi_{j}^{n}}{\Delta y} = \frac{\phi_{jk+1}^{n} - \phi_{jk}^{n}}{\Delta y} \end{aligned} \tag{3.78}$$

  are the numerical approximations of the spatial derivatives.

  The resultant numerical scheme is in a differenced form & consistent and is monotone and, hence, convergent to the entropy satisfying weak solution [21] under the CFL condition:

$$\Delta t^{n} \leqslant \min \frac{1}{\frac{\left|V_{jk}^{n}\,(n_x)_{jk}^{n}\right|}{\Delta x} + \frac{\left|V_{jk}^{n}\,(n_y)_{jk}^{n}\right|}{\Delta y}} \tag{3.79}$$

  where $(n_x)_{jk}^{n}$ and $(n_y)_{jk}^{n}$ are numerical approximation of the normal of the Level Set function ϕ_{jk}^{n}.

- Space and Time Second Order Scheme

  Following what shown for the 1D second order numerical scheme, the time and space second order scheme is obtained directly using the equations 3.75 and 3.76. Hence, considering again the Heun's method for the time derivative, the ENO reconstruction for the spatial derivatives and the exact Riemann solver, we have to give the expression of the numerical Hamiltonian, which is:

2 a function of many variables $f(x, y)$ is convex (concave) if its *Hessian* matrix is positive (negative) semidefinite $\forall x, y$

$$\tilde{H}\left(V_{jk}^{n}, D^{-x}\phi_{jk}^{n}, D^{+x}\phi_{jk}^{n}, D^{-y}\phi_{jk}^{n}, D^{+y}\phi_{jk}^{n}\right) = \quad \dots$$

$$\begin{aligned}
&\left\{\max\left(V_{jk}^{n}, 0\right)\left[\max\left(\max\left(D^{-x}\phi_{jk}^{n}, 0\right)^{2}, \min\left(D^{+x}\phi_{jk}^{n}, 0\right)^{2}\right) + \right.\right. \\
&\quad \left.+ \max\left(\max\left(D^{-y}\phi_{jk}^{n}, 0\right)^{2}, \min\left(D^{+y}\phi_{jk}^{n}, 0\right)^{2}\right)\right]^{\frac{1}{2}} + \\
&+ \min\left(V_{jk}^{n}, 0\right)\left[\max\left(\min\left(D^{-x}\phi_{jk}^{n}, 0\right)^{2}, \max\left(D^{+x}\phi_{jk}^{n}, 0\right)^{2}\right) + \right. \\
&\quad \left.\left.+ \max\left(\min\left(D^{-y}\phi_{jk}^{n}, 0\right)^{2}, \max\left(D^{+y}\phi_{jk}^{n}, 0\right)^{2}\right)\right]^{\frac{1}{2}}\right\}
\end{aligned} \tag{3.80}$$

where the numerical derivatives must be defined by their second order expression given in the equation 3.73 and the equations 3.74, 3.79 stand with the necessary modifications.

To complete the general discussion about the LS equation numerical integration, here is briefly discussed the case of non-convex motion velocities V. This is not the case of the grain burnback analysis problem, where V assumes the meaning of the grain burning rate (always positive, at the most zero) which value does not depend on the normal direction, but only on time and space. So that, in this case the Hamiltonian is also an homogeneous function of degree one in $u = \phi_x, v = \phi_y$. In other words, in the case of a non-convex motion velocity, the expressions of the numerical Hamiltonian for the 1D and the Multi-D problems can be given by the analytical expression, with the spatial derivatives approximated by the average value of the left-/right numerical derivatives (first or second order approximations) with the additional terms of numerical viscosity in order to have a stable scheme, in a Lax Friedrichs fashion (or its local variations)[35; 59] (see appendix J , page f).

A completely general discussion and overview of the numerical schemes for the HJ equations can be however found in the appendix J, page f.

Level Set Equation in Cylindrical Coordinates

For the SRM grain burnback analysis applications, the Level Set equation 3.28 can be written in a useful manner, in cylindrical coordinates (see equation 3.81), in order to exploit the grain and case periodicity and/or symmetry properties, as usual for typical grain configurations.

$$\frac{\partial\phi}{\partial t} + r_b\sqrt{\left(\frac{\partial\phi}{\partial r}\right)^{2} + \left(\frac{1}{r}\frac{\partial\phi}{\partial\theta}\right)^{2} + \left(\frac{\partial\phi}{\partial z}\right)^{2}} = 0 \tag{3.81}$$

where the grid function is represented in cylindrical coordinates $\phi = \phi(r, \theta, z)$, with z motor axis.

The numerical scheme expressions are the same given in the paragraph 3.4.2, page 51, for the first and second order of accuracy in time and space, considering that the grain burning rate is always positive, at most zero. For clarity, the first order in time and space is expressed in equation 3.82, where the i-index is along the azimuthal direction θ, the j-index is along the radial direction r and k-index is along the motor axis direction z.

$$\phi_{ijk}^{n+1} = \phi_{ijk}^{n} - \Delta t^{n} \left\{ r_b|_{ijk}^{n} \left[\max\left(\max\left(\frac{1}{r_j} D^{-\theta}\phi_{ijk}^{n}, 0 \right)^2, \min\left(\frac{1}{r_j} D^{+\theta}\phi_{ijk}^{n}, 0 \right)^2 \right) + \right.\right.$$
$$+ \max\left(\max\left(D^{-r}\phi_{ijk}^{n}, 0 \right)^2, \min\left(D^{+r}\phi_{ijk}^{n}, 0 \right)^2 \right) +$$
$$\left.\left. + \max\left(\max\left(D^{-z}\phi_{ijk}^{n}, 0 \right)^2, \min\left(D^{+z}\phi_{ijk}^{n}, 0 \right)^2 \right) \right]^{\frac{1}{2}} \right. \tag{3.82}$$

3.5 Errors sources: a larger perspective

In this section we want to analyze in a deepened manner the errors sources of the Level Set approach for tracking an interface motion under a given velocity field.

Three different and separated error sources in this kind of approach [59] are present:

- Initialization error
  This error is associated to the building-up of the initial condition of the Level Set problem (see paragraph 3.6, page 53). It is due in particular to the generation, starting from the problem given on the interface Γ, of the problem in the computational domain, where the level set, that represents Γ with its zero level, is defined (a problem in one more dimension).
- Motion Error or Update Error
  This error is due to the numerical solution of the time-dependent Level Set equation 3.28, that needs the use of one of the many techniques described in paragraph 3.4.1, page 44 and paragraph 3.4.2, page 48. As known, each numerical scheme is characterized by its own spatial and time accuracy orders, which affect the error introduced in tracking the boundary motion.
- Measurement Error or Reconstruction Error or Extraction Error
  This kind of error is associated to the fact that in the Eulerian point of view the interface itself does not really exist, if not seen as part of the Level Set. Hence, any application that wants to know where is the interface, or defines any integral or differential property of it, at any time, must *extract* or make a *reconstruction* of the boundary, considering the Level Set field at the same time. As a consequence, accomplishing this work numerically, an error is unavoidably introduced (this operation may be fulfilled by means of contour plotter or other diagnostics [30; 68], or the technique that will be analyzed in paragraph 3.11, page 66). For some applications, truly, this last operation can be avoided, directly extracting, by proper numerical techniques (that will be seen later on, see paragraph 3.11, page 66), the searched geometrical properties of the interface during its motion. The numerical errors that are introduced by that kind of numerical techniques are classified as *measurement error*.

While it is hard to decide how to remove the first and the third error sources, and hence some caution is needed for them, the second one is quite simple to control by means of the choice of the numerical scheme spatial and time accuracy.

Considering also that the numerical scheme accuracy order of the Level Set equation must be at least consistent with the numerical algorithm to build-up the initial condition and to extract, if necessary, the boundary and its properties, and vice versa.

3.6 LS Initial Condition

The level set equation needs a level set to evolve as initial condition, which as the sole constraint and relation with the boundary to evolve to have its zero level coincident with the initial given

front. Hence, giving the initial front to be evolved, only the level zero of the level set is defined. This condition leaves an arbitrary choice on the initialization of the level set starting from the front known initially. Even if some remarks can be done dependently on the considered problem (considering the general case of a 3D problem).

- Surface known analytically
  This is the less applicative, but simplest case, in which the starting front is given by an analytic function. The level set is automatically given by the analytic function that represents the boundary, considered in an implicit fashion.

- Surface known numerically
  In this case there are different possible manners to build-up the initial condition for the level set equation. Considering that the boundary is known in a discrete manner (at zero order of approximation, by points, at first order, by a triangular tessellation of the surface, and so on . . .), we can:
  - consider an implicit function fashion, starting from a point-to-point knowledge of the surface, along a particular direction of the boundary (for example the motor axis for the grain propellant of a solid rocket motor) from which the level set is evaluated (note that the surface itself must be monovalued, considering the particular direction variable as dependent);
  - initialize the grid function ϕ as a Signed Distance Function (SDF) from the front Γ. This is defined by the following expression:

$$\mathrm{SDF}(\vec{x}, \Gamma) = \pm \min_{\forall \vec{x_I} \in \Gamma} \left(d\left(\vec{x}, \vec{x_I}\right) \right) \qquad \forall \vec{x} \in \Omega \tag{3.83}$$

    where

$$d\left(\vec{x}, \vec{x_I}\right) = \left\| \vec{x} - \vec{x_i} \right\|_2 \tag{3.84}$$

    and the sign of the SDF is positive if the point is inner of the surface and negative otherwise, or vice versa (note that this choice defines the outer and the inner, by means of the definition of the normal outward direction).

This last option, as can be applied for a general, even complex given surface, needs some other remarks.
In fact, the use of a Signed Distance Function as initial condition of the LS problem is advised in order to solve numerically the equation 3.28, through the techniques shown before. It has, as matter of fact, the following relevant properties:

- it keeps the level set smooth near the tracked front;
- it allows to build well-posed numerical approximation of the Level Set derivatives;
- it defines a uniform separation for the Level Sets around the front in order to accurately evaluate front properties, as normal direction and curvature.

These characteristics are particularly important when building-up a differenced approximation of the grid function space derivatives, to keep the numerical solution well defined and accurate.
However, the numerical evaluation of the Signed Distance Function is quite algorithmic time consuming expansive. Hence, some attentions are needed to implement it in real applications. In fact, the accuracy on the initial condition is required only near the zero level (that is to say the front to evolve, as the interesting is often limited to it), in a band dependent by the numerical scheme stencil (that is, its spatial accuracy), and hence a discrete value based in grid distances can suffice far away.

3.6.1 SDF building for 3D and Axisymmetric grain geometries

As said in the last paragraph, the only constraint given by the Level Set Method to its Initial Condition is that its level zero is the front to be moved. Hence, the choice and the its building up, can be defined by means of:

- a computational effectiveness point of view, in order to reduce the computational cost of the resultant grain burnback analysis algorithm;
- and by a numerical point of view to have a well position of the related discretized problem.

As a matter of fact, far from trivial cases, we can expect that the design of the grain initial shape, as a trade off between several mission requirements (defined thrust time trend, grain stress analysis as principal ones, and so on...), will be made through an iterative Computer Aided Design (CAD) design process. So that at a given step, the grain initial surface is given in a numerical discrete manner. Hence, to be of practical use, the IC for the LS technique must be built up starting from a numerical known surface. Preferably with a general and automatic procedure from the CAD representation of the grain initial burning surface, and the case or the Thermal Protections inner profile.

A very useful, general and computerised way to do that is just to compute the Signed Distance Function from the grain initial shape Γ given by the equation 3.83, that has the relevant property that $\left|\vec{\nabla}\phi\right| = 1$, with the aforementioned advantages and drawbacks.

An important remark, that deserves a particular discussion, is that as underlined and used by a recent work [108; 107], the Initial Condition built up as Signed Distance Function from the front is directly the solution of the problem, if the grain burning surface velocity is assumed constant in space, as will be shown in paragraph 3.8, page 60.

The main drawback of this way to solve the problem stands in the computational cost necessary to obtain it numerically. In fact, as far from trivial cases, the SDF must be evaluated for each boundary point, for all the points of the domain of interest.

Our idea is, hence, to recover and highly reduce the computational cost required to set numerically the initial condition as Signed Distance Function, considering a computation of it, banded only near the Level zero of interest. The band dimension has to be set dependently on the numerical scheme stencil, in a such manner that, the number of levels considered suffices to build up well posed spatial derivatives and will not affect in the front evolution the solution of the problem.

As input of the algorithm that builds the numerical banded SDF, as made in the work [107], we have considered a StereoLithography (STL) file format as input file, supported by several CAD tools as output format of surfaces representation. A STL representation of a surface is an unstructured discrete tessellation of a surface by means of triangles, listed in the file as vertexes and normal direction to the face, in a such manner that the normal definition follows the right-hand rule of vertexes sorting (see fig. 3.9).

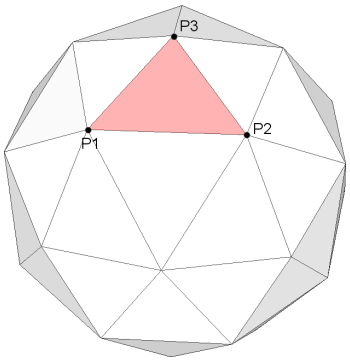

Figure 3.9: STL Representation of a Sphere

The computation of the banded SDF can be, hence, done by means of the evaluation of the minimum distance, in a local grid subdomain for each STL mesh element. For each generic l-th face of the STL surface representation (triangle plane, lines and vertexes, composing it) the distance is evaluated from each grid point (i, j, k) in its block of influence, created locally around the selected face (see figure 3.10):

$$\widetilde{DF_l}\left(i_l, j_l, k_l, l\right) = \min \begin{array}{l} \left\{ d\left(P_{i_l j_l k_l} - \Delta_l\right); d\left(P_{i_l j_l k_l} - \overline{P_{l_1} P_{l_2}}\right); \right. \\ d\left(P_{i_l j_l k_l} - \overline{P_{l_2} P_{l_3}}\right); d\left(P_{i_l j_l k_l} - \overline{P_{l_3} P_{l_1}}\right); \\ d\left(P_{i_l j_l k_l} - P_{l_1}\right); d\left(P_{i_l j_l k_l} - P_{l_2}\right); \\ \left. d\left(P_{i_l j_l k_l} - P_{l_3}\right) \right\} \end{array} \tag{3.85}$$

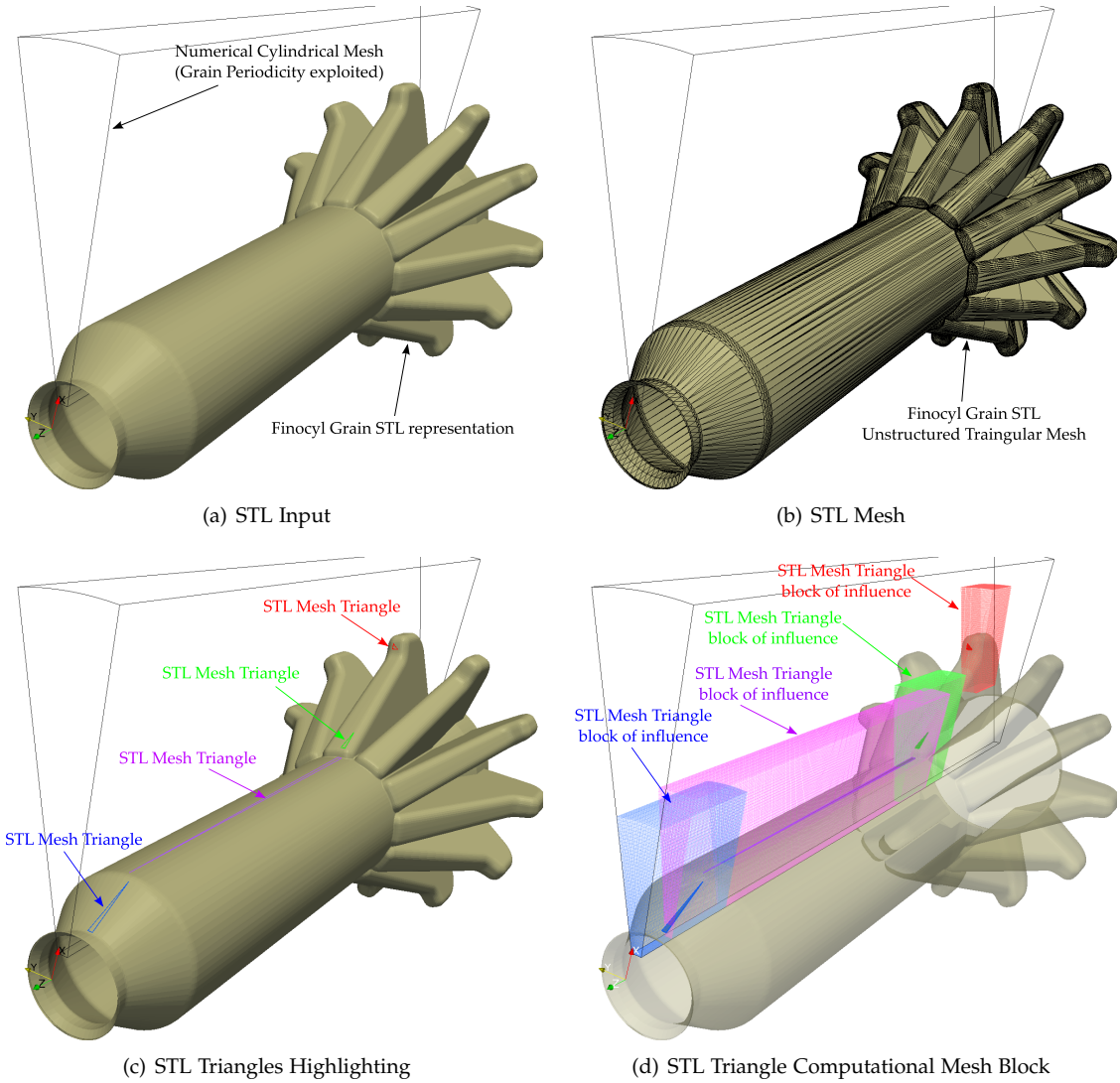

(a) STL Input

(b) STL Mesh

(c) STL Triangles Highlighting

(d) STL Triangle Computational Mesh Block

Figure 3.10: Banded SDF Building from STL file: Triangle Mesh Blocks of Competence

where:

- $P = P\left(i_l, j_l, k_l\right)$ is the generic grid point in the block of competence of the face l;
- $d\left(P_{i_l j_l k_l} - \Delta_l\right)$ is the distance between $P_{i_l j_l k_l}$ and the triangle face plane Δ_l;
- $d\left(P_{i_l j_l k_l} - \overline{P_{l_m} P_{l_n}}\right)$ the distance between the grid point and the vertexes connection lines, for $m, n = 1, 2, 3$ with $m \neq n$;
- and $d\left(P_{i_l j_l k_l} - P_{l_m}\right)$ the distance between the grid point and the generic face vertex, for $m = 1, 2, 3$.

Hence, the resulting numerical Banded Signed Distance Function is given by:

$$\widetilde{SDF}(i,j,k) = \pm \min_{\forall l:\widetilde{DF}_l(i_l,j_l,k_l,l):\phi(i,j,k)\in[\phi_{min};\phi_{max}]} \left(\widetilde{DF}_l(i_l,j_l,k_l,l)\right) \tag{3.86}$$

where ϕ_{min} ; ϕ_{max} represent the positive and negative band cut-off values. These depend on the chosen block of influence dimension selected for the Signed Distance Function and the sign is chosen positive or negative, if the point lies in or out the initial grain surface.

In this way, the evaluation of the initial condition is less computational time consuming than performing the solution of the complete SDF in all the domain, considering the cut-off value and, as consequence, the band initialization limited to the numerical scheme requirements. In the meanwhile, some tests underlined that, with a band enough thick for the building of well posed spatial numerical derivatives of the grid function, the solution is not altered by a banded initialization itself.

Some tests also shown that, even in the case of spatially constant burning rate, where the solution is given by the equation 3.89, it is convenient by a computational point of view, to evaluate the solution, not directly by the SDF evaluation, but as SDF banded evaluation and full matrix LS equation integration in the domain of interest.

Moreover, in order to represent the axisymmetric surfaces of Thermal Protections of the SRM case, a reduced algorithm to build 2D SDFs from a given tabulated list of points has been developed. This is a simplification of the equations 3.85 and 3.86 considering the bi-dimensional nature of the problem. As the computational cost of this procedure is very low, for the typical grids used in GREG, a complete (not-banded) SDF initialization is considered in this case in one of the azimuthal planes. Then the grid of the Thermal Protections is sweet all over the azimuthal planes to obtain the TPs complete grid function.

SDF use for automatic 3D mesh generator

The SDF representation of surfaces in 3D cylindrical or rectangular grids has been exploited also to generate in a automatic way the 3D meshes for a 3D Eulerian Computational Fluid Dynamics (CFD) code with cylindrical multi-blocks structured orthogonal (rectangular and cylindrical grids) grids, able to simulate the pre-ignition transient of SRM[115]. It considers directly as input for the grid generation, the output from the standard CAD (STL) representation of the SRM components: igniter, grain propellant and nozzle. Thus, the generation of the numerical grid is made by the construction of the Signed Distance Function from the CAD surfaces. Once the physical domain has been discretized into each finite volume the SDF from the closest CAD surface is computed and the finite volume is tagged as grain, igniter, nozzle, or bore cell, according to the sign of the distance. This technique lets to an almost fully-automatic grid generation: the user must set only the domain discretization. This technique has been developed with the support of Ph.D. Ing. Stefano Zaghi in the framework of his Ph.D. Thesis[115], from which the figures of the generated meshes are extracted (see figure 3.11).

3.7 LS Boundary Conditions

Naturally the use of finite computational grid to capture the interface motion and solve the Level Set equation requires some boundary conditions at the borders of the numerical lattice. Normally, the numerical solution of the Level Set equation 3.28 by means of up-wind numerical schemes (as in its generalization version given by Godunov schemes) will naturally set the outward-flowing one-sided differences at the boundaries for front that expand under the motion velocity V. Hence, there is not the need of particular attention for these cases.
Other discussions deserve instead the cases of general velocity fields V and also particular starting front symmetries (periodic or mirror symmetric fronts), which particular boundaries conditions can be required for. In particular, in the latter case, it could be important for motion velocity fields that preserve the interface symmetry during its evolution, to exploit these conditions in order to decrease the number of grid points and, consequently, the computational costs.

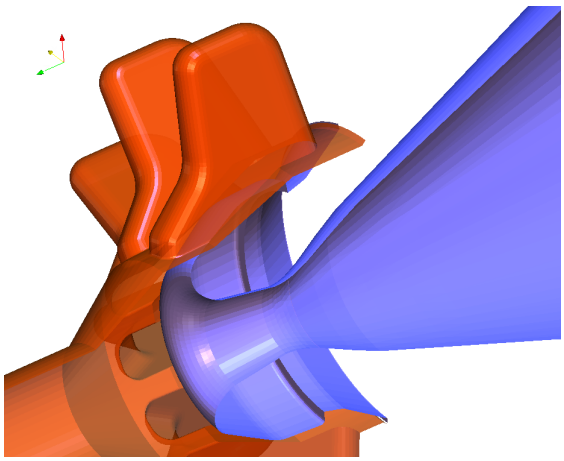

Courtesy of Stefano Zaghi, Ph.D. Thesis[115]

(a) CAD Input

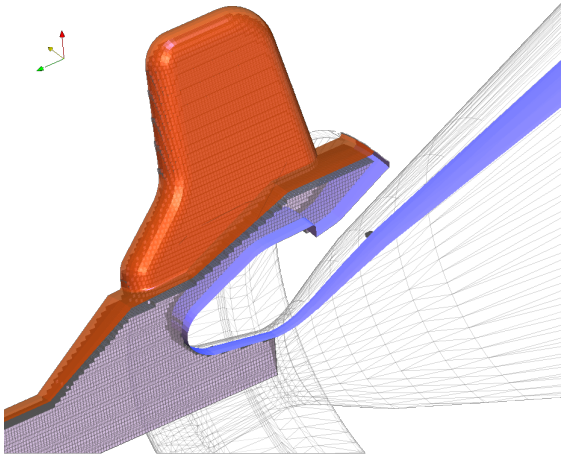

Courtesy of Stefano Zaghi, Ph.D. Thesis[115]

(b) Mesh Generation

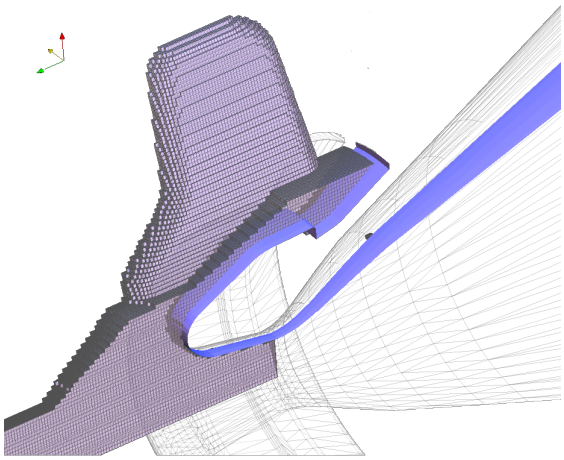

Courtesy of Stefano Zaghi, Ph.D. Thesis[115]

(c) Mesh Details

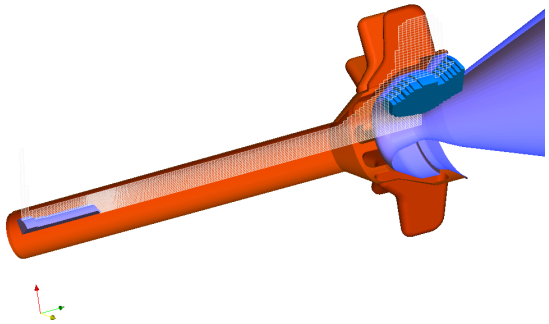

Courtesy of Stefano Zaghi, Ph.D. Thesis[115]

(d) Mesh

Figure 3.11: Output of Mesh and Initial Conditions Generator of the MUG Code

This is, in fact, the typical situation of 3D or 2D grain shapes, receding under a constant in space or constant in the section burning rate (for Q1D internal ballistics models), for which mirroring BCs can be exploited during the grain surface motion.

Hence, the following Boundary Conditions types may represent all the practical cases, limiting the treatment to computational domains with boundaries along the coordinate directions, which in the Eulerian nature of the technique can be achieved in whatever case. The BCs will be expressed for a simple 2D case in rectangular coordinates (x_1, x_2) (with indices along the x_1 direction $j = 1, \ldots, n$ and along the x_2 direction $k = 1, \ldots, m$), but it is straightforward their implementation in cylindrical coordinates as well.

- **Extrapolation BC**
  The ghost node values of the grid function over the boundaries are simply set to a linear extrapolation of the inner node values. This is completely equivalent to consider constant along the considered boundary the cross spatial derivatives (see figure 3.12).

- Along x_1 lower boundary

$$\phi_{j\,0} = \phi_{j\,1} + \frac{\phi_{j\,2} - \phi_{j\,1}}{x_2|_{j\,2} - x_2|_{j\,1}} \left(x_2|_{0\,k} - x_2|_{j\,1} \right) \iff D^{x_2}|_{x_1 = x_1^{low}} = \text{const}$$

- Along x_1 upper boundary

$$\phi_{j\,m+1} = \phi_{j\,m} + \frac{\phi_{j\,m} - \phi_{j\,m-1}}{x_2|_{j\,m} - x_2|_{j\,m-1}} \left(x_2|_{j\,m+1} - x_2|_{j\,m-1} \right) \iff D^{x_2}|_{x_1 = x_1^{up}} = \text{const}$$

- Along x_2 lower boundary

$$\phi_{0\,k} = \phi_{1\,k} + \frac{\phi_{2\,k} - \phi_{1\,k}}{x_1|_{2\,k} - x_1|_{1\,k}} \left(x_1|_{0\,k} - x_1|_{1\,k} \right) \iff D^{x_1}|_{x_2 = x_2^{low}} = \text{const}$$

- Along x_2 upper boundary

$$\phi_{n+1\,k} = \phi_{n\,k} + \frac{\phi_{n\,k} - \phi_{n-1\,k}}{x_1|_{n\,k} - x_1|_{n-1\,k}} \left(x_1|_{n+1\,k} - x_1|_{n-1\,k} \right) \iff D^{x_1}|_{x_2 = x_2^{up}} = \text{const}$$

- **Periodic BC**

The ghost node values are set as direct copy, step to step, to the correspondent alias nodes along the periodicity axis. This is particularly useful when the starting front and the velocity motion field keep the interface periodicity property, to avoid the wasting of computational costs for the simulation (see figure 3.12).

- Along x_1 lower boundary

$$\phi_{j\,0} = \phi_{j\,m-1} \quad \text{with} \quad x_2|_{j\,0} = x_2|_{j\,1} - \left(x_2|_{j\,m} - x_2|_{j\,m-1} \right)$$

- Along x_1 upper boundary

$$\phi_{j\,m+1} = \phi_{j\,2} \quad \text{with} \quad x_2|_{j\,m+1} = x_2|_{j\,m} + \left(x_2|_{j\,2} - x_2|_{j\,1} \right)$$

- Along x_2 lower boundary

$$\phi_{0\,k} = \phi_{n-1\,k} \quad \text{with} \quad x_1|_{0\,k} = x_1|_{1\,k} - \left(x_1|_{n\,k} - x_1|_{n-1\,k} \right)$$

- Along x_2 upper boundary

$$\phi_{n+1\,k} = \phi_{2\,k} \quad \text{with} \quad x_1|_{n+1\,k} = x_1|_{n\,k} + \left(x_1|_{2\,k} - x_1|_{1\,k} \right)$$

- **Mirroring BC**

The ghost nodal values are set, in this case, as direct copy of the correspondent alias nodes along the mirroring axis. This becomes useful again in order to reduce computational costs of front evolution problems that have and preserve this geometrical properties of the interface along its motion (see figure 3.12).

- Along x_1 lower boundary

$$\phi_{j\,0} = \phi_{j\,2} \quad \text{with} \quad x_2|_{j\,0} = 2\,x_2|_{j\,1} - x_2|_{j\,2}$$

- Along x_1 upper boundary

$$\phi_{j\,m+1} = \phi_{j\,m-1} \quad \text{with} \quad x_2|_{j\,m+1} = 2\,x_2|_{j\,m} - x_2|_{j\,m-1}$$

- Along x_2 lower boundary

$$\phi_{0\,k} = \phi_{2\,k} \quad \text{with} \quad x_1|_{0\,k} = 2\,x_1|_{1\,k} - x_1|_{2\,k}$$

- Along x_2 upper boundary

$$\phi_{n+1\,k} = \phi_{n-1\,k} \quad \text{with} \quad x_1|_{n+1\,k} = 2\,x_1|_{n\,k} - x_1|_{n-1\,k}$$

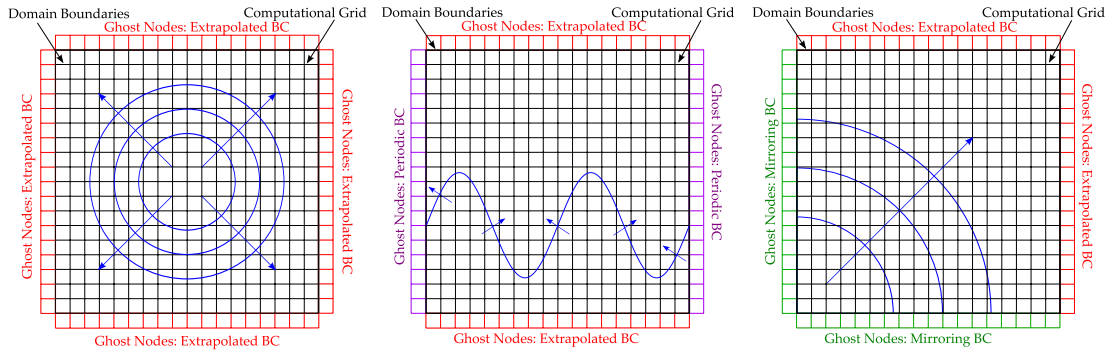

(a) Propagating Circle (b) Propagating Sine (c) Propagating Quarter Circle

Figure 3.12: Samples of BCs in Moving Interfaces with the LSM

3.8 LS Equation Solution in the case of space-constant velocity motion field

Consider now the problem of solving the Level Set equation 3.28, here written again in equation 3.87, in the special case of a motion velocity field directed along the local value of the normal to front itself, for which this form stands, constant in space and time.

$$\begin{cases} \dfrac{\partial \phi}{\partial t} + V \left| \vec{\nabla} \phi \right| = 0 \\ \\ V(\vec{x}, t) = V = \text{const} \end{cases} \tag{3.87}$$

In this case, there is a one-to-one correspondence between the time variable and the motion length of the interface along its normal direction. In the applications to solid propulsion problems, this distance of regression along its normal direction by the burning surface is called, for practical reasons, *web*.

Hence, it is possible to consider in a joint manner the problem as formulated in the *time* variable or in the *web* variable, with the same initial and, if necessary, boundary conditions, as expressed by the equation 3.88.

$$\frac{\partial \phi}{\partial t} + V \left| \vec{\nabla} \phi \right| = 0 \quad \Longleftrightarrow \quad dw = V\, dt \quad \Longleftrightarrow \quad \frac{\partial \phi}{\partial w} + \left| \vec{\nabla} \phi \right| = 0 \tag{3.88}$$

It is simple to check that this equation (3.88) has the following analytic solution:

$$\phi(\vec{x}, w) = \text{SDF}(\vec{x}, \Gamma) - w = \pm \min_{\forall \vec{x_i} \in \Gamma} \left(d(\vec{x}, \vec{x_i}) \right) - w \qquad \forall \vec{x} \in \Omega \tag{3.89}$$

where the $\text{SDF}(\vec{x}, \Gamma)$ is the Signed Distance Function of the point $\vec{x}$ in the domain of integration Ω from the considered starting interface Γ. The Signed Distance Function, in fact, has the property $\left| \vec{\nabla} \phi \right| = 1$ in a "general sense" (the "general sense" attribute is necessary considering that is known, by all said before, that the gradient may become undefined where the interface develops kinks).

Thus, in this special case, neglecting the interface topology and shape, the problem of the motion of a boundary along its normal direction admits an analytic solution, given by the translation in web of the Signed Distance Function to the front. The problem stands, now, on the evaluation of the Signed Distance Function to the starting front itself. This is known analytically only in trivial cases, so that, for general problems, a numerical algorithm for the evaluation of the numerical SDF from a general closed surface is required and computationally very expansive to be computed (as discussed in the paragraph 3.6, page 53).

3.9 Narrow Band Techniques

The simplest manner to implement the Level Set Method is to solve the Level Set equation 3.28 in the entire computational domain, where the problem is initially defined (note that the tracking of the interface motion is limited by the finite computational domain). This is the so called [59] [46] Full Matrix (FM) approach. This approach, in fact, considers a tracking of all the levels of the starting front (for all the possible manners to generate them, starting from the initial front 3.6) updating the "entire matrix" of the grid function in the computational domain. Using the FM approach there are some advantages and drawbacks in solving the starting problem of the moving a given interface:

- data structures and operations are extremely clear and simple to be implemented in Level Set codes;
- if only the Level zero of the grid function is interesting in its evolution, a time computational wasting stands, as really only some grid nodes around the level zero are needed to fulfill the simulation target and build the solution in time (clearly if all the levels are themselves important this is the unique possible approach, considering the use of the Level Set method).

For this last drawback, some efficient implementations of the problem, which consider to work only strictly in a compact support nearby the time-variable considered boundary, have been developed by different authors [42; 57]. These techniques, known as Narrow Banding (NB) approaches or methods, can be seen as an attempt to reach an hybrid Eulerian (as the LS method is in capturing the interface in a fixed numerical lattice)- Lagrangian (for the motion of the compact support attached to the level of interest) motion interface method. In particular, the NB techniques can be distinguished in their manner to build-up the compact support around the zero level:

- a way [42] considers a block (a square in 2D problems, a cube in 3D ones) of mesh nodes where computing the SDF and solving the LS equation;
- the other one [57], instead, develops the compact support basing on bounds (upper and lower) of the levels value.

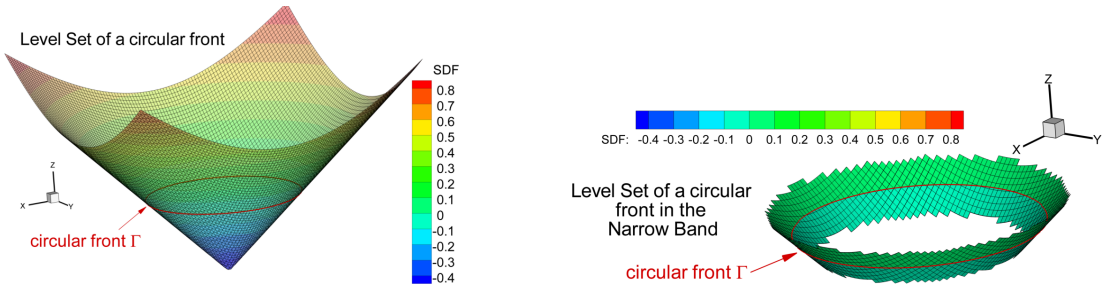

(a) Full Matrix SDF

(b) Narrow Band SDF

Figure 3.13: Full Matrix (FM) & Narrow Banding Techniques

The computational advantages and drawbacks of the use of these kind of techniques can be listed as:

- Saving the overall computational costs
  Considering a d-dimensional interface, it has $O\left(kN^{d-1}\right)$ points, with N the grid point number along a single coordinate direction. The numerical algorithmic computational costs of the *full matrix* and the *Narrow Band* approach for a SDF and a non-SDF initialization are shown (evolution costs are per timestep for the evolution phase) in the table 3.1.

	Initialization	Evolution (per timestep)
LS FM (SDF IC)	$O(kN^{d-1} \cdot N^d)$	$O(N^d)$
LS NB (SDF IC)	$O(kN^{d-1} \cdot N^{d-1})$	$O(kN^{d-1})$
LS FM (non SDF IC)	$O(kN^d)$	$O(N^d)$
LS NB (non SDF IC)	$O(kN^{d-1})$	$O(kN^{d-1})$

Table 3.1: Computational Cost for the NB and FM approaches

For instance, in 3D problems the *full matrix approach* has a computational cost per timestep of evolution that is $O(N^3)$, while for the narrow band methods is $O(kN^2)$. Moreover we have a very different computational cost also for the initialization phase. This is $O(kN^4)$ for the Narrow Banding methods and $O(kN^5)$ for the full matrix approach, for a SDF initialization. Instead, for a non-SDF initialization, the computational costs are $O(kN^3)$ for the FM approach and $O(kN^2)$ for the NB one.

Hence, it is evident that the use of a compact support that follows the boundary motion, allows to drastically reduce the computational costs, both in the initialization phase and in the evolution phase (Level Set equation solution), for the case in which a SDF initialization is required. A different speech is needed, instead, for the case of a non-SDF initialization, as a trade off between the advantages and drawbacks is more necessary. Even if, as discussed before the first one is a completely general method to develop the Level Set IC, with whatever boundary to evolve.

Note that the width of the compact support depends on the Narrow Band technique considered, but above all the numerical scheme stencil dimension, in terms of involved nodes.

- "Local" timestep evaluation
  The choice of the timestep is made in both the approaches (FM & NB) under the CFL condition of the numerical scheme adopted to solve the Level Set equation. But, in a simplified speech, it is possible to state that it applies in response to the maximum characteristics velocity, not simply in response to the front velocity. This means that in the FM approach the timestep can be limited by no interesting grid zones, where the levels are thickened. Considering in such a manner, a useless restriction for the time-marching numerical scheme. Therefore, the Narrow Banding method, performing the timestep calculation only in the moving compact support nearby the level of interest, allows timesteps fitted to the problem itself.

- In some cases the number of the "narrow band nodes" can decrease during the computation, allowing to strongly reduce the computing cost per timestep, as the simulation advance (as in the case of a constant motion velocity field normally directed [28]).

- Increase of the data structures complexity and need of periodic re-initialization
  The data structures necessary to manage the band and its motion in time and the computational costs to access them are more complex with respect to the FM approach. Moreover, as the band is moved (since the level set is updated only in the band), in order to avoid to use non-updated nodes of the LS function a re-initialization technique is necessary to assign the value to that nodes. Hence, the solution must be stopped to assign, after a band motion step, a definition of a "sense value" to the new nodes of the band. This can be made by means of the use of so called *re-initialization techniques* [79; 41; 60; 52; 65]. These solve the problem of the definition of the level set function in the band through the solution of an HJ equation of the type given in the equation 3.90, until steady state is reached and, hence, a SDF in the band is obtained.

$$\phi_t + \text{sign}(\phi)\left(\left|\vec{\nabla}\phi\right| - 1\right) = 0 \tag{3.90}$$

Unfortunately all these techniques are not so much simple to implement. In fact, they tend to move the level of interest to some degree, perturbing it from it's reached location. In such a manner that volumes in or out the interface are not preserved (for that reason different and more complex versions of the previous equation are used in order to limit this effect, that plagued some implementation of the re-initialization techniques).

Concluding it is possible to say, in general terms, that the use of the Narrow Banding techniques can undoubtedly decrease computational costs of the Level Set Method, in the case that a SDF initialization is strongly needed during the front motion. While in the cases that the use of a SDF initialization can be avoided, the need of NB methods may be carefully evaluated. In fact, the aforementioned problems must be faced in terms of volume budget of the resultant technique, and the complication of the algorithm necessary for the re-initialization technique. Hence, in this work, even if some preliminary tests have been performed underlining some of the above-mentioned troubles, the NB methods are not implemented. In fact, the computational time required for each simulation is quite bounded, even with the use of the FM approach, for the typical grids used for the grain burnback simulation.

3.10 Extension of the Velocity Field off the Level Zero

Recalling again the basic idea of the Level Set Method, in the Eulerian approach to the tracking interface problem, we represent the front by an higher dimensional representation related to it: the Level Set function, which Level Zero for all time represents the front itself. This means that passing by the initial front to the Level Set IC, we have to deal with a higher dimensional problem in solving the Level Set equation (recalled in equation 3.91). Hence, even the velocity field of motion (for a front evolving along its normal direction) of the front must be defined in the higher dimensional space, where the problem is solved (see figure 3.14).

$$\phi_t + V_{ext}\left|\vec{\nabla}\phi\right| = 0 \Longrightarrow \begin{cases} \phi = \phi(\vec{x}) \\ V_{ext} = V_{ext}(\vec{x}) \end{cases} \tag{3.91}$$

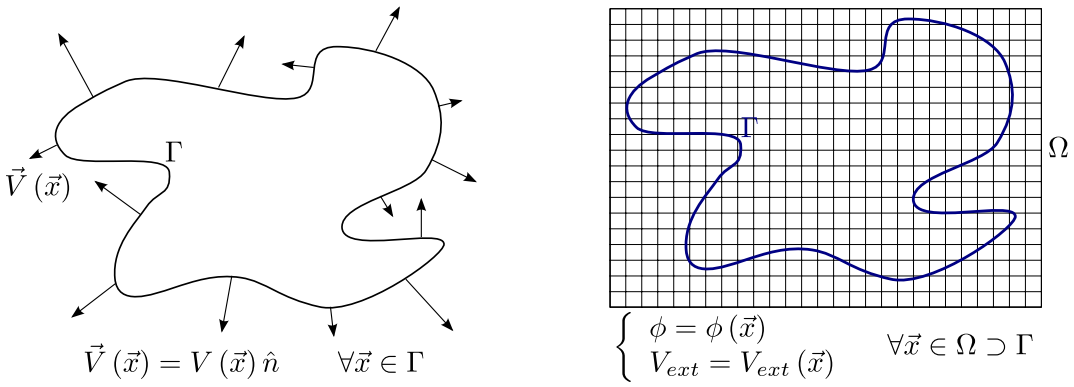

(a) Interface Propagating along its Normal Direction

(b) Level Set Formulation of the Problem

Figure 3.14: Extension of the Velocity Field

The choice of the definition of the V_{ext} field in the domain is, again, as in the case of the Level Set Initial Condition, with some degrees of freedom. In fact, it must only ensure that on the interface itself ,it is coincident with the front motion velocity field (see equation 3.92).

$$V_{ext}(\vec{x}(t)) = V(\vec{x}(t)) \quad \forall \vec{x}(t) \in \Gamma \qquad \Longleftrightarrow \qquad \phi(\vec{x}(t)) = 0 \quad \forall \vec{x}(t) \in \Gamma \tag{3.92}$$

In general, there are three different reasons for building a particular choice of the extension velocity field [59]:

- In some physical problems, the velocity is given only on the interface itself, and there is no natural extension of the velocity off the front, since it is not clear what means physically this definition. In these cases, an extension of the velocity must be specifically constructed.
- In other cases, the speed of the interface changes very rapidly and/or with discontinuities as it moves in the domain. In such cases, the exact location of the Level of interest, where the velocity is defined, determines the speed. Hence, a definition of the velocity from the position itself, rather than from a coarse grid is desirable to describe properly the problem under study.
- Under some other kind of velocity fields (typical of fluid dynamics application of the LSM) instead, the Level Set can tend to bunch up or spread out, that makes the Level Set function very steep or flat. For these cases, the definition of the extension velocity, maintaining the constraint given by equation 3.92, can be made to keep the grid function a Signed Distance Function, even during the evolution of the front. The reason for doing this particular definition of the V_{ext} is to benefit from all the properties of the SDF definition of the Level Set (paragraph 3.6, page 53). It maintains, in fact in the same time, a uniform separation of the Level Set, avoiding in the same time the use of re-initialization techniques (and the problems connected, see paragraph 3.9, page 61).

  This can be achieved defining the $V_{ext}(\vec{x})$ numerically, by the solution of the partial differential equation 3.93.

$$\vec{\nabla} V_{ext} \cdot \vec{\nabla}\phi = 0 \tag{3.93}$$

  We follow [54], in which the algorithm to solve the extension velocities equation 3.93 is presented. Suppose that the Level Set function is a SDF, using the Level Set equation 3.91, we have:

$$\begin{aligned} \frac{d\left|\vec{\nabla}\phi\right|^2}{dt} &= \frac{d}{dt}\left(\vec{\nabla}\phi\cdot\vec{\nabla}\phi\right) = 2\vec{\nabla}\phi\cdot\frac{d\vec{\nabla}\phi}{dt} = \\ &= -2\vec{\nabla}\phi\cdot\vec{\nabla}V_{ext}\left|\vec{\nabla}\phi\right| - 2\vec{\nabla}\phi\cdot\vec{\nabla}\left(V_{ext}\left|\vec{\nabla}\phi\right|\right) \end{aligned} \tag{3.94}$$

  Now, the first term is zero because the building of the extension velocities given by the equation 3.93. In the meanwhile the second term is zero too, because the initial condition is given by a SDF. Hence, the Level Set with the extension velocities, given by the equation 3.93 is kept a Signed Distance Function, if it has an IC given by a SDF.
- In cases for which the problem of the re-initialization is not present, another possibility to construct the V_{ext} field during the Level Set motion is a PDE based method, as suggested in [57]. This method solves an advection equation of the velocity field off the interface, as defined by the equation 3.95.

$$\frac{\partial V_{ext}}{\partial t} + \text{sign}(\phi)\frac{\vec{\nabla}\phi}{\left|\vec{\nabla}\phi\right|}\cdot\vec{\nabla}V_{ext} = 0 \tag{3.95}$$

  This is an Hamilton-Jacobi equation that can be solved with all the robust and accurate numerical schemes presented in the paragraph 3.4.1, page 44 and the chapter J, page f (for example a first order Riemann solver can be used to determine the advection direction of the terms $\text{sign}(\phi)\,n_x$ and $\text{sign}(\phi)\,n_y$).

In the case that the velocity field is constant, or it is dependent by the front curvature (or other intrinsic properties of the front itself), the $V = V_{ext}$ is globally defined and there are not

particular problems to be faced.

In this thesis work, the grain burnback technique results will be shown only for space and time constant (even if the time independence of the velocity field can be simply relaxed) motion fields of the grain burning surface. The reasons for this choice will be discussed in the chapter 4, page 79, where the coupling between the grain burnback analysis model and the SRM internal ballistics model is illustrated.

Notwithstanding, an extension velocity algorithm has been implemented, based on equation 3.95 in a module of GREG. The results of this activity, as not coupled directly with the internal ballistics numerical simulation, will not be shown at all.

However, with respect to the completed coupled solution of the internal ballistic model with the grain burning surface evolution model, some brief remarks can be made. In fact, the typical grain burning rates, that define the V field of the surface motion, are relatively small (of the order of millimeters or tenth of millimeters at the most for practical applications) and with flat variations in the bore during grain burning. Hence, small perturbations of the Level Set function from a SDF are expected even in the case of the definition of the extension velocities from the Q1D model SPINBALL, as defined by equation 3.96 (see figure 3.15).

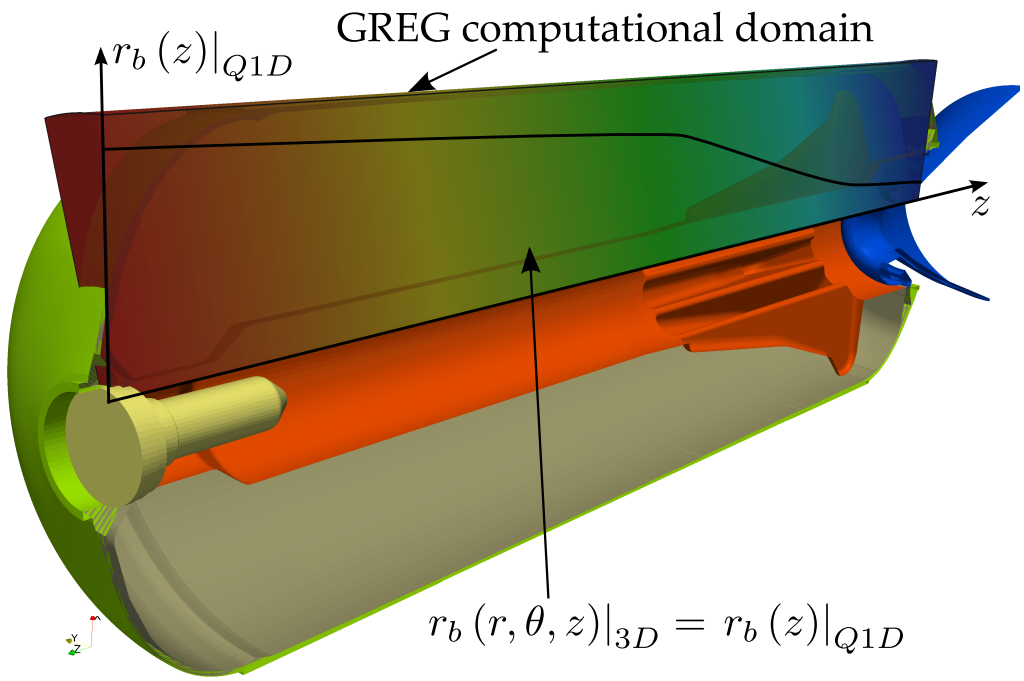

Figure 3.15: Extension Velocities Definition for the Coupling between Q1D Internal Ballistics Model and 3D Grain Burnback Analysis Model

$$V_{ext}(r,\theta,z) = r_b(z)|_{Q1D} \qquad \text{where z is the motor axis (cylindrical coordinates are used)} \tag{3.96}$$

Thus, no particular problems have to be faced in these cases, and the extension of the velocities off the interface can be made in a simpler manner or, in case, with the solution of the equation 3.95.

3.11 Evaluation of the Interface Geometrical Properties

This section is dedicated to the description of the numerical methods able to evaluate the global/integral properties of the surface at different timesteps. This step is mandatory in order to couple the grain burning surface evolution model with oD and/or Q1D internal ballistics model. In fact, up to this point, we have only the evolution of the 3D grain shape in time, with a given motion velocity, in terms of its Level Set representation and not yet the evolution of the integral grain geometrical parameters, which are necessary for the oD and Q1D SRM flowfield models.

As stated before, one of the major advantages of the Level Set Method stands in its ability to evaluate some global interface properties, as volumes, areas and perimeters. But even, it has the skill to simply define the interaction of the grain burning surface with the its motion limit, defined by the Thermal Protections inner surface.

In fact, for the other tracking interface motion techniques (described in the paragraph 3.2.1, page 36 and 3.2.2, page 37), an accurate evaluation of such front properties and the interaction with the TPs boundary surface become very difficult to be accomplished in a simple manner (neglecting for a while the other aforementioned drawbacks in tracking the interface motion with such techniques), as instead the LS approach does.

As matter of fact, it is possible to use some relevant properties of the implicit functions that numerically represents the Level Set, proper to numerically evaluate areas, volumes and perimeters, starting form the lattice discrete form of the ϕ function.

Hence, the evaluation of the grain geometrical parameters, for the application of the level set to grain burning surface evolution with time and its coupling with a Q1D and/or oD internal ballistics numerical model (see the sections 1.4, page 6; 1.5, page 8 and 3.1, page 32), can be done considering the development in a discrete fashion the following equations for a 3D implicit function.

For the evaluation of the volume contained in the generic surface described by the Level Zero of the Level Set $\phi(\vec{x})$, we introduce the use of the Heaviside function, as the equations 3.97 and 3.98 show.

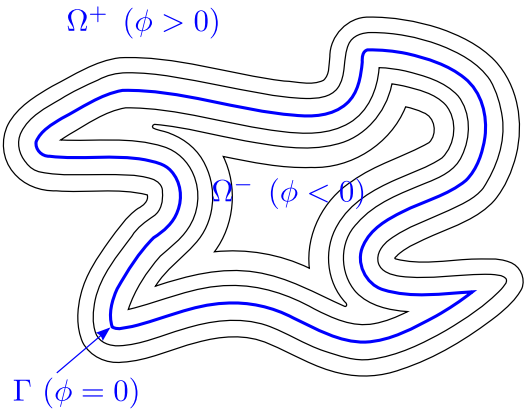

Figure 3.16: Evaluation of Integral Geometrical Properties of an Implicit Function

$$V = \int_{\Omega} [1 - \hbar(\phi(\vec{x}))] \, d\vec{x} \tag{3.97}$$

where $\hbar(\phi)$ is the *Heaviside function* defined as:

$$\hbar(\phi) = \begin{cases} 0 & \text{if } \phi \leqslant 0 \\ 1 & \text{if } \phi > 0 \end{cases} \tag{3.98}$$

and Ω is the complete domain: $\Omega = \Omega^+ \cup \Omega^-$.

While, for the area evaluation, instead, we have to use the Dirac Delta function (see equations 3.99 and 3.100)

$$A = \int_{\Omega} \delta(\phi(\vec{x})) \left|\vec{\nabla}\phi\right| d\vec{x} \tag{3.99}$$

where $\delta(\phi)$ is the *Dirac delta function* defined as:

$$\delta(\phi) = \frac{d\hbar(\phi)}{d\phi} \tag{3.100}$$

In a straightforward manner, volumes and areas evaluation become respectively areas and perimeters evaluation equations if the problem is reduced to a 2D one.

Moreover the implicit functions, as are the way in which Level Set represents the interface to be moved, make both boolean operations and more advanced constructive solid geometry operations very easy to apply (see the table 3.2, where $\phi_1(\vec{x})$ and $\phi_2(\vec{x})$ are two generic implicit functions).

Boolean Operator *	Mathematical Expression
Union	$\min(\phi_1(\vec{x}), \phi_2(\vec{x}))$
Intersection	$\max(\phi_1(\vec{x}), \phi_2(\vec{x}))$
Complement	$-\phi_1(\vec{x})$
Subtraction $(\phi_2 - \phi_1)$	$\max(\phi_1(\vec{x}), -\phi_2(\vec{x}))$

* operators are referred to the interior region

Table 3.2: Boolean Operators for Implicit Functions

In fact, these particular properties provide a very simple mathematical and geometrical representation of the limit, on the grain burning surface evolution, constituted by the Thermal Protections initial surface, as will be shown in the following.

A not trivial matter, instead, is the implementation of the equations 3.97 and 3.99 in a numerical fashion. In fact, the definition of the Heaviside and Dirac Delta, by the numerical point of view, can not directly be made from the equations 3.97 and 3.99[3]. In the same time, these generalized functions must have, in their discrete fashion, some regularity and convergence properties, in order to ensure confidence on the extracted data, as the grid is refined, both in rectangular and in cylindrical systems of coordinates (with major importance given to the second, for its practical applications to the grain burnback analysis).

The standard approximations typically used by the Level Set community stand on a regularization of the Dirac Delta and the Heaviside function. These spreads out the singular definition of these mathematical entities to a meshgrid dependent compact support, by the use of different regularization functions, dependent on the $\phi(\vec{x})$ value, related by the equation 3.100.

$$\begin{array}{ccccc} \text{Analytical} & & & \text{Numerical} & \\ \delta(\phi(\vec{x})) & \Longleftrightarrow & \delta_\epsilon\left(\phi\left(\vec{x}_{i,j,k}\right)\right) & \text{with } \epsilon = \kappa\Delta x & \\ \hbar(\phi(\vec{x})) & \Longleftrightarrow & \hbar_\epsilon\left(\phi\left(\vec{x}_{i,j,k}\right)\right) & \text{with } \epsilon = \kappa\Delta x & \end{array} \tag{3.101}$$

We will focus, now, the attention only on the discretization of the Dirac Delta, which is the most difficult between the two, as the Heaviside one will follow the first. For 1D problems in rectangular coordinates, far from not completely trivial applications of the Level Set Method, the regularization functions define a discretization that has a numerical error ζ of the computed measure of the front, which is related to its moment properties ϖ [89] (see equation 3.102).

$$\varpi(\delta_\epsilon) = q \quad \Longleftrightarrow \quad \Delta x \sum_{-\infty}^{+\infty} \delta_\epsilon\left(x_j - x\right)\left(x_j - x\right)^r = \begin{cases} 1, & r = 0 \\ 0, & 1 \leqslant r < q \end{cases} \quad \Longrightarrow \quad \zeta \leqslant C\Delta x^q \tag{3.102}$$

Some regularization functions, which general form is expressed by the equation 3.103, are then shown in the table 3.3 and figure 3.17.

3 a direct application of the equation 3.99 in a numerical fashion will produce, for whatever numerically represented implicit function, a zero area, while for the equation 3.97 a well defined in terms of regularity and convergence, but very rough evaluation of the Level Zero internal volume

$$\delta_\epsilon(x) = \begin{cases} \dfrac{\psi\left(\frac{x}{\epsilon}\right)}{\epsilon} & \left|\dfrac{x}{\epsilon} \leqslant 1\right| \quad \epsilon = \kappa\Delta x \\ 0 & \left|\dfrac{x}{\epsilon} > 1\right| \quad \epsilon = \kappa\Delta x \end{cases} \tag{3.103}$$

Function	Formula	Moment	Error	Domain
$\psi^L\left(\frac{x}{\epsilon}\right)$	$\min\left(1+\frac{x}{\epsilon}, 1-\frac{x}{\epsilon}\right)$	$\varpi = 2$	$\zeta = O\left(\Delta x^2\right)$	$\epsilon = \kappa\Delta x$
$\psi^{\cos}\left(\frac{x}{\epsilon}\right)$	$\frac{1}{2}\left(1+\cos\left(\frac{\pi x}{\epsilon}\right)\right)$	$\varpi = 1$	$\zeta = O\left(\Delta x\right)$	$\epsilon = \frac{\kappa+1}{2}\Delta x$
$\psi^C\left(\frac{x}{\epsilon}\right)$	$\begin{cases} 1-\frac{1}{2}\left\|\frac{x}{\epsilon}\right\|-\left\|\frac{x}{\epsilon}\right\|^2+\frac{1}{2}\left\|\frac{x}{\epsilon}\right\|^3 & 0 \leqslant \left\|\frac{x}{\epsilon}\right\| \leqslant 1 \\ 1-\frac{11}{6}\left\|\frac{x}{\epsilon}\right\|+\left\|\frac{x}{\epsilon}\right\|^2-\frac{1}{6}\left\|\frac{x}{\epsilon}\right\|^3 & 1 < \left\|\frac{x}{\epsilon}\right\| \leqslant 2 \end{cases}$	$\varpi = 4$	$\zeta = O\left(\Delta x^4\right)$	$\epsilon = 2\Delta x$

Table 3.3: Some choices for the Dirac Delta regularization [14; 85]

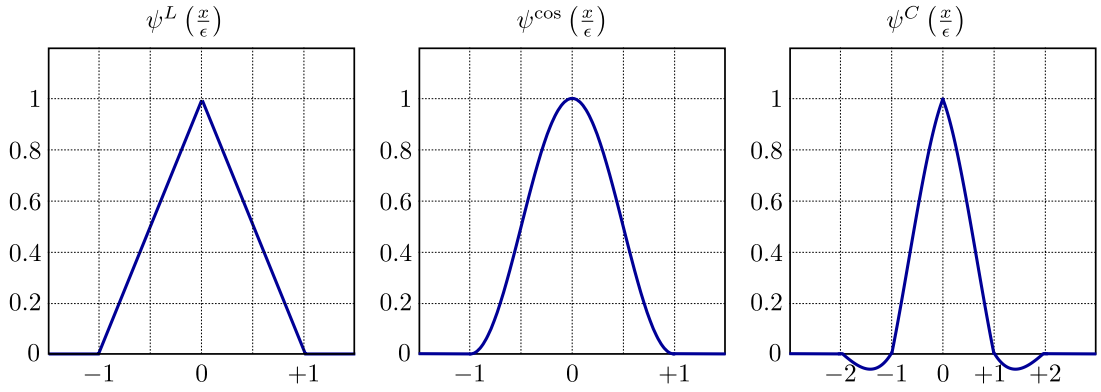

(a) Linear Regularization (b) Cosine Regularization (c) Cubic Regularization

Figure 3.17: Some Choices for the Dirac Delta Regularization [14; 85]

Hence, in these simple 1D problems the regularity and convergence properties of the built regularization of the Dirac Delta and, consequently, of the Heaviside functions are quite simple to be defined.

The not trivial step is represented to how build up the Dirac Delta discretization for multidimensional problems, from the 1D discretization seen before. A very common technique [79; 59], with applications for the Level Set Method, for extending the regularized 1D Dirac Delta function to multidimensional problems, is based simply to define the Delta Dirac depending on the grid function value. This, in fact, is simply related to the grid distance value from the front Γ of the grid point itself (see equation 3.104) [89; 85], with a compact support $\epsilon = \Delta x$ $(\kappa = 1)$ or $\epsilon = 2\Delta x$ $(\kappa = 2)$.

$$\begin{gathered}
\delta_\epsilon\left(\vec{x},\Gamma\right)=\delta_\epsilon\left(d\left(\vec{x},\Gamma\right)\right)\\
\Downarrow\\
\phi\left(\vec{x}\right)\cong\left(\vec{x}-\vec{x}_0\right)\cdot\vec{\nabla}\phi+C\left|\vec{x}-\vec{x}_0\right|^2\\
\Downarrow\\
\left|\vec{x}-\vec{x}_0\right|\cong\frac{\phi\left(\vec{x}\right)}{\left|\vec{\nabla}\phi\left(\vec{x}\right)\right|}\\
\Downarrow\\
\delta_\epsilon\left(\vec{x},\Gamma\right)=\delta_\epsilon\left(d\left(\vec{x},\Gamma\right)\right)=\delta_\epsilon\left(\frac{\phi\left(\vec{x}\right)}{\left|\vec{\nabla}\phi\left(\vec{x}\right)\right|}\right)
\end{gathered}\tag{3.104}$$

The problem of using this kind of regularization is, as found in [85], that such a choice may result an $O(1)$ error in computing the length of the front in 2D problems, or the front surface in 3D ones. This means a completely lack of convergence regularity of the resultant numerical technique, that has been also found with different tests in this thesis work (see paragraphs 5.3, 94). To fix this problem, many different authors in some recent works published in literature ([88; 89; 85; 81; 99; 82]) have underlined this fact and proposed different types of regularizations of the Dirac Delta function, with applications to the Level Set Methods.

In particular, the techniques proposed by Engquist et al. in [88] considered tow different and possible approaches. The first algorithm considers a tensor product of the regularized 1D Dirac Delta functions. While the second one, and simpler among the two, defines a regularization as in the 1D case with a variable compact support of regularization, that depends on the orientation of the front with respect to the computational grid (see equation 3.105).

$$\epsilon_{\text{MultiD}}\left(\vec{\nabla}d\left(\vec{x},\Gamma\right)\right)=\frac{\left|\vec{\nabla}d\left(\vec{x},\Gamma\right)\right|_1}{\left|\vec{\nabla}d\left(\vec{x},\Gamma\right)\right|}\epsilon_{1D}\tag{3.105}$$

Where $|\cdot|_1$ is the 1-norm and the definition of $d\left(\vec{x},\Gamma\right)$ from the Level Set function $\phi\left(\vec{x}\right)$ follows from the equation 3.104. The resultant techniques are shown to be respectively with a second and first order of accuracy [88], for averaged measures of different interfaces with small irregular shifts in the computational grid.

A quite different approach is, instead, presented by Smereka in [99]. The construction uses the technique developed by Mayo [23] in solving the Poisson's equation for elliptic problems with discontinuities. The definition of the Dirac Delta function is, hence, obtained building the numerical solution of the Laplace's equation written by an equivalent problem subject to jump conditions, taking into account the presence of the discontinuity (represented by the Dirac Delta). This approach used in 1D problems brings to a definition of the regularized function that coincides with the linear regularization aforementioned $\psi^L\left(\frac{x}{\epsilon}\right)$ (see table 3.3). But, it can be simply extended to 2D or 3D dimensions in a straightforward manner, by solving the Laplace's equation subject to the jump conditions through the interface discontinuity in 2D or 3D respectively. The resultant interface measure can be first or second order accurate, depending on the numerical finite differences approximation of the Laplace operator, as proved in [99] with some 2D and 3D tests, with the results averaged for small shifts of the computational grid with respect to the front.

In the definition of the technique for evaluating the grain geometrical integral properties, all the mentioned regularization methods of the Dirac Delta (and Heaviside) have been implemented and tested for both rectangular and cylindrical systems of coordinates, as will be shown in the paragraphs 5.3, 94. Unfortunately, all these methods, even the variations due to Engquist and Smereka, have found to be too sensitive with respect to the front position on the computational grid, in a manner that does not allow to have a sufficient regularity property of the computed surface (for 3D problems) or perimeter (for 2D problems). We remember that the

Dirac Delta regularization[4], in particular, since defines the burning surface and perimeters along the motor axis (which relevantly affect the internal ballistics numerical simulation) must be well defined in terms of convergence with mesh refinements, but also of regularity of the computed quantities.

Because of all these remarks and requirements necessary for our implementation of the front measure method, we decided to use a different approach for it, that is computationally more expansive, but that has the required properties for both convergence and regularity. All the above mentioned approaches, in fact, work on the regularization of the discrete Dirac Delta and Heaviside in order to define the integral properties through a capturing of the front (the level zero), from the nodal values of the grid function. On the contrary, this approach defines the Dirac Delta and Heaviside discrete operators by means of a direct evaluation of the perimeters, areas, or volumes, that uses a direct determination (fitting) of the Level zero position through an interpolation of the grid function. This technique (presented in the next paragraph) is based on the recent works of Min and Gibou [106; 114], which allow a simple and straightforward implementation in both Cartesian and cylindrical coordinates.

3.11.1 Multidimensional Dirac Delta and Heaviside discretization

In this paragraph, we follow the works published by Min and Gibou in [106; 114].

The approach for evaluating the position (and hence, the areas, volumes and perimeters properties) of the Level Zero, from the Level Set numerical representation of the 3D surface, is based on a decomposition of each grid cells into a union of simplices. This technique applies for both Cartesian and cylindrical computational grids and gives, as proved by the authors, and enforced in the paragraph 5.3, page 94, a robust second order accurate discretizations of Dirac Delta and Heaviside functions, independent of the underlying grid and therefore stable under perturbations (or small movements) of the interface [106; 114].

A simplex, or n simplex is a convex hull of a set of $(n+1)$ affinely independent points, so a triangle in 2D and a tetrahedron in 3D problems.

Simplices provide a very straightforward manner to compute perimeters, areas and volumes of an implicit function defined on their vertexes. The generic (Cartesian or polar) 2D four-sided cell can be decomposed into simplices in a very simple through the diagonal, as shown in the figure 3.18 and the equation 3.106.

$$\begin{aligned} [0,1]^2 &= \Delta P_{00}P_{10}P_{11} \cup \Delta P_{00}P_{01}P_{11} \\ [0,1]^2 &= \Delta P_{00}P_{10}P_{01} \cup \Delta P_{10}P_{01}P_{11} \end{aligned} \tag{3.106}$$

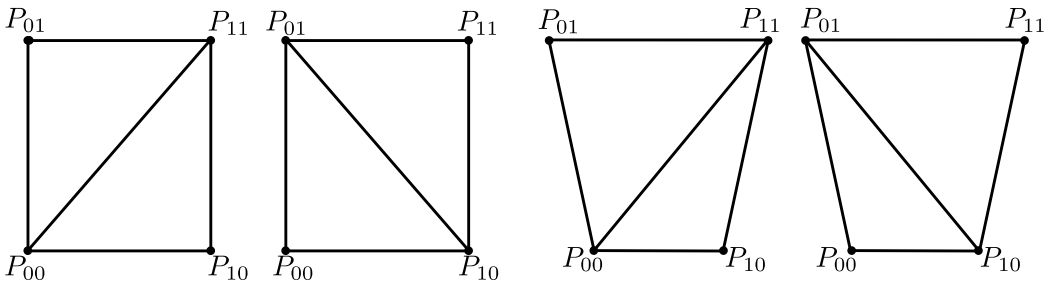

(a) Cartesian Coordinates (b) Polar Coordinates

Figure 3.18: 2D Mesh Cell Decomposition into Simplices

4 the problem is less important, but present also for the Heaviside function

The generic (Cartesian or polar) 3D cell with six-sided faces, instead, can be decomposed into five tetrahedrons by the so called middle cut triangulation [25], see figure 3.19 and equation 3.107.

$$\begin{aligned}
[0,1]^3 &= \Delta P_{000}P_{100}P_{010}P_{000} \cup \Delta P_{110}P_{100}P_{010}P_{111} \cup \Delta P_{101}P_{100}P_{111}P_{001} \cup \\
&\cup \Delta P_{011}P_{111}P_{010}P_{001} \cup \Delta P_{111}P_{100}P_{010}P_{001} \\
[0,1]^3 &= \Delta P_{001}P_{101}P_{011}P_{001} \cup \Delta P_{111}P_{101}P_{011}P_{110} \cup \Delta P_{100}P_{101}P_{110}P_{000} \cup \\
&\cup \Delta P_{010}P_{110}P_{011}P_{000} \cup \Delta P_{110}P_{101}P_{011}P_{000}
\end{aligned} \tag{3.107}$$

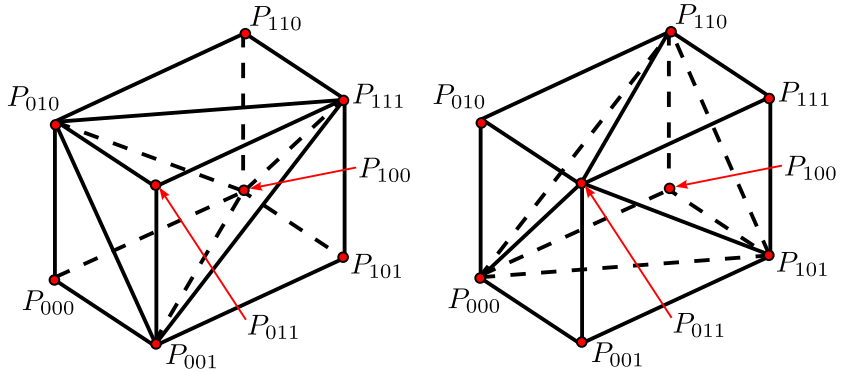

(a) Cartesian Coordinates

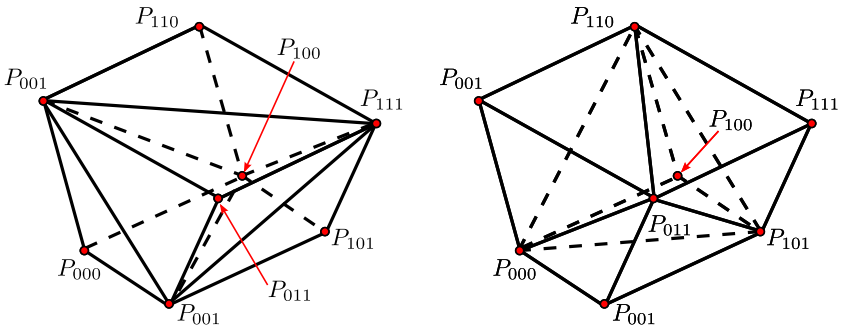

(b) Cylindrical Coordinates

Figure 3.19: 3D Mesh Cell Decomposition into Simplices

Hence, in a such manner the problem is moved in the definition of the interface position on a generic simplex. In fact, the decomposition of the generic cell into simplices does not create new vertexes, in which the grid function must be defined.

Now, the intersection of the front Γ with a generic simplex S ($S \cap \Gamma$) and the inner volume included between the interface and the simplex ($S \cap \Omega^-$) are defined by polytopes (for example convex hulls of five vertexes), which areas and volumes are not simple to be evaluated. But, again they can be decomposed into simplices, for which the evaluation of volumes and areas is straightforward.

In fact, the volume of the generic n-simplex in the space $(x_1, \cdots, x_n)^T$ is given by the equation 3.108, that gives the expression in 3D of the volume of the tetrahedron and in 2D, the triangle area. While, to evaluate the areas in 3D and the segment lengths in 2D, the simple geometrical expressions for a triangle area and the distance between two points can be used.

$$Vol(S) = \frac{1}{n!}\left|\det\begin{pmatrix} (x_1|_1 - x_1|_0) & \cdots & (x_1|_n - x_1|_0) \\ \vdots & & \vdots \\ (x_n|_1 - x_n|_0) & \cdots & (x_n|_n - x_n|_0) \end{pmatrix}\right| \tag{3.108}$$

At this point, what remains to do is to study all possible cases of intersections between the front Γ and the generic simplex, in function of the grid function values. Using the grid function values on the simplex vertexes, we linearly interpolate ϕ on S, thus, Γ and Ω^- are geometrically hyperplane and halfspace. We remark that two geometrical configurations given by the intersection between a simplex S and a hyperplane Γ and between a simplex S and a halfspace Ω^- are equivalent if they have the same number of vertexes below or above, the hyperplane Γ. Therefore, in order to classify all the possible configurations, it suffices to count the number of negative or positive values of the grid function ϕ in each simplex, as given by the equation 3.109 [106].

$$\eta(\phi, S) = n(P_i : \phi(P_i) < 0 \quad \forall P_i \in S) \tag{3.109}$$

Hence, in 2D the possible values of $\eta(\phi, S)$ are 0, 1, 2 or 3, and the geometrical entities that defines the hyperplane $S \cap \Gamma$ and the hyperspace $S \cap \Omega^-$ necessary to compute them are shown in the tables 3.4,3.5 and figures 3.20,3.21.

$\eta(\phi, S)$	ϕ_0	ϕ_1	ϕ_2	Q_0	Q_1
0	+	+	+		
1	−	+	+	P_{01}	P_{02}
2	−	−	+	P_{02}	P_{12}
3	−	−	−		

Table 3.4: Geometrical Entities that define $S \cap \Gamma$ in 2D

$\eta(\phi, S)$	ϕ_0	ϕ_1	ϕ_2	Q_0	Q_1	Q_2
0	+	+	+			
1	−	+	+	P_0	P_{01}	P_{02}
2	−	−	+	P_0	P_1	P_{02}
				P_{02}	P_{12}	P_{02}
3	−	−	−	P_0	P_1	P_2

Table 3.5: Geometrical Entities that define $S \cap \Omega^-$ in 2D

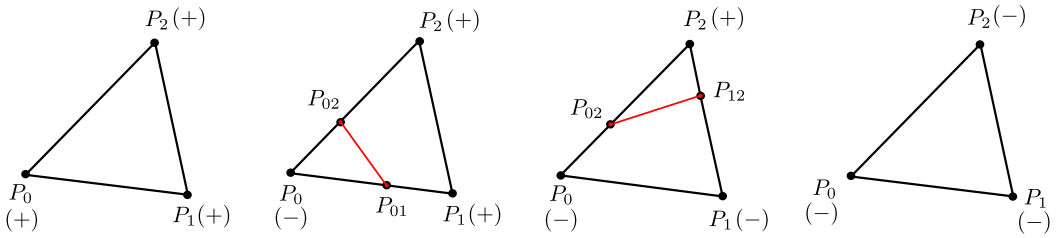

(a) $\eta(\phi, S) = 0$ (b) $\eta(\phi, S) = 1$ (c) $\eta(\phi, S) = 2$ (d) $\eta(\phi, S) = 3$

Figure 3.20: Geometrical Entities that define $S \cap \Gamma$ in 2D

The position of the generic P_{ij} point, intersection between the interface Γ and the generic simplex S is simply given by a linear interpolation of the grid function values at the segment nodes, as the equation 3.110 shows.

$$P_{ij} = P_j \frac{\phi(P_i)}{\phi(P_i) - \phi(P_j)} - P_i \frac{\phi(P_j)}{\phi(P_i) - \phi(P_j)} \tag{3.110}$$

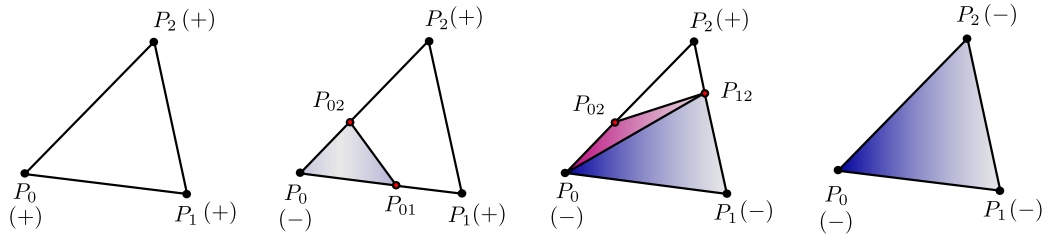

(a) $\eta(\phi, S) = 0$ (b) $\eta(\phi, S) = 1$ (c) $\eta(\phi, S) = 2$ (d) $\eta(\phi, S) = 3$

Figure 3.21: Geometrical Entities that define $S \cap \Omega^-$ in 2D

The expression of $S \cap \Gamma$ and $S \cap \Omega^-$ can be resumed in the following expressions 3.111 [114].

$$\begin{cases} \int_{\Omega \cap \Delta P_0 P_1 P_2} d\Omega \cong H_0 + H_1 + H_2 = H_S \\ \\ \int_{\Gamma \cap \Delta P_0 P_1 P_2} d\Omega \cong \delta_0 + \delta_1 + \delta_2 = \delta_S \end{cases} \tag{3.111}$$

The generic coefficients $H_i; \delta_i$ are functions of the six arguments. As the discretization in the equation 3.111 is not dependent on the order of the indexing of the vertexes, only the expression of one coefficient suffices so that all the other coefficients expressions directly follow it (see equations 3.112, 3.113 and 3.114) with an indices permutation.

$$\begin{cases} H_0 = H_0(\phi_0, \phi_1, \phi_2, P_0, P_1, P_2) \\ \delta_0 = \delta_0(\phi_0, \phi_1, \phi_2, P_0, P_1, P_2) \end{cases} \tag{3.112}$$

$$\begin{cases} H_1(\phi_0, \phi_1, \phi_2, P_0, P_1, P_2) = H_0(\phi_1, \phi_0, \phi_2, P_1, P_0, P_2) \\ H_2(\phi_0, \phi_1, \phi_2, P_0, P_1, P_2) = H_0(\phi_2, \phi_0, \phi_1, P_2, P_0, P_1) \end{cases} \tag{3.113}$$

$$\begin{cases} \delta_1(\phi_0, \phi_1, \phi_2, P_0, P_1, P_2) = \delta_0(\phi_1, \phi_0, \phi_2, P_1, P_0, P_2) \\ \delta_2(\phi_0, \phi_1, \phi_2, P_0, P_1, P_2) = \delta_0(\phi_2, \phi_0, \phi_1, P_2, P_0, P_1) \end{cases} \tag{3.114}$$

Therefore, the expressions of the H_0 and δ_0 are given in the table 3.6.

$\eta(\phi, S)$	ϕ_0	ϕ_1	ϕ_2	$H_0(\phi_0, \phi_1, \phi_2, P_0, P_1, P_2)$	$\delta_0(\phi_0, \phi_1, \phi_2, P_0, P_1, P_2)$
0	+	+	+	0	0
1	−	+	+	$\frac{A(P_{01}P_{02}P_0)}{3}\left(1 + \frac{\phi_2}{\phi_2-\phi_0} + \frac{\phi_1}{\phi_1-\phi_0}\right)$	$\frac{L(P_{01}P_{02})}{2}\left(\frac{\phi_2}{\phi_2-\phi_0} + \frac{\phi_1}{\phi_1-\phi_0}\right)$
2	−	−	+	$\frac{A(P_0P_1P_2)}{3} - \frac{A(P_{02}P_{12}P_3)}{3}\frac{\phi_2}{\phi_2-\phi_0}$	$\frac{L(P_{02}P_{12})}{2}\frac{\phi_2}{\phi_2-\phi_0}$
3	−	−	−	$\frac{A(P_0P_1P_2)}{3}$	0

* note that $\delta(\phi) = \delta(-\phi)$ and $H(\phi) = -H(-\phi)$
** all the other cases can be obtained by an indices permutation

Table 3.6: Heaviside and Dirac Delta expressions in 2D of H_0 and δ_0

For 3D problems, the possible values of $\eta(\phi, S)$ are 0, 1, 2, 3 or 4. Hence, the geometrical entities that define the hyperplane $S \cap \Gamma$ and the hyperspace $S \cap \Omega^-$, necessary to define them are shown in the tables 3.7,3.8 and figures 3.22,3.23.

$\eta(\phi, S)$	ϕ_0	ϕ_1	ϕ_2	ϕ_3	Q_0	Q_1	Q_2
0	+	+	+	+			
1	−	+	+	+	P_{01}	P_{02}	P_{03}
2	−	−	+	+	P_{02}	P_{03}	P_{13}
					P_{02}	P_{12}	P_{13}
3	−	−	−	+	P_{03}	P_{13}	P_{23}
4	−	−	−	−			

Table 3.7: Geometrical Entities that define $S \cap \Gamma$ in 3D

$\eta(\phi, S)$	ϕ_0	ϕ_1	ϕ_2	ϕ_3	Q_0	Q_1	Q_2	Q_3
0	+	+	+	+				
1	−	+	+	+	P_{01}	P_{02}	P_{03}	
2	−	−	+	+	P_0	P_1	P_{02}	P_{13}
					P_{12}	P_1	P_{02}	P_{13}
					P_0	P_{03}	P_{02}	P_{13}
3	−	−	−	+	P_0	P_1	P_2	P_{13}
					P_0	P_{03}	P_2	P_{13}
					P_{23}	P_{03}	P_2	P_{13}
4	−	−	−	−	P_0	P_1	P_2	P_3

Table 3.8: Geometrical Entities that define $S \cap \Omega^-$ in 3D

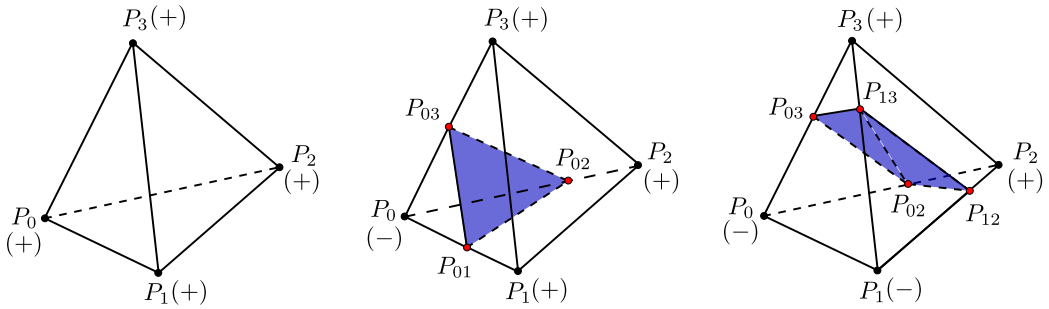

(a) $\eta(\phi, S) = 0$ (b) $\eta(\phi, S) = 1$ (c) $\eta(\phi, S) = 2$

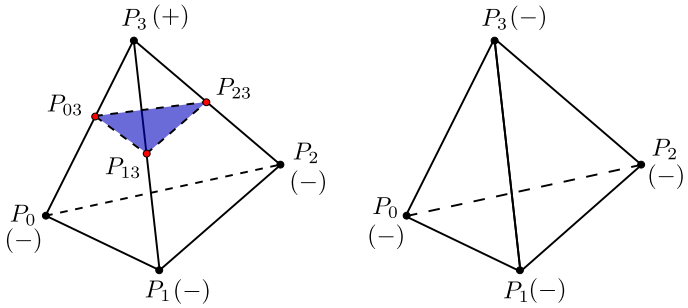

(d) $\eta(\phi, S) = 3$ (e) $\eta(\phi, S) = 4$

Figure 3.22: Geometrical Entities that define $S \cap \Gamma$ in 3D

Similarly to 2D cases, the coefficients of the Dirac Delta and Heaviside discretized functions depend on eight arguments, in a independent manner by the order of them. So the equations 3.115, 3.116, 3.117, 3.118 stand directly, as the in 2D case.

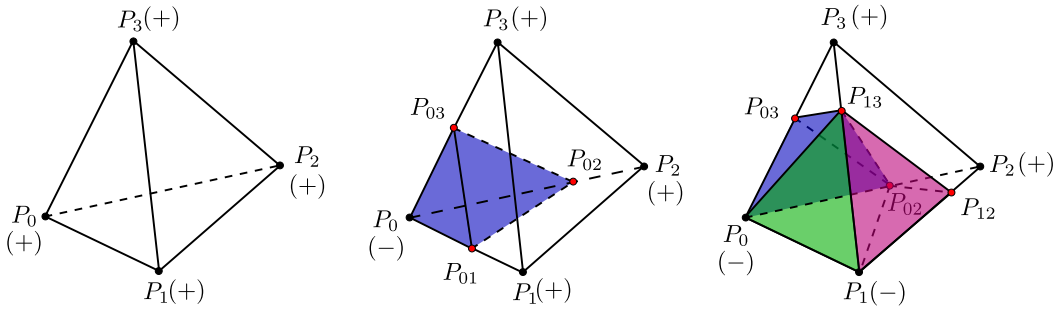

(a) $\eta(\phi, S) = 0$ (b) $\eta(\phi, S) = 1$ (c) $\eta(\phi, S) = 2$

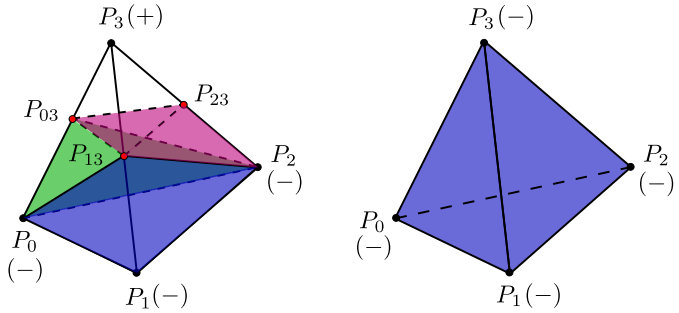

(d) $\eta(\phi, S) = 3$ (e) $\eta(\phi, S) = 4$

Figure 3.23: Geometrical Entities that define $S \cap \Omega^-$ in 3D

$$\begin{cases} \int_{\Omega \cap \Delta P_0 P_1 P_2 P_3} d\Omega \cong H_0 + H_1 + H_2 + H_3 = H_S \\ \int_{\Gamma \cap \Delta P_0 P_1 P_2 P_3} d\Omega \cong \delta_0 + \delta_1 + \delta_2 + \delta_3 = \delta_S \end{cases} \tag{3.115}$$

$$\begin{cases} H_0 = H_0(\phi_0, \phi_1, \phi_2, \phi_3, P_0, P_1, P_2, P_3) \\ \delta_0 = \delta_0(\phi_0, \phi_1, \phi_2, \phi_3, P_0, P_1, P_2, P_3) \end{cases} \tag{3.116}$$

$$\begin{cases} H_1(\phi_0, \phi_1, \phi_2, \phi_3, P_0, P_1, P_2, P_3) = H_0(\phi_1, \phi_0, \phi_2, \phi_3, P_1, P_0, P_2, P_3) \\ H_2(\phi_0, \phi_1, \phi_2, \phi_3, P_0, P_1, P_2, P_3) = H_0(\phi_2, \phi_0, \phi_1, \phi_3, P_2, P_0, P_1, P_3) \\ H_3(\phi_0, \phi_1, \phi_2, \phi_3, P_0, P_1, P_2, P_3) = H_0(\phi_3, \phi_0, \phi_1, \phi_2, P_3, P_0, P_1, P_2) \end{cases} \tag{3.117}$$

$$\begin{cases} \delta_1(\phi_0, \phi_1, \phi_2, \phi_3, P_0, P_1, P_2, P_3) = \delta_0(\phi_1, \phi_0, \phi_2, \phi_3, P_1, P_0, P_2, P_3) \\ \delta_2(\phi_0, \phi_1, \phi_2, \phi_3, P_0, P_1, P_2, P_3) = \delta_0(\phi_2, \phi_0, \phi_1, \phi_3, P_2, P_0, P_1, P_3) \\ \delta_3(\phi_0, \phi_1, \phi_2, \phi_3, P_0, P_1, P_2, P_3) = \delta_0(\phi_3, \phi_0, \phi_1, \phi_2, P_3, P_0, P_1, P_2) \end{cases} \tag{3.118}$$

And the expressions of the H_0 and δ_0 are given in tables 3.9 and 3.10.

$\eta(\phi, S)$	ϕ_0	ϕ_1	ϕ_2	ϕ_3	$H_0(\phi_0, \phi_1, \phi_2, \phi_3, P_0, P_1, P_2, P_3)$
0	+	+	+	+	0
1	−	+	+	+	$\frac{V(P_0P_{01}P_{02}P_{03})}{4}\left(1+\frac{\phi_1}{\phi_1-\phi_0}+\frac{\phi_2}{\phi_2-\phi_0}\right)$
2	−	−	+	+	$\frac{V(P_0P_{02}P_{03}P_{13})}{4}\left(1+\frac{\phi_2}{\phi_2-\phi_0}+\frac{\phi_3}{\phi_3-\phi_0}\right)+$ $+\frac{V(P_0P_{02}P_1P_{13})}{4}\left(1+\frac{\phi_2}{\phi_2-\phi_0}\right)+$ $+\frac{V(P_{02}P_1P_{12}P_{13})}{4}\frac{\phi_2}{\phi_2-\phi_0}$
3	−	−	−	+	$\frac{V(P_0P_1P_2P_3)}{4}-\frac{V(P_{03}P_{13}P_{23}P_3)}{4}\frac{\phi_3}{\phi_3-\phi_0}$
4	−	−	−	−	$\frac{V(P_0P_1P_2P_3)}{4}$

* note that $\delta(\phi)=\delta(-\phi)$ and $H(\phi)=-H(-\phi)$
** all the other cases can be obtained by an indices permutation

Table 3.9: Heaviside expressions in 3D of H_0

$\eta(\phi, S)$	ϕ_0	ϕ_1	ϕ_2	ϕ_3	$\delta_0(\phi_0, \phi_1, \phi_2, \phi_3, P_0, P_1, P_2, P_3)$
0	+	+	+	+	0
1	−	+	+	+	$\frac{A(P_{01}P_{02}P_{03})}{3}\left(\frac{\phi_1}{\phi_1-\phi_0}+\frac{\phi_2}{\phi_2-\phi_0}+\frac{\phi_3}{\phi_3-\phi_0}\right)$
2	−	−	+	+	$\frac{A(P_{01}P_{02}P_{03})}{3}\left(\frac{\phi_1}{\phi_1-\phi_0}+\frac{\phi_2}{\phi_2-\phi_0}+\frac{\phi_3}{\phi_3-\phi_0}\right)$
3	−	−	−	+	$\frac{A(P_{03}P_{13}P_{23})}{3}\frac{\phi_3}{\phi_3-\phi_0}$
4	−	−	−	−	0

* note that $\delta(\phi)=\delta(-\phi)$
** all the other cases can be obtained by an indices permutation

Table 3.10: Dirac Delta expressions in 3D of δ_0

Note that with this procedure, it is also possible to extract the Level zero from the Level Set grid function, with a STL representation. In fact, the surface $\Gamma \cap S$ is represented by a series of triangles, as the discrete StereoLithography representation of a surface needs.

3.11.2 0D & Q1D Grain/Bore Geometrical Properties Evaluation

In order to apply the aforementioned numerical procedures to compute the grain flowfield coupling geometrical properties, some other clarifying remarks are needed. In fact, not all of them have the same importance in the main target to allow the numerical simulation of the internal ballistics over the IT:

- The burning surface (S_b) for 0D models) and the burning perimeter (P_b) for Q1D models (burning perimeter) leads the burning mass flow rate entering in the bore, defining the motor pressure time history and the global mass balance of the numerical simulation. Hence, a rude and not consistent evaluation of these parameters strongly influence the accuracy of the internal ballistics numerical simulation, especially if mass balance is not respected.
- Instead the port area (A_p) and the wet perimeter (P_w) for Q1D internal ballistic models and the wet surface (S_w) for 0D models are necessary to account respectively geometrical bore variation, friction terms and the amount of uncovered liner and case thermal protections

(for TPs optimal dimensioning). Therefore, even not much accurate evaluation of these parameters can be accepted, even if desired, as they influence, in a very secondary manner, the flowfield properties in the bore.

Now, using the robust numerical definition of the Dirac Delta and the Heaviside shown in the paragraph 3.11.1, page 70, all the grain and bore geometrical parameters for 0D and Q1D internal ballistics models can be easily obtained with the use of the boolean algebra of the implicit surfaces. The inputs for them are given:

- by the Level Set at the given timestep evolved by the LSM, which its level zero is the grain burning surface at the given time;
- by the case grid function initialized as a SDF from a 3D STL file, or an axisymmetric profile (see paragraph 3.6.1, page 55).

For the 0D geometrical parameters, we have that the evolution of the volume bore $V_b(t)$, of the grain volume $V_g(t)$, of the burning surface $S_b(t)$ and of the wet surface $S_w(t)$ are given respectively by the equations 3.119, 3.120, where the subscripts g and c means respectively grain and case.

$$V_b(t^n) = \sum_{ijk} H_{ijk} = \sum_{ijk} \left(\sum_{S \in \Delta_{ijk}} H_S \left(\max \left(\phi^n_{ijk}\Big|_g , \phi_{ijk}\Big|_c \right) \right) \right) \tag{3.119}$$

$$V_g(t^n) = \sum_{ijk} H_{ijk} = \sum_{ijk} \left(\sum_{S \in \Delta_{ijk}} H_S \left(\max \left(-\phi^n_{ijk}\Big|_g , \phi_{ijk}\Big|_c \right) \right) \right) \tag{3.120}$$

$$S_b(t^n) = \sum_{ijk} \delta_{ijk} = \sum_{ijk} \left(\sum_{S \in \Delta_{ijk}} \delta_S \left(\phi_{ijk}\Big|_g : \max \left(\phi^n_{ijk}\Big|_g , \phi_{ijk}\Big|_c \right) = \phi^n_{ijk}\Big|_g \right) \right) \tag{3.121}$$

$$S_w(t^n) = \sum_{ijk} \delta_{ijk} = \sum_{ijk} \left(\sum_{S \in \Delta_{ijk}} \delta_S \left(\max \left(\phi^n_{ijk}\Big|_g , \phi_{ijk}\Big|_c \right) \right) \right) \tag{3.122}$$

Here the first sums are made over the meshgrid cells with the indices i, j and k. While the sums over the index S for $S \in \Delta_{ijk}$ are referred to all the simplices in which the generic cell is decomposed, given by the middle cut triangulation (see figure 3.19, page 71).

The Q1D geometrical parameters, port area $A_p(x,t)$, burning perimeter $P_b(x,t)$ and wet perimeter $P_w(x,t)$ are defined by the equations 3.123, 3.124 and 3.125, where the k-index identify the computational grid nodes along the motor axis.

$$A_p(\tilde{k}, t^n) = \sum_{ij} H_{ij} = \sum_{ij} \left(\sum_{S \in \Delta_{ij}} H_S \left(\max \left(\phi^n_{ij\tilde{k}}\Big|_g , \phi_{ij\tilde{k}}\Big|_c \right) \right) \right) \tag{3.123}$$

$$P_b(\tilde{k}, t^n) = \sum_{ij} \delta_{ij} = \sum_{ij} \left(\sum_{S \in \Delta_{ij}} \delta_S \left(\phi_{ij\tilde{k}}\Big|_g : \max \left(\phi^n_{ij\tilde{k}}\Big|_g , \phi_{ij\tilde{k}}\Big|_c \right) = \phi^n_{ij\tilde{k}}\Big|_g \right) \right) \tag{3.124}$$

$$P_w(\tilde{k}, t^n) = \sum_{ij} \delta_{ij} = \sum_{ij} \left(\sum_{S \in \Delta_{ij}} \delta_S \left(\max \left(\phi^n_{ij\tilde{k}}\Big|_g , \phi_{ij\tilde{k}}\Big|_c \right) \right) \right) \tag{3.125}$$

For the definition of a burning perimeter, in a consistent manner with respect to the burning surface, the local burning perimeter given by the equation 3.124 is completed with the definition of a consistent burning perimeter $\tilde{P}_b\left(k:\widehat{k+1},t^n\right)$, given by the equation 3.126.

$$\begin{aligned}\tilde{P}_b\left(k:\widehat{k+1},t^n\right) &= \sum_{ijk:\widehat{k+1}} \delta_{ijk:\widehat{k+1}} \frac{1}{\Delta z} = \\ &= \sum_{ijk:\widehat{k+1}} \left(\sum_{S\in\Delta_{ijk:\widehat{k+1}}} \delta_S \left(\phi_{ijk}\big|_g : \max\left(\phi^n_{ijk}\Big|_g, \phi_{ijk}\big|_c \right) = \phi^n_{ijk}\Big|_g \right) \right) \frac{1}{\Delta z}\end{aligned} \tag{3.126}$$

In this case, the burning perimeter is defined along the motor axis as an "averaged value" of the burning perimeter contained in the $k:\widehat{k+1}$ planes orthogonal to the motor axis. In such a manner that the burning surface between such planes is defined simply by the multiplication of it for the grid discretization along the motor axis.

4

SPINBALL/GREG Coupling

The grain burnback model GREG is able to give to the SPINBALL flowfield Q1D unsteady model all the Q1D geometrical parameters necessary to compute the bore geometry and the propellant grain products inlet flow, due to combustion processes. Hence, with the technique discussed in the paragraphs 3.11, page 66, it evaluates the port area, burn perimeter and wet perimeter along the motor axis and their evolution in time, even for the submergence zone, if present. In this brief chapter we discuss the way in which the two models are coupled in order to simulate the overall combustion time of a given Solid Rocket Motor.

In principle, the problem of solving the internal ballistics and the grain burning surface evolution are completely coupled to each other. By a part the coupling is through the aforementioned evolution of the Q1D geometrical parameters given by the 3D grain burning surface evolution model of the chamber and by the other through the local burning rate values (see equations 2.1 and 3.28).

A first decoupling, related to the solution of the numerical problem in a discretized manner, is to stagger the time solution of a problem with respect to the other. In fact, it is possible to assume that during the flowfield timestep the flowfield conditions in the chamber are not influenced, in a relevant manner, by the grain geometrical evolution during that time interval. This hypothesis indeed introduces a very small approximation in the internal ballistics solution, considering that the burning surface evolution occurs at a significantly slower rate (grain burning rate, of the order from millimiters to tenth of millimiters per second) than the flowfield development ones (that are of the order of meters per seconds).

Taking this reasonable assumption, since GREG can deal with space and time variables burning rates, two ways of coupling can be now considered. The first one is to consider a so called "on-line coupling" between the bore flowfield solver and the grain burnback model. In this approach, the solution of the flowfield and of the grain evolution problem are made during the simulation in a staggered manner (see figure 4.1). Hence, this requires a coupling algorithm for the two models and a grain burnback analysis model able to accomplish the 3D grain burning surface evolution with space and time variable motion velocities (the grain burning rate). Moreover, the two models (grain burnback and flowfield solver) have to march with the same timestep, that is typically defined by the internal ballistics solver one (the order of magnitude of a typical timestep for the Q1D model for a meshgrid with a $\Delta x = O\,(\mathrm{cm})$ is 10^{-5} s). A dual timestep can be also used, exploiting the remarked fact that the characteristic times of the grain burnback are much wider that the ones of the internal ballistics, in order to reduce the computational time required for the coupled simulation. In such a manner that the geometrical evolution is updated for the Q1D solver only once for different timesteps of the flowfield solver itself. Note that in this way of coupling, as the grain burning rate is defined spatially constant in each section of the 3D grain regression model, the properties of symmetry and/or periodicity of the grain shape are preserved. Hence, these properties can be exploited in the grain burnback analysis, in order

to make accurate meshgrids of a slice of the azimuthal domain using cylindrical coordinates. At now, there is not any work in the literature on the internal ballistics numerical simulation using this coupled approach.

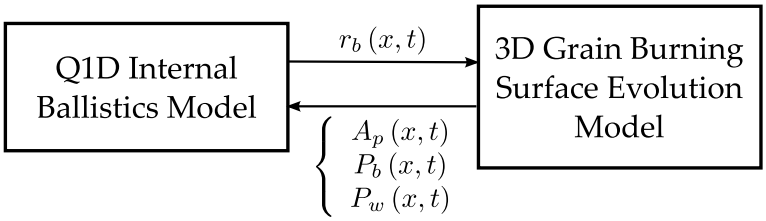

Figure 4.1: On-line coupling grain burnback analysis and internal ballistic solver

The second coupling way, instead, considers a so called "off-line" coupling between the two models. In this approach, the evolution of the grain burning surface is made with a constant burning rate, once for all times for a given motor, prior to the execution of the numerical simulation of the internal ballistics. In such a manner, the grain burnback solver GREG is used in order to create tables of the bore and grain geometrical properties in the web variable, in terms of port area, burning perimeter and wet perimeter and in the cavities (submergence, slots, floaters), when present (see figure 4.2). The coupling with the Q1D internal ballistics solver is, hence, obtained by means of the access to these tables through an interpolation procedure, during the internal ballistics numerical simulation. The input for the table access is given by the local web variable, as defined in equation 4.1.

$$web\,(x,t) = \int_0^t r_b\,(x,t)\,dt \tag{4.1}$$

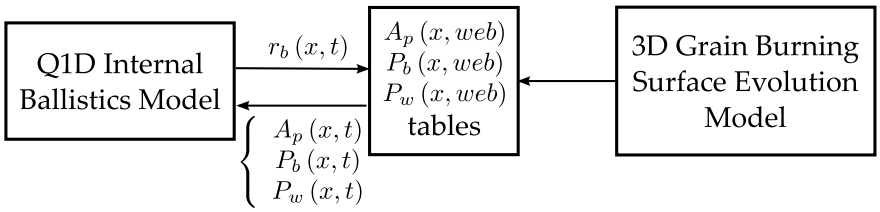

Figure 4.2: Off-line coupling grain burnback analysis and internal ballistic solver

This second approach assumes certainly some approximations on the evolution of the grain combustion surface related to the grain burning rate variations along the motor axis, that can be due to the total pressure drops and to the erosive burning. Some kind of motor configurations in fact are subjected to these phenomena that can strongly lead the SRM internal ballistics, especially when high velocities in the bore establish. With this "off-line" approach, hence, the variations with the axial direction of the burning rate are accounted during the flowfield solution. While their effects are neglected for the 3D burning surface evolution, as this is made with a constant burning rate before the internal ballistics simulation.

Hence, in the case of relevant variations along the motor axis of the grain burning rate, these approximations may become important in terms of the evolution of the bore geometry, but above all in the evolution of the overall burning surface in time, in particular during the tail off phase. This phase, in fact, as described in the paragraph 1.3, page 4, in mainly led by the decreasing of the grain burning surface in time, that depends strongly on the reconstruction of the grain burning surface evolution in time during the Quasi Steady State. Hence, all the approximations introduced by this coupling way are expected, in such cases, to introduce small approximations during the QSS, while even relevant approximations during the TO phase. From another point

of view, with this kind of coupling, the grain burnback evolution can be made once for all for a given motor in an accurate manner. Under these hypotheses, we remember that, as shown in the paragraph 3.8, page 60, the solution for the grain burning surface evolution is known to be a signed distance function from the initial grain surface, as used in [107] and remarked in [113].

In both cases, then, as expressed during the description of the on-line coupling and for the same reasons related to the staggering of the internal ballistics solution with respect to the grain burning surface regression, the updating of the grain geometry can be made at every timestep of the flowfield solution, or only every defined small interval of time, freezing the geometry during them. In the on-line coupling, this reasonable solution has a strong impact on the computational time required for the overall numerical simulation, since the 3D grain burning surface evolution has computational time greater than the internal ballistics solver.

Instead, in the off-line coupling, this has less important effects on the computational time, since the interpolation procedure and the access to the grain geometrical tables can be made using the fact that, by its definition, the $web(x,t)$ variable is an increasing function of the time $\forall x$. In the meantime, the computational cost for the 3D grain burnback analysis of the given SRM is always the same, as it is made once for all the internal ballistics simulation of a such SRM.

In this work, we consider the off-line coupling at each timestep between the grain burnback module and the flowfield Q1D unsteady model. Hence, the solution of the grain burning surface evolution with time (web) is built up by means of the integration of the Level Set equation with a constant burning rate, starting from the banded SDF initial condition, defined by the STL files of the grain and TPs surface. Then, the GREG model generates tables of the Q1D grain geometrical properties that the SPINBALL module for the geometrical updating interpolates during the internal ballistics simulation. We remark that, the solution for the problem of the 3D evolution of the grain burning surface, it is known to be a SDF for the grain propellant starting shape. However, the way to solve the Level Set equation has found to be faster than the setting up the whole SDF. Moreover, this approach is more general and can be useful, in further developments for the on-line coupling between the grain burnback analysis model and the internal ballistics one.

4.1 SPINBALL & GREG Meshgrids Coupling

The coupling between the 3D mesh of the GREG model and the 1D mesh of SPINBALL is obtained by defining a nodal congruence relation between the SPINBALL mesh and the GREG mesh along the motor axis, from motor head to nozzle throat area section. The GREG mesh is typically more or equally refined with respect to the first (see figure 4.3).

This coupling between the two meshes is necessary in order to define the correct interface value of the nozzle throat area. In fact, this is particularly important in order to ensure the "physical" outflow mass from the nozzle throat area and, hence, to define correctly the quasi steady flowfield conditions during the Quasi Steady State. This relation is chosen, also, in order to avoid an interpolation of the geometrical quantities computed by the GREG model. In particular, in this manner the definition of the burning perimeter for the Q1D model can be easily obtained by the equation 4.2.

$$\tilde{P}_{bj} = \frac{\sum_{i(j)} S_{bi(j)}}{\Delta x} \tag{4.2}$$

Where with i are indicated the indices of the GREG axial grid, with j the ones of the SPINBALL grid and $i(j)$ are the indices of the GREG grid that are in the j-th SPINBALL cell. We remember that the definition of the grain burning perimeter becomes very important in order to define the correct inlet mass flow rate into the chamber due to grain combustion, and thus to characterize the SRM bore flowfield conditions.

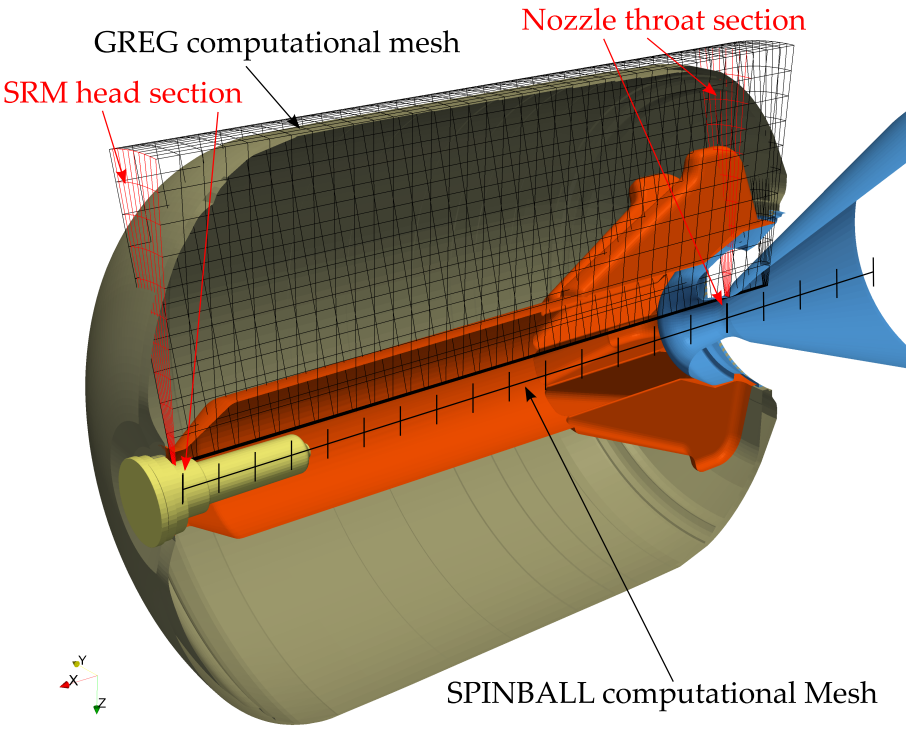

Figure 4.3: SPINBALL & GREG computational meshes coupling

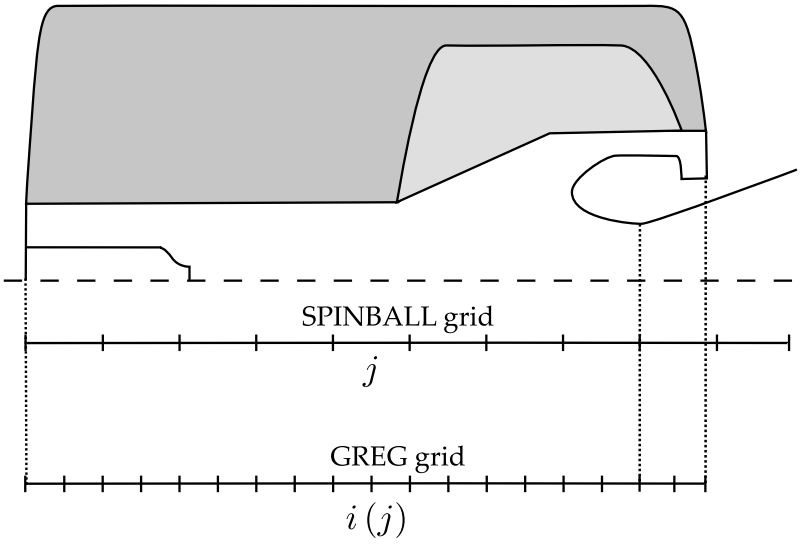

Figure 4.4: GREG-SPINBALL motor axis meshes coupling

In fact, the cell inlet grain propellant mass flow rate is directly given, in a consistent manner with the definition of the total burning surface, by the equation 4.3, evaluated with the definition of the cell burning perimeter given by the equation 3.126.

$$\dot{m}_{bj} = \rho_p r_{bj} \tilde{P}_{bj} \Delta x \tag{4.3}$$

The updating of the grain geometrical properties necessary to the SPINBALL gasdynamics model (port area, burning perimeter, wet perimeter and the geometrical parameters of the cavities, where present) is, then, made by means of a linear interpolation of the off-line tables created by GREG, at each timestep of the flowfield solution.

Part II

Results

5

GREG Validation

In this section some results, carried out through the use of the Level Set Method, will be shown. In particular some 2D test cases present in literature are discussed, as validation of the numerical scheme built-up to solve the Level Set equation 3.28 for pointwise normal directed motion field. Moreover subsequently, some other test cases will be shown to describe the properties of the numerical techniques presented in the paragraph 3.11, page 66, able to define the front integral properties of the level zero, from the level set representation of the front.

The numerical scheme adopted for all the test cases is a Godunov-type scheme first or second order (ENO with `minmod` flux limiter) with an exact Riemann solver for the approximation of the spatial term of the Level Set equation and a one-step Runge-Kutta method (Euler method, first order) or a Heun's method (second order) for approximation of the temporal derivative (see paragraph 3.4.2 , page 51). The overall numerical scheme is a space and time first or second order accurate explicit time-marching numerical scheme, with a 3 grid nodes for the first order and a 5 grid nodes for the second order, "up-sided down T" stencil. A constant front motion velocity $V = 1$ is considered for all the cases.

Hence, to summarize, the numerical tests that will be performed are:

- a 1D Test Case as validation and accuracy order tester [31];
- two 2D Test Cases as validation with qualitative [31] and quantitative comparisons [49];
- some test cases for the characterization of the techniques for the grain geometrical properties evaluation, presented in paragraph 3.11, page 66.

It is important to underline that for the Level Set method, the presented test cases are the only ones which have been found in literature in order to validate the method and the numerical code, for the case of constant motion velocity field.

In particular, about the application of the LSM to the grain burnback analysis, instead, only recently this technique has been applied for this particular purpose. Hence, even if some recent works have been presented [95; 98; 107], it is impossible to take out from them detailed, quantitative and not trivial test cases in order to accomplish code-to-code comparisons, except for the one that will be presented in the paragraph 6.2, page 112.

5.1 1D Test Case

The accuracy order of the space and time first or second order numerical scheme (see paragraph 3.4.2, page 48) is tested considering a simple 1D test case, present also in literature [31], of a cosine curve motion ($\vec{V} = \hat{n} \Longrightarrow V = 1$), as given by the equation 5.1.

$$\phi(x, t = 0) = \cos(2\pi x) \qquad 0 \leqslant x \leqslant 1 \tag{5.1}$$

The Level Set equation, that has to be integrated numerically, is for an explicit fashion level set function, given by the equation 5.2. Periodic boundary conditions are imposed at $x = 0$ and $x = 2\pi$, as naturally the problem itself suggests.

$$\frac{\partial \phi}{\partial t} + V\sqrt{1 + \left(\frac{\partial \phi}{\partial x}\right)^2} = 0 \tag{5.2}$$

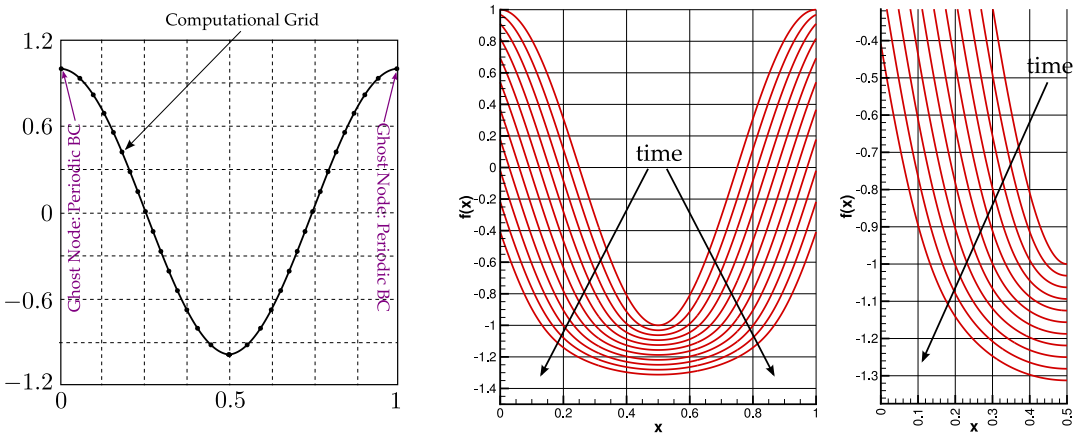

(a) Initial and Boundary Conditions

(b) Propagating Sine

Figure 5.1: Cosine Curve Evolution in Time

As made in [31], in order to characterize the numerical schemes accuracy order, we consider now a Richardson's extrapolation. Hence, we assume that the solution can be expressed as:

$$\phi^{ex}(x,t) = \phi^{h}(x,t) + Ch^{R} + O\left(h^{R+1}\right) \tag{5.3}$$

where:

- $\phi^{ex}(x,t)$ is the exact solution;
- $\phi^{h}(x,t) \rightarrow$ is the numerical solution yielded with a mesh width h.

The accuracy order of the numerical solution R can be evaluated by means of the Richardson Extrapolation through the expressions 5.4.

$$R\left(\phi^{h}, \phi^{\frac{h}{2}}, \phi^{\frac{h}{4}}\right) = \frac{1}{\log(2)} \cdot \log\left(\frac{\left|\phi^{\frac{h}{2}} - \phi^{h}\right|}{\left|\phi^{\frac{h}{4}} - \phi^{\frac{h}{2}}\right|}\right) \tag{5.4}$$

The accuracy order, obtained directly on the computed level set functions for a sequence of dyadic grids with different levels of resolution, is shown in table 5.1. The second column reports the results for the first order numerical scheme, while the third column the ones for the second order scheme. The results are obtained using a discrete 2-norm, as did in [31].

Mesh size (cells number)	$\bar{R}_1\left(\phi^{h}, \phi^{h/2}, \phi^{h/4}\right)$	$\bar{R}_2\left(\phi^{h}, \phi^{h/2}, \phi^{h/4}\right)$
100, 200, 400	0.95262	1.7548
200, 400, 800	0.96603	1.8228
400, 800, 1600	0.97722	1.8852
800, 1600, 3200	0.98558	1.9294
1600, 3200, 6400	0.99123	1.9587

Table 5.1: Accuracy order of the first and second order scheme for a 1D cosine evolving curve

For this test case, the analytical solution does not exist and, consequently, no direct evaluation of the truncation error is possible.

Moreover, the reference test case is a little different with respect to the one reproduced here. In fact, in [31] the authors introduced a small diffusion, due a small dependence of the velocity along the normal direction from the front local curvature and used an approximate Riemann solver instead of the exact one (the so called Osher-Sethian, see the appendix J, page f for more details). However, it is possible to argue that the results obtained are in line with the reference ones and, as expected, around the first and second order of accuracy respectively.

5.2 2D Test Cases

The 2D test cases that are considered to validate and evaluate the aforementioned numerical scheme are:

- the Wenzel's test case [49]: a Double saw-teeth
- the Osher-Sethian's Test Case [31]: a 2D Star shaped front

5.2.1 Wenzel's Test Case

The double saw-teeth front is known analytically. Hence, the Initial Condition is directly obtained by means of putting in an implicit function fashion the two rectilinear segments of the interface, which are given in the equation 5.5.

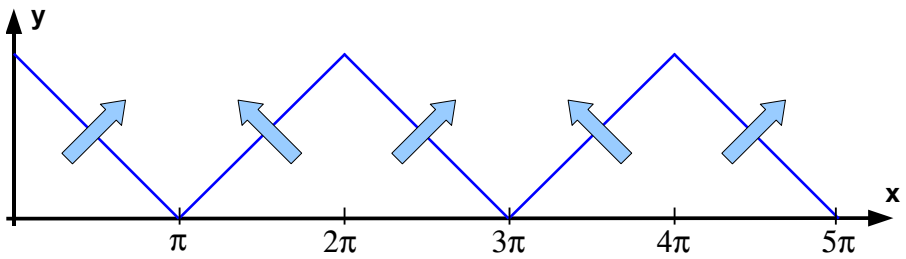

Figure 5.2: Wenzel's test case: double saw-teeth

$$\phi(x, y, t = 0) = \begin{cases} x + y - \pi = 0 & 0 \leqslant x < \pi \\ -x + y + \pi = 0 & \pi \leqslant x \leqslant 2\pi \end{cases} \tag{5.5}$$

Wenzel, in solving this test problem, considered a spectral method to evaluate the left-right side derivatives, coupled with an exact formulation of the Riemann solver given by Hirsch [55], for two mesh resolutions for computing the solution (32-points grid and 64-points grid).

For the simplicity of the front, however the solution of the interface evolution is known even analytically.

In fact, in order to obtain the analytical solution of the problem, it is simply necessary to divide the domain, into (see figure 5.4):

- a subdomain which is not influenced by the rarefaction fan that develops at leading edge;
- and a subdomain which is influenced of it.

Into each subregion the spatial derivatives can be simply calculated

- for the subdomain influenced by the rarefaction fan: $0 \leqslant x \leqslant \frac{V t}{\sqrt{2}} \leqslant \pi$, we have

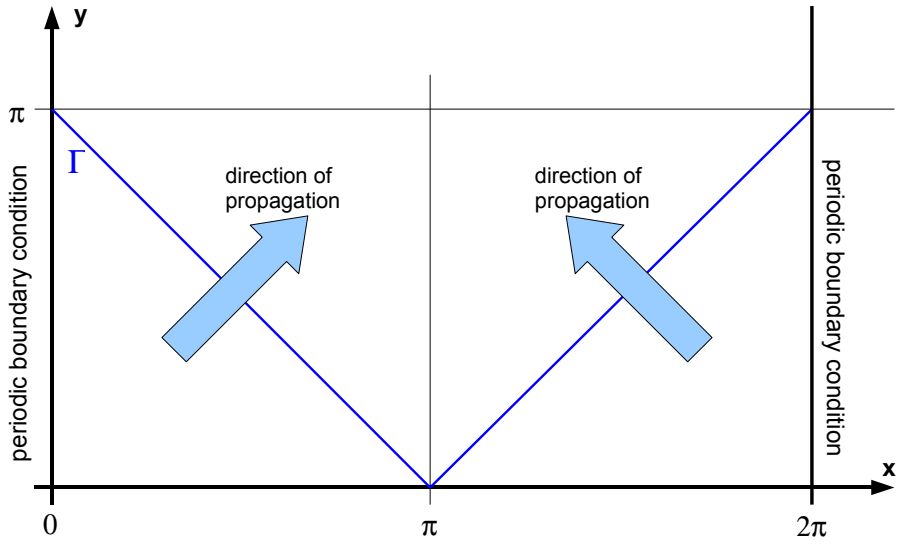

Figure 5.3: Wenzel's test case: domain of interest

$$\frac{\partial \phi}{\partial x} = -\frac{x}{\sqrt{(Vt)^2 - x^2}} \qquad \frac{\partial \phi}{\partial y} = 1 \tag{5.6}$$

- while for the subdomain not influenced by the rarefaction fan: $\frac{Vt}{\sqrt{2}} \leqslant x \leqslant \pi$

$$\frac{\partial \phi}{\partial x} = \pm 1 \qquad \frac{\partial \phi}{\partial y} = 1 \tag{5.7}$$

Hence, by the Level Set equation 3.28 also the time derivative of the ϕ function can be evaluated, as given by the equation 5.8.

$$\frac{\partial \phi}{\partial t} = -V\sqrt{\left(\frac{\partial \phi}{\partial x}\right)^2 + \left(\frac{\partial \phi}{\partial y}\right)^2} = \begin{cases} -V\sqrt{1 + \dfrac{x^2}{(Vt)^2 - x^2}} & \text{for} \quad 0 \leqslant x \leqslant \dfrac{Vt}{\sqrt{2}} \\ -V\sqrt{2} & \text{for} \quad \dfrac{Vt}{\sqrt{2}} \leqslant x \leqslant \pi \end{cases} \tag{5.8}$$

Integrating in time the equation 5.8, the solution is hence obtained:

$$\phi(x, y, t) = \begin{cases} \phi(x, y, t = 0) - x - \sqrt{(Vt)^2 - x^2} & \text{for} \quad t \leqslant \dfrac{\sqrt{2}x}{V} \\ \phi(x, y, t = 0) - V\sqrt{2}t & \text{for} \quad t \geqslant \dfrac{\sqrt{2}x}{V} \end{cases} \tag{5.9}$$

In particular, Wenzel considered two probe points of the solution and he follows their position in time. These points correspond to the two basic features that the problem has to capture, as validation of the numerical scheme considered, according to the Huygens' principle (see figure 5.4):

1. the cusps at the back of the front must retain their shape;
2. the circular rarefaction waves must develop at the leading edges.

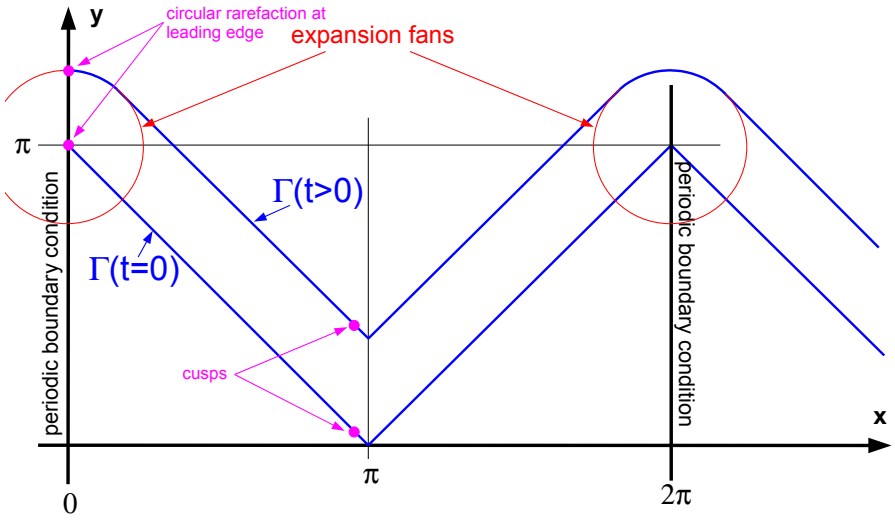

Figure 5.4: Propagation of the front according to the Huygens' principle

As shown in the figure 5.5, the GREG results agrees completely with Wenzel's results for tracking the point subjected to the expansion fan in time (note that the different time scale for Wenzel may be due to a non dimensional time). While our results are even better than the ones presented by Wenzel for the cusp tracking. This is in particular due to these main facts:

- the spectral methods are known to perform quite poorly results when discontinuities are present in the solution and for a small number of mesh points [49]
- even if spectral method have an infinite theoretical accuracy order, what we are seeing is the precision of the scheme, not the accuracy order

In the figure 5.6, some grid function fields for different times are presented for the 64 grid, with a computational domain in the x_2 direction from 0 to 2π, where the level zero is highlighted with a black thick line.

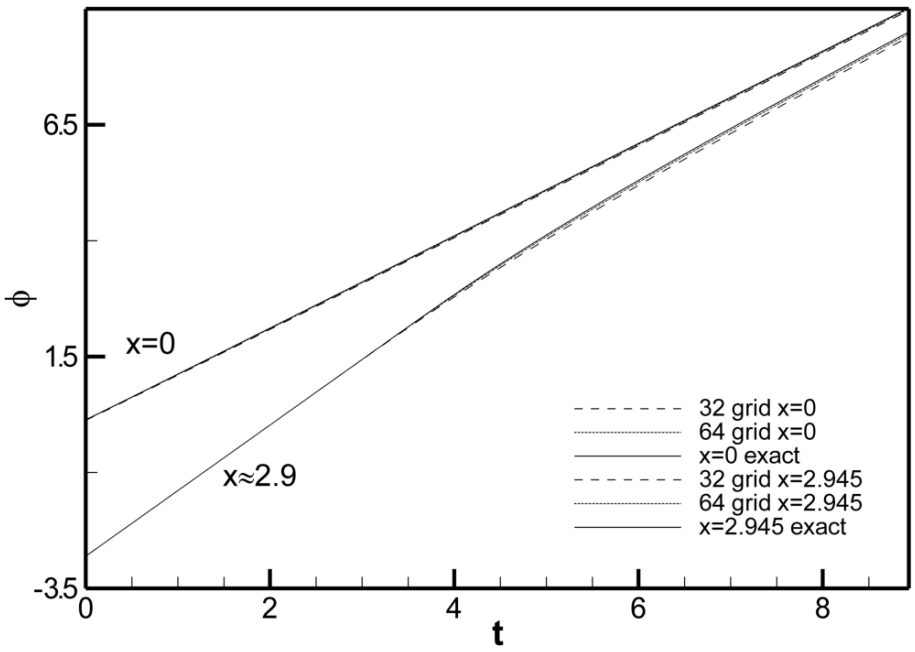

(a) GREG results

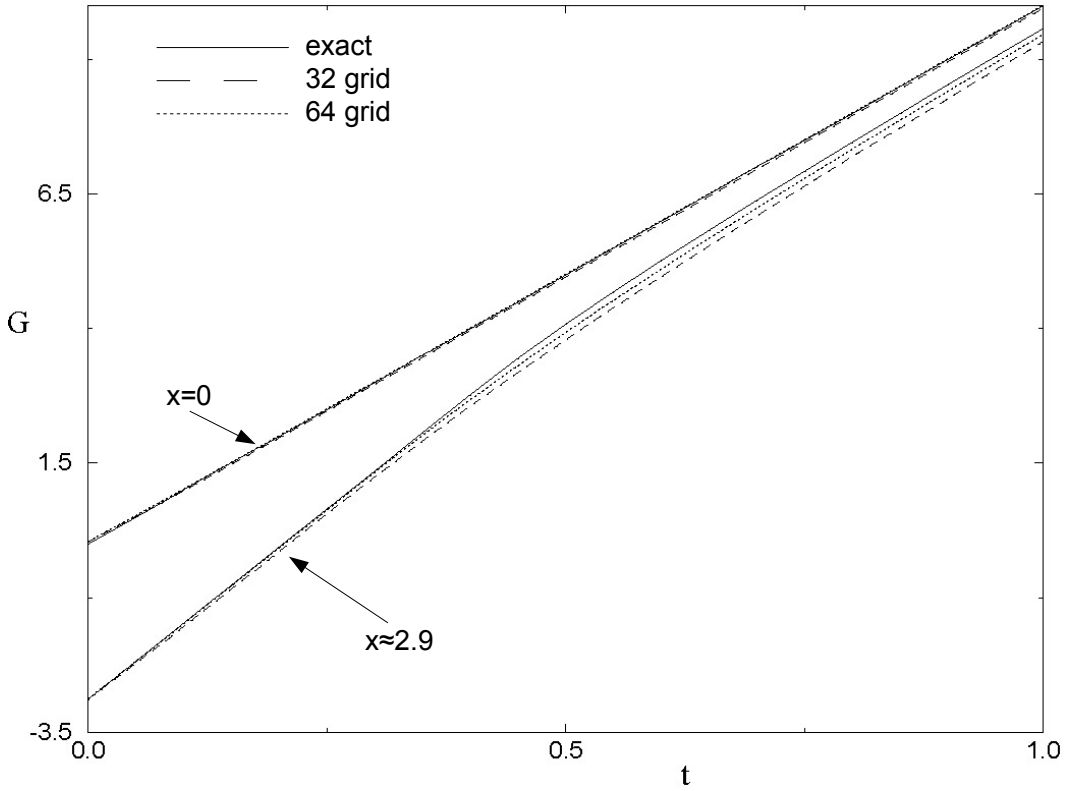

(b) Wenzel's results

Figure 5.5: Wenzel's Test Case results comparison

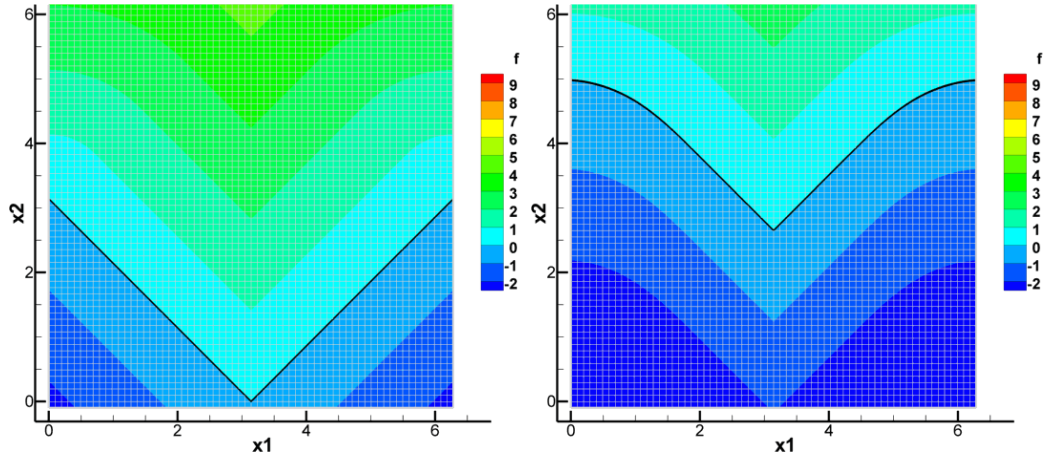

(a) step 0 ; time = 0.0

(b) step 30 ; time = 1.874

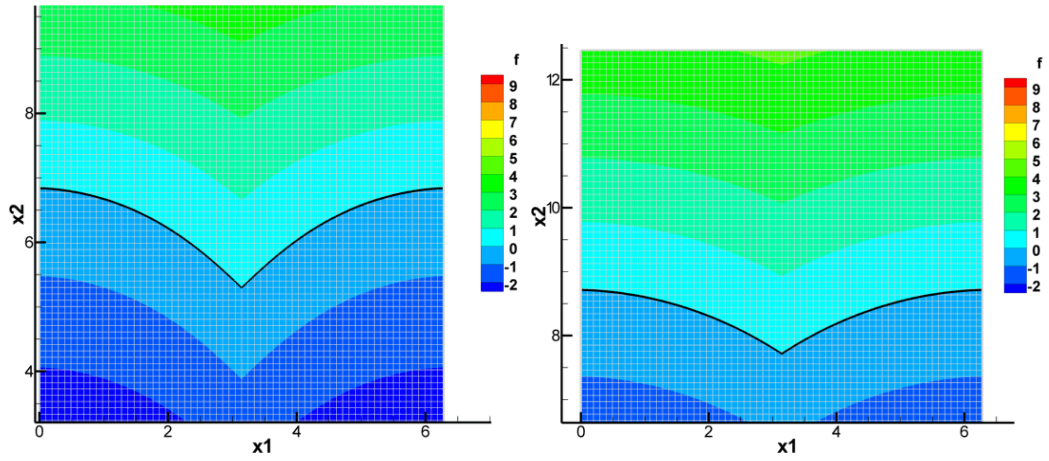

(c) step 60 ; time = 3.749

(d) step 90 ; time = 5.636

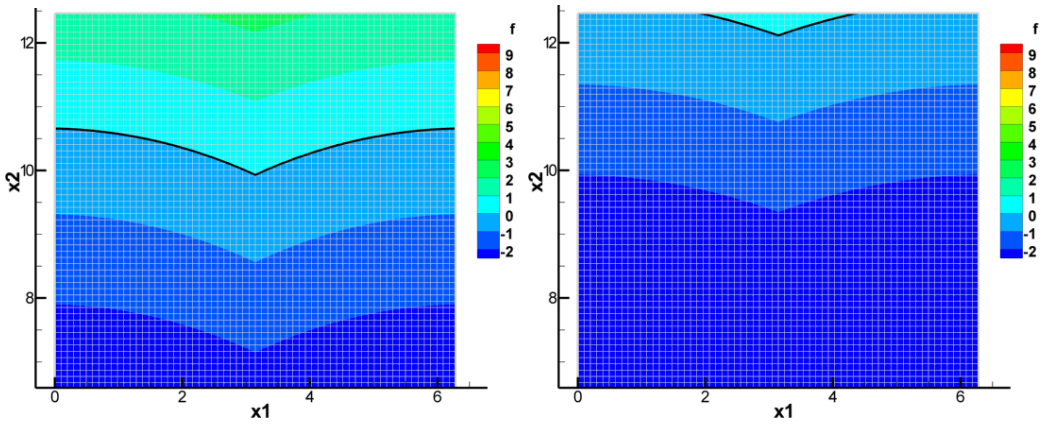

(e) step 120 ; time = 7.587

(f) step 150 ; time = 9.619

Figure 5.6: Some fields for different timesteps

5.2.2 Osher-Sethian Test Case

As second qualitative validation, we perform another calculation present in literature due to Osher and Sethian [31].

The test case is represented by the evolution along the normal direction of a star-shaped front, given by the following equation.

$$\phi(r, \vartheta, t = 0) = 0 \; : \; r(\vartheta) = \frac{R_c + R_f}{2} + \frac{R_f - R_c}{2} \sin(n_p \vartheta) \qquad \vartheta \in [0\,;\, 2\pi] \tag{5.10}$$

In the equation 5.10, R_f is the *star fillet radius*, R_c the *star cusp radius* and n_p the *number of star points*, as referred also in the figure 5.7.

The IC can be simply set exploiting the front in an explicit manner, with respect to the radius variable, as expressed by the equation 5.11.

$$\phi(r, \vartheta, t = 0) = r - \left(\frac{R_c + R_f}{2} + \frac{R_f - R_c}{2} \sin(n_p \vartheta) \right) \qquad \vartheta \in [0\,;\, 2\pi] \tag{5.11}$$

We propose the same example shown in [31], considering the following data:

$$R_c = 0.035 \quad R_f = 0.165 \quad n_p = 7$$

in a Cartesian rectangular mesh with 300×300 points.

Note, as underlined, that the initial front develops sharp corners which then open up as the front itself burns, approaching a circle as $t \to \infty$ [28]. In the original article Osher and Sethian used a second order Hamilton-Jacobi scheme (the so called Osher-Sethian scheme, see the appendix J, page f for more details) with a constant timestep $t = 0.0005$ that fulfills for all time the CFL-condition. Instead we tested our time and space first order accurate scheme with the exact Riemann solver. As no quantitative comparison can be made from what published in the original article, only our results are showed (however in a qualitative agreement with the one obtained by the cited authors).

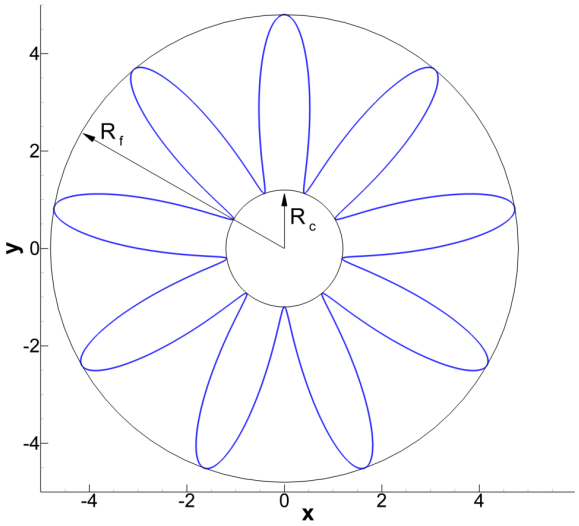

Figure 5.7: Star shaped front

It is important to note that in all cases a rectangular mesh grid can never be able to follow correctly the evolution of a star-shaped front in the case of $V = \text{const}$ and n_p odd (as generally used in Solid Rocket Motors). In fact, whatever rectangular mesh is unable to respect the corners formation lines, in correspondence of the star cusps.

For this reason, in order to study the evolution of these particular geometries, that are very common also in solid rocket motor grain shapes (2D and, especially, 3D grains), some other tests have been performed considering a polar Cartesian meshgrid. A star shaped front with the following properties is thus considered:

$$R_c = 1.2 \quad R_f = 2.4 \quad n_p = 9$$

for which the following tests are performed:

- a complete evolution for all the front (figure 5.9), with a periodic boundary condition for the azimuth in $\theta = 0$ rad and $\theta = 2\pi$ rad;

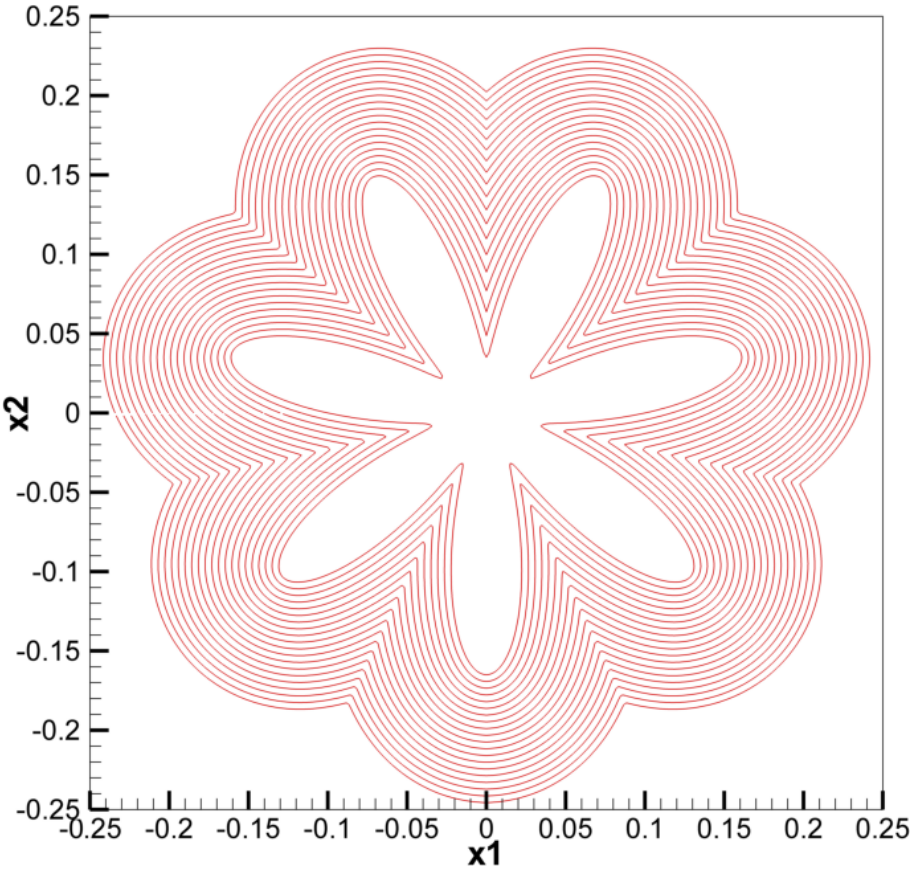

Figure 5.8: Star-shaped front burning out $V = 1$, $t = 0.0$; ≈ 0.08

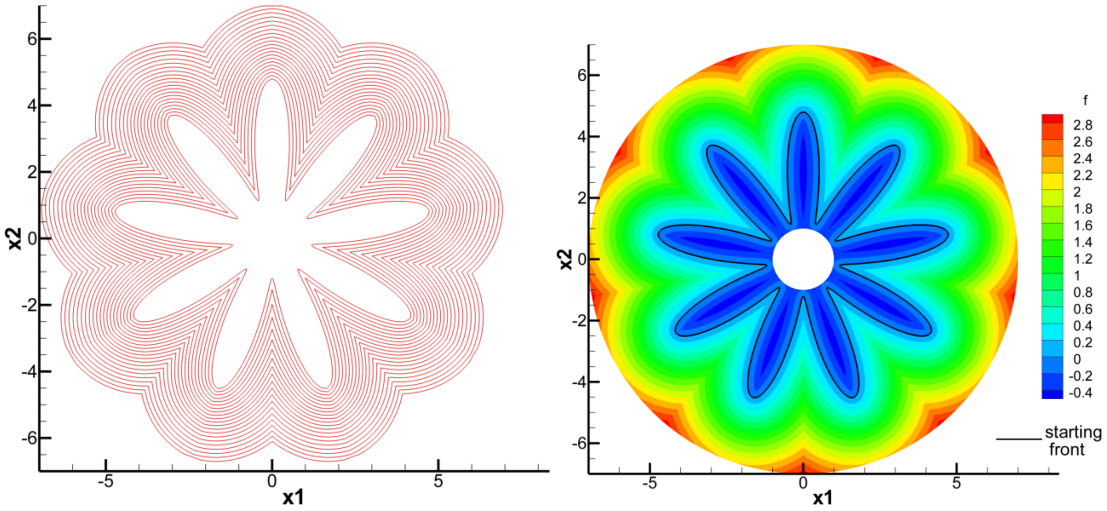

(a) Star-shaped front burning out: $V = 1$, $t = 0.0$; ≈ 2.2 (b) SDF as initial condition for the star-shaped evolution problem

Figure 5.9: Star-shaped with 9 points: 180×200 grid-point (along θ and r direction)

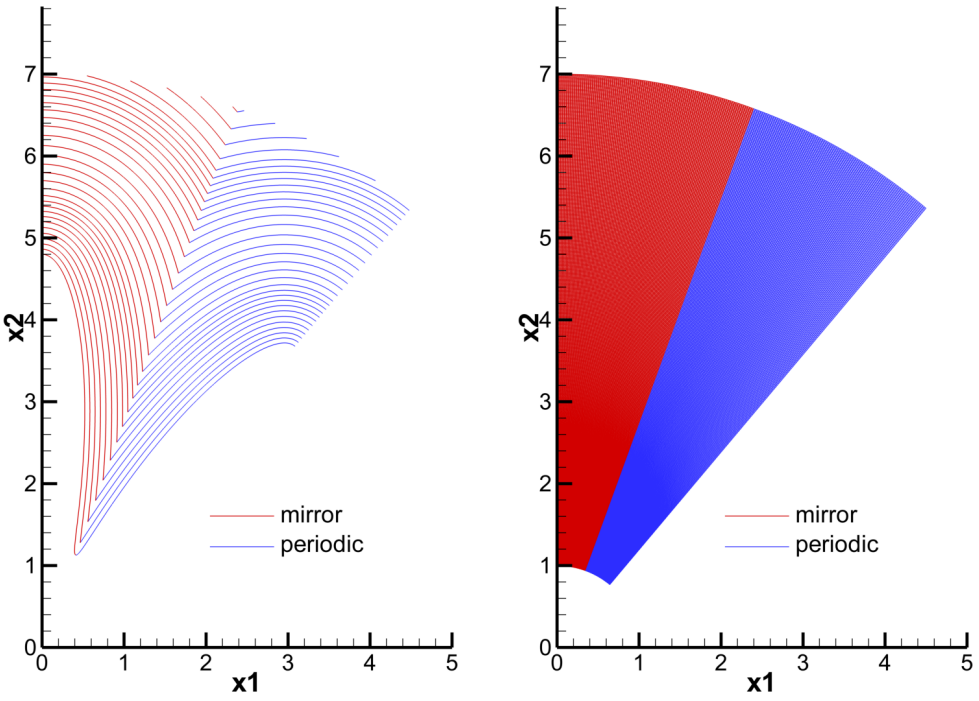

(a) Star-shaped front burning out: $V = 1$, $t = 0.0\,;\approx 2.9$

(b) Both numerical grids

Figure 5.10: Comparison between periodic and mirroring boundary conditions of the star-shaped front

- a test respecting the front periodicity figure 5.10, with periodic boundary conditions for the azimuth in $\theta = 0$ rad and $\theta = \dfrac{2\pi}{n_p}$ rad, with a 200×400 grid points;
- a test considering the front mirror properties of a star slice figure 5.10, with mirroring boundary conditions for the azimuth, with a 100×400 grid points.

From the results of the simulations, with periodic and mirroring boundary conditions, the solutions are exactly alike at round-off machine precision, as expected. Note that the use of that kind of boundary conditions of the problem allows to hardly decrease the grid points number, and consequently the computational costs for the simulation.

5.3 Evaluation of Grain Geometrical Properties: Techniques Validation

The evaluation of the level zero interface properties in 2D sample problems has been defined at the beginning by considering the standard regularized Dirac Delta and Heaviside function used in the Level Set community [79; 59]. These technique are extracted from a previous work [14], in which the discrete Delta Dirac is represented by a cosine function (see table 3.3 and figure 3.17). The definition of the Heaviside regularization follows the one of the Dirac Delta function, considering their relation, given by the equation 3.100, page 67.

A grid convergence analysis is hence carried out for the numerical technique of areas, volumes and perimeters evaluation, in order to find out the reliability of the computed grain geometrical parameters, as output of the grain burnback analysis. As shown in the paragraph 3.11, page 66, the technique is for computing areas and perimeters for 2D problems and volumes and surfaces for 3D ones. Hence, it is possible to consider simple 2D test cases to obtain results valid even for 3D cases in order to evaluate the technique properties, without lack of generality.

Hence, a simple test case is chosen, in which the analytical computation in well known. This consists in a simple circular front not evolving, which grid function can be in a straightforward manner built as SDF. Area and perimeter of this circle were, hence, evaluated for different grid resolutions and different value of the front smearing parameter ϵ, using a rectangular Cartesian coordinate system (see figure 5.11).

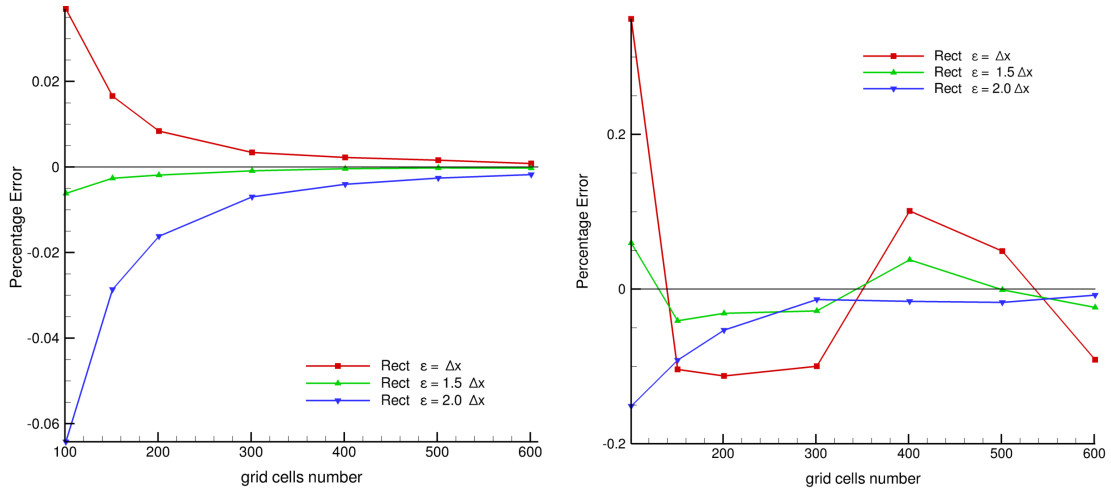

(a) Area Evaluation

(b) Perimeter Evaluation

Figure 5.11: Percentage Error for Areas & Perimeters evaluation techniques

Making reference to the figure 5.11, it is possible to underline the following remarks:

- the area evaluation technique has an asymptotic convergence as the grid is refined, in a independent manner from the smearing factor or the coordinate system used. This is reasonable considering that the procedure is not much sensible to how much the front itself is smeared out. The smearing of the Heaviside function through the level zero helps in diminishing the procedure error with respect to a simple "completely in" area evaluation procedure (only cells that are not interested by the interface are accounted). However, an asymptotic convergence behaviour of the technique can be ensured just by the "completely in" part of the area computation expression, as the grid is refined. But, the precision of the technique should be very low in such a rough choice of the discretized Heaviside function.
- The perimeter calculation technique, instead, does not behave regularly and a grid asymptotic convergence is not ensured for any value of the smearing parameter. In particular, this behaviour can be ascribed to the high sensitivity of the Dirac delta approximation to the position of the front respect to grid. Hence, some care must be devoted to the use of the perimeters (or surfaces in 3D) evaluation as grid is refined, since grid convergence may not be present. Despite this less of asymptotic convergence, it is possible to underline that the error even for wide grids has a percentage error less than 0.5%.

These results have underlined some problems with respect to the technique itself. Hence, a deepened understanding has been suggested and carried on the problem itself, through a literature review of the recent techniques of the Dirac Delta and Heaviside function numerical representation. In fact, these results have been found to be expected considering the recent mathematical support given by some authors' work [88; 89; 85; 81; 99; 82]. As a matter of fact, all the referenced works confirm the aforementioned remark on the lack of the grid convergence property in the computation of perimeters in 2D problems (or surfaces in 3D ones), when the 1D Dirac Delta function is directly used in multidimensional problems.

We remember that we expect to have some confidence on the convergence properties of the technique itself. But also, for the use of these geometrical parameters (perimeters, areas, volumes) in the internal ballistics numerical simulation, we must ensure some regularity properties of the computed quantities in time and space.

Hence, we have tested with very simple problems, using or not, the Level Set for the evolution of the interface, the techniques presented by different authors [88; 89; 85; 81; 99; 82]. The target of this investigations is to understand which technique can ensure all the aforementioned properties we want for the Dirac Delta regularized function in multidimensional problems[1].

For this purpose, the multidimensional Dirac Delta functions built with the technique described by Engquist [88; 89; 85; 81] and Smereka [99; 82] have been obtained in polar coordinates in order to investigate their use in the grain burnback problem[2]. The results yielded are discussed hereunder: only the figures for the cosine regularization are shown, as the same results are valid also for the linear regularization (refer to the paragraph 3.11, page 66).

The tests matrix considers only 2D problems, without lack of generality, in both Cartesian and Polar system of coordinates (see table 5.2).

Coordinates System	Interface	Level Set use
Cartesian	Line parallel to one axis	no
Cartesian	Circle	no
Polar	Circle	no
Polar	Osher-Sethian Star	yes

Table 5.2: Test Matrix for the evaluation of the multidimensional Delta Dirac regularizations

The techniques considered are:

- the standard 1D Dirac Delta regularizations: with the cosine and the linear smearing functions;
- the Engquist technique to account in the 1D Dirac Delta the front multidimensional effects with 1D cosine regularization (but same results are also obtained with a linear regularization);
- the Smereka technique.

The following remarks can, hence, be made considering the results shown in the figures 5.12, 5.13, 5.14 and 5.15, which refer to the circle test case in Cartesian rectangular coordinates and to the Osher-Sethian test case in polar coordinates.
As expected for a line moving in a Cartesian rectangular grid, parallel to a coordinate axis, the line itself is measured at round off error, with respect to its exact length (in a not dependent manner from the compact support in which the Dirac Delta is defined (refer to the table 3.3, page 68)). In fact, this represents a 1D problem in such a computational grid (results not shown as the percentage error is at round-off).

For a spreading circle in a Cartesian rectangular grid which account multidimensional aspects, the regularizations given by Smereka and Engquist 5.13 define a better convergence behaviour of the computed interface measure with respect to the classic 1D techniques 5.12. However, this convergence behaviour must be interpreted in an averaged sense (as remarked by the authors) and, hence, for small motions of the front with respect to the grid (see figure 5.13). The classic

1 note that the problem in terms of Heaviside regularization is less felt, as underlined before, and however, the Heaviside definition follows from the one of the Dirac Delta function
2 we remember that the use of cylindrical coordinates is preferred in SRM grain applications

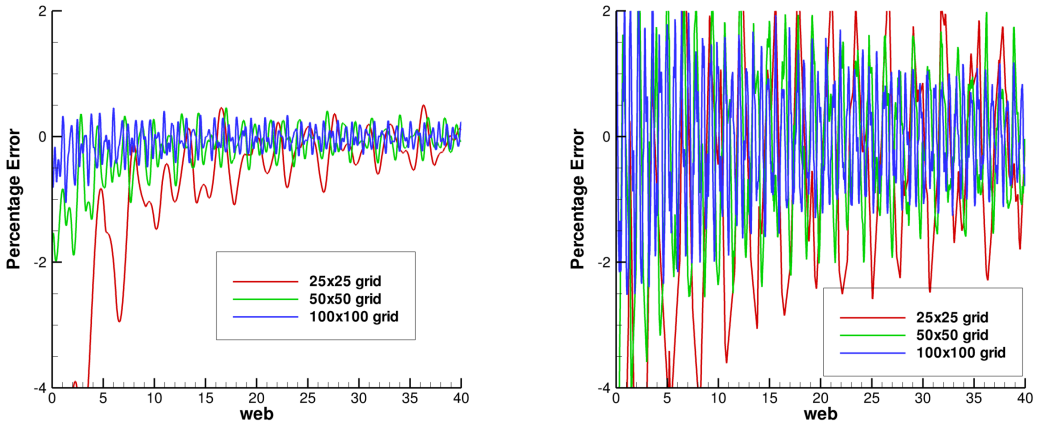

(a) Harmonic function regularization 1D

(b) Linear function regularization 1D

Figure 5.12: Percentage Error for a circle spreading in a rectangular grid: standard technique

1D Dirac Delta regularization, instead, does not behave regularly as the grid is refined 5.12.

For the spreading circle in a polar grid, as the problem becomes again 1D, we have again a round off evaluation error with respect to the exact solution, as proof of the correct implementation of discrete Dirac Delta metric correction.

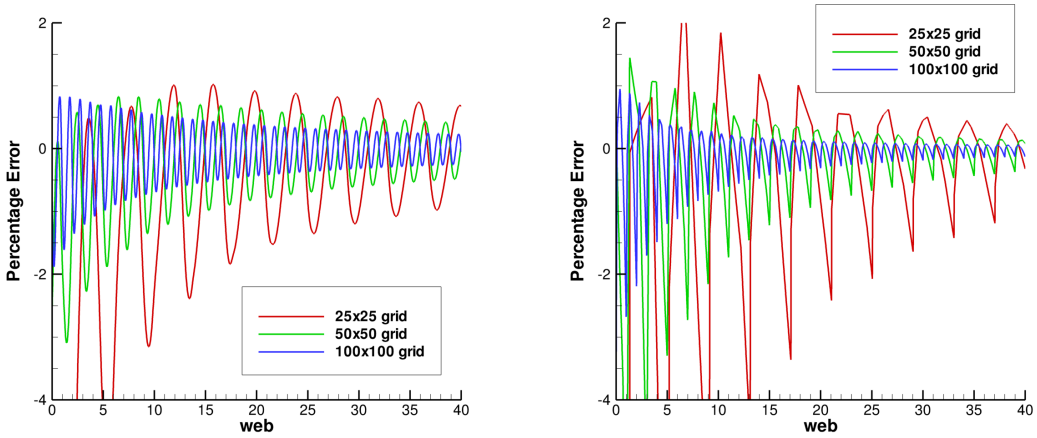

(a) Harmonic function regularization 2D (Engquist correction)

(b) Linear function regularization 2D (Smereka building-up)

Figure 5.13: Percentage Error for a circle spreading in a rectangular grid: multidimensional Dirac Delta

Instead for a Osher Sethian star, evolving with the Level Set Method along its normal direction, the results are very different considering the multidimensional corrections due to Engquist or Smereka 5.15 with respect to the 1D Dirac Delta regularization as explained in figure 5.14.

These differences are underlined the more the multidimensional aspects of the interface with respect to the grid are present. The solid thick lines with symbols in the figures 5.14 and 5.15 define the level zero measure with a linear interpolation procedure on the meshgrid.

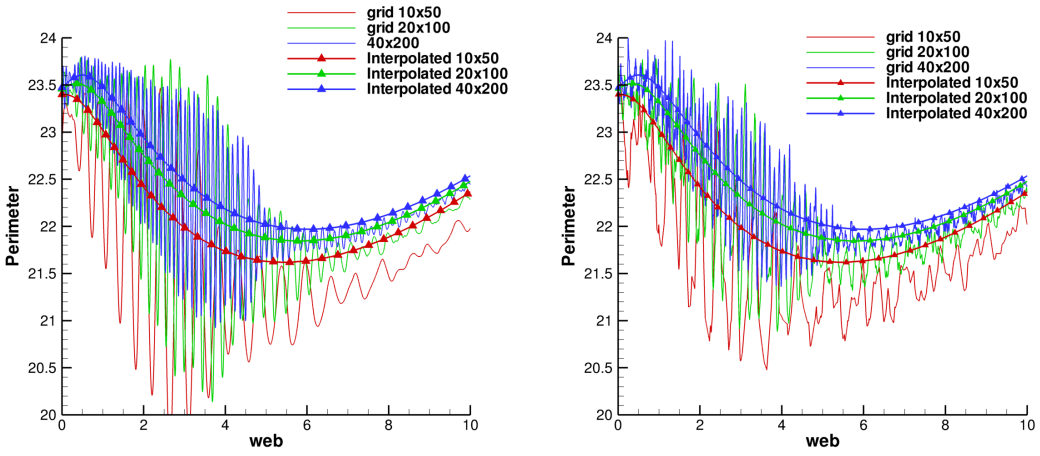

(a) Harmonic function regularization 1D

(b) Linear function regularization 1D

Figure 5.14: Perimeter Evaluation for a Star evolving along its normal direction in a polar grid: standard technique

Note that, the regularity for grid refinements of the computed front length is improved for what concern the convergence properties in average, with the Engquist and Smereka regularization techniques 5.15. However, the regularity property of the computed perimeter during the front evolution is still too sensitive to small movement of the front within the computational lattice. Hence, the numerical noise in the solution is still high, moreover the precision with respect to the interpolated solution is quite low, in such a manner that becomes difficultly useful for its direct application to the grain burnback problem by a numerical point of view.

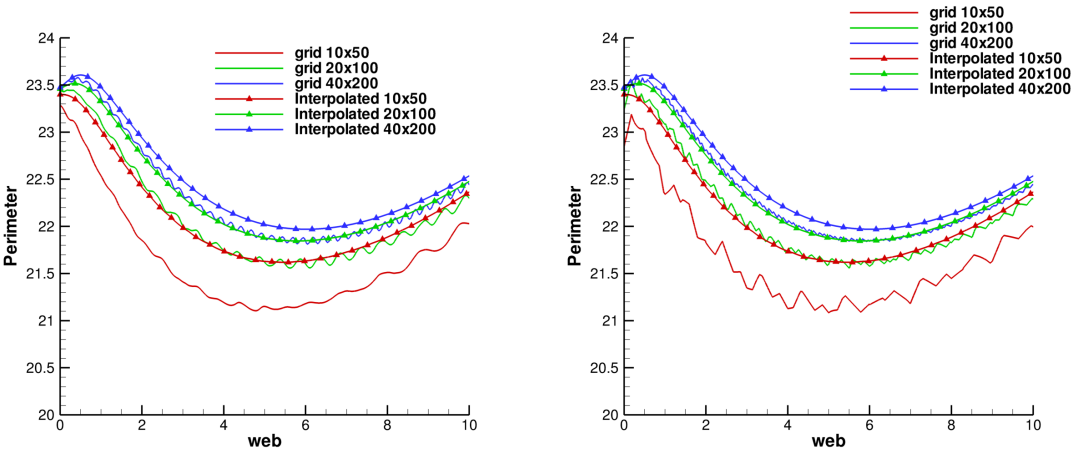

(a) Harmonic function regularization 2D (Engquist correction)

(b) Linear function regularization 2D (Smereka building-up)

Figure 5.15: Perimeter Evaluation for a Star evolving along its normal direction in a polar grid: multidimensional Dirac Delta

Hence, as underlined, even the multidimensional corrections of the regularized Dirac Delta function appear to not fulfill the requirements needed for evaluating the interface geometrical properties. Especially considering that the computed quantities have to be used in an internal

ballistics code, which results can suffer the noise and the precision of the grain burnback input. In fact, while an averaged grid convergence regularity is obtained, the techniques are still too sensible to small movements of the front in the numerical lattice. In particular, the perimeter evolution in time (or web, in case of constant motion velocity) is affected by an high numerical noise, which becomes intolerable for the target.

Obviously, a Level zero interpolation technique to build Dirac Delta and Heaviside function, as the one presented in the paragraph 3.11.1, page 70, is much expensive in terms of the computational time required ,to evaluate the interface integral geometrical properties, than a regularization of the Dirac Delta and Heaviside. However, it ensures both a pointwise grid convergence regularity, and not in the mean, and a regularity in the time evolution of the computed geometrical quantities. These characteristics, in fact, are necessary in order to use the computed geometrical data within the internal ballistics numerical simulation, in order to avoiding the introduction of numerical noise, that could affect the numerical simulation itself. Moreover the precision obtained, consequent to the direct reconstruction of the level zero location from the grid function values in the cell grid, ensures in the same time a precision higher than with the previous techniques. This again becomes important in order to have and ensure confidence in the internal ballistics numerical simulation.

All this is also clear considering the figure 5.16. In this figure in fact, the procedure discussed in the 3.11.1, page 70 for constructing the Dirac Delta and Heaviside functions is compared to the Engquist one for a 3D test finocyl grain shown. In particular, the evolution of the burning surface in the web variable, and of the wet perimeter and the burning perimeter are compared in some locations along the motor axis.

At last, on the new implemented technique for the evaluation of the level zero 0D and Q1D properties, a simple test case of a moving cylinder in a cylindrical mesh is shown. Even if the solution is known analytically, the problem is solved with the Level Set approach. Results confirm the second order of spatial accuracy of the technique, as defined in [106; 114], both for the Volume Evaluation and the Area Evaluation, as shown in the figure 5.17.

In the table 5.3, moreover, the average values of the percentage error is shown for the area and the volume computation, as given by the equation 5.12 for a generic variable f.

Grid	Area $\bar{\epsilon}_{\%}$	Volume $\bar{\epsilon}_{\%}$
10	-1,142267E-002	-4,568636E-002
20	-2,855744E-003	-1,142286E-002
40	-7,139884E-004	-2,85583E-003
80	-1,784556E-004	-7,138814E-004

Table 5.3: Area and Volume Percentage Errors for grid refinements

Grid	Area Accuracy Order	Volume Accuracy Order
10,20,40	1,999983	1,999805
20,40,80	1,999747	1,999871

Table 5.4: Area and Volume Accuracy Orders for the dyadic grids

While the resultant accuracy orders for the dyadic grids are given in table 5.4, in which the expression of the accuracy order by the Richardson analysis given in the equation 5.4 is used.

$$\epsilon_{\%} = \frac{f_{exact} - f_{numerical}}{f_{exact}} 100 \tag{5.12}$$

The meshes have been refined in a dyadic way to check the grid convergence, only in the azimuthal direction, to which the technique for evaluating the Level zero properties is sensitive. In fact, in the direction along the cylinder axis, the problem is simply the same with no grid

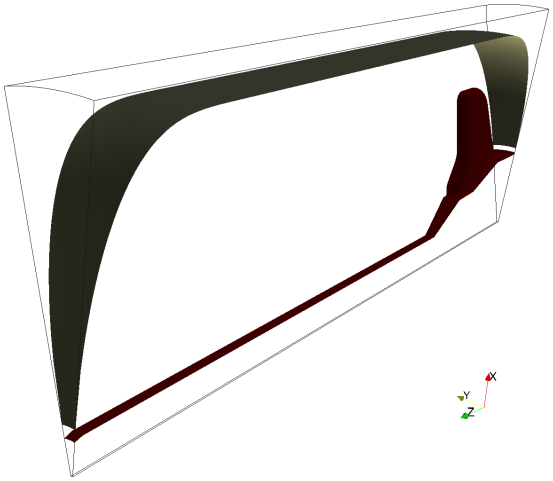

(a) Finocyl Test Grain

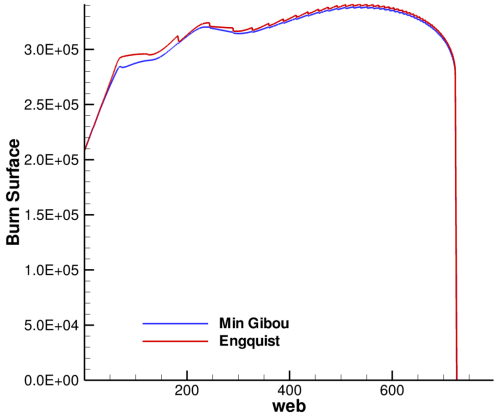

(b) Burning Surface

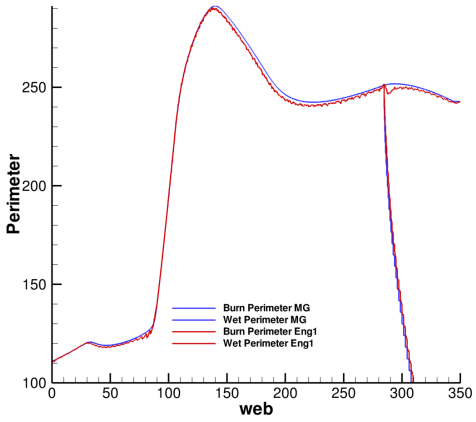

(c) Finocyl Region

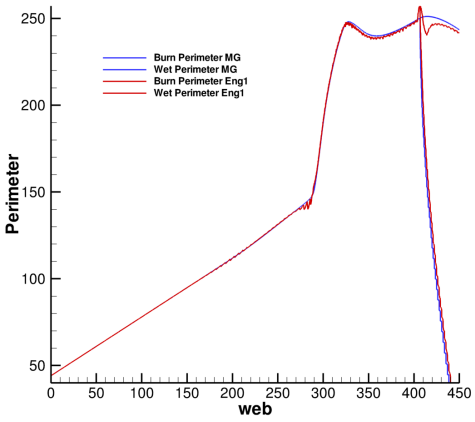

(d) Conical Fins transition region

Figure 5.16: Min Gibou - Engquist techniques comparisons for a 3D finocyl test grain

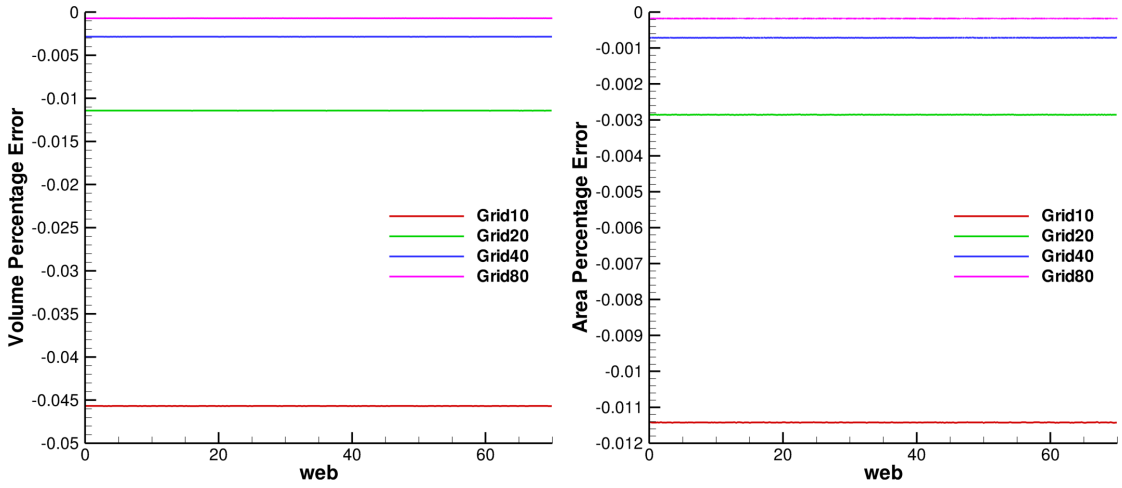

(a) Volume Percentage Error

(b) Area Percentage Error

Figure 5.17: Grid Convergence Analysis for a Cylinder moving with constant velocity in a cylindrical mesh

sensitivity. Along the radial direction, the Level Set representing the evolving cylinder is linear and hence no effects of the grid convergence can be seen, using a major number of points, or even, the second order numerical scheme implemented.

6

GREG Results

This chapter will present some results carried out with Grain REGression model for the 3D grain burning surface evolution with time. In all cases the grain surface evolution is not directly coupled with the internal ballistics numerical solver SPINBALL. Hence, a constant in time and space motion velocity along the normal direction is imposed for the grain evolution. The results of the grain burnback analysis are then used for the internal ballistics simulation, using the off-line coupling presented in the chapter 4, page 79. The grain burnback analysis will be presented for three SRMs, which internal ballistic simulations, performed with the SPINBALL model, will be analyzed in the chapter 7, page 130:

- Zefiro 23 (Z23), second stage of the new European launcher Veicolo Europeo di Generazione Avanzata (VEGA), that the European Space Agency (ESA) is developing;
- NAWC Motor n. 6 and NAWC Motor n. 13: two tactical SRMs simulated and experimented at the Naval Air Warfare Center, which grain shapes and geometrical data are available in literature [108; 107; 64], since intense testing and simulation activities have been made recently.

The 3D evolution of the grain shapes for the three motors will be shown, together with the 0D and Q1D grain geometrical paramaters necessary for the 0D and/or Q1D internal ballistics numerical simulation. A grid convergence analysis on the computed 0D parameters will be made. Moreover, where published data are present, a comparison with the literature data will be made: in particular for NAWC Motor n. 6 a code-to-code comparison will be carried out. For what concern the first SRM, Zefiro 23, all the data related will be shown in non-dimensional scales for non-disclosure reasons, since the VEGA launcher is still under development[1].

6.1 Zefiro 23

Zefiro 23 grain is a 3D aft-finocyl grain with a complex Thermal Protections axisymmetric surface, as grain boundary, as shown in figures 6.2 and 6.3[2].

The Zefiro 23 grain burnback analysis has been made with the GREG model, considering a constant burning rate in space and time. In fact, as stated in the chapter 4, page 79, an off-line coupling between the grain regression model (GREG) and the internal ballistics model (SPINBALL) is considered in this thesis work.

The grain starting configuration and the TPs initial surface, as limit for the grain evolution, are obtained directly as STL surfaces, from CATIA software. In particular, the TP initial surface is an axisymmetric surface, and hence it has been simplified in a given profile of points (radius versus motor axis), directly given in a tabulated manner by CATIA (see figure 6.1).

1 for all the geometrical data related to Zefiro 23 the author want to thanks AVIO Group S.p.a. for the courtesy
2 the author want to thanks AVIO Group S.p.a. that grants all the required motor data

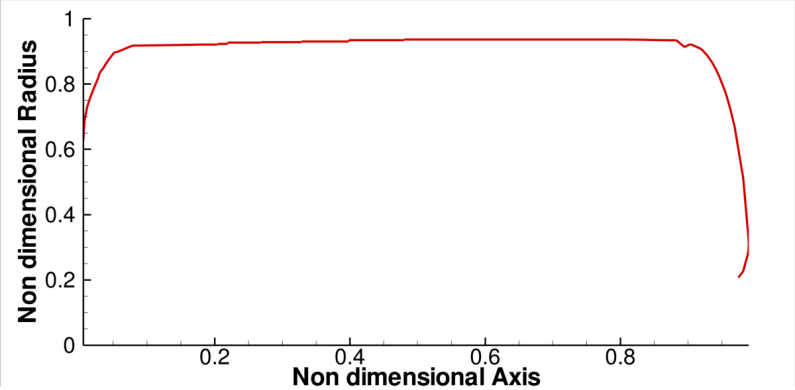

Figure 6.1: Z23 Thermal Protections Surface

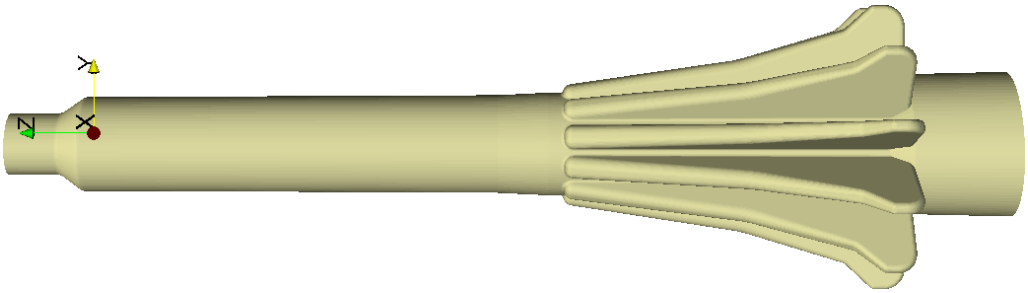

Figure 6.2: Z23 STL initial grain surface representation

The grain initial surface is an aft-finocyl grain with 11 star points, given by about 43000 triangles in the unstructured STL representation of the 3D grain initial surface (see figure 6.2).

Both the grain starting surface and the TPs surface are initialized as SDF in the chosen grid, coupled along the axial direction with the SPINBALL one. In particular, only a part of the 360 degrees are meshed in the GREG cylindrical grid, exploiting the star periodicity. Hence, mirroring BCs are imposed on the theta planes to the Level Set function at each timestep, so that the domain meshed is ranging, in terms of theta angle, from 0 degrees to 360/22 degrees, as clear in the figure 6.3.

Figure 6.4 shows the 3D evolution obtained by GREG, under the constant burning rate assumption, for different web values. The computational mesh considered is composed by 50 cells along the azimuthal direction, 100 cells along the radial direction and 400 cells along the head-nozzle throat axial direction, in cylindrical coordinates, as shown in the figure 6.3.

For the Zefiro 23 grain burnback analysis, a grid convergence analysis has been made too with respect to the evaluation of the global 0D parameters: burning surface, wet surface and bore volume evolution in the web variable (see figure 6.5). The grids considered are defined by $25 \times 50 \times 200$ cells, $50 \times 100 \times 400$ cells, $100 \times 200 \times 800$ (the first number defines the number of cells along the azimuthal direction, the second, along the radial direction and the third, along the motor axis from head to nozzle throat section) in the computational domain given in the figure 6.3 (360/22 degrees for the azimuthal direction).

We remark that the algorithm proposed for the grain burning surface evolution is enough fast. As matter of fact, the aforementioned grid resolutions have required for the Zefiro23 SRM, respectively, about 2 minutes, 12 minutes and 2 hours on a commercial single processor machine (2.40 GHz), with about the same order of magnitude of computational time required to set-up the initial conditions.

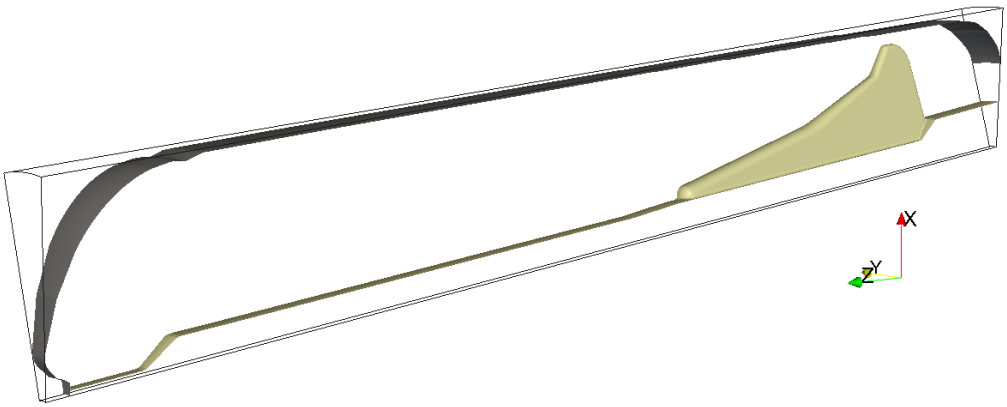

Figure 6.3: Z23 SDF initial grain surface level zero for grain and TP surface in the computational domain

In the figures 6.6 and 6.7, some visualizations of the Level Set grid function for different web values are shown, for the intersection of the grain grid function and the case one (built from the Thermal Protections inner profile), as defined in paragraph 3.11, page 66.

In figure 6.5, it is possible to remark a convergence behaviour of the 0D computed quantities, as the mesh is refined. In particular, the numerical noise in the burning surface area, present for the low grid level resolution, disappears as the grid is refined, due to the greater accuracy through which the grain and TPs surface are represented in their interaction. In the table 6.1, moreover, the percentage errors for the three meshgrid between the STL grain initial surface and the GREG computed ones are shown, as defined by the equation 6.1.

$$\epsilon_{\%} = \frac{S_b|_{STL} - S_b\,(web = 0)|_{GREG}}{S_b|_{STL}} \cdot 100 \tag{6.1}$$

The results underline that a good representation of the initial burning surface is obtained already starting with the first level of grid resolution and, considering the higher grid resolutions, the IC burning surface is in a grid convergence behaviour.

Grid	Percentage Error
$25 \times 50 \times 200$	-0.3320
$50 \times 100 \times 400$	-0.0323
$100 \times 200 \times 800$	-0.0076

Table 6.1: Percentage Error on the Initial Burning Surface (STL-GREG)

To conclude the grain burnback analysis, the curves of the Zefiro23 port area, burning perimeter and wet perimeter, along the motor axis and for different web values are shown in the figures 6.8, 6.9 and 6.10, for the aforementioned middle grid dimension ($50 \times 100 \times 400$). The definition of burning and wet perimeter is consistent with the overall burning and wet surface, as equation (6.2) explains.

$$P_{bj} = \frac{S_{bj}}{\Delta x} \qquad P_{wj} = \frac{S_{wj}}{\Delta x} \tag{6.2}$$

This is particularly evident in the rising of the perimeters values in the rear part of the star fins, that gives, as concentrated in one cell for the mesh chosen, a high value of the computed burning perimeter, in a consistent manner with the definition 6.2.

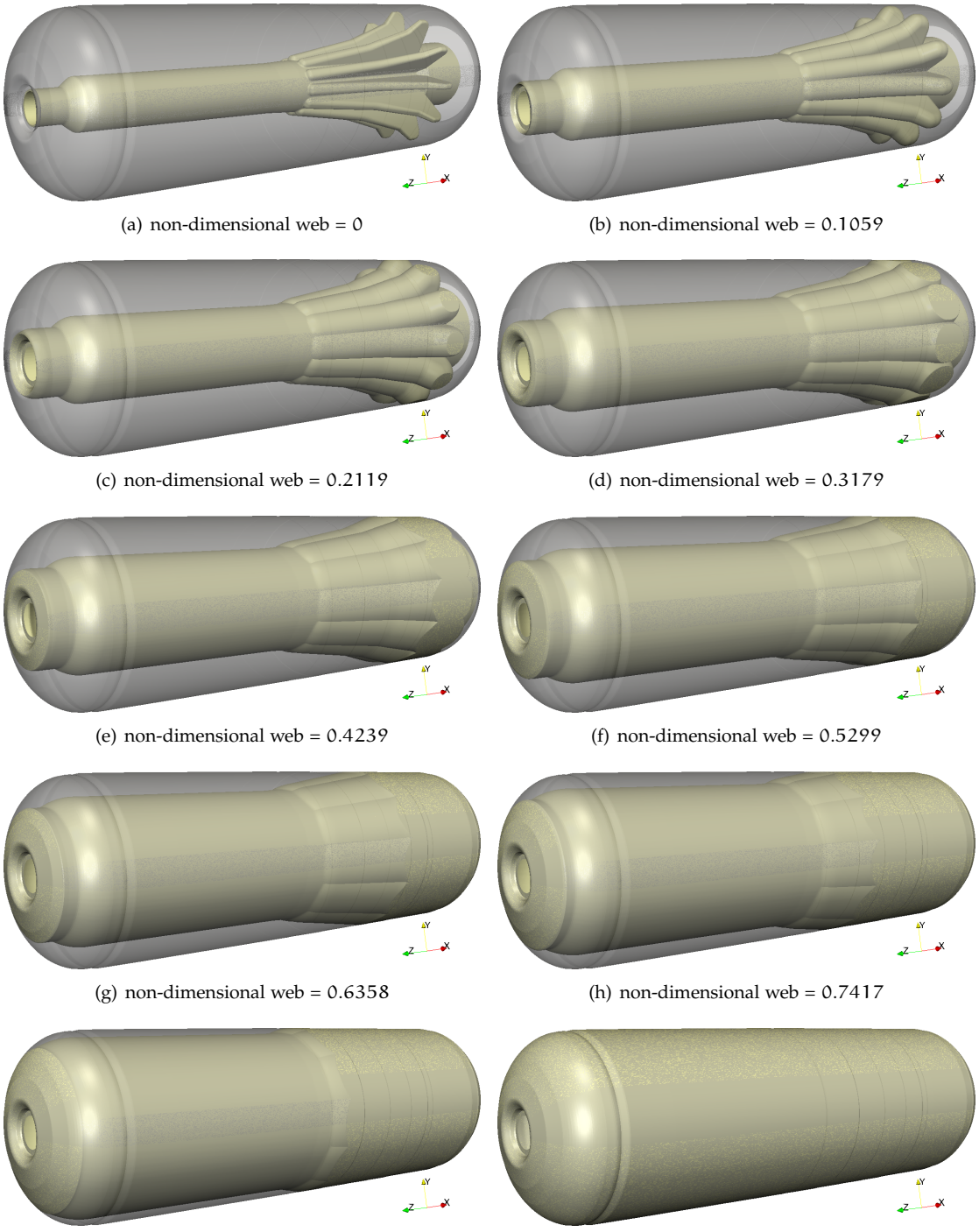

(a) non-dimensional web = 0

(b) non-dimensional web = 0.1059

(c) non-dimensional web = 0.2119

(d) non-dimensional web = 0.3179

(e) non-dimensional web = 0.4239

(f) non-dimensional web = 0.5299

(g) non-dimensional web = 0.6358

(h) non-dimensional web = 0.7417

(i) non-dimensional web = 0.8478

(j) non-dimensional web = 1

Figure 6.4: Z23 grain burning surface evolution

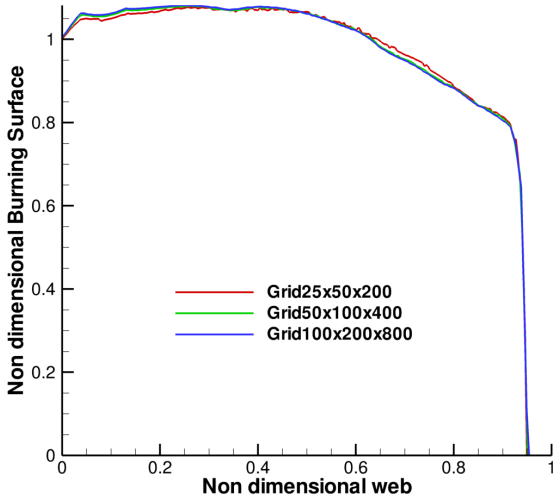

(a) Burning Surface

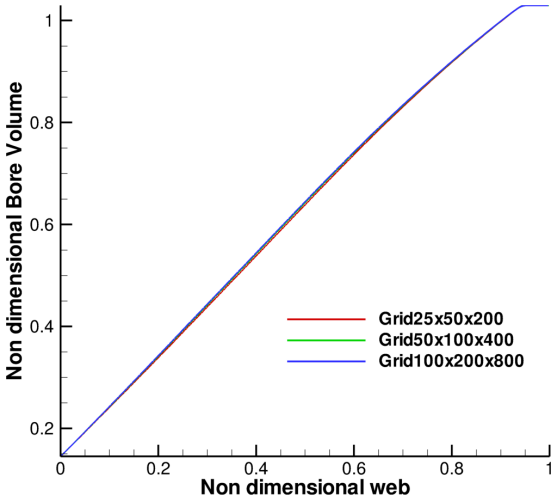

(b) Bore Volume

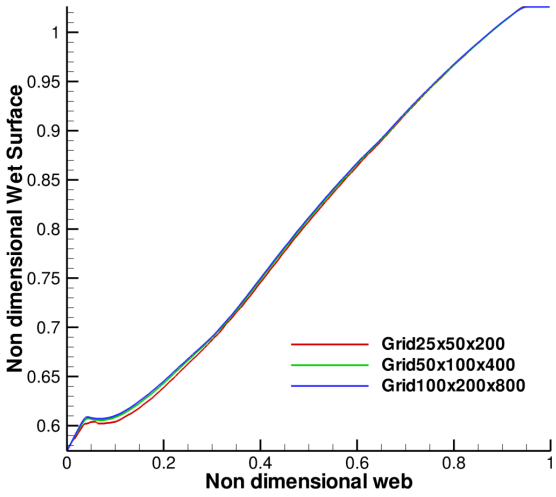

(c) Wet Surface

Figure 6.5: Grid Convergence Analysis for Zefiro23 0D grain geometrical parameters

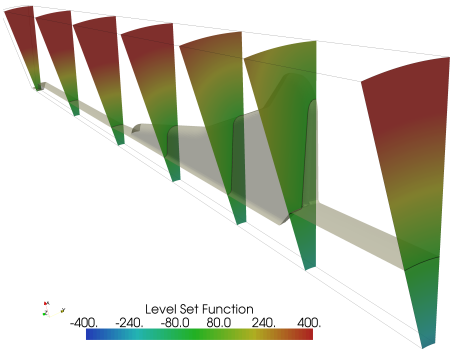

(a) non-dimensional web = 0

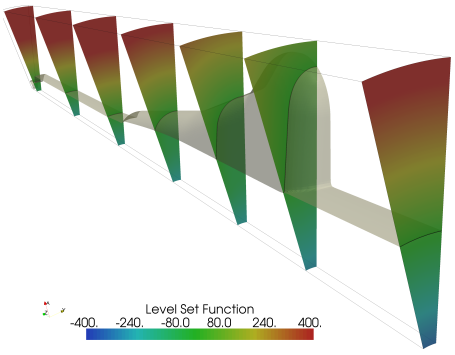

(b) non-dimensional web = 0.1059

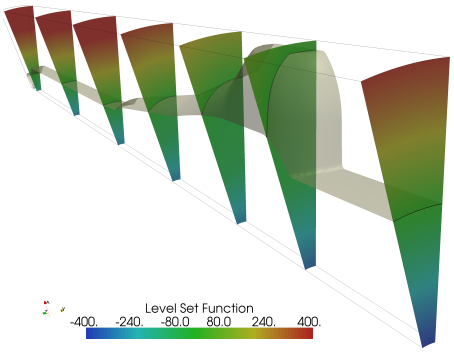

(c) non-dimensional web = 0.2119

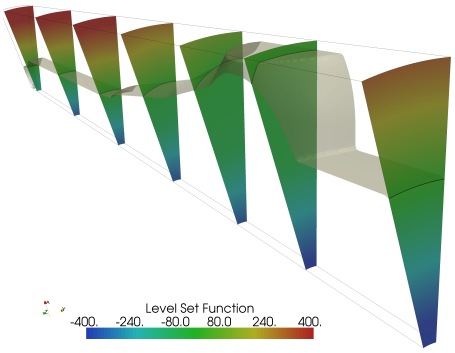

(d) non-dimensional web = 0.3179

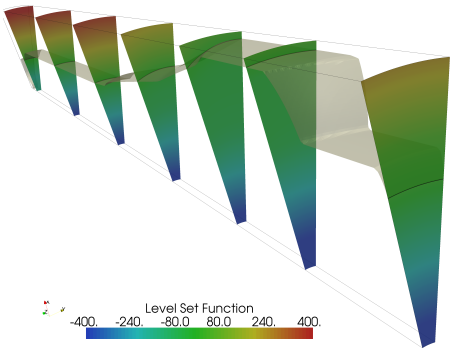

(e) non-dimensional web = 0.4239

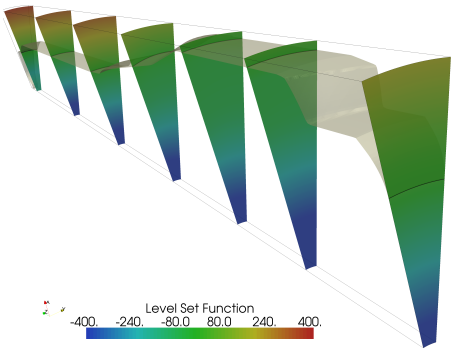

(f) non-dimensional web = 0.5299

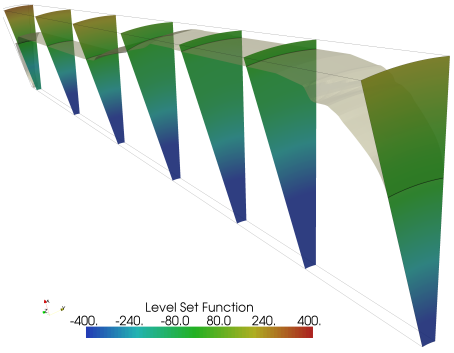

(g) non-dimensional web = 0.6358

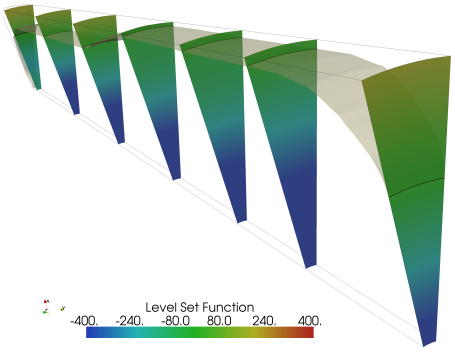

(h) non-dimensional web = 0.7417

Figure 6.6: Z23 Level Set function evolution: axial slices

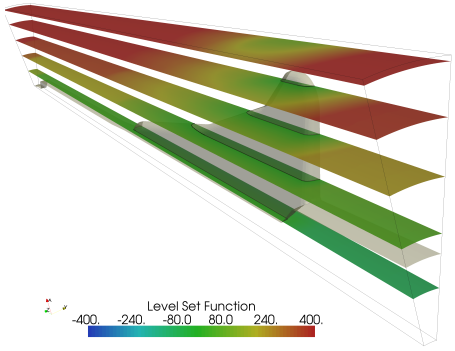

(a) non-dimensional web = 0

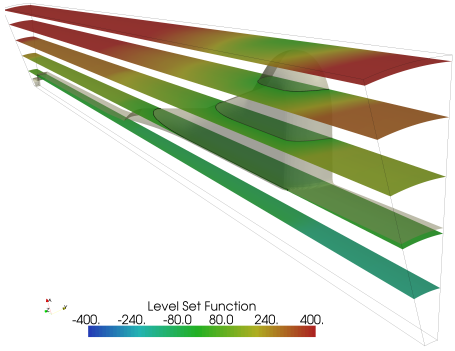

(b) non-dimensional web = 0.1059

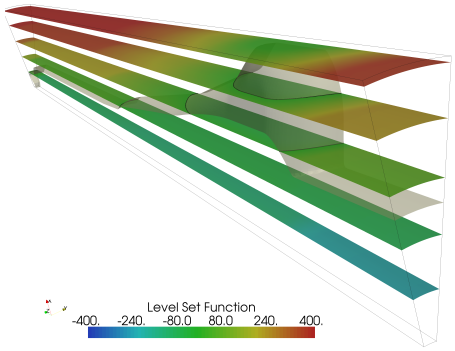

(c) non-dimensional web = 0.2119

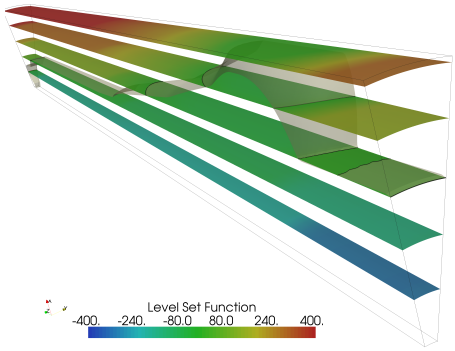

(d) non-dimensional web = 0.3179

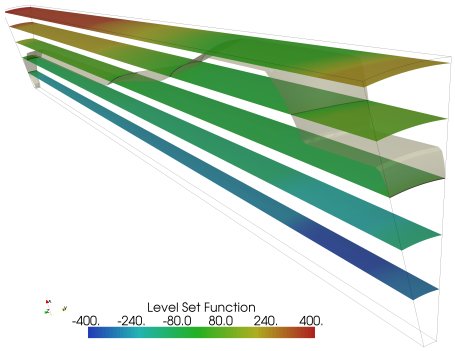

(e) non-dimensional web = 0.4239

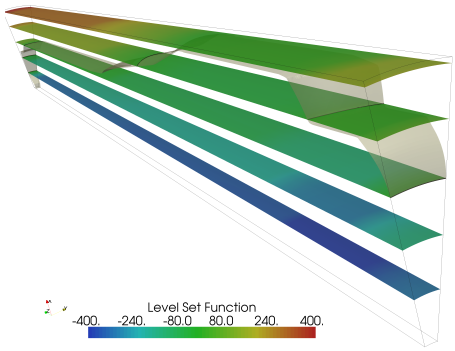

(f) non-dimensional web = 0.5299

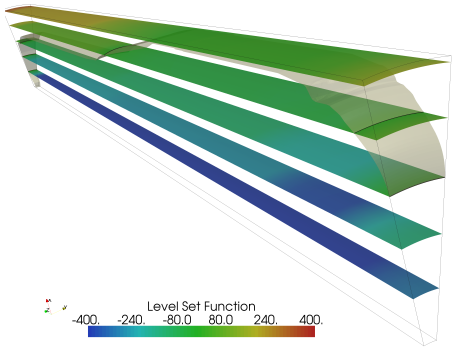

(g) non-dimensional web = 0.6358

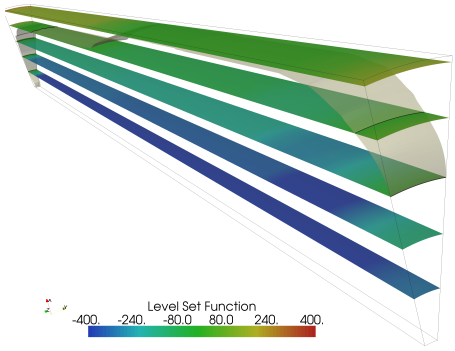

(h) non-dimensional web = 0.7417

Figure 6.7: Z23 Level Set function evolution: radial slices

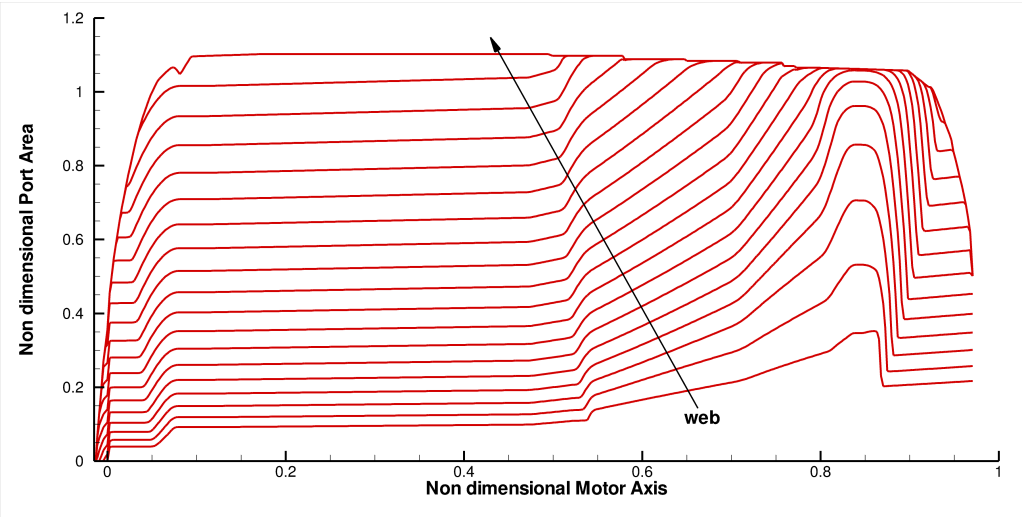

Figure 6.8: Z23 Port Area Evolution in web

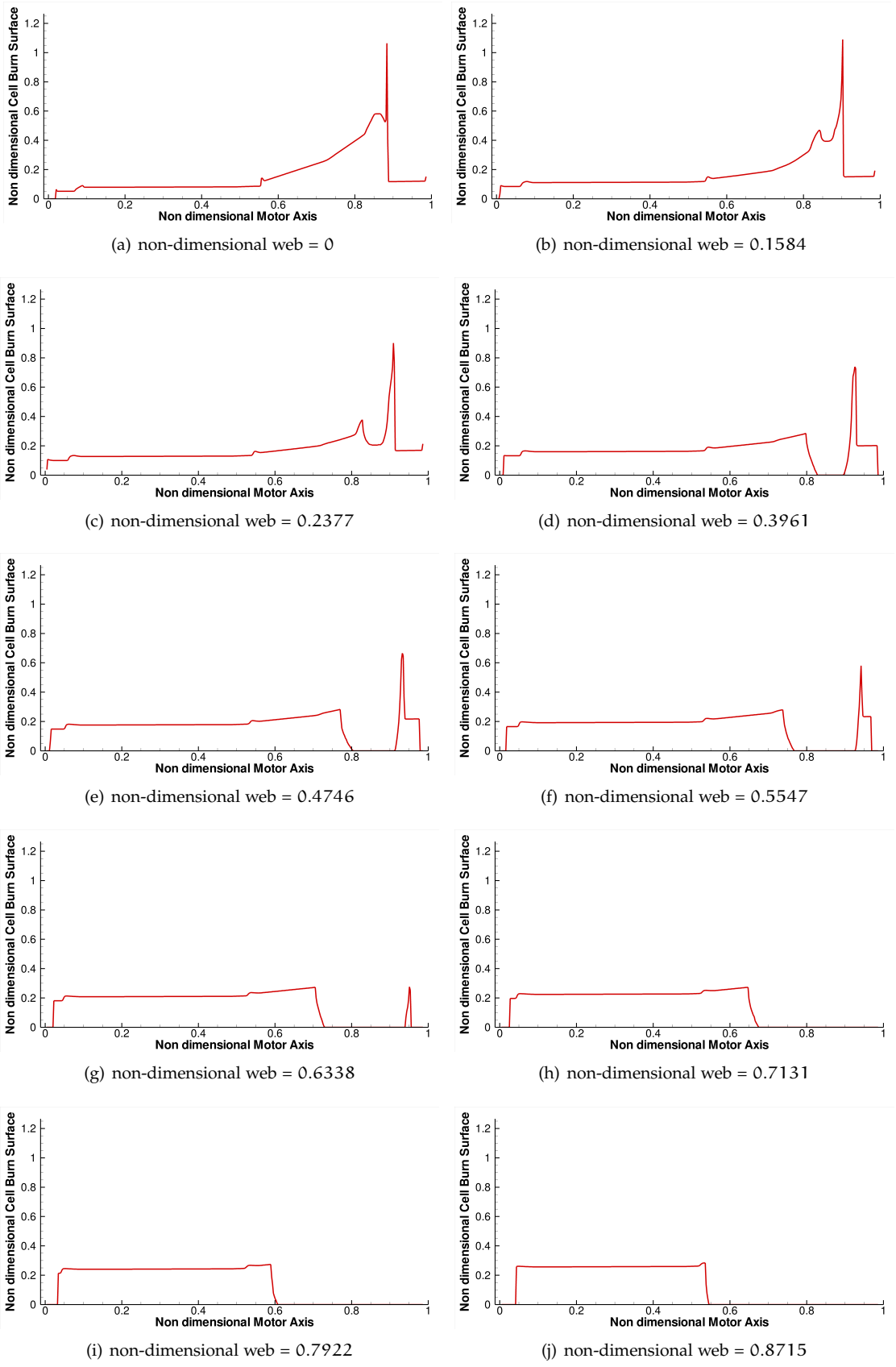

(a) non-dimensional web = 0

(b) non-dimensional web = 0.1584

(c) non-dimensional web = 0.2377

(d) non-dimensional web = 0.3961

(e) non-dimensional web = 0.4746

(f) non-dimensional web = 0.5547

(g) non-dimensional web = 0.6338

(h) non-dimensional web = 0.7131

(i) non-dimensional web = 0.7922

(j) non-dimensional web = 0.8715

Figure 6.9: Z23 cell burning surface evolution

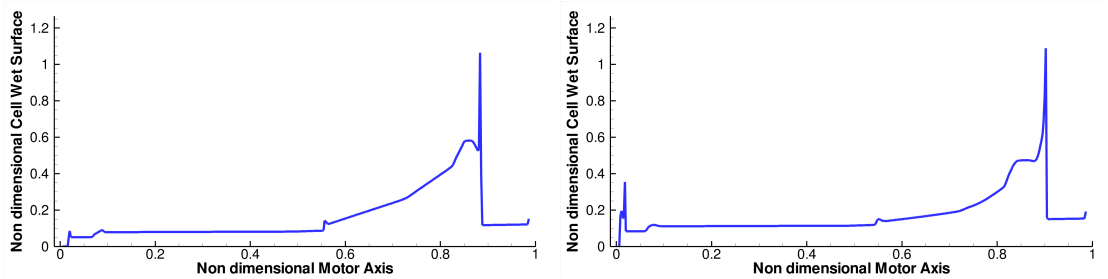

(a) non-dimensional web = 0

(b) non-dimensional web = 0.1584

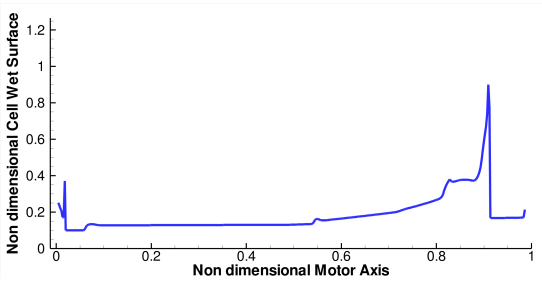

(c) non-dimensional web = 0.2377

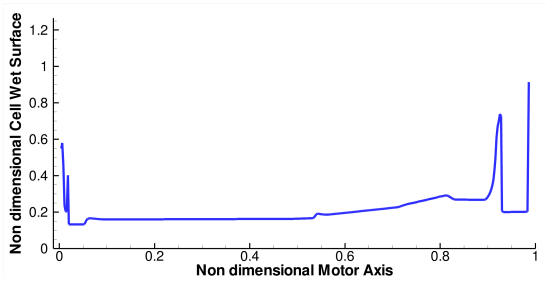

(d) non-dimensional web = 0.3961

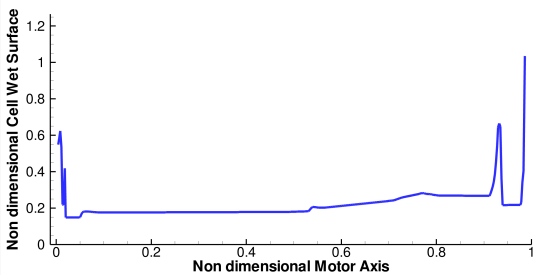

(e) non-dimensional web = 0.4746

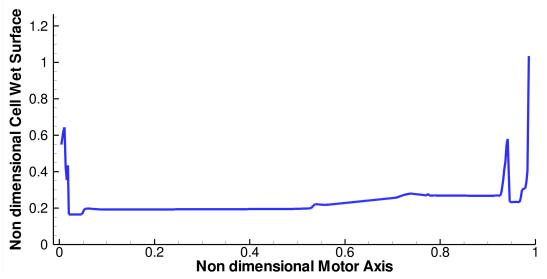

(f) non-dimensional web = 0.5547

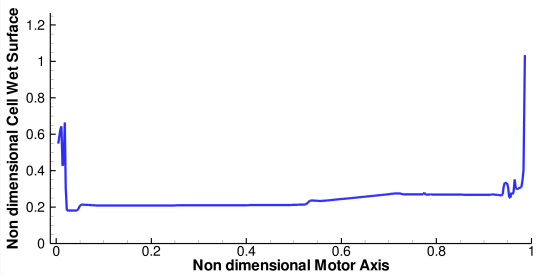

(g) non-dimensional web = 0.6338

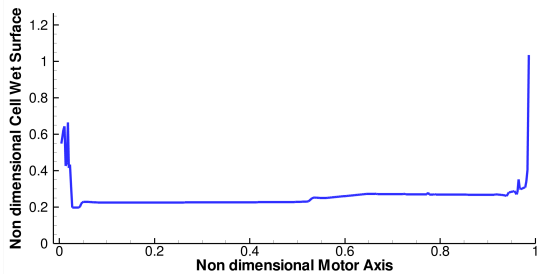

(h) non-dimensional web = 0.7131

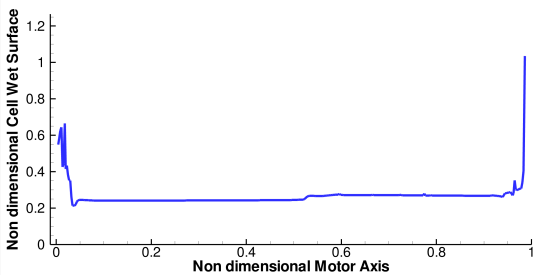

(i) non-dimensional web = 0.7922

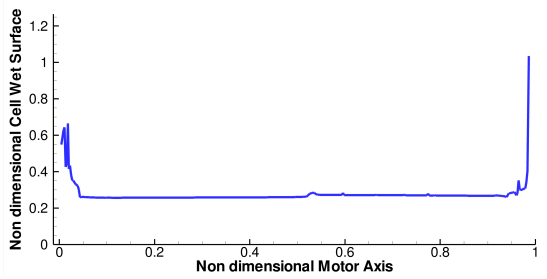

(j) non-dimensional web = 0.8715

Figure 6.10: Z23 cell wet surface evolution

6.2 NAWC Motor n. 6

NAWC tactical motor n. 6 grain burnback is simulated using the GREG model. This motor has been analyzed using the initial motor and grain configuration given in two literature works [107; 64] and reported in the figure 6.11.

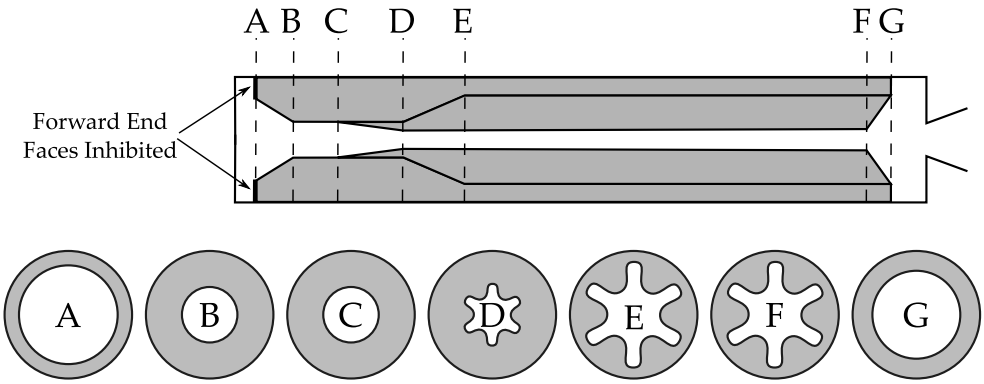

Figure 6.11: NAWC Motor n. 6 geometry

The SRM geometrical data are given in the table 6.2.

Section	x [mm]	w [mm]	R_1 [mm]	R_2 [mm]	R_3 [mm]	R_4 [mm]	η [°]	ξ [°]	n
A	4.826	15.24	48.26	63.5	48.26	–	30	0	6
B	30.226	39.7002	23.7998	63.5	23.7998	–	30	0	6
C	146.812	39.8272	23.6728	63.5	23.6728	–	30	0	6
D	299.212	39.8272	15.6972	63.5	23.6728	4.8768	30	0	6
E	375.412	28.2702	15.6972	63.5	34.7218	4.8768	30	0	6
F	1670.812	27.559	15.748	63.5	35.941	4.9276	30	0	6
G	1696.212	27.559	35.941	63.5	35.941	–	30	0	6

Table 6.2: NAWC Motor n. 6 Geometrical Data

The geometrical entities necessary to define the section star-shaped configuration of the finocyl grain are defined in the figure 6.12, with the classical seven stars parameters: n number of star points (6), R_2 grain outside radius, R_4 cusp radius, R fillet radius, w web thickness, ξ star angle and η star point semi-angle (in the table 6.2 in the figure 6.12 are also given some others parameters given present in the original references to characterize the SRM grain geometrical configuration).

The forward end faces of the grain propellant have been inhibited in order to allow the pulsers and the instrumentation to be open to the chamber at all times. The throat diameter for NAWC Motor n. 6 is $D_t = 46.736$mm.

The grain shape is a finocyl grain with a high length-to-diameter ratio, of about 15 (SRM length is about 1.8 meters and the case diameter about 0.12 meters), and with a low port-to-throat area ratio. The 3D representation of the SRM grain propellant shape is given in the figure 6.13.

The STL file of the grain initial surface is defined by about 4000 triangles in the unstructured tessellation of the grain finocyl shape. From this representation of the grain shape, the Level Set IC is built as a Signed Distance Function, using the technique presented in the

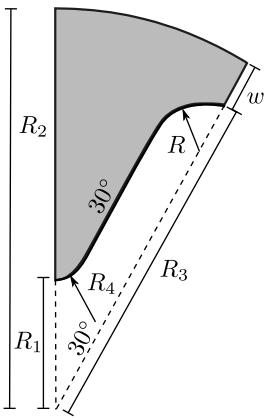

Figure 6.12: Star 2D parameters definition

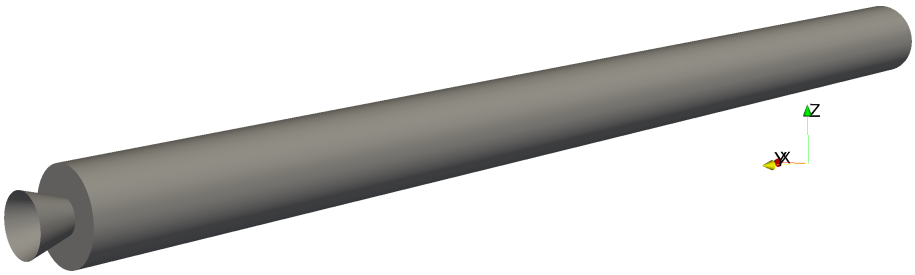

(a) Case

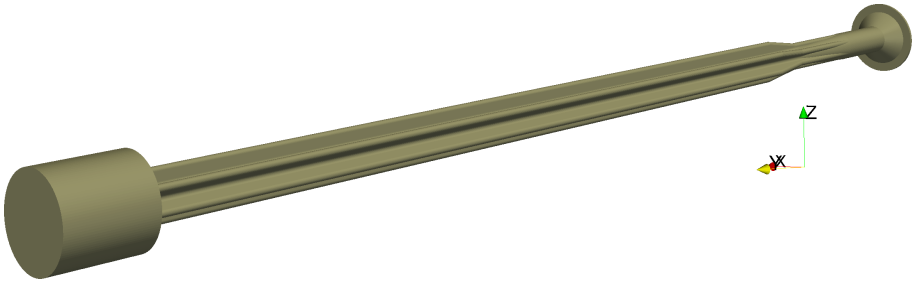

(b) Mandrel

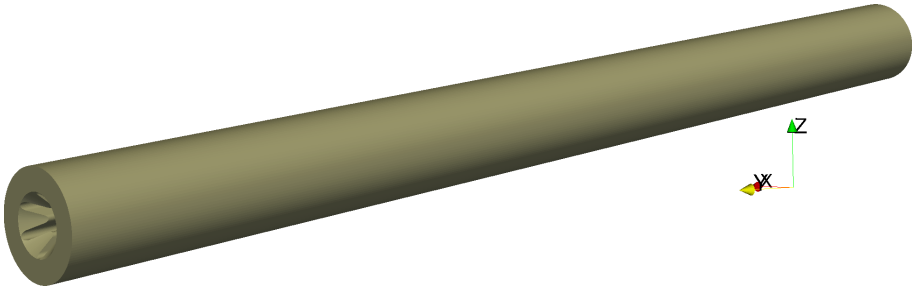

(c) Grain

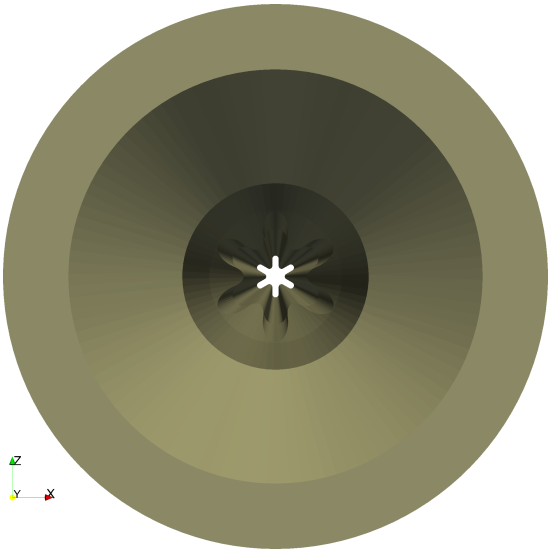

(d) Grain Forward View

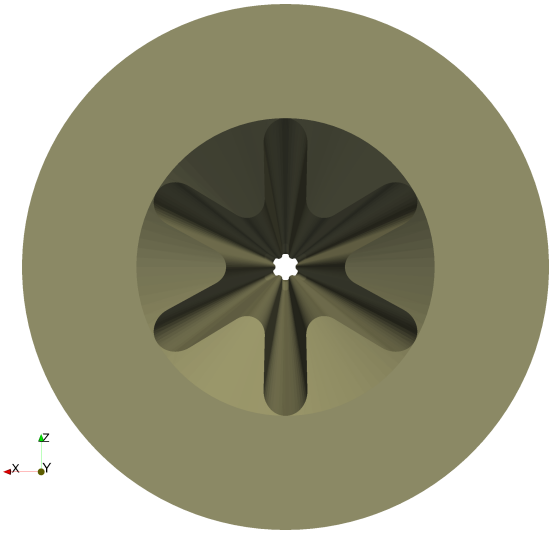

(e) Grain After View

Figure 6.13: NAWC Motor n.6 Motor Geometry

paragraph 3.6.1, page 55. The case surface is, instead, simply defined by a cylindrical shape. Hence, it is initialized as an implicit grid function in a very straightforward manner as SDF, through its analytical representation (see equation 6.3).

$$\phi_c(r, \theta, z) = \phi_c(r) = r - R_{case} \tag{6.3}$$

In the figure 6.14 the Initial Condition for the Level Set solution of the grain burnback is shown, in which again the star symmetry is exploited in order to limit the computational cost required for the same grid spatial discretization. Hence, mirroring BCs are imposed along the azimuthal directions 0° and 30°, while for the other boundaries, extrapolation BCs are defined.

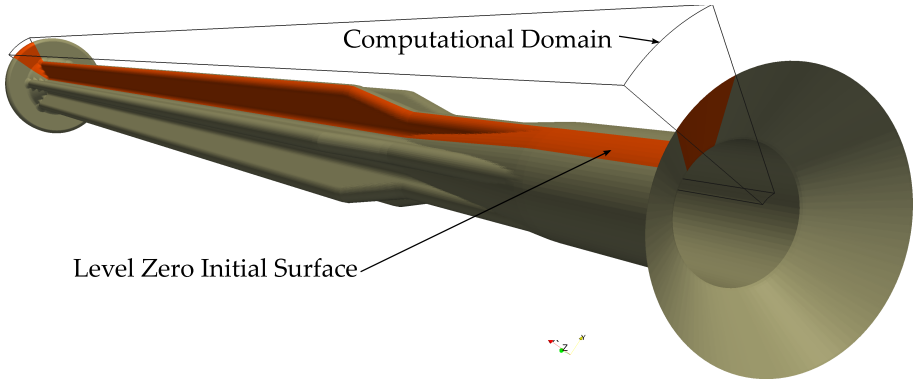

Figure 6.14: NAWC Motor n. 6 Level Set Initial Grain surface representation

As made in the paragraph 6.1, page 102 for Zefiro 23, a convergence analysis has been made to check the results sensitivity to mesh refinements, on both the Initial Condition and the computed solution, in terms of integral parameters[3]. In the table 6.3, the percentage error of the STL file and the computed Level zero grain shape burning surface is shown as given by the equation 6.1. It points out a higher sensitivity to the mesh resolution along the motor axis, as expected for the aspect ratio of the SRM than along the others directions (in particular along the radial direction). This is underlined in the table 6.3, comparing the percentage error for the $100 \times 200 \times 400$ meshgrid with respect to the $50 \times 100 \times 800$ meshgrid.

Grid	Percentage Error
$10 \times 25 \times 50$	-1.9210
$25 \times 50 \times 100$	-0.8116
$50 \times 100 \times 200$	-0.4385
$50 \times 100 \times 400$	-0.2820
$100 \times 200 \times 400$	-0.2220
$50 \times 100 \times 800$	-0.1808

Table 6.3: Percentage Error on the Initial Burning Surface (STL-GREG)

For this SRM a code-to-code comparison is also possible. In fact, the NAWC Motor n. 6 grain burnback has been made also in [107], and the results are given in terms of the 0D grain geometrical parameters, grain burning surface and bore volume. In [107], the authors consider a grain burning surface evolution with time and space constant burning rate too, with a different method to accomplish the 3D grain evolution. In fact, they exploit the fact that, in the case of a uniform constant burning rate assumption, the solution of the problem, as underlined in the paragraph 3.8, page 60, is known analytically. This is given by the SDF from the front, that however, must be constructed in a numerical manner. They use the STL 3D surfaces representation to built up the SDF in a rectangular computational grid, with a technique to which the

3 we remember that the first number defines the number of cells along the azimuthal direction, the second, along the radial direction and the third, along the motor axis from head to nozzle throat section

initialization technique for defining the GREG Initial Condition has been inspired, with some modifications. The results of the burning surface grid convergence are drawn out in the figure 6.15, where at the right plot the comparison with Rocgrain[107] is also presented.

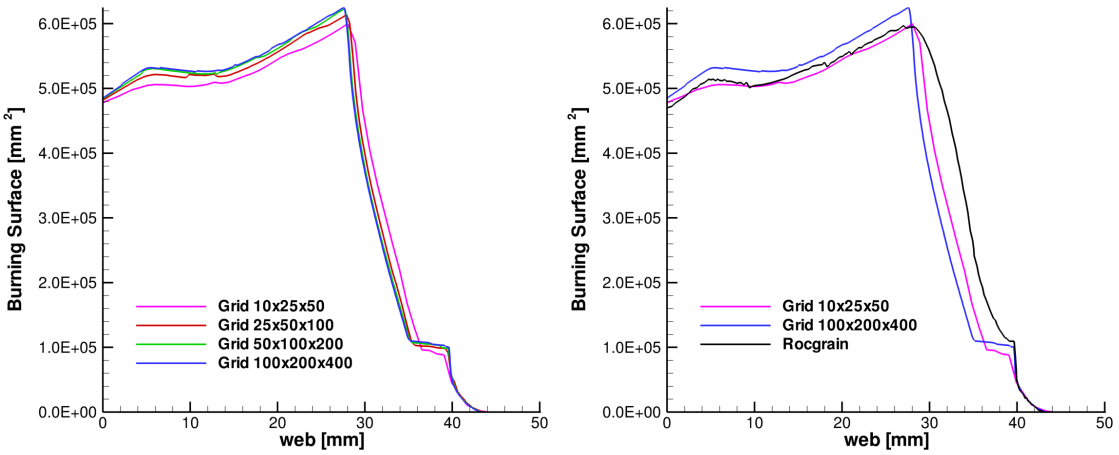

(a) Grid Convergence for the Burning Surface

(b) Comparison with Rocgrain code[107]

Figure 6.15: Burning Surface Grid convergence analysis and comparison with Rocgrain code

As in the case of Zefiro 23, a global grid convergence behaviour can be underlined. In fact, as the meshgrid is refined, the burning surface in web plot leans toward the last refined grid. For the comparison with the Rocgrain[107] code instead, an accordance between the GREG model and the Rocgrain one is shown, especially in the last part of the two curves. While in the rest the accordance is not so good, if not in a global trend. Unfortunately, it is not possible to argue the reasons for that differences, because there are not enough details in [107] to understand what Cartesian rectangular grid dimensions have been chosen to produce the results published. Notwithstanding, considering the wider grid $10 \times 25 \times 50$, we see a similar behaviour in the first part. In the same time, a different initial value (lower for Rocgrain) for the grain burning surface is also shown. This can be due to two different reasons: a different CAD model for the initial grain[4] and/or a discrepancy between the STL grain surface model and the grid dependent grain representation, in terms of grid function. In all cases, we remark that the GREG representation of the initial surface is enough accurate (see table 6.3) and the confidence on the computed results can be given by the good results of the convergence analysis performed.

The bore volume (combustion chamber volume) evolution in the web variable is shown in the figure 6.16, where the left plot represents the grid convergence analysis for the same computational grid shown before While the right plot is the comparison with the Rocgrain code[107].

Moreover, it is possible to underline that the initial and final values for the combustion chamber volume seem to be underestimated by Rocgrain with respect to GREG code. While the slopes of the curves are quite near considering the wider grid for GREG[5]. The same remarks made before are still valid. Hence, the global behaviour of the two curves is quite similar, but since no details of the computational grid used in [107] is presented, whatever deepened analysis cannot be made.

Two last remarks are however possible. The use of a rectangular grid cannot preserve at all the grain periodicity during its evolution (or its sliding in the web variable, see equation 3.89, page 60), with some effects on the 3D evolution computed that are greater the wider is the computational mesh considered. The use of cylindrical coordinates for the problem discretization, instead, as GREG does, allows to consider computational meshes that are very thick if compared to rectangular grids. For the latter, in fact, all the 360° must be discretized, while instead in the

4 the authors in [107] used Pro-E software

5 this is not surprising, considering that the derivative of the volume bore evolution is just the burning surface evolution

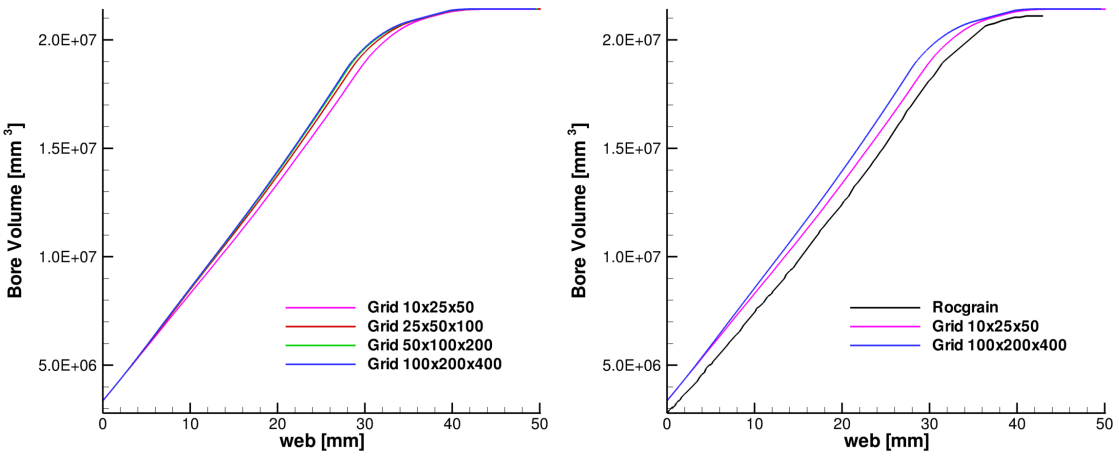

(a) Grid Convergence for the Bore Volume

(b) Comparison with Rocgrain code[107]

Figure 6.16: Bore Volume Grid convergence analysis and comparison with Rocgrain code

case of cylindrical meshgrids, appropriate mirroring Boundary Conditions can be imposed to solve the problem[6].

However, also the bore volume integral for the GREG code shows a convergence regularity, as the meshgrid is refined. Moreover, we underline that as the grain goes to burn out, the volume for the different computational meshes tends to approximate the case cylinder volume (the case shape for NAWC Motor n. 6), as expected. The spatial accuracy obtained for this value, as proved in the paragraph 5.3, page 94, is second order. The grid convergence is also shown in the figure 6.17 for the wet surface, pointing out a regular behaviour in terms of convergence and the known second order of spatial accuracy of the technique for evaluating areas, perimeters and volumes, as the grain is totally consumed.

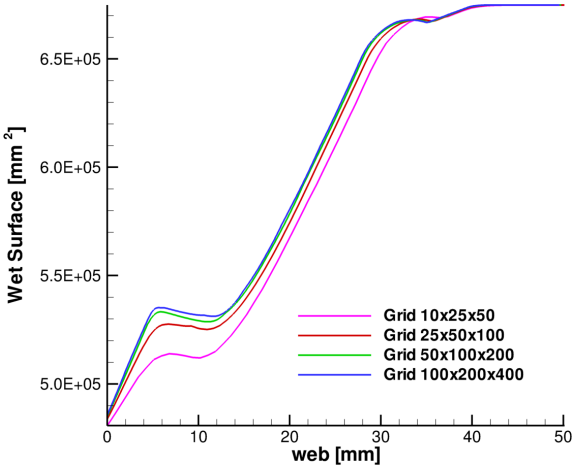

Figure 6.17: Wet Surface Grid convergence analysis

In the figures 6.18, 6.19 and 6.20, the evolution of the Q1D grain geometrical pointwise parameters: port area, burning perimeter and wet perimeter is shown for the middle grid $50 \times 100 \times 200$.

The 3D visualizations of the NAWC Motor n. 6 grain burning surface evolution are shown in the figures 6.21 and 6.22. Whereas, in the figure 6.23, some plots of the grid function evolution in web are drawn out.

6 for example the last meshgrid in cylindrical coordinates is $100 \times 200 \times 400$; it "corresponds", if a correspondence can be made, to at least a $1200 \times 200 \times 400$ meshgrid in rectangular coordinates

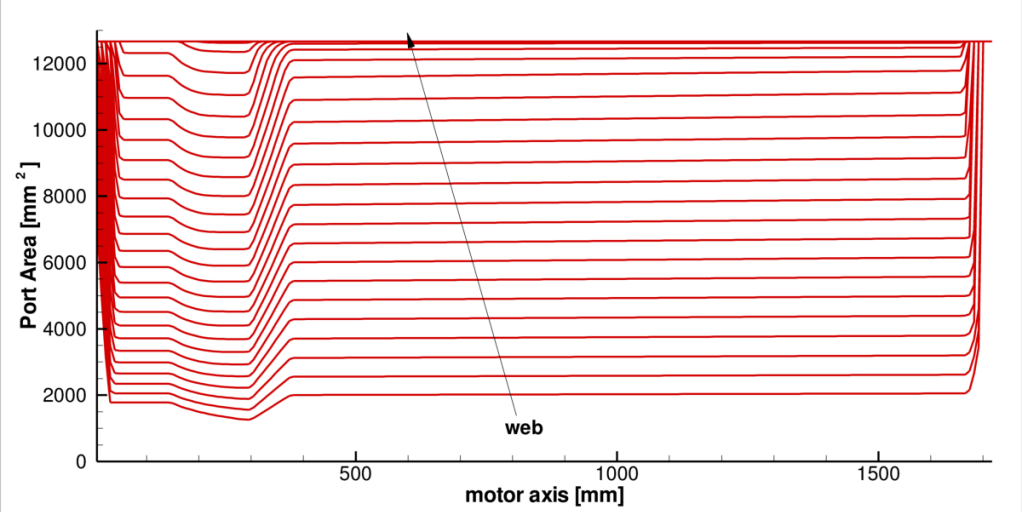

Figure 6.18: NAWC Motor n. 6 Port Area evolution in web

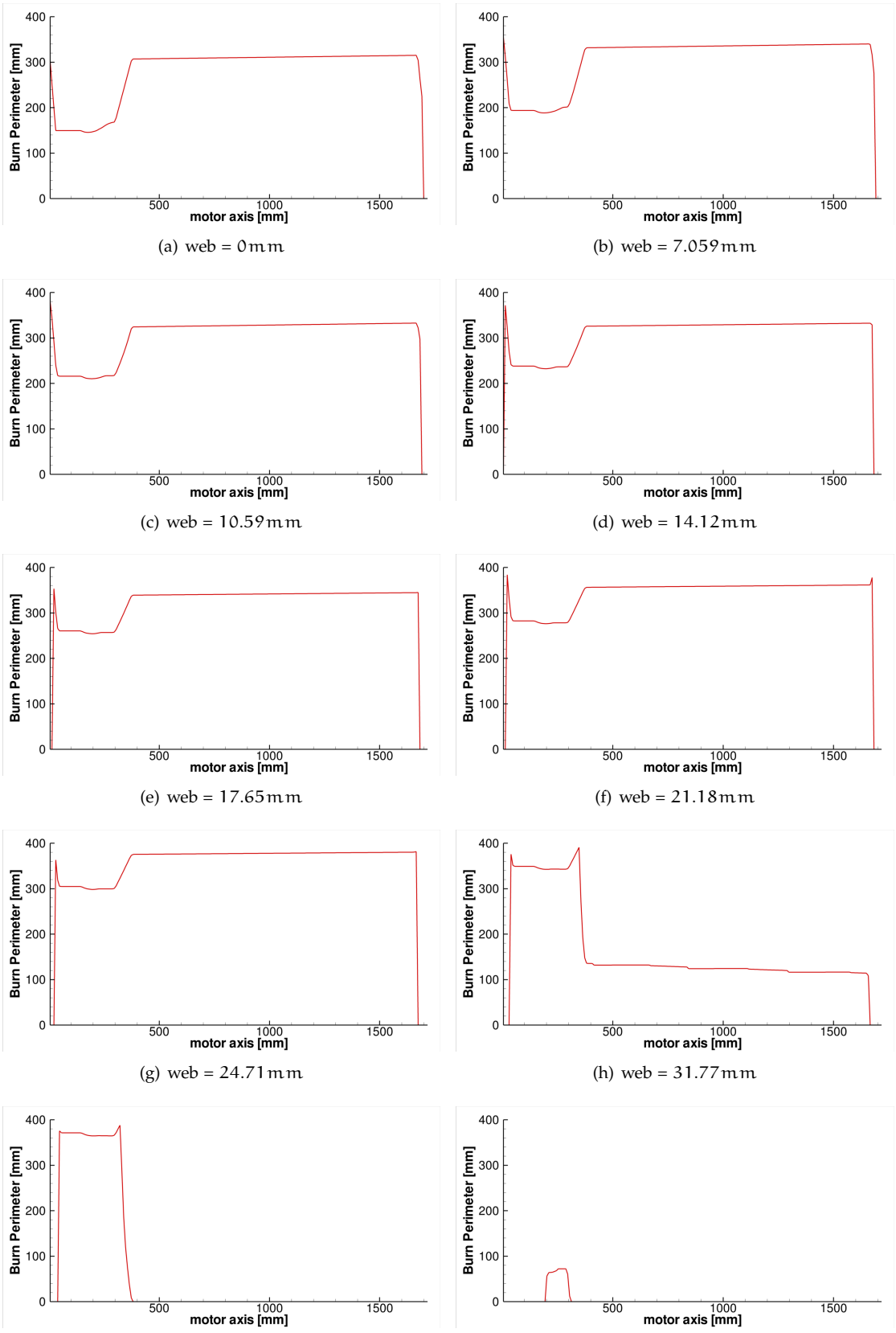

(a) web = 0mm

(b) web = 7.059mm

(c) web = 10.59mm

(d) web = 14.12mm

(e) web = 17.65mm

(f) web = 21.18mm

(g) web = 24.71mm

(h) web = 31.77mm

(i) web = 35.30mm

(j) web = 42.36mm

Figure 6.19: NAWC Motor n. 6 burning perimeter evolution

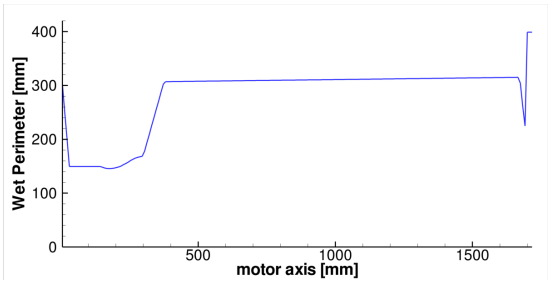

(a) web = 0

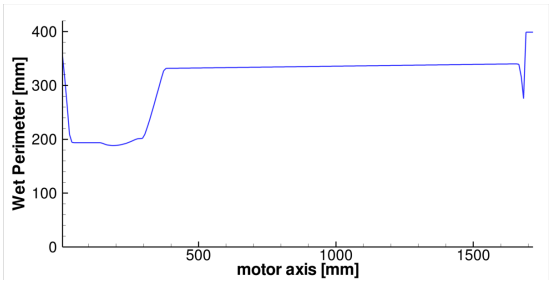

(b) web = 7.059mm

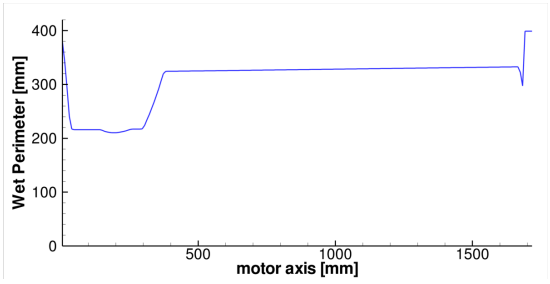

(c) web = 10.59mm

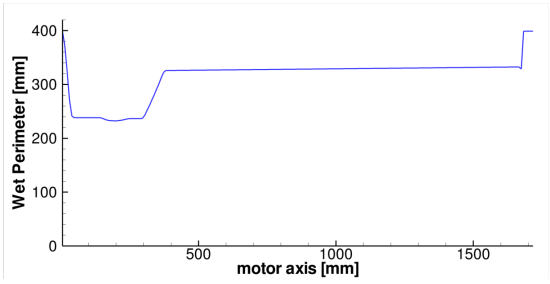

(d) web = 14.12mm

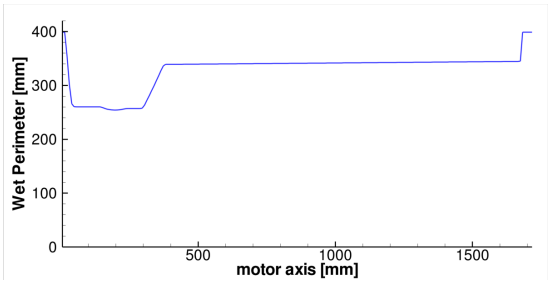

(e) web = 17.65mm

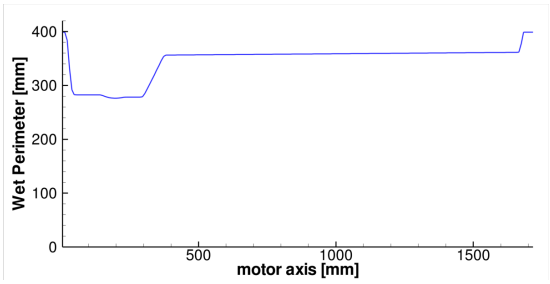

(f) web = 21.18mm

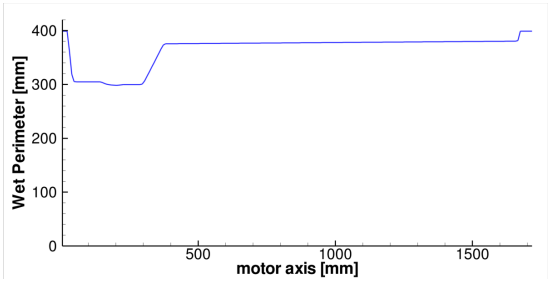

(g) web = 24.71mm

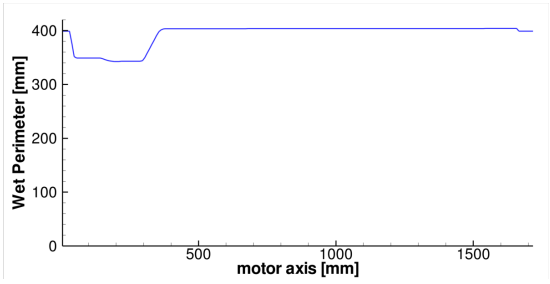

(h) web = 31.77mm

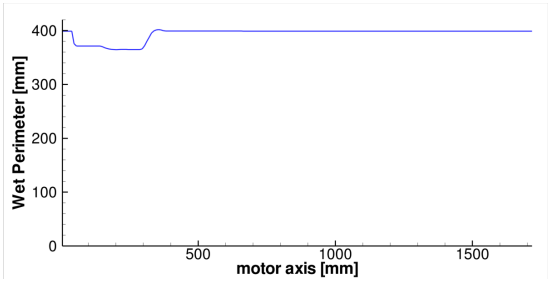

(i) web = 35.30mm

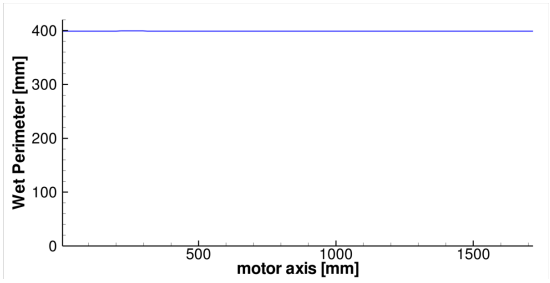

(j) web = 42.36mm

Figure 6.20: NAWC Motor n. 6 wet perimeter evolution

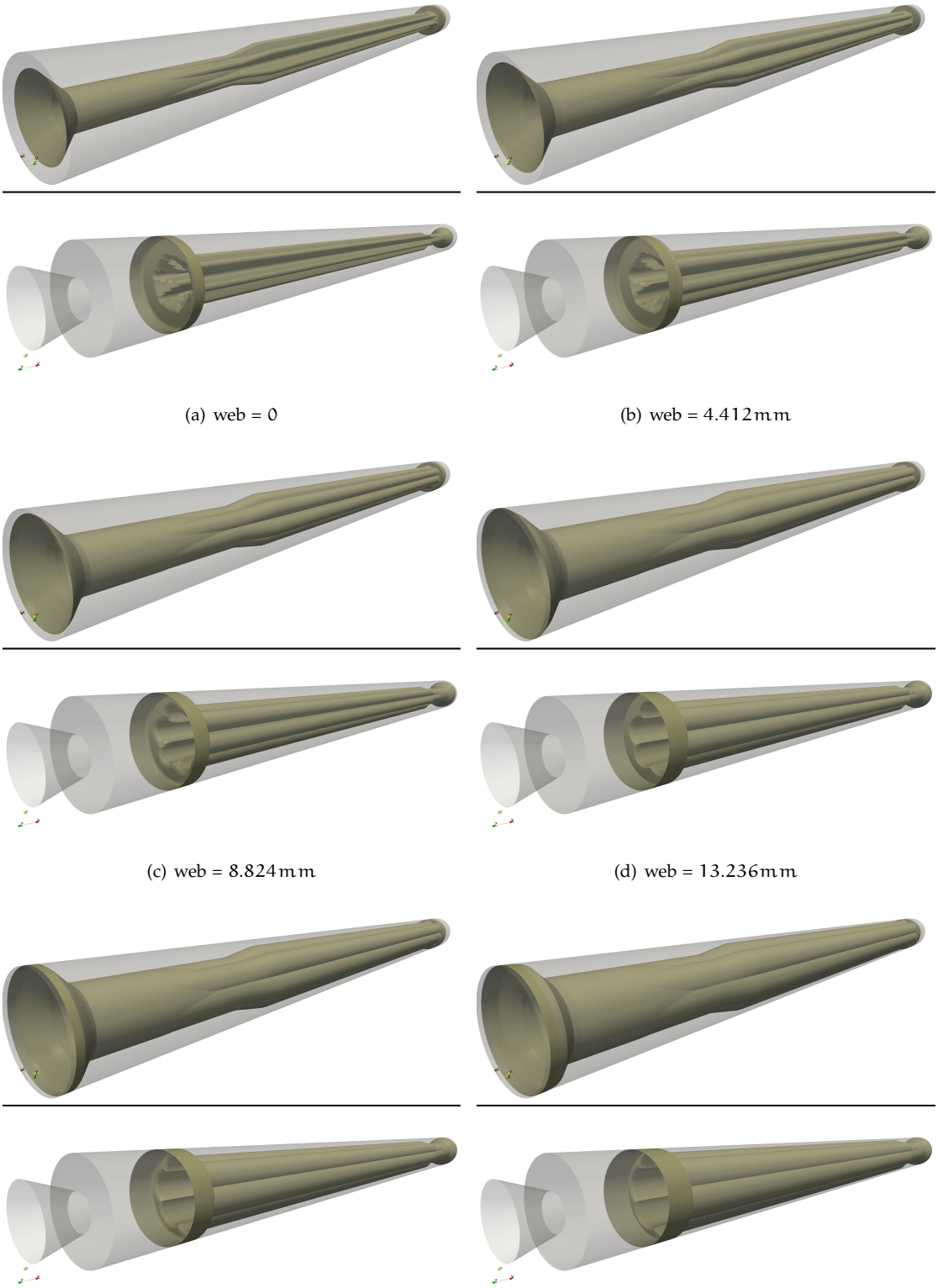

(a) web = 0

(b) web = 4.412mm

(c) web = 8.824mm

(d) web = 13.236mm

(e) web = 17.648mm

(f) web = 22.060mm

Figure 6.21: NAWC Motor n. 6 grain burning surface evolution

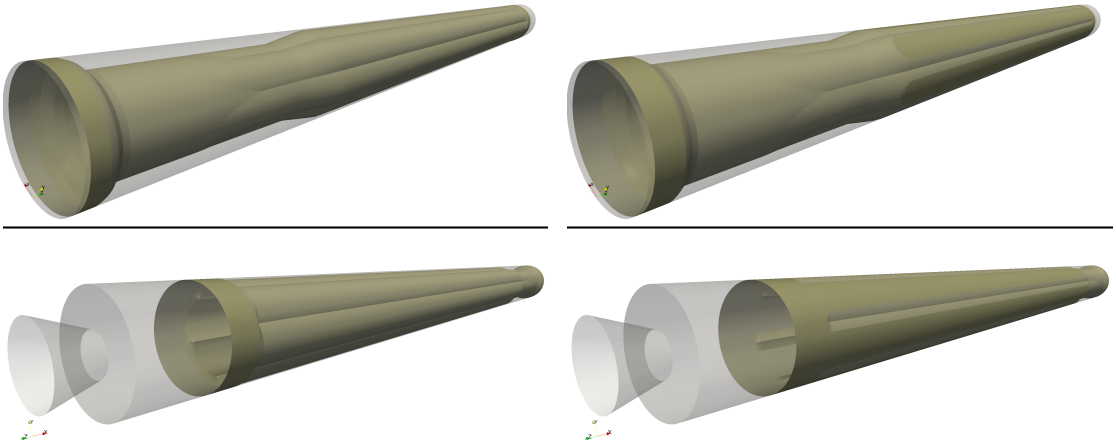

(g) web = 26.472mm

(h) web = 30.884mm

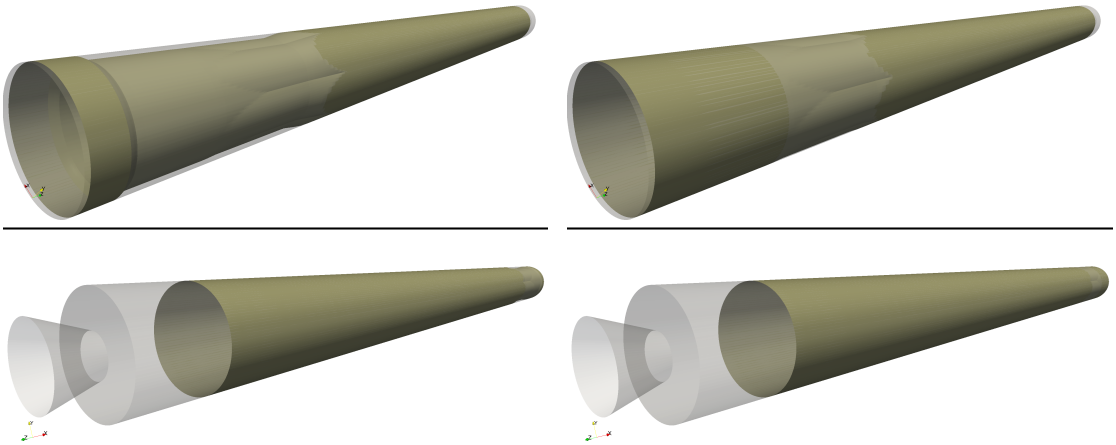

(i) web = 35.296mm

(j) web = 39.708mm

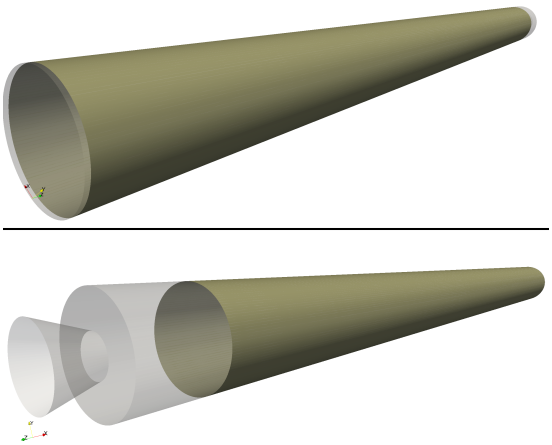

(k) web = 44.120mm

Figure 6.22: NAWC Motor n. 6 grain burning surface evolution (cont.)

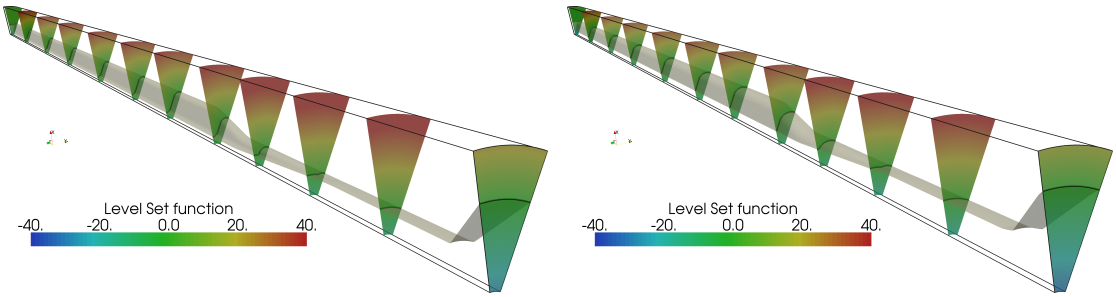

(a) web = 0mm

(b) web = 4.412mm

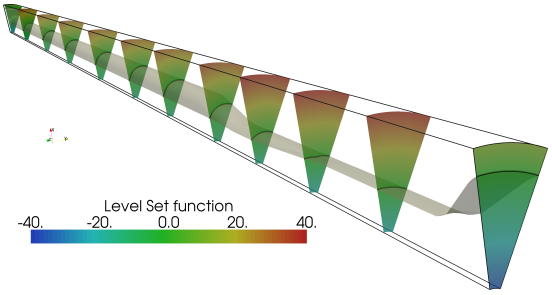

(c) web = 8.824mm

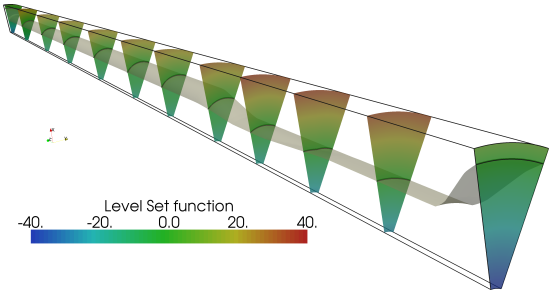

(d) web = 13.236mm

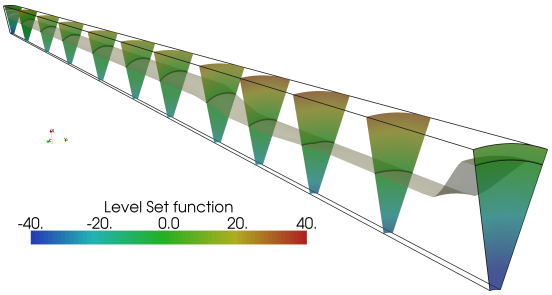

(e) web = 17.648mm

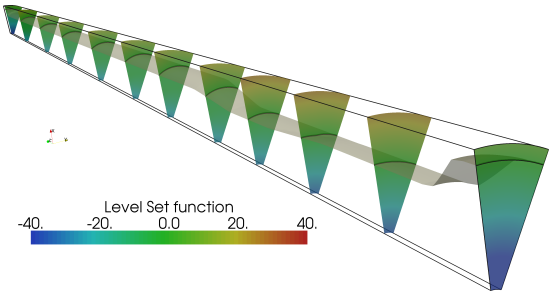

(f) web = 22.060mm

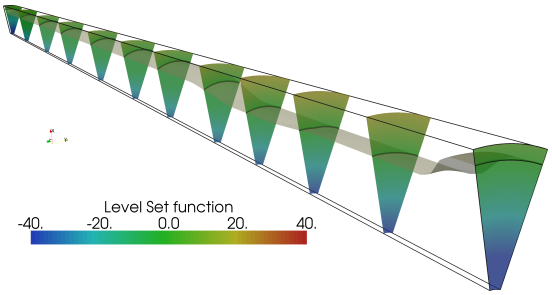

(g) web = 26.472mm

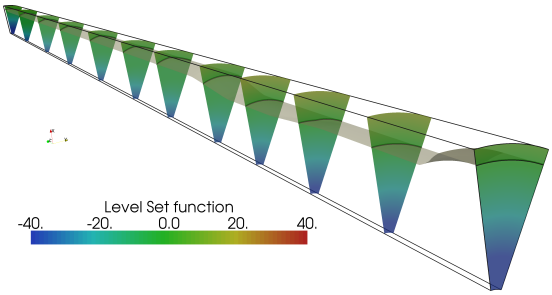

(h) web = 30.884mm

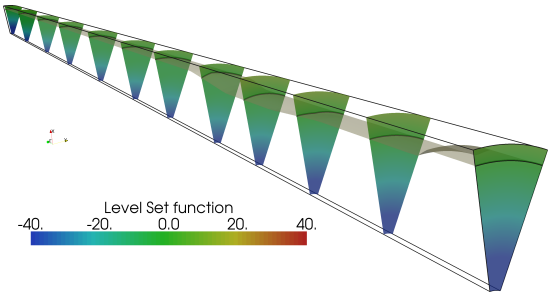

(i) web = 35.296mm

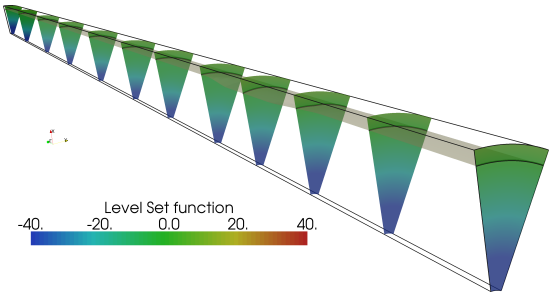

(j) web = 39.708mm

Figure 6.23: NAWC Motor n. 6 Level Set function evolution

6.3 NAWC Motor n. 13

The same analysis performed for Zefiro 23 and NAWC Motor n. 6 is performed also for NAWC Motor n. 13, for which the geometrical data are reported in literature [108]. The NAWC Motor n. 13 has a simple conical shape of the grain propellant and a very simple cylindrical case, as shown in the figure 6.24. The coordinates of the tagged points in the figure 6.24, necessary for the definition of the grain profile are given in the table 6.4. The nozzle throat has a diameter of 26.416 mm and the case, a diameter of 121.92 mm, while the SRM is length about 860 mm. NAWC Motor n. 13 3D view is drawn out in the figure 6.25.

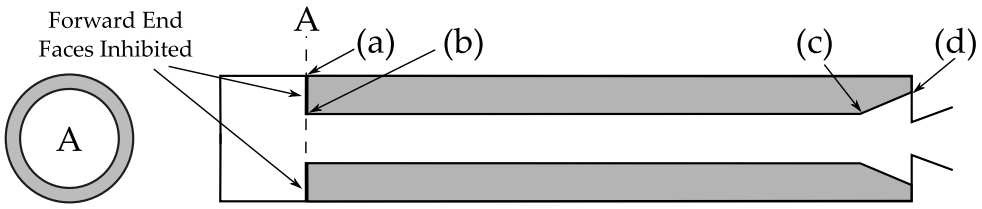

Figure 6.24: NAWC Motor n. 6 geometry

Point	motor axis abscissa [mm]	Radius [mm]
(a)	152.4	60.96
(b)	152.4	38.1
(c)	809.498	38.1
(d)	850.392	46.5582

Table 6.4: NAWC Motor n. 6 geometry data

Hence, the grain and case grid functions are initialized as 2D SDF in the plane rx in cylindrical coordinates. As the problem is axisymmetric, the solution in easily computed in a 2D fashion, with very low computational cost (see figure 6.26).

The same analyses performed for the previous SRMs have been made in terms of: convergence to the analytical initial burning surface for a mesh refinement process (see table 6.5) and convergence behaviour of the 0D grain integral parameters (see figure 6.27).

Grid	Percentage Error
25×50	0.38082646
50×100	0.06104255
100×200	0.00667573
200×400	0.00006648

Table 6.5: Percentage Error on the Initial Burning Surface (analytical-GREG)

The convergence of the initial burning surface is due only to the way in which the meshgrid dependent Level Set function of the conical shape is representing the connection between the starting grain cylinder-cone shape. In fact, no efforts have been done in order to position a mesh node of the connection itself, as it will move during the front evolution.

For the 0D geometrical parameters grid convergence, we remark a grid dependent effect on the computed burning surface due to the on-off selection of a grid grain surface with respect to the grain and case surface, as defined in the paragraph 3.11.2, page 76. This effect, in fact, is less evident as the computational grid is refined. Certainly a more refined and smooth evaluation of the grain surface from the grain and case level set functions, can reduce this grid effect, that however is very limited enhancing the mesh points number. This case is particularly prone to this effect because of the fact that the combustion surface evolution is nearly parallel to the coor-

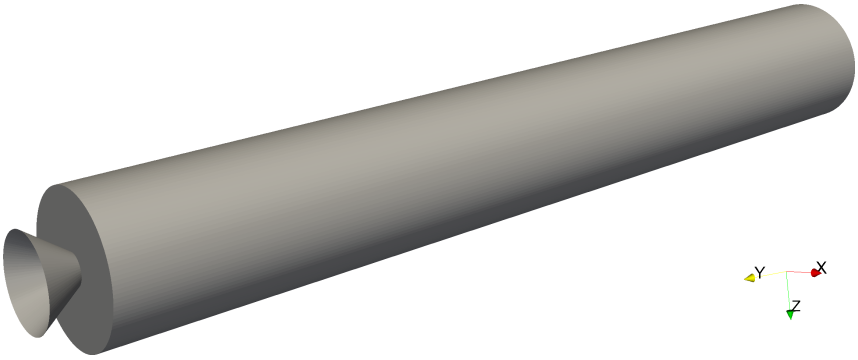

(a) Case

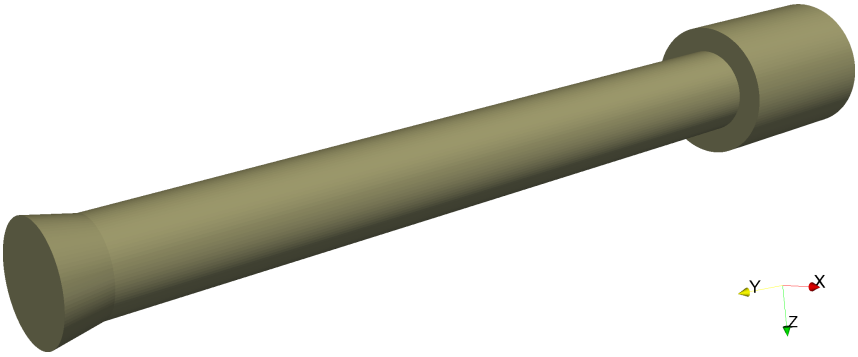

(b) Mandrel

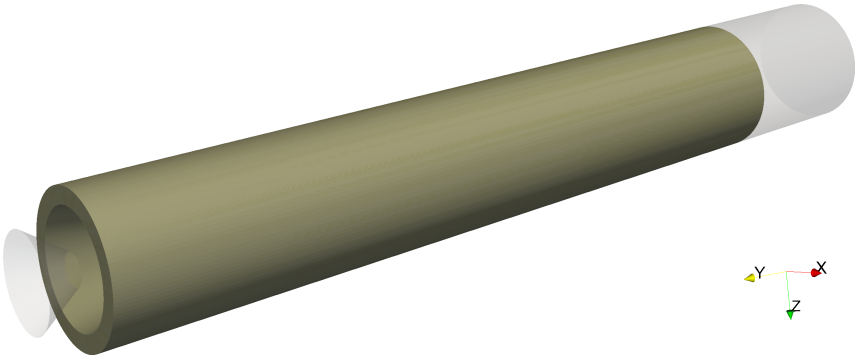

(c) Grain

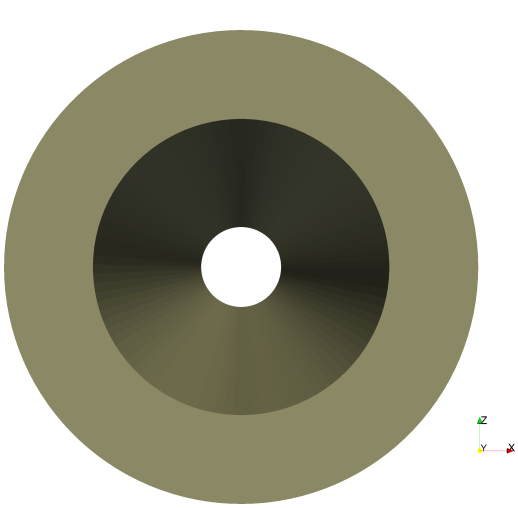

(d) Grain Forward View

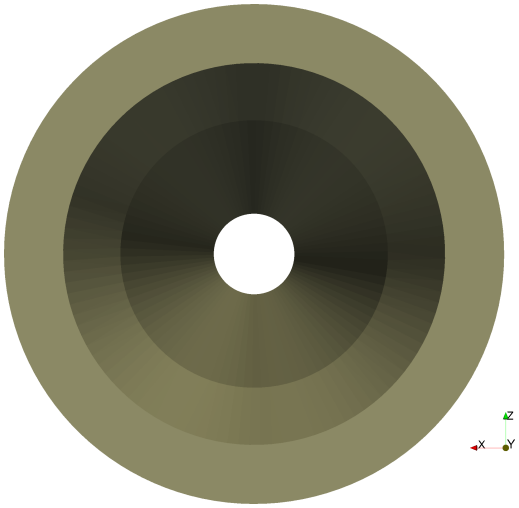

(e) Grain After View

Figure 6.25: NAWC Motor n.13 Motor Geometry

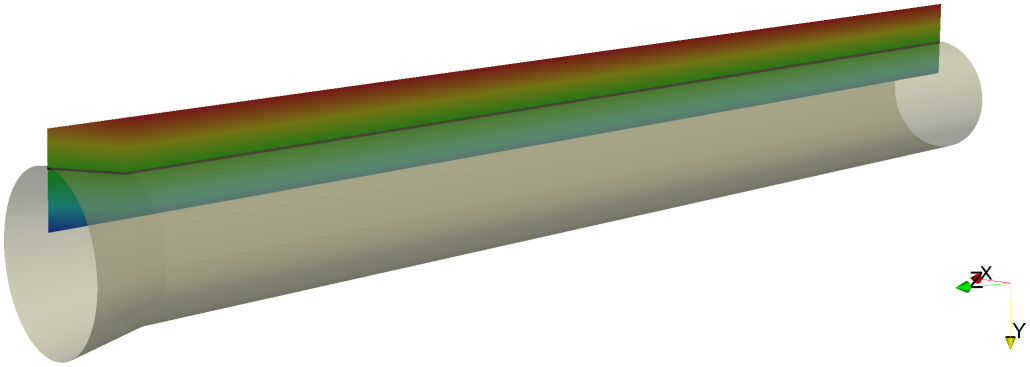

(a) Grain

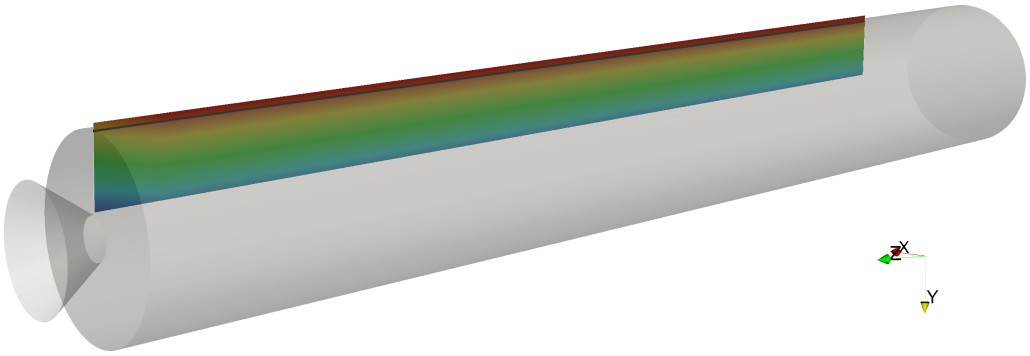

(b) Case

Figure 6.26: NAWC Motor n.13 Level Set IC

dinates lines (cylindrical mesh). Hence the grain propellant surface and case surface interaction define the experienced behaviour of the burning surface curve.

Instead, the wet surface and the bore volume evolution are very well represented in all cases, to be almost unnoticeable from a mesh grid to another.

Then, the 3D evolution of the NAWC Motor n. 13 burning surface and the Level Set function evolution are shown for different web values in the figures 6.28, 6.29 and 6.30. While the evolution of the Q1D grain and bore geometrical parameters are given, for the 100×200 grid, in the figures 6.31, 6.32 and 6.33.

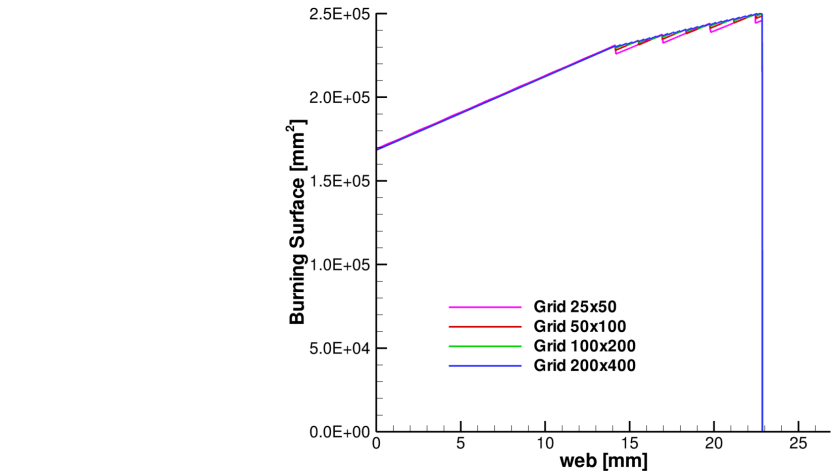

(a) Burning Surface

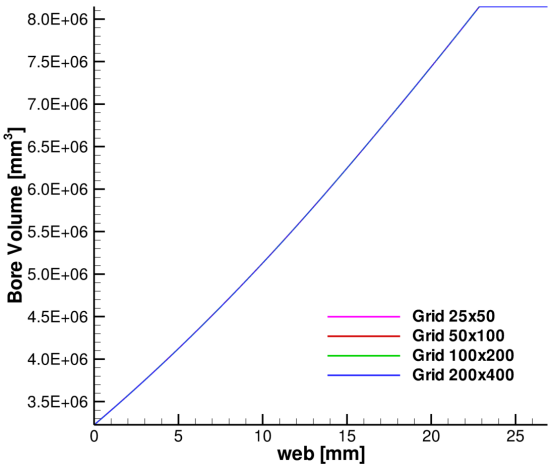

(b) Bore Volume

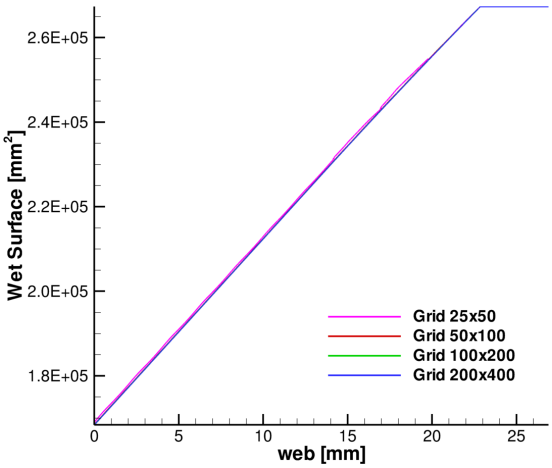

(c) Wet Surface

Figure 6.27: Grid Convergence Analysis for NAWC Motor n. 13 0D grain geometrical parameters

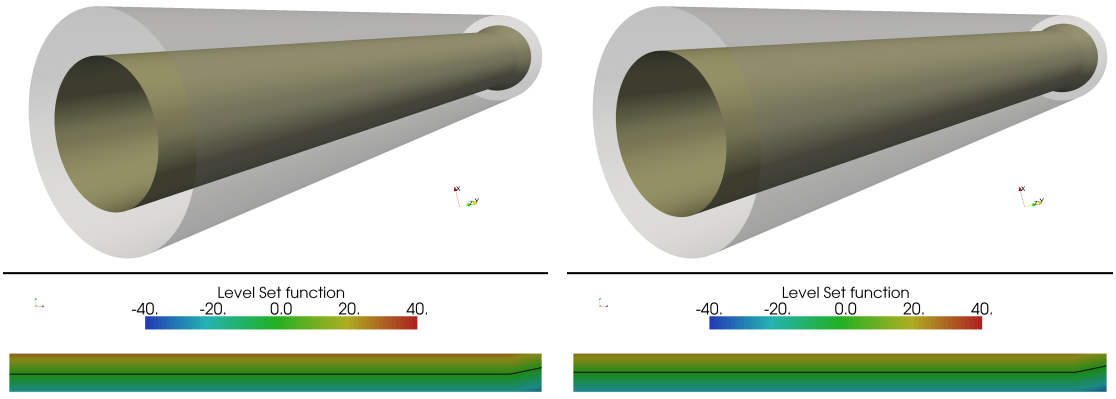

(a) web = 0mm

(b) web = 2.3114mm

Figure 6.28: NAWC Motor n. 13 grain surface and Level Set function evolution

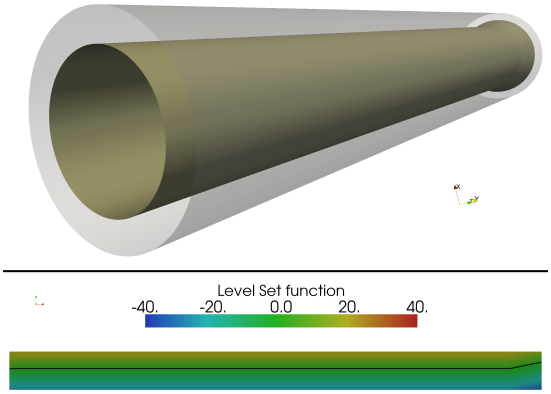

(c) web = 4.6281mm

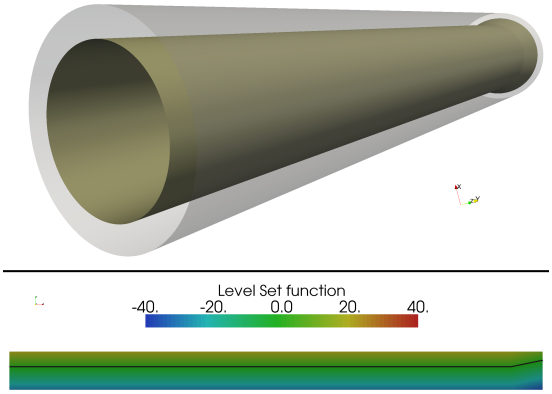

(d) web = 6.9342mm

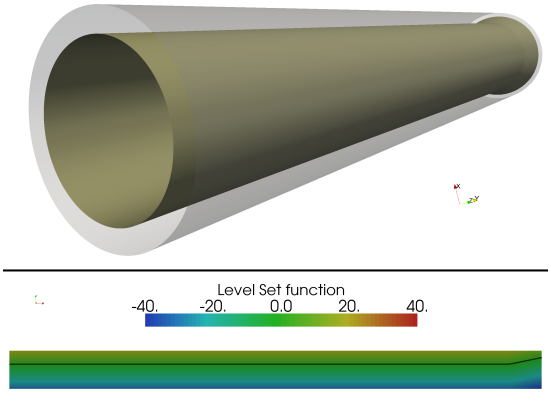

(e) web = 9.2456mm

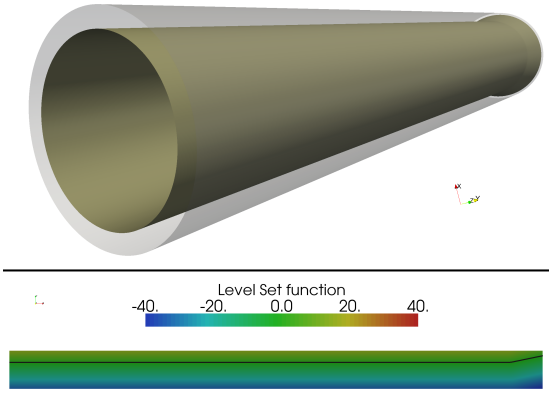

(f) web = 11.5570mm

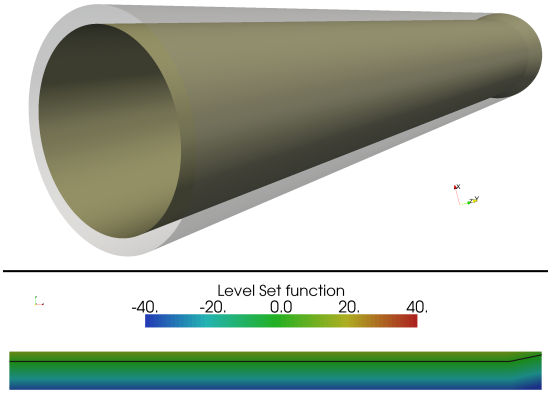

(g) web = 13.8684mm

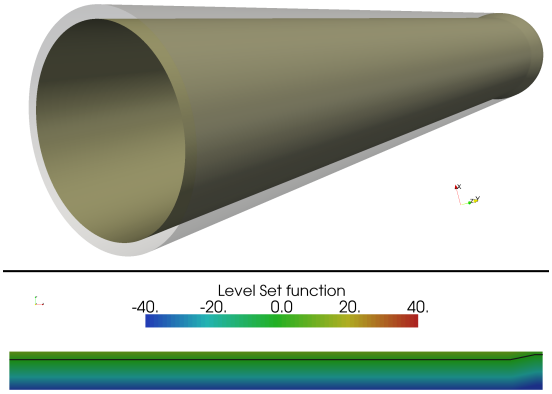

(h) web = 16.1798mm

Figure 6.29: NAWC Motor n. 13 grain surface and Level Set function evolution (cont.)

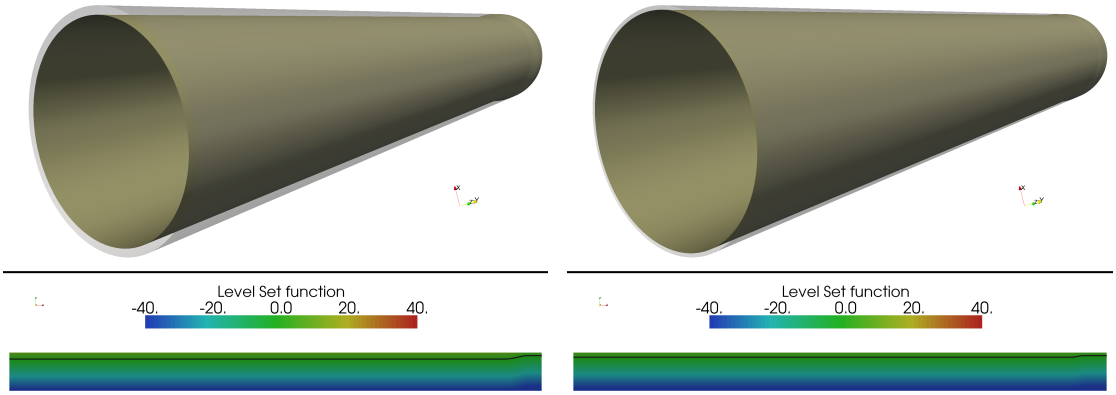

(k) web = 18.4912mm

(l) web = 20.8027mm

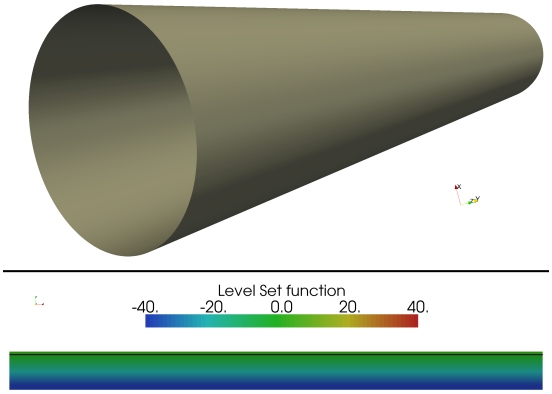

(m) web = 23.1141mm

Figure 6.30: NAWC Motor n. 13 grain surface and Level Set function evolution (cont.)

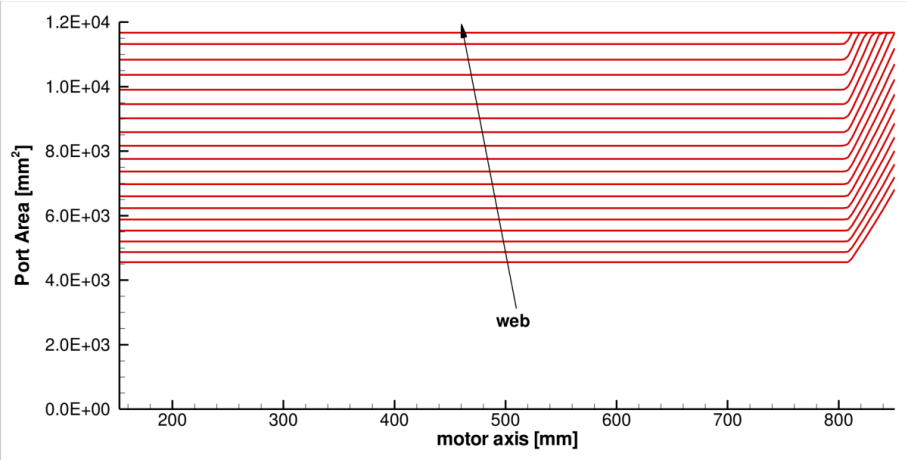

Figure 6.31: NAWC Motor n. 13 Port Area evolution in web

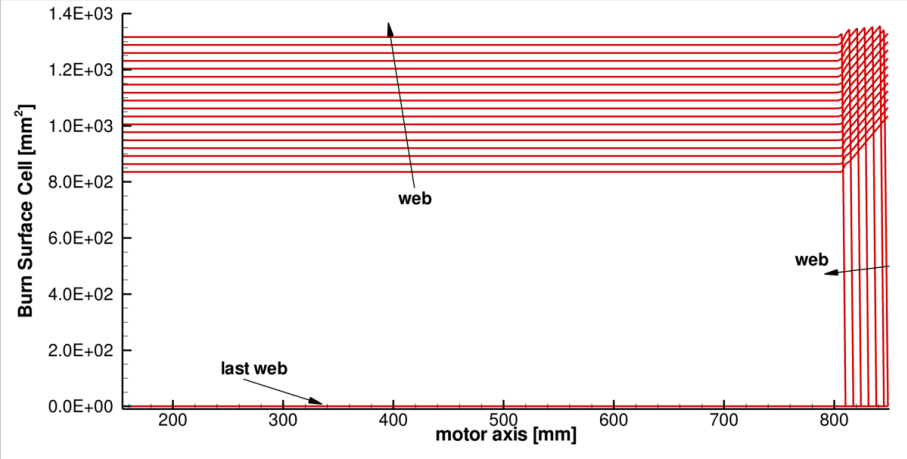

Figure 6.32: NAWC Motor n. 13 Cell Burning Surface evolution in web

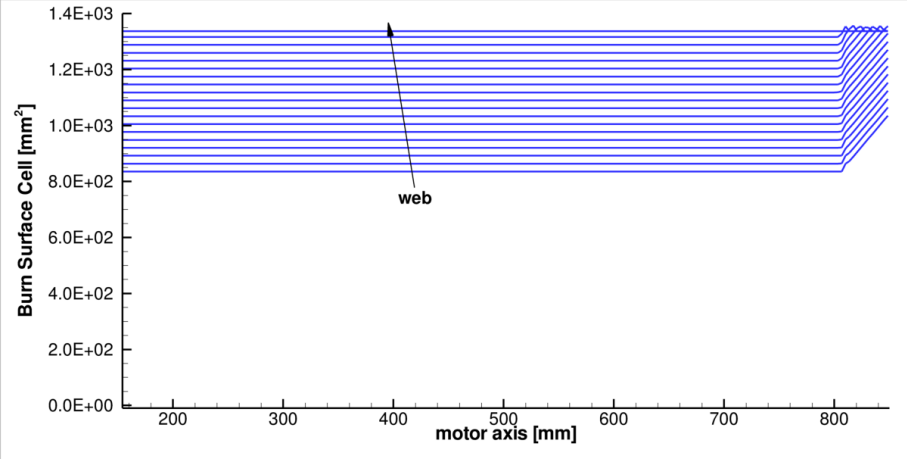

Figure 6.33: NAWC Motor n. 13 Cell Wet Surface evolution in web

7

SPINBALL Results

In this chapter the internal ballistics numerical simulation yielded with Solid Propellant rocket motor Internal Ballistics model will be presented for the SRMs which grain burnbacks are provided by the Grain REGression model model in the chapter 6, page 102:

- Zefiro 23;
- NAWC Motor n. 6 and NAWC Motor n. 13.

In all cases, the coupling between the grain burnback model and the Q1D unsteady internal ballistics solver, provided by SPINBALL, is made with an off-line coupling, as explained in the chapter 4, page 79.

The results will investigate the capability of the SPINBALL model to predict and reconstruct the behaviour of the analyzed SRM. The comparison will be made with the experimental data provided by SFTs of the SRMs. Moreover, the capability of the model presented will be analyzed in terms of a more accurate representation of the internal ballistics flowfield conditions, during the entire combustion time, with respect to simpler 0D internal ballistics models.

For Zefiro 23 SRM all the experimental data, motor configuration and grain propellant properties have been kindly provided by AVIO Group S.p.a., which the author want to thank. For the NAWC Motors n. 6 and n. 13, all the motor configuration data, propellant composition and the available experimental measures performed are extracted from different works recently published in literature [62; 50; 108]. These motors have been fired in the Naval Air Warefare Weapons Division (NAWCWD) at China Lake in order to develop an improved understanding of linear and non linear combustion instability in solid propellant rocket motors. This very intense experimental and numerical simulation activity has been provided in the literature, in several works [50; 100; 62; 92; 72; 71; 64; 47; 108] published during the last decade, which allow to place the presented SPINBALL model in the landscape of the SRM internal ballistics numerical simulation tools.

7.1 Zefiro 23

The results shown in this section are related to the numerical simulation of the SRM Zefiro23 internal ballistics, by means of the presented SPINBALL model. Zefiro 23 is the second solid stage of the new European launcher VEGA, that the European Space Agency is developing (see figure 7.1). The SRM grain configuration and grain burnback have been already illustrated and analyzed in the paragraph 6.1, page 102. Zefiro 23 charges a HTPB1912 propellant, for a propellant mass of about 23 tons, with a finocyl grain and a submergenced nozzle. It is long about 6 meters, with a burning time of about 77 seconds, a vacuum specific impulse of 288 seconds, a maximum vacuum thrust of 1200 kN, a MEOP of 106 bars and a nozzle expansion ratio of 25[105]. The SRM geometrical configuration of grain shape and casing, already shown in paragraph 6.1, page 102, is a finocyl aft-star grain configuration with a submergenced nozzle and a complex TPs internal surface.

(a) VEGA

(b) P80FW

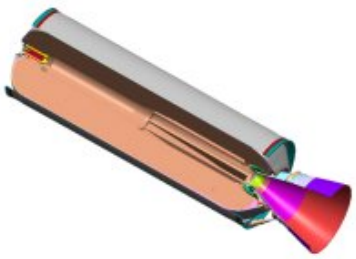

(c) Zefiro 23

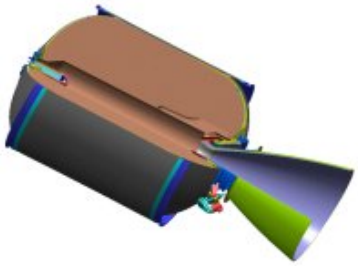

(d) Zefiro 9

Figure 7.1: VEGA launcher solid stages

A 3D view of the SRM is shown in the figure 7.2.

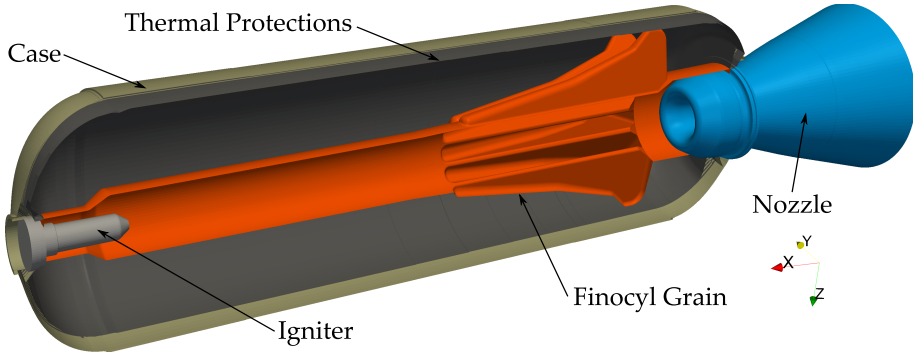

Figure 7.2: Zefiro 23 geometrical configuration

In this paragraph the Q1D model presented will be used in the reconstruction phase of the Zefiro 23 SRM Static Firing Test. In fact, Z23, as will be underlined in the following, is a motor prone to a large nozzle throat variation during motor operative condition. At now, a prediction simplified model for the nozzle ablation phenomena is not yet implemented and integrated in the SPINBALL code. However, the relevant nozzle throat area evolution of the motor must be certainly taken into account in the numerical simulation, in order to define realistic SRM internal

ballistics flowfield conditions. Hence, before the numerical simulation of the SRM with the Q1D model, the SRM non-ideal parameters (hump and combustion efficiency) of the motor will be evaluated, together with the nozzle throat area evolution law in time, as they affect the SRM internal ballistics during the QSS and TO phases in a relevant manner, as will be shown in the following. In particular, this will be made through the SFT reconstruction of Zefiro 23 SRM with the technique presented in the appendix H, page b. As clear in the presentation of the 0D SFT reconstruction model, in fact, all the output parameters of the model represent a unique set of possible reconstruction of the experimental data. These set of data will be then applied in the Q1D numerical simulation, as input.

The effects of the use of such a chain of reconstruction will be discussed and motivated in the light of the achieved results by the Q1D model, with respect to the experimental data (represented by the Head End Pressure time history).

7.1.1 0D Reconstruction of the SFT

The 0D quasi steady state model for the SRM SFT (or SRM experimental data) reconstruction, presented in the appendix H, b, is used to evaluated the non-ideal behaviour parameters of the Zefiro 23 internal ballistic (the hump law and the combustion efficiency) and the nozzle throat area evolution in time.

The inputs for the Zefiro 23 are imposed as the nominal conditions defined for the SFT. The propellant characterization of the APN law is considered an input, coming from the Crawford Bomb experimental studies on the SRM propellant. While the evolution in web of the burning surface comes directly from the GREG model (see paragraph 6.1, page 102). The head end pressure (HEP) trace, coming from the SFT pressure transducers and used in the 0D model as input, together with the SRM thrust measure (which is not shown as of no relevance in this work), is shown in the figure 7.4 (red curve).

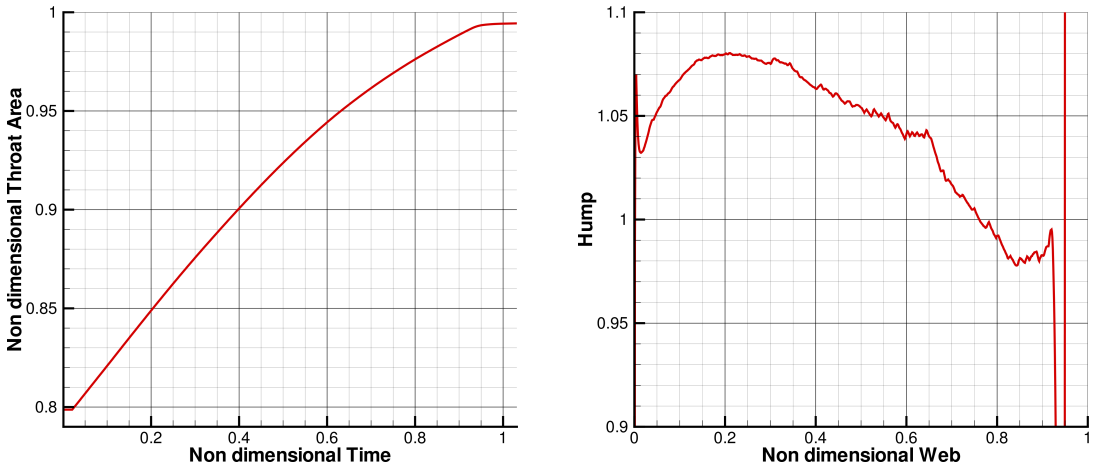

(a) Throat Area evolution in time

(b) Hump vs web

Figure 7.3: Zefiro 23 0DQSS SFT reconstruction output

In particular, in the figure 7.3, the output curves of the hump, with the scale factor included, and the nozzle throat area evolution in time are shown.

A combustion efficiency $\eta_{c^\star}$ is also obtained. While the η_{c_F} evolution in time will be not given, as it is not scope of this work to characterize the nozzle performances, while instead the SRM internal ballistics.

From the figure 7.3, it is possible to underline the following remarks: the hump shape is less or more, the classical "hump shape" and the SRM has a very relevant variation of the nozzle throat area, that is about 24.5% with respect to its initial value. Hence, for this type of SRM,

the nozzle throat erosion must be estimated in some manner and can not totally neglected in performing the numerical simulation of the motor internal ballistics.

7.1.2 SPINBALL Results: Internal Ballistic of the whole combustion time

The Zefiro 23 internal ballistics numerical simulation with the SPINBALL model is here presented.

The same inputs used for the 0D reconstruction model have been imposed. Hence, the propellant characterization in terms of APN coefficients, the grain propellant density and the combustion products thermophysical properties variation with pressure (by the assumption of chemical equilibrium) are given.

A first numerical simulation is considered without any calibration parameter (no hump, no combustion efficiency and a linear throat area evolution, between the final and initial values). The results obtained in terms of computed head end pressure time history are shown in the figure 7.4, in comparison with the experimental curve and the computed pressure for the quasi steady 0D model without calibration parameters (which chamber pressure estimation is simply given by the equation H.1).

As expected, with the assumption of a rough evolution of the nozzle throat area and without any other parameter characterizing the SRM non-ideal behavior, both the models (0D and Q1D) have a displacement of the numerical pressure from the experimental one. The interesting fact consists, however, in the very small displacement between the pressure curves of the two different models (Q1D and 0D), which causes will be analyzed in the following. Note that, certainly, some difficulties for the quasi steady 0D model are related and underlined in the HEP numerical curve for the very rough evaluation of the IT effects, on the whole combustion time. These effects will be analyzed with the use of the SPINBALL model in the paragraph 7.1.3, page 138, related to the inability of the 0D model to represent the Ignition Transient phenomena.

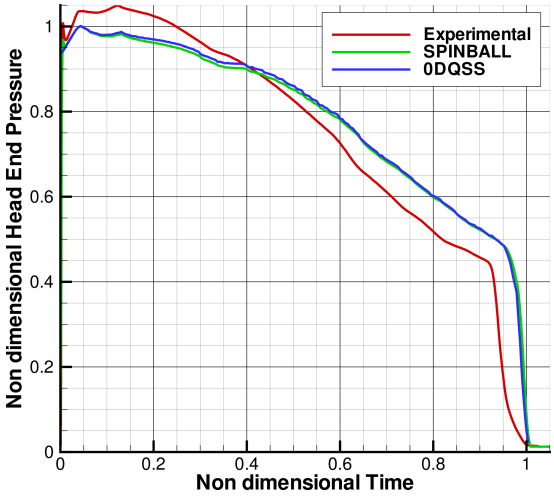

Figure 7.4: Zefiro 23 SFT HEP Experimental-Numerical No Calibration Comparison

For what concern the IT (see figure 7.5), even a rough calibration of the Q1D unsteady model gives, as strong heritage of the SPIT model, a very good accordance with the experimental data during the motor start-up. In this IT simulation the effect during this phase of the combustion efficiency is not considered, as it is a global parameter. While instead the geometrical evolution of the grain propellant surface is activated.

In the following, the use of the 0DQSS calibration parameters, coming from the SFT reconstruction, will be analyzed as input for the SPINBALL model. The attention is particularly focused on the benefits and drawbacks of their use and their dependence on the modelling chosen, as well as on the reconstruction of the experimental results obtained. Therefore, the hump vs web and nozzle throat area evolution in time, presented in the figure 7.3, together with the combustion efficiency have been used in the Q1D internal ballistics model.

Figure 7.5 shows the comparison between the new numerical curve and the experimental one, which the 0D quasi steady model commands to be the solution of the problem in the 0D SFT reconstruction. A strong benefit in the accordance between the two curves is clearly obtained, as expected, and the reasons of this effect is investigated by means of the analysis of the Q1D results.

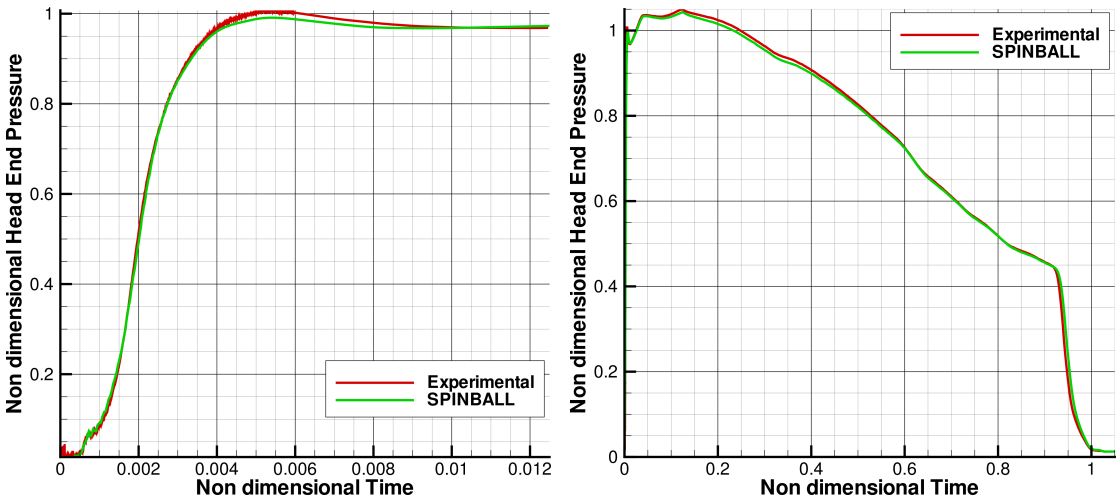

(a) Ignition Transient

(b) Overall combustion time

Figure 7.5: Zefiro 23 HEP Experimental-Numerical comparisons

In fact, as shown in the figure 7.6, Z23 is a slow SRM in terms of combustion velocity, with low flowfield velocities along the motor axis, far from nozzle entrance and from the ignition transient. Consequently, we have low values of the flowfield Mach number, so that the total pressure drops are low. Moreover, as the velocities are low, the erosive burning is totally negligible with respect to the APN term (see figure 7.6(c)), that is the predominant term of the burning rate; again except from the IT phase which will be analyzed in a deepened manner in the following. In particular, the figure 7.6(b) wants to draw the effects on the temperature flowfield, for different times, of the pressure dependent thermophysical properties of grain propellant products and the combustion efficiency. They have the effect to change the enthalpy of the source terms put in the chamber and hence the temperature of the mixture of gases in the bore, as the pressure varies in time.

In order to analyze the little differences between the 0D and the Q1D model internal ballistics simulations, we consider now the comparison between some equivalent entities: the instantaneous and global mass budget in the SRM, the burning rate and the grain burning surface. These are shown in the figures 7.7 and 7.8. Where the figure 7.8 is a magnification of figure 7.7 in the non-dimensional time interval 0.05-0.6, where the HEP pressure traces show the major disagreement. All these quantities characterize in the 0D quasi steady model the pressure point of work of the SRM, and hence are used to understand and outline the reasons of the small differences between the HEP traces shown by the 0D and the Q1D model.

As matter of facts, comparing the steady mass flow rate of the 0D with the Q1D propellant inlet mass flow rate and the outlet mass flow rate in the nozzle throat area (see figures 7.7(a) and 7.8(a)), it is possible to underline two facts. Firstly, the differences between the Q1D inlet mass flow rate from grain and outlet from the nozzle are negligible but present. They can be quantified more or less all under the 0.5% of the instantaneous mass flow rate, as expected for the quasi steady state phase. The second important fact is that the Q1D mass flow rate is under the 0D one, except during the tail off.

$$\dot{m}_{in} = \sum_{j} \rho_p P_{bj} r_{bj} \Delta x \qquad \dot{m}_{out}|_{throat} = \rho_t u_t A_t \tag{7.1}$$

This is not attributable directly to the difference of the computed instantaneous combustion surface (see figures 7.7(d) and 7.8(c)), which are very similar. On the contrary, for the Q1D model the computed burning surface is a few greater than the 0DQSS one. Instead, the driving parameter to explain the small difference in the HEP is rather the difference of the burning rate

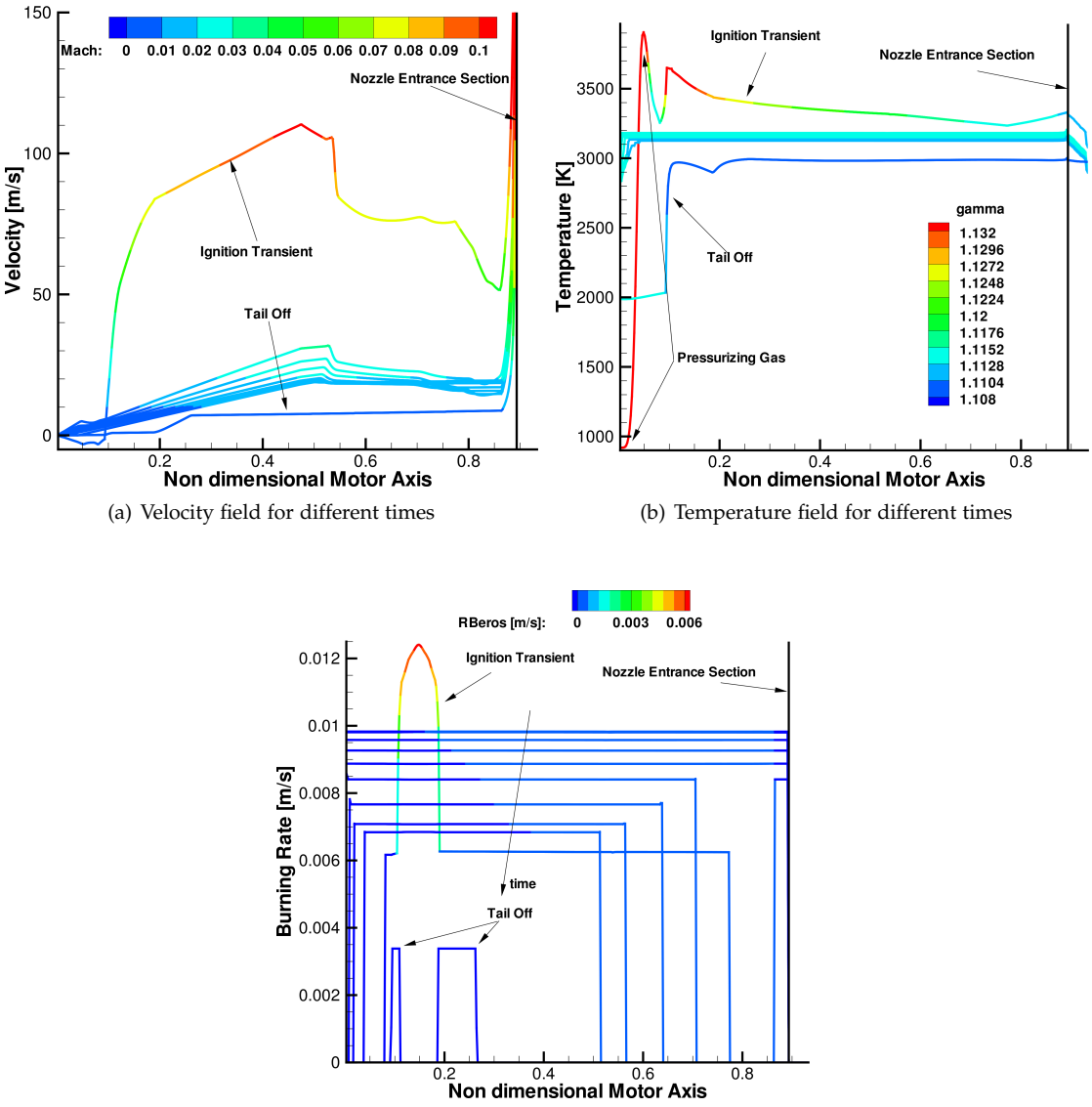

(a) Velocity field for different times

(b) Temperature field for different times

(c) Burning Rate field for different times

Figure 7.6: Zefiro 23 Q1D Analysis during the overall combustion time

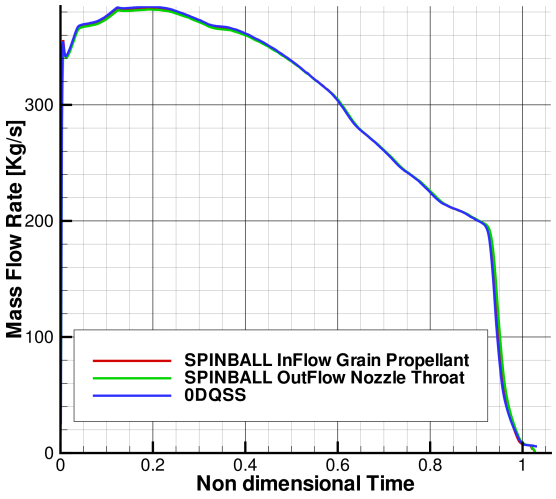

(a) Inflow and OutFlow Mass Flow Rate Comparison Q1D-oD

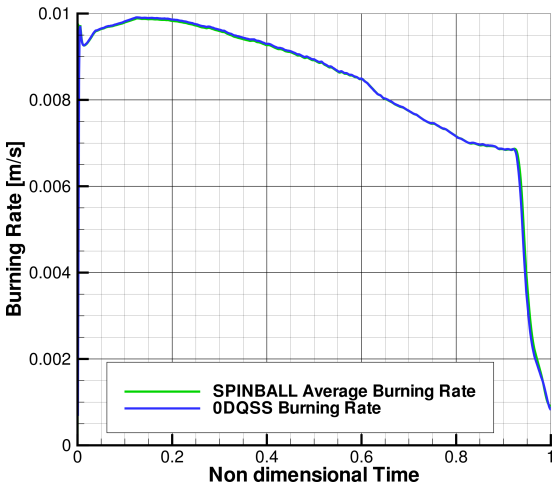

(b) Equivalent Burning Rate Comparison Q1D-oD

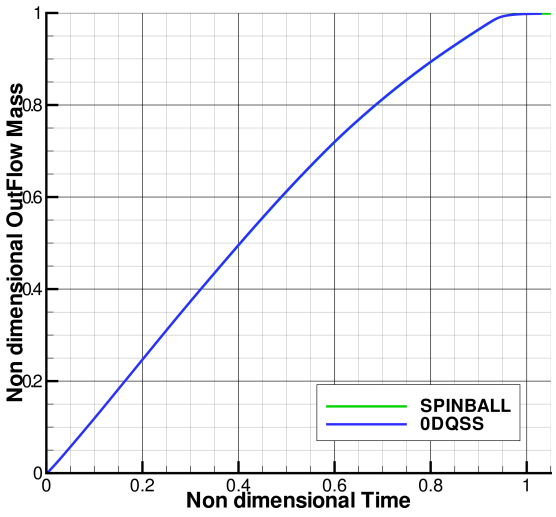

(c) OutFlow Mass Comparison Q1D-oD

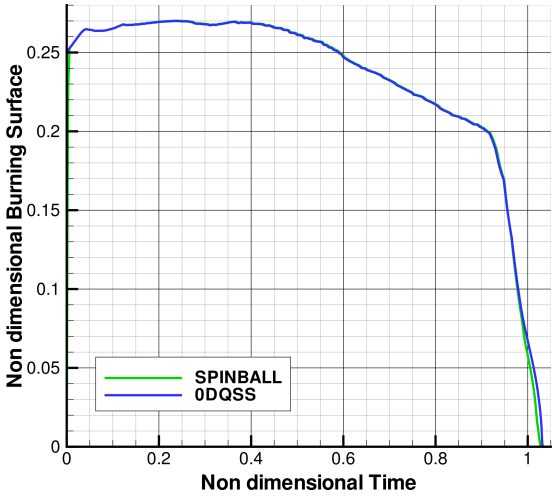

(d) Comparison between oD and Q1D Burning Surface Evolution

Figure 7.7: Zefiro 23 Q1D - oD Mass Budget Comparisons

values of the 0D model and the equivalent burning rate of the Q1D. These remarks, moreover, underline that for the SRM considered, the assumption of the off-line coupling does not insert a relevant approximation in the coupling between the Q1D flowfield solver and the grain surface evolution one. In fact, we have the very small variations along the motor axis of the burning rate, as underlined also by the figure 7.6).

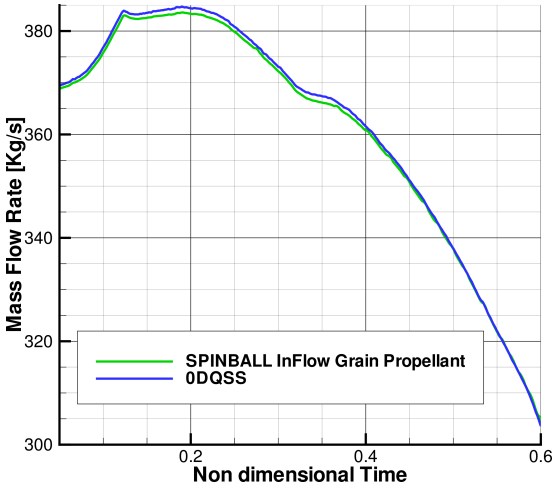

(a) Mass Flow Rate Comparison Q1D-0D

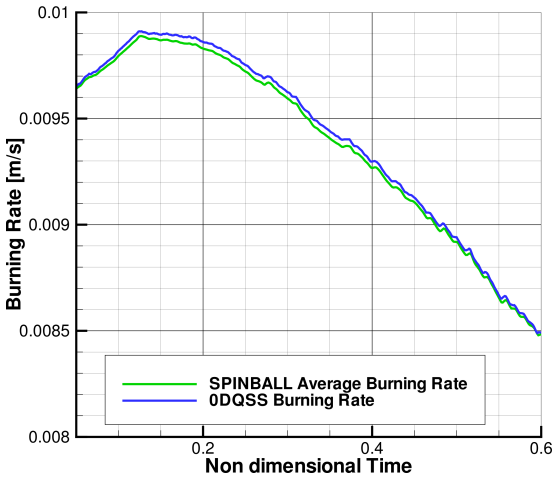

(b) Equivalent Burning Rate Comparison Q1D-0D

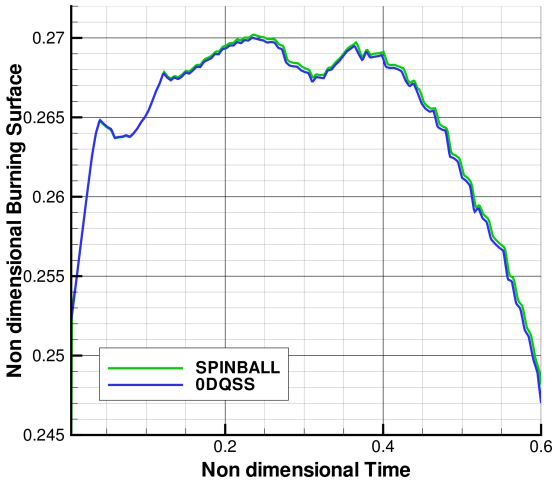

(c) Comparison between 0D and Q1D Burning Surface Evolution

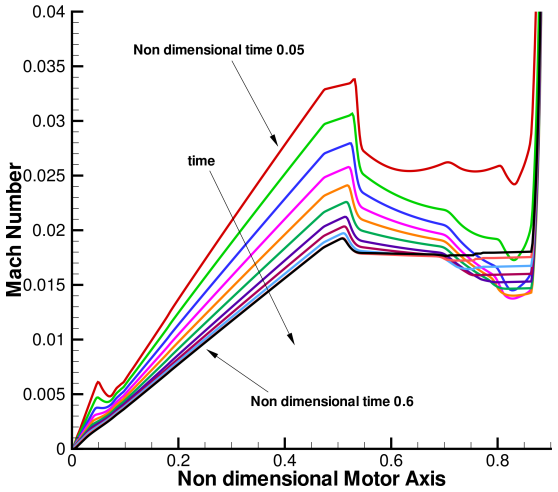

(d) Mach field during the interval 0.05-0.6 non-dimensional time

Figure 7.8: Zefiro 23 Q1D - 0D Mass Budget Comparisons during interval 0.05 - 0.6 non-dimensional time

Hence, the difference between the SPINBALL HEP and the experimental one can be explained considering the comparison between the average Q1D burning rate and the 0D burning rate, defined in the equation (7.2) and equation (7.3), respectively.

$$\widetilde{r_{bQ1D}} = \frac{\dot{m}_{in}}{\rho_p \sum_j P_{bj} \Delta x} \tag{7.2}$$

$$r_{b0D} = \frac{\dot{m}_{QSS}}{\rho_p S_b} \tag{7.3}$$

Figure 7.8(b) justifies the small difference between the two pressure traces, as related on the difference of the computed burning rates. The Q1D model, in fact, takes into account the small

total pressure drops and the evaluation of the APN with the static pressure, which depends on the motor bore geometry and the grain burning surface along the motor axis. All these effects become lower as the time advances and the grain propellant reaches the thermal protections. In fact, we have a better agreement of the SPINBALL HEP curve with the experimental one, according to the figure 7.5, which is just related to the lower pressure total drops as the grain propellant is consumed in time, that can be related to the Mach field in time (see figure 7.8(d)). Moreover, as the contribution of erosive burning is completely negligible (see figure 7.6(c)), there is also a very small, but present, contribution of the unsteady effects, that the 0DQSS does not take into account.

Certainly, as consequence, the tail off of the two HEP curves are different. In particular, the Q1D curve has a small delay with respect to the 0DQSS one. This is due to the fact that the former computed HEP history is all under the latter for the time interval before the TO, while as constraint, the nominal propellant mass is the same. In fact, we have different burning surfaces evolution during this phase and a consequent delay between the two outflow mass flow rate curves. Moreover, the unsteady effects, that the 0D quasi steady model does not account at all, during tail off become important in describing the depressurization of the combustion chamber.

All the analyses performed on Z23 SRM show that the set of the non-nominal SRM behaviour parameters is dependent in a slight manner on the internal ballistics simulation model itself. Hence, the use of the non-ideal reconstruction parameters and the nozzle throat area evolution in time, as calibration parameters for the Q1D model proposed is possible and permitted for this SRM. But, this fact depends directly on the analyzed motor characteristics and chamber flowfield conditions enabled by the Q1D model. In the same time, in a such kind of SRMs type, the use of a more refined internal ballistics model can be a further proof of the SRM nominal behaviour with respect to simpler 0D quasi steady models. Moreover, it has the advantage to be a single tool to perform the internal ballistics numerical simulation for the entire combustion time.

Note that the total propellant masses discharged during the SRM simulation, for the 0D model and the Q1D model, differ only about 0.02% of the total propellant mass charged. This difference can be considered to have negligible effects on the numerical simulations and, in particular, to be due to the different interpolation on the grain propellant geometrical tables given by the GREG model.

7.1.3 Effects of the Geometrical Evolution during the IT

This section is devoted to analyze in a deepened manner the effects of the bore geometry variations during the IT. Moreover, the effects of the IT simulation on the overall SRM simulation mass budget are investigated. In fact, a simple quasi steady, but even, unsteady 0D model, is not able to describe at all the IT phenomena, both in the prediction and in the reconstruction of the internal ballistics of a SRM. The results shown in the figure 7.10 refer to the simulation which numerical HEP has been shown in the figure 7.5 previously (left figure). In that simulation, we remember that the combustion efficiency is not active and a constant value of the hump is used. As supposed in [108] and as figure 7.9 underlines, the flame spreading and the igniter jets impinging directly on the motor burning surface have some effects in terms of non-uniform regression of the motor grain geometry during the motor start-up. This is underlined in particular in the web field curves in time during the IT (see figure 7.9(a)). While, figure 7.9(b) draws out the overall burning rate field and the erosive component contribution to it, for some instans during the IT. As shown in figure 7.9(b), the phenomenon of a non-uniform regression is particularly located in the impingement region of the plume of the igniter radial nozzles jets, where the flowfield velocities are high. In fact, the igniter jets impinging with high velocity on the burning surface define a high burning rate, with an erosive contribution with the same order of magnitude, or even predominant, with respect to the APN term. While, for the grain regions where the igniter jets are not impinging directly, the burning rate is defined by a smaller burning rate, due mainly to the APN term. Hence, in these regions the non-uniformity of the

grain regression is due to the flame spreading effects, that defines different ignition times along the motor axis.

In figure 7.10(b), the ignition transient effects on the overall motor mass budget are shown. During this phase, in fact, the overall mass outlet through the nozzle is, for the case under analysis, about 1% of the overall propellant mass.

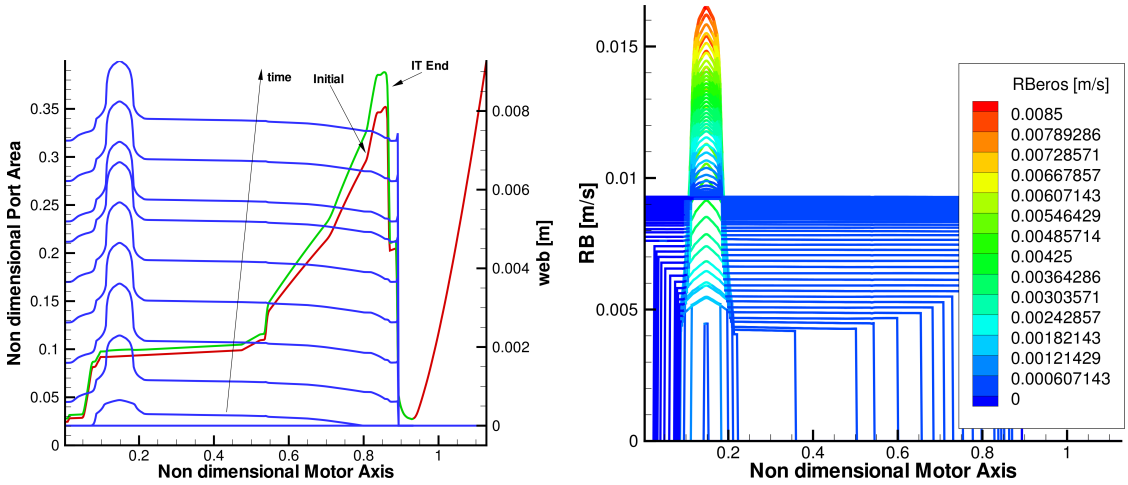

(a) Bore Geometrical and Web Evolution

(b) Burning Rate and Erosive Burning field

Figure 7.9: Zefiro23 Q1D SPINBALL Geometrical Evolution Analysis during the IT

Another remark is the fact underlined in figure 7.10(b). In fact, considering only the simulation of the IT, a blocked geometry approach for the grain geometry during the motor start-up is, as expected, an acceptable assumption, as the burning surface evolution has some effects only in the final part of the IT. While, as shown in figure 7.9(a), the port area evolution is quite bounded.

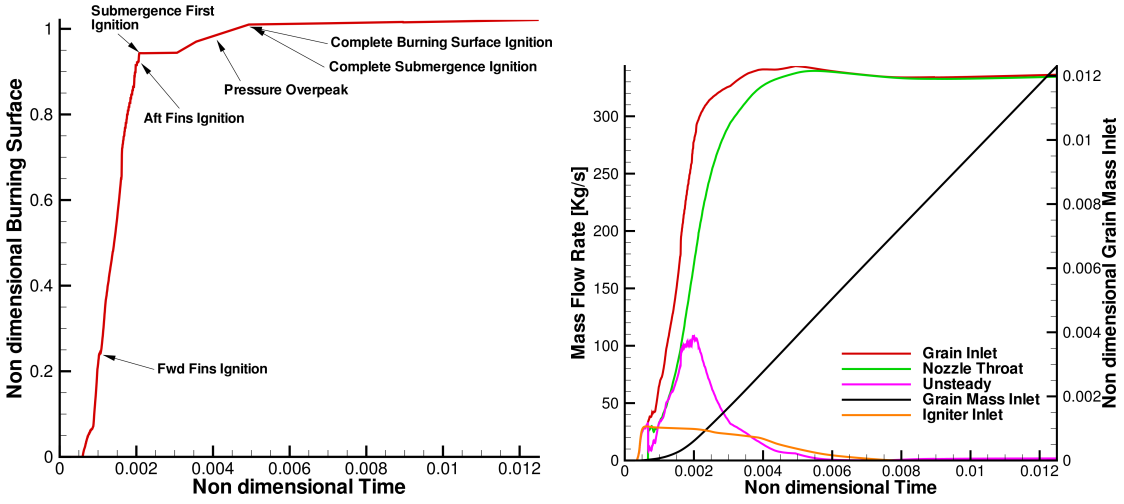

(a) Burning Surface

(b) Mass Budget and Mass Flow Rate Budget

Figure 7.10: Zefiro23 Q1D SPINBALL Mass Budget and Burning Surface Evolution during the IT

Certainly, all the described effects have a difficultly evaluable consequence in the use of the 0D reconstruction parameters for the calibration of the Q1D unsteady model. In fact, the interval of time in which the IT happens is very small with respect to the quasi steady state, for this class of SRMs. However, the proposed Q1D model enabling the numerical simulation of the overall SRM combustion time, goes towards a finest numerical simulation and understanding of the

overall SRMs internal ballistics and, hence, towards a better characterization of these non-ideal parameters.

7.1.4 Effects of the combustion efficiency variation

This very brief section wants to illustrate the differences in the computed Head End Pressure due to a small and reasonable variation of the combustion efficiency. As presented in the paragraph 2.1, page 13, these effects can be taken into account by the infinite gases approach of the gasdynamical flowfield model developed in SPINBALL.

Hence, for the same simulation with the same input, a small variation of the combustion efficiency is considered between around 0.97 to 0.99. The resultant computed Head End Pressure time history are shown in figure 7.11, where small but, however, considerable differences are present in two pressure traces, as expected.

A similar difference, in terms of HEP curves, must be expected also considering a constant thermophysical properties assumption for the grain combustion gases, with respect to the one considered in SPINBALL, as dependent by the local pressure value. Certainly these effects are dependent on the propellant type and on the range of the pressure, which the SRM experiences during its operative time. However, the differences could be, as shown, of the order of 1 to 10 bars. Hence, they can be relevant in a fine tuning calibration of the internal ballistics model for SFTs or real flights reconstructions and in the consequent determination of the SRM non ideal parameters.

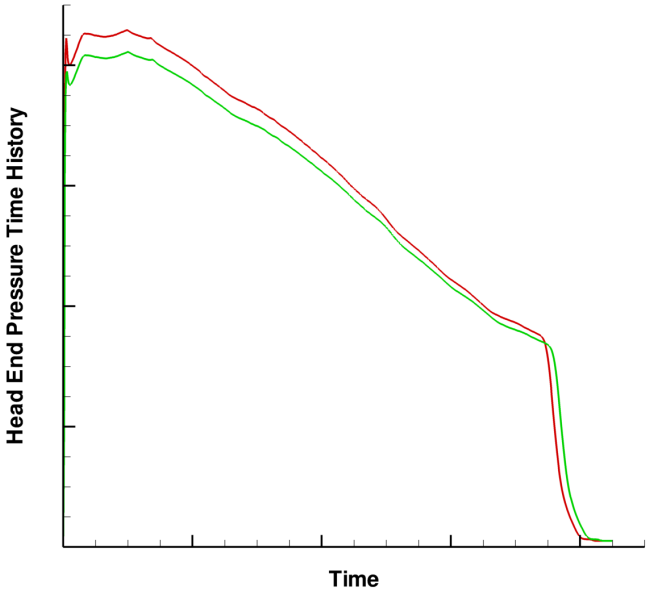

Figure 7.11: Effects on the HEP for a small variation of the combustion efficiency

7.2 NAWC Motor n. 6

NAWC Motor n. 6 is a useful motor to underline the effects of the erosive burning in the SRM internal ballistics and in the motor flowfield conditions during time. Hence, it is a useful SRM to be simulated in order to check and validate the results obtained with the proposed Q1D model. Moreover, this is a SRM analyzed quite in depth in literature [47; 50; 64; 62; 92; 100], for reasons related to the combustion instability testing and the understanding of the phenomena itself, carried out at the NAWCWD in China Lake.

The motor grain and its geometrical configuration, shown in the paragraph 6.2, page 112, is a aft-finocyl grain with a cylindrical case and a very low initial value of the ratio port to throat area (around 1 for the initial configuration).

The propellant used is a reduced smoke propellant with additives, which composition is reported in table 7.1. It has a burning rate of 0.678 cm/s at 6.9 MPa, a pressure exponent of the APN law of 0.36 and a density of about 1800 Kg/m^3 [62; 50].

Component	Mass Percentage
AP	82 %
HTPB	12.5 %
RDX (ciclotrimethylene-trinitramine)	4 %
carbon black	0.5 %
ZrC	1 %

Table 7.1: NAWC Motor n. 6 Propellant Composition

The thermophysical properties of the grain propellant combustion products are evaluated starting from propellant composition with the CEA code [38; 44]. The assumption made is the reaching of the chemical equilibrium condition for the combustion reactions, evaluated for some pressure values, in the pressure operative range of the motor (from about 1 to about 140 bars). No nozzle area variation is evidenced by the experimental results. Hence, a constant value of the nozzle throat diameter and a fixed nozzle configuration is considered during the internal ballistics numerical simulation.

A first attempt is considered in order to predict the head end pressure time history of NAWC motor n. 6, with a simple 0D quasi steady model. This model is simply based on the classical 0D equilibrium pressure, coming from mass flow rate equilibrium condition (see equation 7.4), without the use of any calibration and non-ideal parameter (hump and combustion efficiency).

$$p(t) = \left(\rho_p \, a(T_i) \; c^\star(t) \, \frac{S_b(web(t))}{A_t} \right)^{\frac{1}{1-n}} \tag{7.4}$$

The comparison of the numerical simulation yielded with the nominal input data reported in the literature for the SRM, and the experimental measure of the head end pressure time history is illustrated in figure 7.12.

In the same figure 7.12, the HEP of the RocballistoD code is shown, as published in [108], in order to have a comparison with another internal ballistics numerical simulation

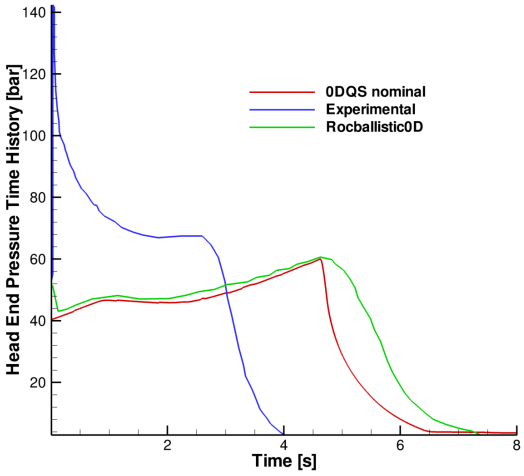

Figure 7.12: HEP numerical/experimental comparison: Numerical 0D quasi steady and RocballistoD [108]

code with a similar model. The 0D quasi steady code curve should be translated in time, as its validity is over the IT, when quasi steady state conditions for the SRM are reached. However, in the NAWC motor n. 6 HEP experimental trace is quite difficult to define the reaching of quasi steady state conditions. Hence, we plotted the numerical curve not translated in time, as this choice does not alter the comparisons we are going to made.

Really, RocballistoD code is more complete with respect to the one we are considering now. In fact, it is an unsteady and not quasi-steady model of the bore flowfield. Moreover, it considers a modelling also of the dynamic burning effect on the overall burning rate, based on the ZN model (discussed in the paragraph 2.2.3, page 23).

The comparison of the numerical results (figure 7.12) with the experimental one shows that both 0D numerical modelling of the internal ballistics do not describe at all the initial and relevant pressure spike, that brings the pressure inside the bore to about 140 bars. In fact, both the 0D numerical simulations define a pressure trend that is led by the behaviour of the grain combustion surface, shown and analyzed in the paragraph 6.2, page 112, which has after the Ignition Transient, a trend due to a progressive grain. Also the inclusion of the unsteady term in the mass balance equation and the dynamic burning effects during the unsteady motor start-up by RocGrainoD code do not explain the huge pressure peak and the following pressure decreasing experienced by the experimental analysis, with a behaviour opposite with respect to the burning surface that is instead increasing.

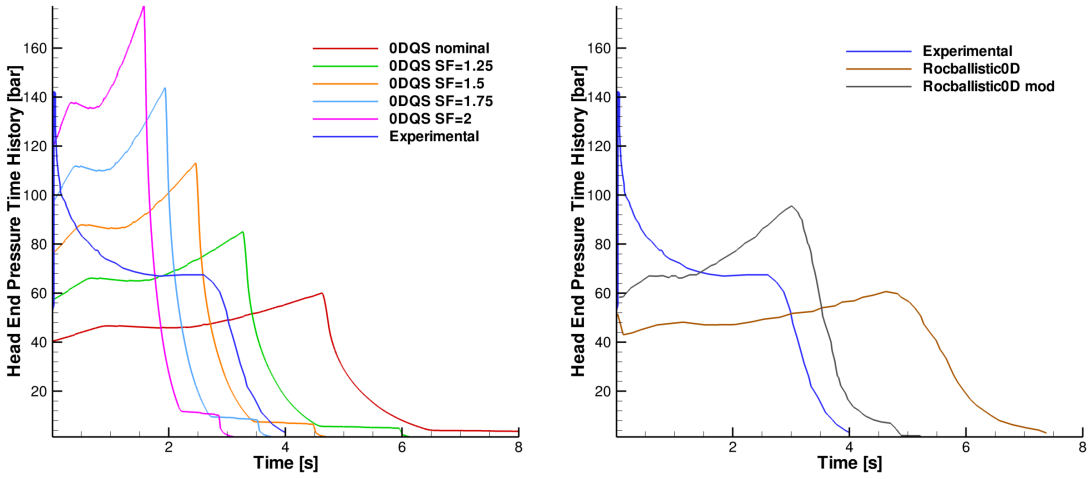

(a) Experimental and Numerical 0D quasi steady simulation

(b) Experimental and RocballistoD simulation [108]

Figure 7.13: HEP numerical/experimental comparisons for 0D models with modified APN law

Some speculations on the cause of the pressure peak, that can be found in literature, range from the erosive burning to the igniter ejection during the motor start-up [108; 64].

Even the artificial enhancing of the a constant of the APN burning rate quasi-steady model, also made in [108], as expected, does not give a better correlation with the experimental pressure trace, as illustrated in the figure 7.13 for both the 0D models.

The second step, hence, is the numerical simulation of the NAWC Motor n. 6 with the Q1D model. As expected, in fact, because of the star-aft motor design and low port to throat area configuration, the erosive burning contribution is present for the motor under analysis. Effect that simple 0D quasi steady or unsteady numerical models are not able to describe at all.

Hence, the NAWC Motor n. 6 is numerically simulated also with the SPINBALL model, including and not including the erosive burning effect on the internal ballistics. The computed HEP time history of the numerical simulation with SPINBALL is shown in the figure 7.14(a),

where the erosive burning effect in accounted as presented in the paragraph 2.2.2, page 22. We use the standard LR model with the modifications due to Lawrence and Beddini, with the standard value for the β empirical parameter ($\beta = 53$), as suggested by Lenoir-Robillard[4] and used in [108]. In the figure 7.14(b), instead, the HEP curves are shown together with the experimental one, for the NAWC Motor n. 6 numerical simulations yielded with different codes: SPINBALL, Rocballist1D[108] and SPP[64].

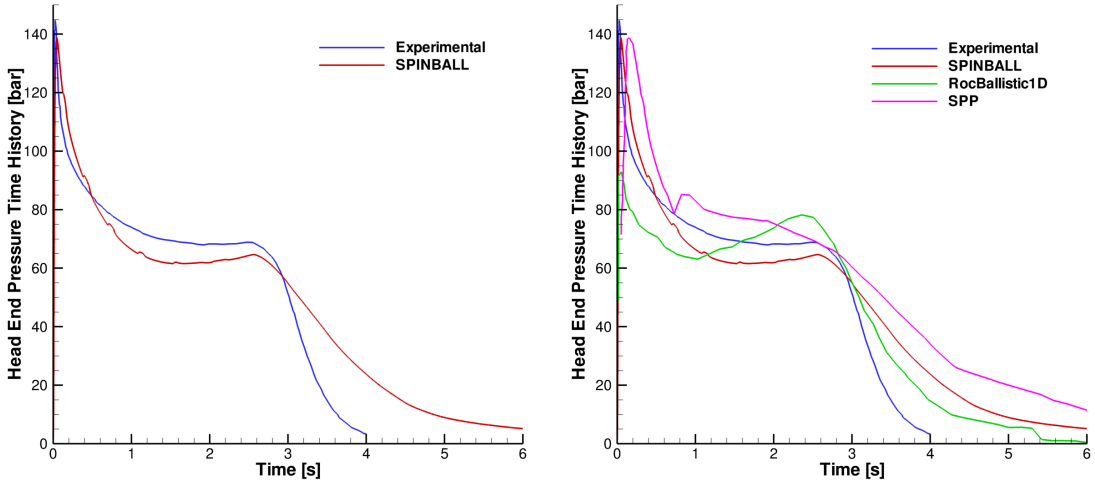

(a) Experimental and Numerical Q1D

(b) Experimental, Numerical Q1D simulation and other codes comparisons [108; 64]

Figure 7.14: HEP numerical experimental comparisons for Q1D internal ballistics modeling

Unfortunately, even if the SRM data are widely published in literature, it has not been possible to recover any information about the igniter configuration. Hence, even if possible with the SPINBALL code, no numerical simulation of the Ignition Transient is performed to obtain the Q1D results. For this reason, the grain burning surface is ignited with different imposed time chains: from an instantaneous ignition, to a spatial delayed of ignition from the head end to the after end of the grain propellant, with different reasonable times for the complete ignition of the combustion surface. Notwithstanding, all these tests have shown to result with a very small effect on the positioning of the numerical initial pressure spike. Hence, this means that the numerical curve may be in the comparison with the experimental one, slightly translated in time, of a time interval related to the error made in the IT imposed for the numerical simulation. This is very similar to what done in [108], since the Rocballist1D has not the ability to simulate the IT phenomena. While, no details are reported in [64] in order to understand which kind of erosive burning model is implemented in the SPP code, neither if the IT numerical simulation is performed.

It is interesting to note that even if a fine tuning of the erosive burning rate model is not performed, a very good correlation with the HEP experimental data is achieved with SPINBALL code. In particular, we have a very good reconstruction of the initial pressure peak, of the pressure following decreasing and the following plateaux, up to the knee of the pressure curve, before the TO. While the lack of agreement shown during the Tail Off is attributable, instead, in part to the differences between the two curves accumulated during the QSS and to the missing of the dynamics burning model that may have some effects in unsteady phase, even if it has a small one during the IT. But the main cause, to which is related the lack of agreement during the TO phase, can be probably due to the way in which the grain burnback model and the internal ballistics model are coupled, as will be analyzed in the following.

However, as said before, the global trend of the experimental curve is well captured in a very satisfactory way. Hence, the pressure spike (missed of about 10 bars), the pressure decreasing

and the successive plateaux (disagreement of about 10 bars again) are quite well simulated especially for a not-tuned simulation, while the tail off chamber blowing down is quite overestimated.

Comparing, now, the results of the different codes reported in literature in [108; 64], for respectively, Rocballist1D and SPP, we seem to have a better capturing of the experimental HEP trend. In fact, both the numerical simulations with the other codes miss the global curve behaviour; the second code in a very relevant manner.

Considering the figure 7.15, now, a quantification of the effects of the erosive burning on the chamber flowfield conditions during the whole combustion time can be made. Figure 7.15 explains, in particular, the SRM behaviour shown the first part of the QSS, when the pressure spike is present. In fact, considering the components of the overall burning rate, separated into the APN component and erosive burning component plotted for different times (see figure 7.15), it is underlined just the wide effect on the burning rate of the erosive burning, especially during the first part of the QSS. When the burning rate variation along the motor axis is strongly defined by the erosive burning effects rather than to the APN term. So that, as pointed out also in [108], it is possible to state that the pressure spike, but more in general, the overall internal ballistics of NAWC motor n. 6 is led by the erosive burning. While the effect of the dynamic burning, even if present in the initial unsteady phase, is so small to be a second order effect. During the subsequent phases, in fact, as the port area increases, the flowfield velocity inside the chamber are lower, reducing consequently the erosive burning contribution, which is however present until almost the last part of the tail off (see again 7.15).

This effect can be seen moreover considering the Mach field evolution, together with the bore geometry evolution, given in terms of port area, in figure 7.16. This underlines the wide total pressure drops to which the SRM is prone, especially at its start-up ((about 20 bars), because of the low port to throat area of the initial grain design. While during the grain combustion we have their decreasing because of the bore geometrical variations (with an enlarging of the port to throat area ratio) and the mass addition variations in time and space.

Moreover, the figures 7.16 and 7.14 underline the big non-uniform geometrical evolution to which the grain burning surface is prone, especially in the first part of the QSS. These are due because of two competitive effects. The first one is related to the total pressure decreasing along the motor axis, which defines also a decreasing of the pressure of the APN term. While the second effect is the increasing of the flowfield cross velocities, that enhances the erosive burning effect. The wide variations in the burning rate along the motor axis define that the off-line coupling, through which the grain burnback solver GREG and the SPINBALL internal ballistics solver are coupled, represents an approximation on the 3D grain geometry evolution, especially during the TO phase. In fact, the effects of non-uniformity of the burning rate are partially accounted in the evolution of the 3D burning surface of the grain propellant with the off-line coupling, as discussed in the chapter 4, page 79. We remember that, however, up to now a completely coupled 3D grain burnback/internal ballistics flowfield solver have not been yet published in literature. Notwithstanding, certainly the off-line coupling has an effect on the predicted tail off curve shape, because in this phase the accuracy of the grain surface evolution in time becomes more relevant than in the previous SRM operative phases. This fact is believed to be the main cause for the displacement between the SPINBALL HEP and the experimental one, during the Tail Off.

Moreover, as also suggested in [108], and underlined in the paragraph 7.1.3, page 138, the effects of the IT numerical simulation on the predicted HEP and in general on the internal ballistics should give a augmented description capability of the SRM behaviour. As they account also the non-uniformity of the grain evolution related to the SRM ignition sequence and the igniter simulation.

In particular, a finest representation of the initial pressure overpeak during the motor start-up can be obtained considering also some IT effects on it. We refer mainly to the possible effects of the igniter and of the possible further grain erosive burning on the igniter jets impingement region (as experienced in paragraph 7.1.3, page 138); but also to the small, but present (as underlined in [108]), dynamic burning effect. These phenomena can modify in the direction of

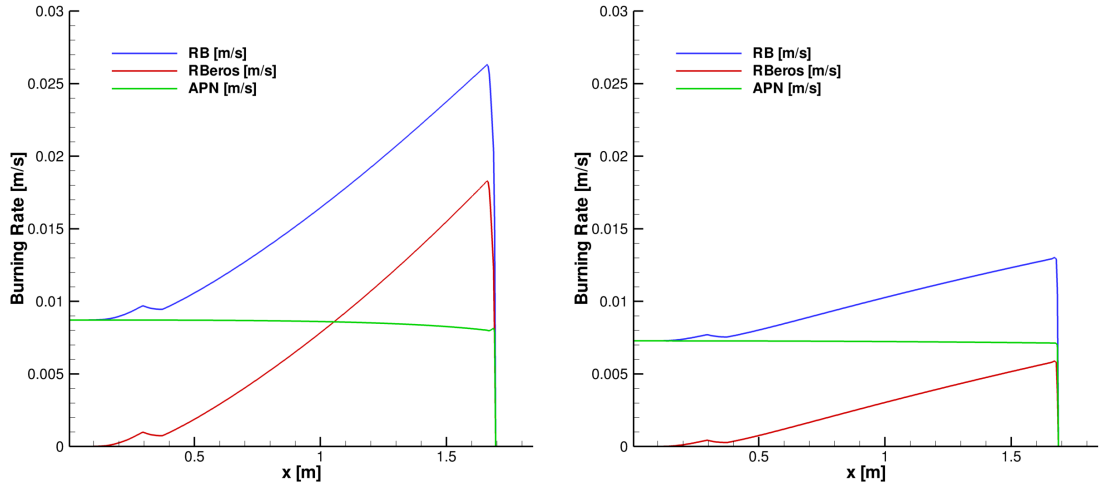

(a) time = 0.05 s

(b) time = 0.5 s

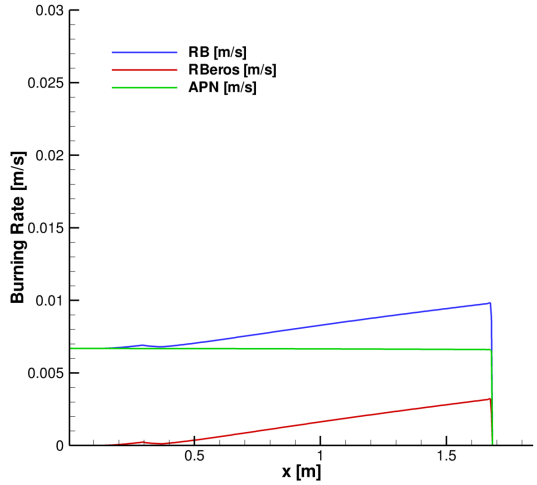

(c) time = 1 s

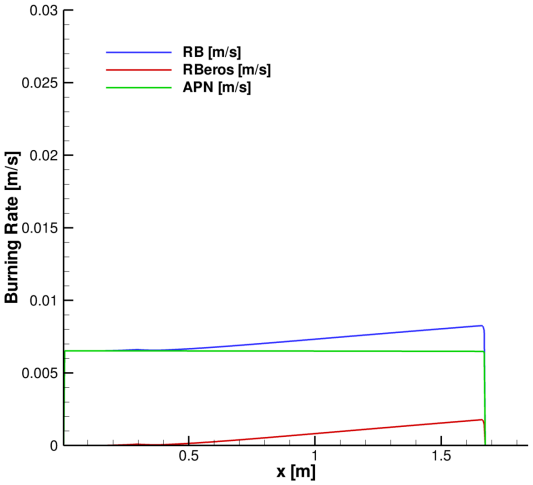

(d) time = 2 s

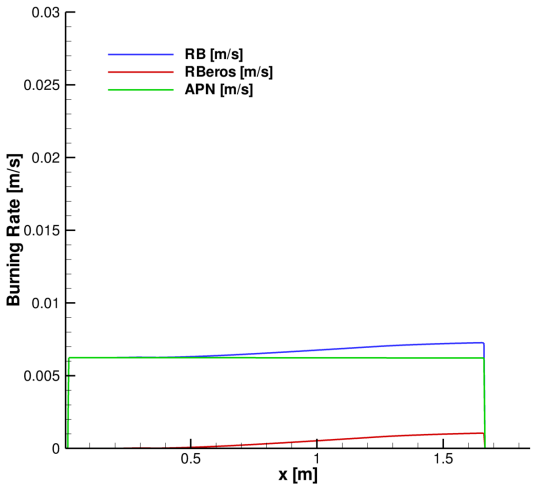

(e) time = 3 s

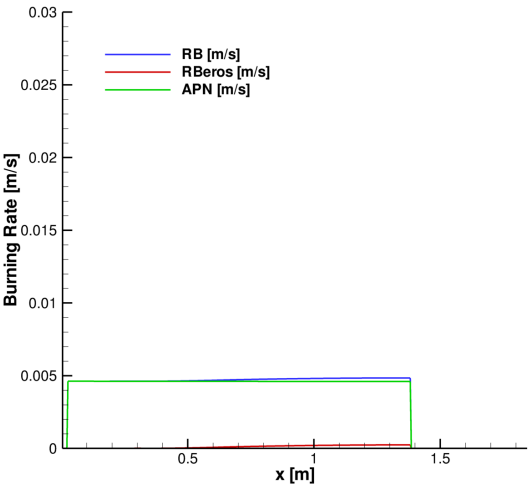

(f) time = 4 s

Figure 7.15: Burning Rate: overall, APN and erosive for different instants

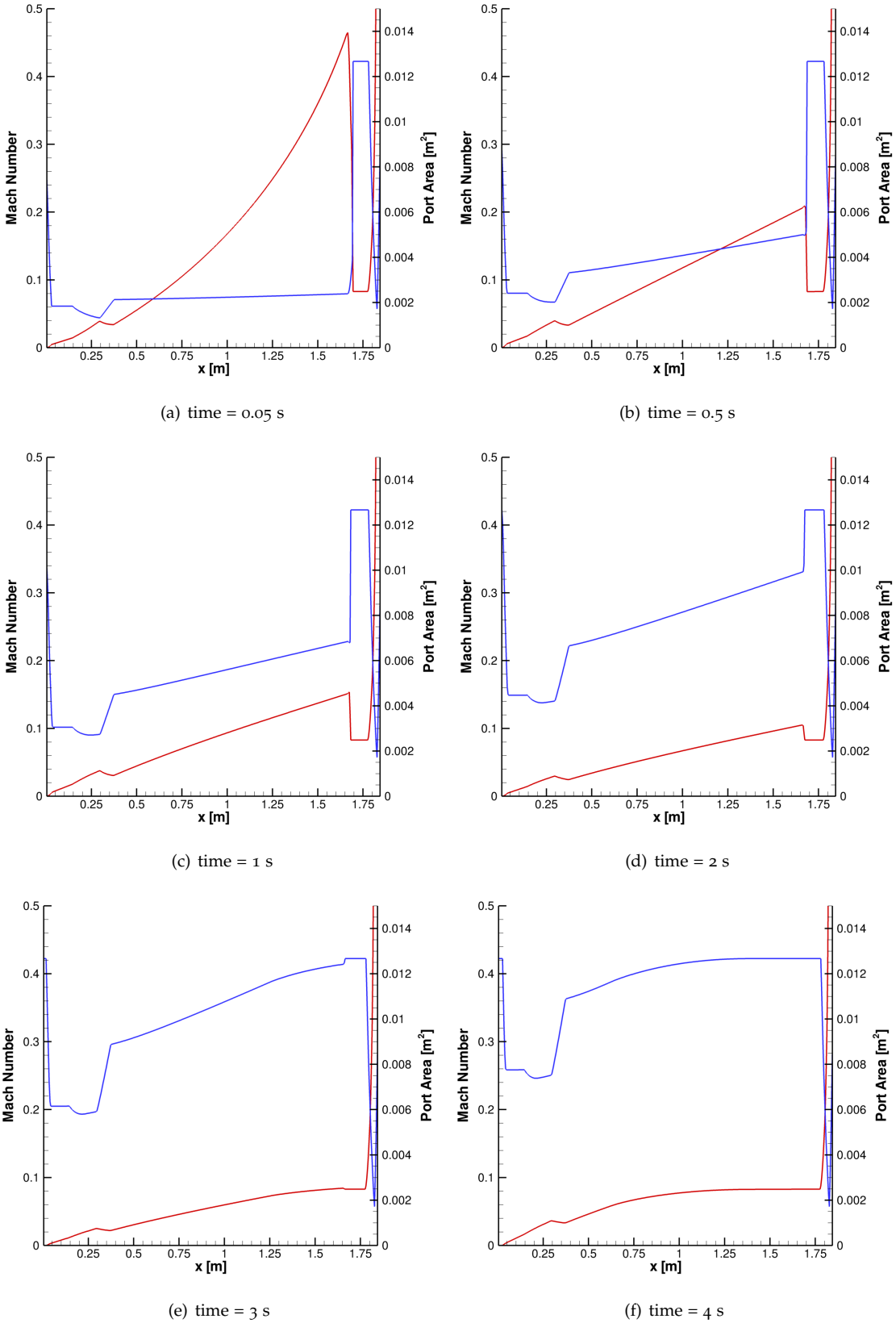

(a) time = 0.05 s

(b) time = 0.5 s

(c) time = 1 s

(d) time = 2 s

(e) time = 3 s

(f) time = 4 s

Figure 7.16: Mach Number field and port area geometry for different instants

an further enhancement on the SRM HEP spike in the last phase of the IT. However, it is clear by the analyses carried out that the pressure spike is for the major part driven by the grain erosive burning effect, due to the main flow in the combustion chamber, as shown.

In addition to possible modeling improvements, unknowns on the experimental and nominal input data used for the numerical simulation may also contribute, in an indeterminable way, to the disagreement between experimental and numerical pressure traces. However, as discussed before, the global trend of the experimental curve is successfully taken and these effects seem to be refinements of the internal ballistics numerical simulation presented. Thus, the results of the numerical simulation could be certainly improved in terms of agreement with the experimental data by a fine tuning exercise of the empirical and input coefficients of internal ballistics numerical simulation.

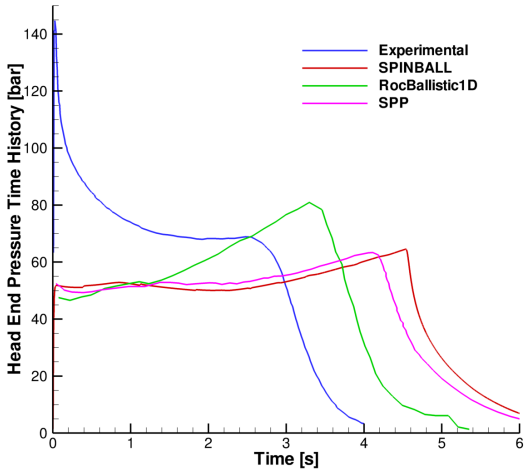

Figure 7.17: HEP numerical experimental comparisons without erosive burning: SPINBALL, Rocballist1D[108] and SPP [64]

As last analysis on the erosive burning driven behaviour of the SRM, the Q1D numerical simulation without the erosive burning effect is compared with the ones published in [108; 64], yielded with Rocballist1D and SPP deactivating the erosive burning (see figure 7.17). The differences between the SPINBALL model with and without the erosive burning are so evident, and quite widely discussed before. Moreover, the comparisons between the instantaneous grain inlet mass flow rate and the burning surface evolution in time are shown in figure 7.18, for the 0D quasi steady model and the Q1D model (with and without erosive burning). We want in fact to stress the attention on the effects of the different modelings in the characterization of the motor HEP evolution and to underline the huge differences obtained with a Q1D model with respect to a 0D model, in terms of prediction capability and description of the internal ballistics driving phenomena.

These enforce how all the SRM internal ballistics is driven by this phenomena, because of the grain shape and also how the combustion surface evolution in time changes because of the erosive burning effects. While all the small, but present, differences, especially in the first part of the QSS, between the SPINBALL without the erosive burning contribution and the 0D quasi steady model, are related to the total pressure drops along the motor axis already analyzed, that the 0D model can not take into account. Certainly these effects result in different evolutions in time of the burning surface, propellant mass inlet and averaged burning rate, as defined in the equation 7.2, and shown in figure 7.18.

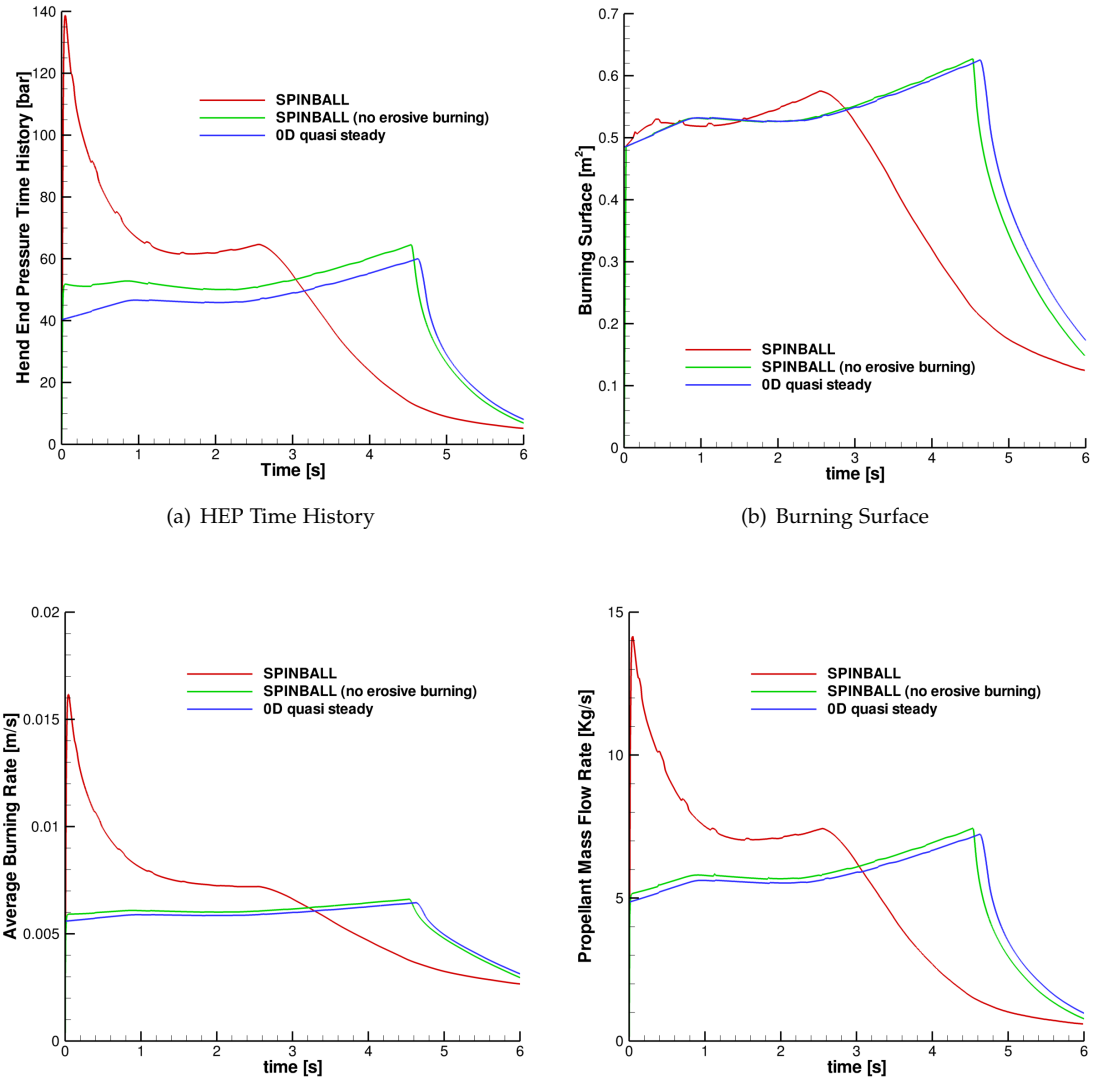

(a) HEP Time History

(b) Burning Surface

(c) Burning Rate

(d) Propellant Mass Flow Rate

Figure 7.18: Models Comparison: SPINBALL Q1D, SPINBALL Q1D without erosive burning and 0D quasi steady model

7.3 NAWC Motor n. 13

NAWC Motor n. 13 is also analyzed in order to further test the SRM internal ballistics simulation tool developed. The SRM data are available in literature [47; 62; 108; 71], as for the previous motor NAWC n. 6.

The motor grain and its geometrical initial configuration, shown in the paragraph 6.3, page 123, is represented by a simple cylindrical grain, with a cone shape at the aft-end of the motor. The case is a simple cylindrical case.

The propellant used in motor n. 13 is the NWR11b propellant, which composition is reported in the table 7.2. It has a burning rate of 0.541 cm/s at 6.9 MPa, a pressure exponent of the APN De Vieille Saint Robert of 0.461 [62; 108] and a density of about 1700 Kg/m^3 [93; 71].

Component	Mass Percentage
AP	83 %
HTPB	11.9 %
Oxamide	5 %
carbon black	0.1 %

Table 7.2: NAWC Motor n. 13 Propellant Composition

As for the NAWC motor n. 6, the thermophysical properties of the grain propellant combustion products have been evaluate starting from the propellant composition with the CEA code [38; 44], for some pressure values, in the pressure operative range of the motor (from about 1 to about 50 bars). No nozzle area variation is defined by the experimental results. Hence, a constant value of the nozzle throat diameter and the nozzle configuration is considered during the internal ballistics numerical simulation.

As for the NAWC n. 6, a first attempt to make the numerical simulation of the SRM internal ballistics is considered with a simple 0D quasi steady model (as expressed by the equation 7.4), without any kind of calibration parameter.

The nominal input available in literature is considered.

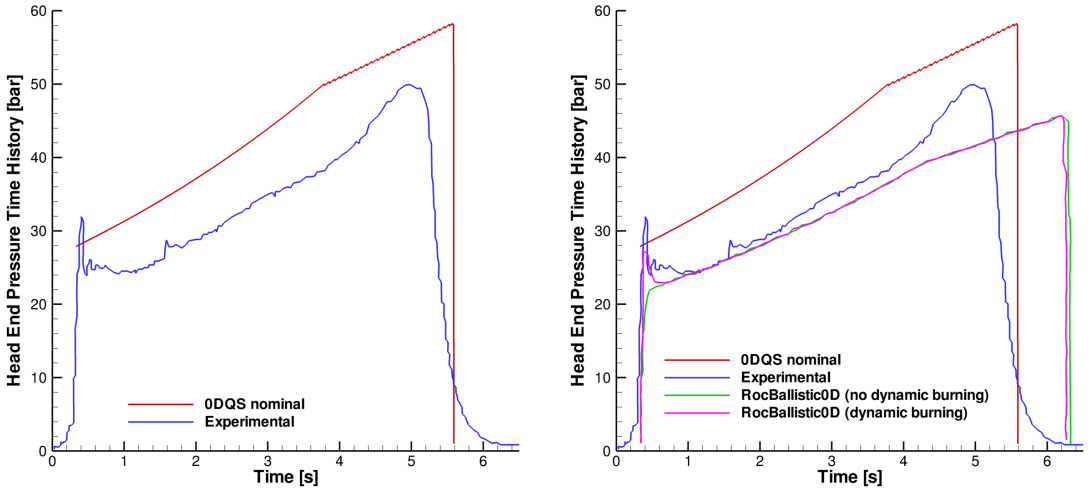

(a) Experimental and Numerical 0D quasi steady simulation

(b) Experimental, Numerical 0D quasi steady simulation and RocballistoD simulation (with and without dynamic burning contribution) [108]

Figure 7.19: HEP experimental numerical comparisons for 0D internal ballistics models

The comparison between the HEP obtained with the 0D quasi steady model and the experimental pressure trace is shown in figure 7.19(a). While the figure 7.19(b) considers also the

numerical pressure trend published in [108], with a 0D unsteady model with and without the dynamic burning contribution (named RocballistoD).

As for the NAWC n. 6, all the details related to the igniter configuration miss in the SRM description of the SRM present in the literature. Hence, the ignition transient is not simulated in all the numerical simulations here presented. However, the 0D quasi steady model and the RocballistoD unsteady model are not able to describe the IT phenomena. Hence, in order to compare the numerical HEP curve with the experimental one, a translation of the numerical simulation of about 0.33 s (in accordance with [108]) is made for the simulation timeline. Figure 7.19 shows that using the nominal input, as reported in literature, the simulated pressure trace is be all higher with respect to the experimental one. This fact is experimented also in [71], where a 0D internal ballistics model with the ZN and an empirical flame modelling for the grain combustion processes, are considered to simulate NAWC Motor n. 13.

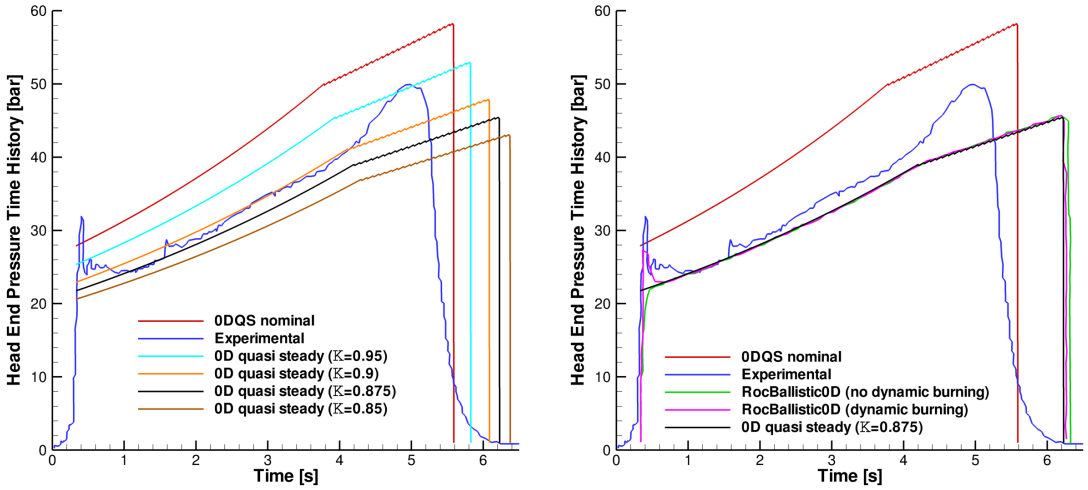

(a) Experimental, Numerical 0D quasi steady simulations variation of the K parameter

(b) Experimental, Numerical 0D quasi steady simulations

Figure 7.20: HEP experimental numerical comparisons for 0D internal ballistics models

Thus, in order to catch a better correlation of the numerical simulation with the experimental data, a parametric study based on the variation of a calibration parameter K is made (see equation 7.5). This study is made in order to account for all non-idealities with respect to the nominal parameters. By a part to consider, through the hump, the burning rate uncertainties related to a scale factor effect and by the other to describe the chemical non-equilibrium of the grain combustion processes, with the combustion efficiency (the K parameter want to be the product of the two, in order to catch the numerical results yielded in [108]).

$$p(t) = \left(\rho_p \, a(T_i) \, K c^\star(t) \, \frac{S_b(web(t))}{A_t}\right)^{\frac{1}{1-n}}$$
$$K = h(web(t)) \, \eta_{c^\star} \tag{7.5}$$

Results on this investigation with the use of the 0D quasi steady model can be seen in the figure 7.20. These indicate that a very good correlation, in terms of numerical simulation performed with RocballistoD model, can be achieved by means of the use of a K value of 0.875. In the same time, difficultly these difference can be attributable to unsteadiness effects during the QSS accounted with one model with respect to the other. Note that the numerical noise in the 0D quasi steady numerical pressure traces is due directly to the numerical noise present in the combustion surface input given by GREG, already discussed in the paragraph 6.3, page 123. This evidence certainly puts in some doubts the input values reported in literature, because seems to

be quite unrealistic the low value found, to be attributable only to the combustion efficiency or to the scale factor.

Hence, as suggested in [71], a 0D simulation has been made considering a constant, pressure independent, flame adiabatic temperature of 2300 K, in order to have some correspondence with the experimental pressure trace. Even if, as also underlined by the authors, this seems to be too low with respect to the ideal adiabatic flame temperature of the propellant. The results of this simulation are shown for the 0D quasi steady model in the figure 7.21.

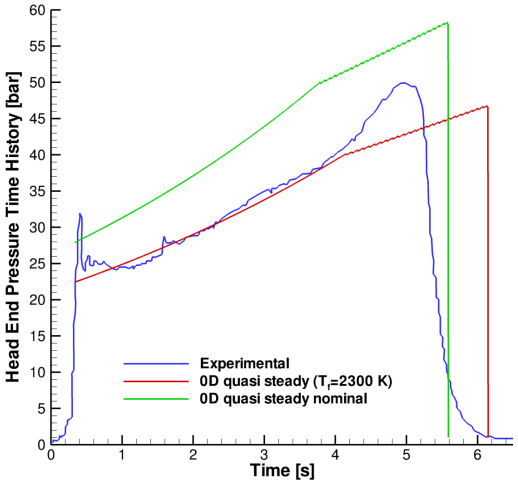

Figure 7.21: HEP Experimental-Numerical Comparison: nominal and modified adiabatic flame temperature

Notwithstanding, some remarks on the SRM internal ballistics numerical simulation can surely be done. The global QSS behaviour of the motor is quite well captured with both the 0D models (RocballistoD and the 0D model used). The dynamic burning has not effects on the overall burning rate during the QSS, so that the slope of the pressure rising is quite well defined, since related only to the progressive behaviour of the grain shape. The pressure peak occurring during the end of the IT, not present in both the 0D quasi steady model and RocballistoD with the solely APN contribution to the burning rate, seems to be related to a dynamic burning effect. This result is also obtained in other different articles [71; 72] where simple 0D models have been used too, but this point will be also discussed in the following. The last part of the experimental pressure trace, where we see a pressure rising, suddenly before the tail off phase and the consequently the tail off phase are not captured at all and are quite difficult to be explained, as in countertrend with the burning surface evolution.

Hence, for the problems encountered with respect to the input data found in literature, the Q1D numerical simulations are made considering a modified adiabatic flame temperature of the grain propellant of 2300 K, as discussed before. In fact, the determined K parameter, in a 0D model can be seen as the product of the combustion efficiency by the scale factor parameter, and hence it can be attributable in an undefined manner to their product. While in the Q1D model this difference becomes relevant, as the combustion efficiency and the scale factor have different effects of the pressure trace, as experienced by some numerical simulations performed.

The pressure traces for the Q1D model, with and without the erosive burning activated, can be seen in the figure 7.22, where also the burning surface, the average burning rate and the propellant grain mass flow rate are shown.

Hence, it is possible to remark that for the NAWC Motor n. 13, on the contrary to the motor n. 6, the total pressure drop effect is very small. In fact, they have a a maximum value, that can be estimated in around 0.5 bar, during the initial phase of the QSS. This is certainly related to the small values of the Mach number realized in the combustion chamber (see figure 7.23). In the meantime, the small, but present, differences between the pressures trace, yielded activating the erosive contribution to the burning rate and not, are, instead, attributable for the majority to the small effects of the erosive burning (as underlined in figure 7.23). Surely, with respect to the NAWC Motor n. 6, the effect of the erosive burning, as expected, is quite bounded. In fact, the predominant contribution to the grain burning rate is given by the quasi-steady pressure term of the APN De Vieille Saint Robert law, as figured out in figure 7.23. Moreover, during the grain recession, the crossflow velocities responsible for the erosive burning effect, decrease, as the port area increases (see the Mach number field). Hence the initial small contribution of the erosive burning decreases in time. These effects are responsible of the differences, in figure 7.22,

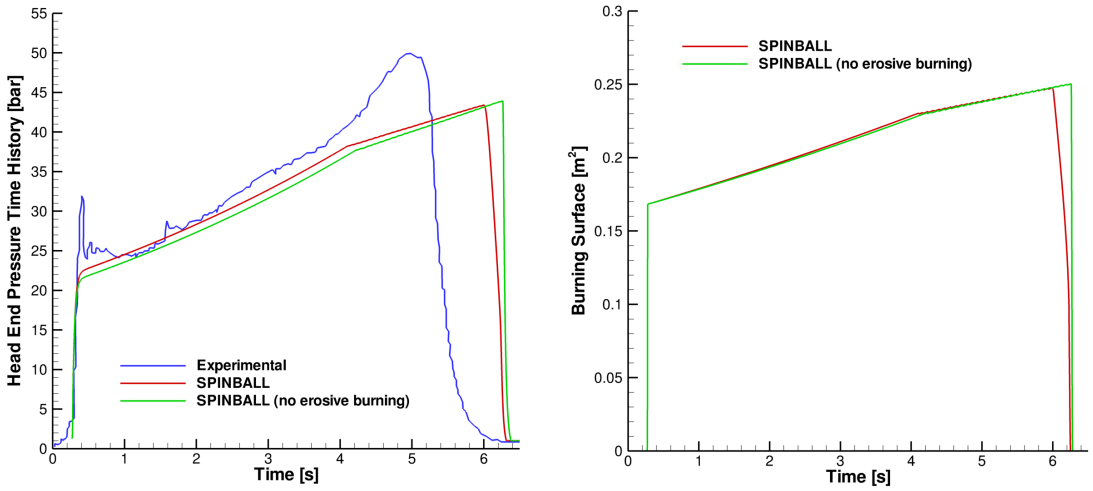

(a) HEP Time History

(b) Burning Surface

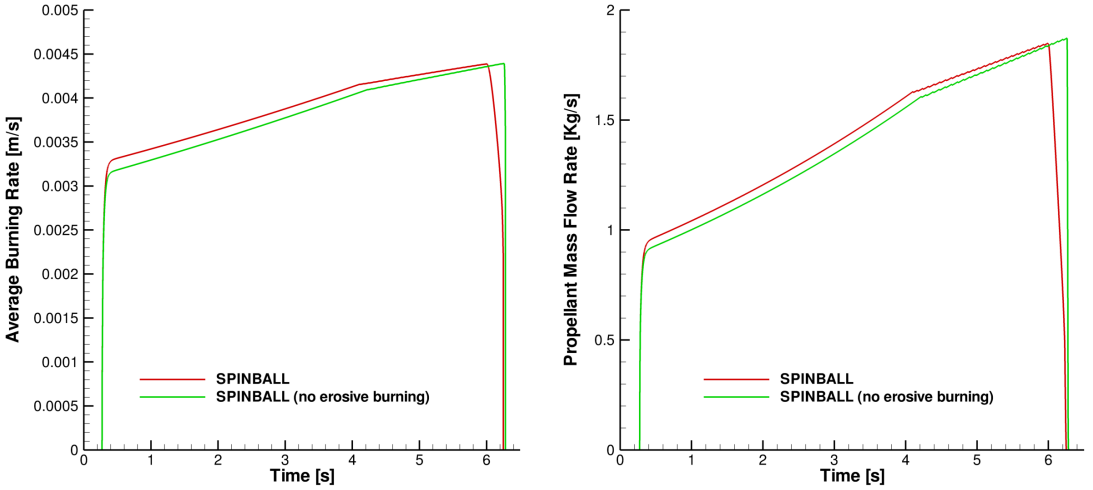

(c) Burning Rate

(d) Propellant Mass Flow Rate

Figure 7.22: SPINBALL Q1D, SPINBALL Q1D without erosive burning models comparison

between the two average burning rates (see figure 7.22(c)). Consequently we have the presence of small differences in the burning surface evolution in time (figure 7.22(b)), and at the end, to a different pressurization history of the combustion chamber between the case of the activation of the erosive burning and not (figure 7.22(a)).

Another relevant fact, present in the experimental HEP trace that deserves some remarks, is related to the pressure spike experienced in this motor, at the end of the Ignition Transient. In fact, on the contrary to the NAWC n. 6 motor, the pressure spike is not captured at all in the Q1D numerical simulation with the erosive burning activated. Two main mechanisms are proposed in the literature for the explanation of this pressure spike. The first one is associated to the low value of the characteristic length of this motor, given by equation 7.6, as the ratio between the bore volume and the nozzle throat area. This has shown to induce a so called bulk-mode instability due to the coupling of the bulk-mode pressure oscillations with the combustion dynamic burning effects [72; 71].

$$L^* = \frac{V_b}{A_t} \tag{7.6}$$

In [108; 72], indeed, the pressure spike is simulated with success with a simple 0D unsteady numerical simulation of the chamber flowfield conditions, using the dynamic burning model of Zeldovich-Novozhilov (see paragraph 2.2.3, page 23). In particular in the second one [108], with a Q1D unsteady model of the internal ballistics, the pressure peak is captured deactivating the erosive contribution of the burning rate and using the ZN model to describe the dynamic burning.

The second explaining mechanism for the pressure spike is, instead, attributed to an ignition phenomena and/or as caused by an erosive burning effect [47; 64]. In other words, the phenomenon is similar to what is experienced for the numerical simulation of the Zefiro 23 Ignition Transient, illustrated in the paragraph 7.1.3, page 138. This is related to the combined effects: the igniter jet erosive burning of the grain propellant surface and the igniter tail off, during the end of the IT.

Unfortunately, as no details are given of the igniter configuration for the NAWC motor n.13, it is not possible to perform a numerical simulation during the IT. Hence, it is quite difficult to have a clear idea of the nature of the pressure spike in this case, as also a dynamic burning model, at the state of the art, is missing in the SPINBALL model.

A part from the problems experienced and underlined (also in [72]) with the motor input data, the Q1D and 0D models draw out both a quite well prediction of the global motor behaviour. This can be resumed by the comparison between the experimental and numerical HEP, underlining the effects of the various phenomena on the internal ballistics numerical simulation for this SRM. Certainly, in order to have a better agreement between the numerical and the experimental pressurization history, some other investigations on the nominal input data and on the semi-empirical models fine tuning should be required. However, what remains at this point something related to a complete non-nominal behaviour of the NAWC motor n. 13, that is not predictable by our models, but also by the ones published in the literature [108; 72], is the pressure trend just before the tail off phase. In [72], the authors hypothesized that this SRM behaviour could be accounted considering the axial variation of the burning rate, arising from the inclusion of the erosive burning, and also the total pressure drops for this motor (that their 0D can not describe). In the light of the results yielded with the SPINBALL model and the Rocballist1D[108], this hypothesis seem to be excluded. Hence, we suppose that this experienced pressure trace in the last part of the SRM QSS could be seen in a non-nominal behaviour of the motor. In fact, the rest of the internal ballistics of the SRM is quite well captured. This hypothesis, however, should need an intense study to be proved in terms its possible causes (however possible with the presented tool), that goes over the scope of this work.

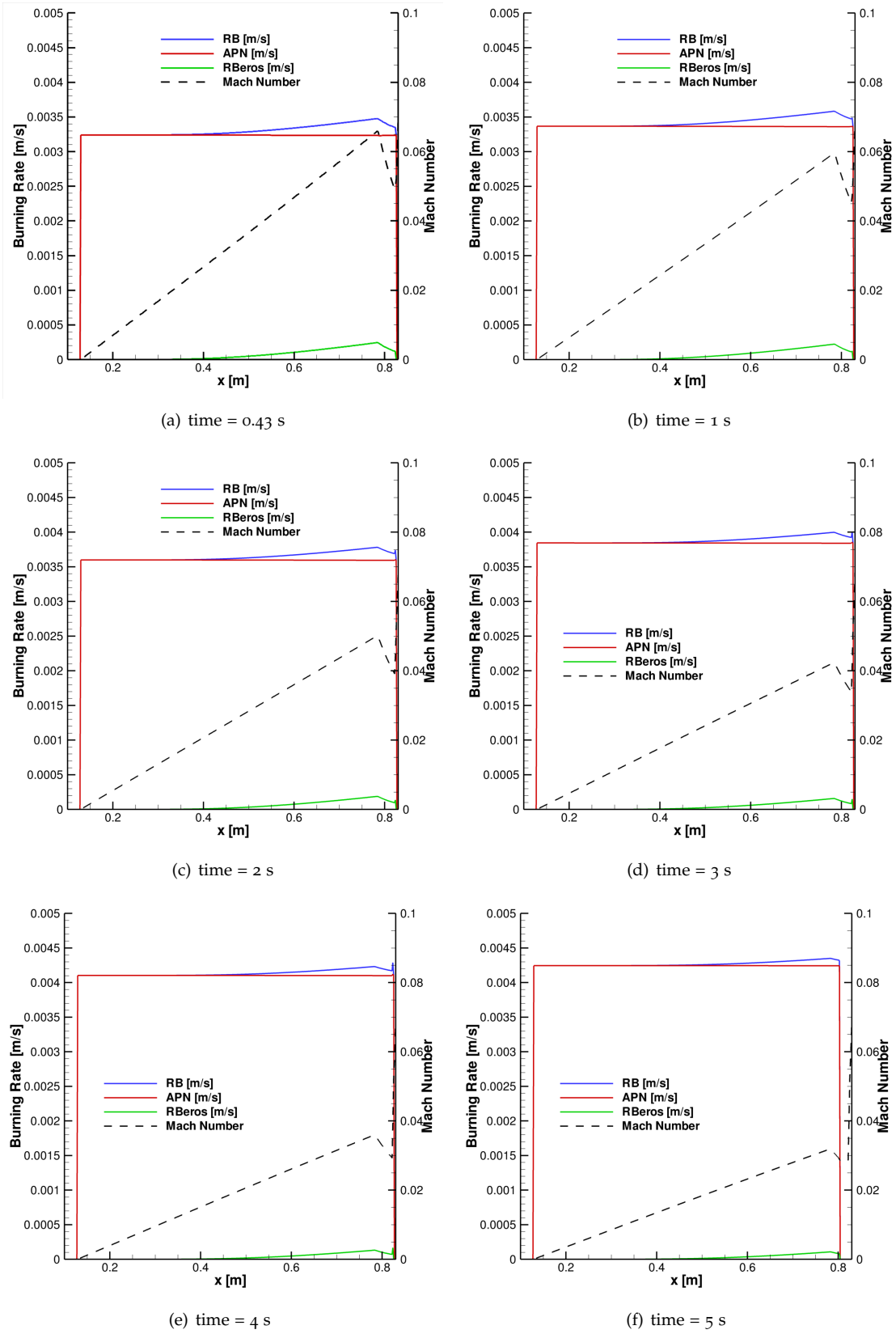

(a) time = 0.43 s

(b) time = 1 s

(c) time = 2 s

(d) time = 3 s

(e) time = 4 s

(f) time = 5 s

Figure 7.23: Burning Rate components and Mach Number field for different instants for the SPINBALL simulation with erosive burning

Conclusions

In this study a Q1D unsteady internal ballistics numerical simulation model has been developed to simulate the Solid Rocket Motors internal flowfield conditions during all the motor combustion time, from ignition to burn out. The main result is a main step towards a major understanding and modeling capability of main physical, chemical, complex interacting phenomena that lead SRMs behaviour and, consequently their performaces and mission capabilities. Some of these phenomena, in fact, are still not well understood, at the present state of the art of the SRMs modelling capabilities.

In particular, the result of the research activities carried out can help all the design and development phases related to the realization of a SRM, as propulsion system for space applications, by both research and industrial points of view. The internal ballistics simulation tool developed can, in fact, overcome the modeling lacks related to the use of simple 0D quasi-steady or unsteady models, typically used up to now, for the SRM internal ballistics analyses during Quasi Steady State and Tail Off phase. In the same time the Q1D model keeps the computational time required for the entire combustion time numerical simulation bounded. Hence, it can be used as a simulation tool both for refined design feasibility and parametric studies with the variation of the main SRM design options, and for the prediction and the post-firing test reconstruction analyses of a given SRM.

At the state of the art of the open literature, in fact, it is quite difficult to find SRM internal ballistics models able to simulate the entire motor combustion time, from the Ignition Transient to Tail Off. Hence, the original idea of this thesis work is to present a model, more accurate than the ones typically used up to now for the numerical simulation of the SRM simulations. By an industrial point of view, this can help in reducing the huge experimental analyses related to their development and design. But also, by an academic point of view, it represents an analysis and simulation capability of the overall SRM internal ballistics, useful in order to have a better understanding of a motor nominal and off-design performances key driving mechanisms.

The activities which have led to this final goal can be summarized into two main steps, described as follows.

The first step has been the development of a numerical simulation model, able to accurately describe the grain burning surface evolution during time. In fact, the main driving mechanism that dictates the SRM internal ballistics is represented by the grain burning surface evolution and the bore geometrical variations, related to the solid propellant combustion processes occurring the motor chamber.

In particular, the choice of the technique developed and implemented has gone towards a completely general method for the tracking interface problem solution. In fact, it has applications more far and away distant than the application to the grain burnback analysis. This has allowed to have a completely general method, useful to deal with the motion along the normal direction of whatever complex 3D grain shape, even with topological changes, with possible merging and breaking of the grain surface, by means of the Level Set Method. Even if the scientific audience, in recent works, has considered the use of the Level Set technique with applications to the grain burnback analyses, the way in which this method has been developed for the purpose is quite a novel and never presented approach for the considered problem.

Typically, in fact, the other published works using the Level Set Method for the study of the grain burning surface evolution in time, consider the numerical integration of the Level Set

equation in Cartesian rectangular grids. In such a manner, the symmetry and/or periodicity properties the grain shapes, held even by the more complex and 3D grain propellant geometries, are not exploited at all. Hence, these properties are not respected during the front motion, if maintained because of particular grain velocity along the normal direction (for example constant, for the majority of the published works).

In the numerical model developed, instead, the Level Set equation integration has been made in cylindrical meshes, exploiting, in the same time, the grain propellant shape symmetry properties during its motion. This allows moreover to limit the computational domain, or for the same computational grid dimension, to have a higher accuracy in the numerical simulation of 3D grain burning surface evolution.

Moreover, in order to deal with the typical complex 3D grain shapes used in real motor applications, as finocyl grains, a novel, smart and automatic initialization technique of the Level Set problem has been developed. This is based on a banded Signed Distance Function construction, that uses directly the CAD representation of the grain propellant combustion surface. In such a manner, the grain burnback analysis can be directly made from the grain design and production process of the mandrel. In fact, the input necessary to set the Level Set Initial Condition is given by the grain surface StereoLithography representation, in which the introduced approximations are related only to the numerical approximation of a 3D surface by its triangular tessellation. Hence, for ballisticians applications no difficult for the 3D grain surface prototyping or modeling is necessary. The same procedure, moreover, can be utilized also to build an automatic cylindrical structured mesh for a 3D CFD numerical simulation of the flowfield conditions during the motor start-up.

At last, in order to couple the 3D grain burnback solver with the SRM internal ballistics model, an intense review of the Dirac Delta and Heaviside regularization techniques with application on Level Set technique (and other applications too), has been made. This study has been made in order to avoid the known problems of regularity and convergence of the standard methods, widely used in the Level Set community, to extract the level zero geometrical properties, such areas, surfaces, volumes and perimeters. In fact, this has carried to the implementation of a completely automatic and robust second order Dirac Delta and Heaviside regularization method that applies to both Cartesian rectangular and cylindrical structured grids, due to Min and Gibou and recently appeared in relevant publications. Moreover, in this framework, the use of the boolean algebra of the implicit functions to evaluate the grain and case/Thermal Protections casing interfaces interaction is a novel solution, that seems to be not explicitly used and published until now, in the open literature.

All these novel aspects in solving the problem of the grain burnback analysis have been introduced and implemented in a completed automatic numerical simulation model, for the study of the grain burning surface evolution in time, named GREG (completely developed starting by scratch). The GREG model, as results, is able to deal with whatever complex grain initial shape and Thermal Protections boundary surface and to describe its motion along the normal direction.

In the second part, the development and updating of the mathematical, physical and numerical models of an existing internal ballistics numerical simulation model, named SPIT, have been carried out. This work has been necessary in order to overcome the limits of the code to yield, with very successfully results, numerical simulations of the solely IT phase.

In this direction, a re-formulation of the gasdynamical solver has been made with the target to account for the variations with pressure of the grain combustion products and the non-ideal chemical equilibrium of the exothermic grain combustion processes, through the combustion efficiency. In such a manner, the potential possibility to account also the effect, especially during the final part of the QSS and during the TO, of the motor casing Thermal Protections ablation phenomena is ensured, if the introduction of a proper ablation model for them, will be introduced.

A review and updating of the grain burning rate models has also been made, in order to represent the effects, in some cases very relevant, of the erosive burning on the SRM internal

ballistics. These effects, in fact, can be important not only during the IT, as SPIT considers, but also during QSS phase.

All these activities have been defined the implementation and the development of a Q1D numerical simulation tool for the SRM internal ballistics numerical simulation, during the entire combustion time, named SPINBALL. This model has been, hence, coupled with the 3D grain burning surface evolution model GREG. The result can be considered, at now, a novel approach for the overall combustion time numerical simulation of SRMs.

Thus, the analysis and the numerical simulation of three SRMs has been made: Z23, NAWC Motors n. 6 and 13. The results yielded by SPINBALL have shown that the presented approach can be successfully used for the numerical simulation of the entire SRM combustion time, from the motor start-up to its burn-out. Hence, the developed numerical tool can be used both for preliminary analyses, for selecting the motor main motor design options, but also for the reconstruction and prediction of selected SRMs configurations.

In this framework, certainly, some characterization activities on the semi-empirical parameters of the sub-models used are necessary. But this can be achieved by means of some parametric analyses, which the proposed approach allows, thank to the low computational time required to perform each simulation. Notwithstanding, the motor NAWC n. 6 and 13 have shown an acceptable level of correlation with the experimental data, provided by blind numerical simulations with the use of the nominal motor input parameters, without a fine tuning of the sub-models.

Moreover, the use of the SPINBALL model, for the simulation of the Z23 SFT, allows to state the ability of the model as reconstruction tool of a motor behaviour, if the necessary non-ideal parameters characterization (hump and combustion efficiency) and nozzle throat area evolution is made. In particular, it has been used to validate the 0D quasi steady model, underlining the possible effects of a more accurate modelling, on the SRM internal ballistics reconstruction.

Then, the numerical simulation of the ignition transient of Z23 has underlined as the taking into account for the grain geometrical variations has very low effects on the IT numerical simulation. However, it may have, instead, sensible effects in the mass budget for full internal ballistics computations.

The Z23 IT numerical simulation has, moreover, shown that the causes of the pressure spike, during the last part of the IT, are related to the combined concurrent effects of the igniter Tail Off and of the erosive burning, due to igniter jet impingement on the grain surface. While, during the QSS, the erosive burning effects for this motor are very small, almost negligible, with respect to the quasi steady burning rate contribution.

The numerical simulation of the two NAWC motors n. 6 and 13 have enforced the ability of the model in capturing and representing the main driving internal ballistics phenomena. In particular, the NAWC motor n. 6 simulation has defined, in agreement with a previous published work, that the nature of the pressure peak immediately after the IT is due to a very relevant erosive burning, due to the motor selected configuration. This effect for this motor is particularly relevant, in such a manner, to deviate the pressure trace from the one related to the progressive grain surface design, affecting completely the internal ballistics of the motor. The results have underlined a good agreement of the predicted HEP time history with respect to the experimental one, with a quantitative and qualitative agreement of the motor real behaviour.

In the opposite, the numerical simulation of motor NAWC n. 13, has shown that the erosive burning effect is not directly responsible for the pressure peak at the end of the Ignition Transient. This, instead, can be attributable to both dynamic burning effects and erosive/ignition transient effect, similar to what experienced in Z23. While, during the Quasi Steady State of the motor, the erosive burning contribution to burning rate is small, but with a not completely negligible effect on the motor behaviour.

In conclusion, a general, robust, efficient and automatic 3D model for the study of the grain burning surface evolution has been presented with successfull results. This model can be easily

coupled with 0D and Q1D models to study the internal ballistics of SRMs. A Q1D unsteady model to study and analyze the internal ballistics of SRM from motor start-up to burn-out has also been presented. This model has shown great potentials and, thus, represents a promising tool to obtain a more accurate representation of the internal ballistics driving phenomena and their characterization, with respect to more simple 0D models, typically used for the simulation of the SRMs during the QSS and TO.

Certainly, the path for a complete understanding of the SRM issues related to internal ballistics is far to be closed. In fact, the involved phenomena are typically multi-physical non-linear and complex interacting with each other. In this framework, the need of the implementation of a dynamic burning model, such the one suggested by Zeldovich-Novozhilov is quite straightforward and possible. In fact, it should allow to study the so called L^* effects, related to combustion stability and flowfield/combustion coupled phenomena.

Moreover, the implementation of a nozzle Thermal Protections ablation model able to characterize the phenomena which can affect typically the SRM behaviour should be considered. This model could be a reduced and simplified representation of the more complex ablation/erosion phenomena, with semi-empirical parameters, coming from experimental tests and/or more refined models of the coupled ablation/flowfield mechanisms.

Another step could be related to the description of the possible acoustic instabilities related to vortex shedding/acoustic coupling phenomena, to which some SRMs configurations area prone (P80FW and Ariane 5) during QSS. In fact, these bring typically to a chamber main acoustic frequencies excitation and thrust oscillations, small but sustained, that are important at the system level of a SRM design. In order to characterize these phenomena, a reduced model of the vortex sound, that is generated by the shear layer instability could be considered. It should describe the two loops involved in the driving mechanism of the vortex shedding phenomena, as they appear in specific geometrical and flowfield conditions during QSS. Hence, the presented Q1D model becomes mandatory, in order to try the representation of such acoustic effects. Moreover, the 3D grain burnback model presented can also help in the understanding of such phenomena, giving to 3D flowfield Navier Stokes models, the 3D geometrical configuration of the SRM, during which the buffets happen.

At last, a complete coupled grain burnback/internal ballistics flowfield model with the on-line coupling way is a result at the horizon. Such an approach for the SRM numerical simulation has been never published, until now, in the open literature. It could be very useful, in fact, in order to have a finest representation of the effects on the internal ballistics, in case of burning rates with high axial non-uniformity, as experienced and underlined in the results analysis of the NAWC motor n. 6.

Appendices

H

0D Quasi Steady Model

A quasi steady 0D model has been developed by Department of Mechanics and Aeronautics (DMA) Space Propulsion quasi Research (SPqR) Team for the determination and reconstruction, during the QSS and TO phases, of the non-ideal parameters behavior of the motor and the nozzle throat area evolution. These parameters take into account the non-ideal behaviour of a SRM with respect to:

- the grain propellant combustion rate, typically coming from small tests for the propellant characterization and the uncertainties on the grain propellant burning surface evolution, both taken into account with the hump parameter;
- the non-ideal equilibrium point of the grain combustion products exothermic chemical reactions, considered in the combustion efficiency;
- and the nozzle efficiency to characterize, typically, divergence, boundary layer losses and frozen flow effects in the nozzle expansion flow.

In particular, the procedure presented here, since used in this thesis work, is able to evaluate the hump law, the nozzle throat erosion/ablation, the combustion and nozzle efficiency, in the assumption of a simple 0D quasi-steady model for the internal ballistics. It considers as input the following experimental data:

- the grain propellant mass loaded;
- the initial and final nozzle throat area values;
- the propellant combustion characterization in terms of a and n of the APN combustion law;
- the combustion products characterization and the adiabatic flame temperature evaluation, by means of the chemical equilibrium assumption for the grain propellant combustion reactions;
- the propellant density;
- the nominal evolution of the combustion surface in web, assuming a spatially constant burning rate, in accordance with the 0D model;
- and the head end pressure and thrust measures, from the SRM firing data (typically SFT).

The SFT reconstruction, in terms of the mathematical procedure, can be described, as follows. Assuming the use of a 0D quasi steady state model, the pressure in the chamber is given by the equation (H.1). Where the non-ideal parameters have been introduced and the explicit dependence of the quantities is given.

$$\tilde{p}(t) = \left(\rho_p \, a(T_i) \, h(web(t)) \, \eta_{c^\star} \, c^\star(t) \, \frac{S_b(web(t))}{A_t(t)} \right)^{\frac{1}{1-n}} \tag{H.1}$$

The burning rate model is the classical APN model given by the equation (H.2).

$$r_b = a(T_i) \left(\frac{p}{p_{ref}} \right)^n \tag{H.2}$$

The combustion efficiency and the characteristic velocity are, then, defined in the equations (H.3) and (H.4), respectively.

$$\eta_{c^\star} = \frac{\int_0^{t_b} \frac{\tilde{p}(t) \, A_t(t)}{c^\star(t)}}{M_p} \tag{H.3}$$

$$c^\star(t) = \frac{\sqrt{\frac{RT_f(t)}{\mathcal{M}(t)}}}{\Gamma(\gamma(t))} \tag{H.4}$$

Where all the propellant combustion products thermophysical properties and the adiabatic flame temperature are assumed to be variable with pressure. These parameters are given by the chemical equilibrium evaluation of the propellant exothermic reactions products (evaluated, for example, with the computer program for calculation of complex Chemical Equilibrium compositions and Applications (CEA)[38; 44] code).

The nozzle efficiency, therefore, is given by the equation (H.5), where with "tilde" are indicated the measured data of the head end pressure pressure and of the SRM thrust.

$$\eta_{c_F}(t) = \frac{\tilde{F}(t)}{c_F(t) \, \tilde{p}(t) \, A_t(t)} \tag{H.5}$$

Hence, the equations (H.1), (H.3) and (H.5) represent a set of $2N+1$ equations, where N is the number of the chosen samplings of the reconstruction in time.

In this set of equations, the unknowns are $3N+1$: the evolution of the nozzle throat area $A_t(t)$, the combustion efficiency $\eta_{c^\star}$, the nozzle efficiency $\eta_{c_F}(t)$ and the hump law $h(web(t))$.

The problem, hence, is mathematically unclosed without any further assumption. The simplest assumption on the unknowns can be set on the throat area evolution law, considering the following constraints: the experimental data define its initial and final value and this law can be assumed to be monotone increasing.

To set these N values, with imposed starting and final values, a simple model for the ablation/erosion of the nozzle throat area can be considered [40]. It assumes that the mass flow rate and, consequently, the regression velocity of the throat area is dependent through a calibration coefficient on the heat fluxes due to convection from the chamber hot gases, as expressed in the equation (H.6). Thus, the convective heat flux coefficient can be given by semi-empirical laws, like the Bartz[3] one.

$$\dot{D}_{throat} = k_{ab} h_c (T_{throat} - T_{wall}) \tag{H.6}$$

At last, we consider the case that the attention is only focused on the internal ballistics, without the availability of the experimental thrust data, i.e. in the case of an instrumented flight. The problem can be, in this case, rearranged in terms of $N+1$ equations (pressure and combustion efficiency definition) and $2N+1$ unknowns (hump law, nozzle throat evolution and combustion efficiency), without any characterization of the nozzle efficiency. The problem, hence, is still unclosed and can be closed in the same manner of the previous one: modelling or choosing a nozzle throat evolution in time, with the constraints of its final and initial values.

I

Instability of the marker particles seen in a Hamilton-Jacobi fashion

In this section we follow what analyzed in [31]. We want to to show in some details the aforementioned difficulties of the marker and particles techniques in solving a class of problems, which can be described by an Hamilton-Jacobi equation (the case of motion velocity along the normal direction included). In fact, these Lagrangian techniques do not embed in their formulation an entropy condition, which is required for the solution of the problem and present, instead, in the Level Set formulation.

Consider, hence, the general first order 1D Hamilton-Jacobi equation, with a smooth initial condition:

$$\begin{cases} \phi_t + H(\phi_x) = 0 \\ \phi(x, t=0) = \phi(x_0(s), 0) = \phi_0(s) \end{cases} \tag{I.1}$$

Differencing this respect to x, we have an hyperbolic equation similar to conservation laws (as shown in the paragraph 3.3.2, page 43)

$$\frac{\partial \phi_x}{\partial t} + \frac{\partial H(\phi_x)}{\partial x} = 0$$

The method of the characteristics says that:

$$\phi_x = \text{const} \quad \text{along} \quad \frac{dx}{dt} = \frac{dH(\phi_x)}{d\phi_x}$$

Introducing, now, the metric g and the azimuth θ:

$$\begin{cases} g(s,t) = \sqrt{x_s^2 + y_s^2} \\ \theta = \tan^{-1}\left(\frac{y_s}{x_s}\right) \end{cases} \qquad \text{where} \qquad \begin{cases} x = x(s,t) \\ \phi = \phi(s,t) \end{cases}$$

it is possible to write down immediately for the case of $V = 1$ (equation 3.4), the following equation, which is a particular form of the equation 3.7:

$$\begin{cases} \theta_t = 0 \\ g_t = \theta_s \end{cases} \quad \Longrightarrow \quad \begin{bmatrix} \theta \\ g \end{bmatrix}_t = \begin{bmatrix} 0 & 0 \\ 1 & 0 \end{bmatrix} \begin{bmatrix} \theta \\ g \end{bmatrix}_s$$

This last is a slightly ill-posed non-strictly hyperbolic system, which solution is simply given by:

$$\begin{cases} \theta = \theta_0(s) \\ g = g_0(s) + t\,\theta_0'(s) \end{cases}$$

It is ill-posedness is clearly manifested as $g(s,t) \to 0$, condition that corresponds to a characteristics coalescence of the starting problem that occurs for the time:

$$t_{blow-up} = \min\left(\frac{g_0(s)}{\theta_0'(s)}\right)$$

This may be even seen for the general 1D Hamilton-Jacobi equation I.1 when the second derivatives of the $\phi(x)$ loses to be monovalued, as a consequence of the intersection of different characteristics (note that the problem may create shock in its derivative formulation):

calling $u = \phi_x$ the derivative form of the equation I.1 is

$$\frac{\partial u}{\partial t} + \frac{\partial H(u)}{\partial x} = 0 \quad \Longleftrightarrow \quad \frac{\partial u}{\partial t} + \frac{\partial H}{\partial u}\frac{\partial u}{\partial x} = 0$$

considering the solution blowing-up:

$$\frac{\partial H(u)}{\partial x} = \frac{\partial H(u)}{\partial x_0}\frac{\partial x_0(u)}{\partial x} = \frac{\frac{\partial H(u)}{\partial x_0}}{\frac{\partial x(u)}{\partial x_0}}$$

now, by the integration in time of the characteristic line equation

$$\frac{\partial x(u)}{\partial x_0} = \frac{\partial\left(x_0 + \frac{dH}{du}(t-t_0)\right)(u)}{\partial x_0} = 1 + \frac{\partial\left(\frac{dH}{du}\right)}{\partial x}t = 1 + \left.\frac{\partial^2 H}{\partial u^2}\right|_{u=u_0}\frac{\partial u_0}{\partial x}t$$

consequently the blow-up time is:

$$t_{blow-up} = \frac{1}{\max\left(\left.\frac{\partial^2 H}{\partial \phi_x^2}\right|_{u=u_0}\frac{\partial^2 \phi_0}{\partial x^2}\right)}$$

This time, considering the Hamiltonian expression for the given problem

$$H(\phi_x) = V\sqrt{1+\phi_x^2}$$

assumes the expression:

$$t_{blow-up} = \frac{1}{\max\left(\frac{(\phi_0)_{xx}}{\left(1+(\phi_0)_x^2\right)^{\frac{3}{2}}}\right)} = -\min\left(\frac{1}{K(x,t=0)}\right)$$

where K is the curvature of the front. This equation is exactly alike the equation 3.12, obtained in another way.

J

Some Schemes for the Hamilton-Jacobi Equation

J.1 1D Hamilton-Jacobi Equations

The general form of a numerical scheme for the one dimensional Hamilton-Jacobi equation can be expressed as:

$$\phi_j^{n+1} = \phi_j^{n+1} - \Delta t\, \tilde{H}\left(\phi_x^-, \phi_x^+\right) \tag{J.1}$$

so that, in order to give the expression of a particular numerical scheme, it suffices to show the form of the correspondent numerical Hamiltonian $\tilde{H}\left(\phi_x^-; \phi_x^+\right)$.

Lax-Friedrichs (LF) [21]

For the Lax Friedrichs (LF) scheme, we have[1]:

$$\tilde{H}_j^{LF}\left(u_j^+, u_j^-\right) = H\left(\frac{u_j^+ + u_j^-}{2}\right) - \frac{1}{2}\alpha\left(u_j^+ - u_j^-\right) \tag{J.2}$$

where:

$$u_j^\pm = D^\pm \phi_j = \pm\frac{\left(\phi_{j\pm1} - \phi_j\right)}{\Delta x}$$

$$\alpha = \max_{\phi_x \in [\phi_x^{min}; \phi_x^{max}]} \left|\frac{dH\left(\phi_x\right)}{d\phi_x}\right| = \max_{u \in [u^{min}; u^{max}]} \left|\frac{dH\left(u\right)}{du}\right|$$

The scheme is monotone for:

$$u^\pm \in \left[u^{min}; u^{max}\right]$$

The maximum and the minimum values in the previous expressions are chosen over the entire computational domain. Hence, the main consequence of this "global approach" is that the same value of the dissipation coefficient α (that control the numerical viscosity introduced by the method[2]) is used in regions where the "velocities" $(dH/d\left(u\right))$ are small and large indifferently. This decreases the quality of the solution because of the increasing of the amount of the numerical dissipation in regions where this is not necessary (so while the method is stable and

1 other such schemes of this general type, like Lax-Wendroff and Fromm's method, could be used too

2 note:

$$\frac{u_j^+ - u_j^-}{2} = \Delta x\, D_j^2 \phi \approx \Delta x \frac{d^2\phi}{dx^2}$$

so that:

$$\frac{1}{2}\alpha\left(u_j^+ - u_j^-\right) \approx \alpha \Delta x \frac{d^2\phi}{dx^2}$$

will give an accurate solution as the mesh is refined, it can be smeared out and lost accuracy in some parts in a mesh).

The previous disadvantage of use of global dissipation coefficient is passed by the introduction of a local evaluation of the α, as given in the equation J.2. This allows to introduce the following derived scheme from the LF one:

- **Stencil Lax-Friedrichs (SLF)**
  The evaluation of the dissipation coefficient is made only considering grid points in a neighbourhood of the generic point (i.e. for $x_j \to [x_{j-3}, x_{j+3}]$).

- **Local Lax-Friedrichs (LLF) [33]**

$$\tilde{H}_j^{LLF}\left(u_j^+, u_j^-\right) = H\left(\frac{u_j^+ + u_j^-}{2}\right) - \frac{1}{2}\alpha\left(u_j^+, u_j^-\right)\left(u_j^+ - u_j^-\right) \tag{J.3}$$

  where, this time:

$$\alpha\left(u_j^+, u_j^-\right) = \max_{u \in I(u^-;u^+)} \left|\frac{\partial H(u)}{\partial u}\right|$$

  and the interval I is so defined:

$$I\left(u_j^-, u_j^+\right) = \left[\min\left(u_j^-, u_j^+\right), \max\left(u_j^-, u_j^+\right)\right] \tag{J.4}$$

  Similarly to LF-scheme, Local Lax Friedrichs (LLF) is monotone (for the prove of it, see the appendix of [35]) if:

$$u^{\pm} \in \left[u^{min}; u^{max}\right]$$

  where the maximum and the minimum values are calculated inside the stencil domain of each numerical scheme.

Roe-Fix (RF) [33] [35]

The *Roe-Fix* [79] [35] scheme uses the Roe's upwind method, with built-in numerical artificial dissipation, with a LLF entropy correction to avoid entropy violating expansion shock developing at sonic points. The numerical Hamiltonian for Roe Fix (RF) scheme is hence given by:

$$\tilde{H}\left(u_j^+, u_j^-\right) = \begin{cases} H\left(u_j^*\right) \quad \text{with} \quad u_j^* = \begin{cases} u_j^+ & \text{if} \quad dH/du \leqslant 0 \\ u_j^- & \text{if} \quad dH/du \geqslant 0 \end{cases} \Longrightarrow \begin{cases} \text{if } dH/du \text{ does not change} \\ +++\text{sign in } u \in I(u^-;u^+) \end{cases} \\ H\left(\frac{u_j^+ + u_j^-}{2}\right) - \frac{1}{2}\alpha\left(u_j^+, u_j^-\right)\left(u_j^+ - u_j^-\right) \Longrightarrow \begin{cases} \text{if } dH/du \text{ changes} \\ \text{sign in } u \in I(u^-;u^+) \end{cases} \end{cases} \tag{J.5}$$

The RF-scheme, as LF and LLF, has the property to be monotone (for the prove of it see appendix of [35]) for:

$$u^{\pm} \in \left[u^{min}; u^{max}\right]$$

where is considered the evaluation of the maximum and minimum values inside the numerical scheme stencil.

Godunov (G) [5]

Considering a piecewise constant initial data, it is possible to consider a numerical method that gives the exact (the lowest dissipative scheme) solution for the one dimensional conservation law 3.31, evaluating the exact solution of the Riemann problems arising at cells interfaces [5]. The correspondant numerical Hamiltonian is given by:

$$\tilde{H}_j^G\left(u_j^+, u_j^-\right) = \underset{u\in I\left(u_j^-, u_j^+\right)}{\text{ext}} H(u) \tag{J.6}$$

where the operator ext is given by the following expression:

$$\underset{u\in I\left(u_j^-, u_j^+\right)}{\text{ext}} = \begin{cases} \min\limits_{u\in\left[u_j^-; u_j^+\right]} & \text{if} \quad u_j^- \leqslant u_j^+ \\ \max\limits_{u\in\left[u_j^+; u_j^-\right]} & \text{if} \quad u_j^- > u_j^+ \end{cases} \tag{J.7}$$

Note that the numerical Hamiltonian $\tilde{H}_j^G$ with the ext operator could also be found in the equivalent formulation given in [31] [34]:

$$\tilde{H}_j^G\left(u_j^+, u_j^-\right) = \underset{u\in I\left(u_j^-, u_j^+\right)}{\text{ext}} H(u) = \text{sign}\left(u_j^+ - u_j^-\right) \min_{u\in\Upsilon\left(u_j^-, u_j^+\right)} \left(\text{sign}\left(u_j^+ - u_j^-\right) H(u)\right)$$

where:

$$\Upsilon\left(u_j^-, u_j^+\right) = I\left(u_j^-, u_j^+\right) = \left[\min\left(u_j^+, u_j^-\right), \max\left(u_j^+, u_j^-\right)\right]$$

The numerical scheme, in its equivalent formulations, is monotone if:

$$\Delta t \leqslant \frac{\Delta x}{\max\left|\frac{dH}{du}\right|}$$

In the case of the Hamiltonian is convex, for that is valid $d^2H/du^2 > 0\,(<0) \quad \forall u$, the exact solution of the Riemann problem is given by the known cases [18]:

(i) fully supersonic

$$\tilde{H}_j^G\left(u_j^+, u_j^-\right) = H\left(u_j^-\right) \qquad \text{if} \left(\left.\frac{dH}{du}\right|_{u_j^-} > 0\,;\ \left.\frac{dH}{du}\right|_{u_j^+} > 0\right)$$

(ii) fully subsonic

$$\tilde{H}_j^G\left(u_j^+, u_j^-\right) = H\left(u_j^+\right) \qquad \text{if} \left(\left.\frac{dH}{du}\right|_{u_j^-} < 0\,;\ \left.\frac{dH}{du}\right|_{u_j^+} < 0\right)$$

(iii) transonic expansion

$$\tilde{H}_j^G\left(u_j^+, u_j^-\right) = 0 \qquad \text{if} \left(\left.\frac{dH}{du}\right|_{u_j^-} \leqslant 0 \leqslant \left.\frac{dH}{du}\right|_{u_j^+}\right)$$

(iv) transonic shock

$$\tilde{H}_j^G\left(u_j^+, u_j^-\right) = \begin{cases} H\left(u_j^-\right) & \text{if} \left(\left.\frac{dH}{du}\right|_{u_j^-} > w_s \geqslant 0 \geqslant \left.\frac{dH}{du}\right|_{u_j^+}\right) \\ H\left(u_j^+\right) & \text{if} \left(\left.\frac{dH}{du}\right|_{u_j^-} \geqslant 0 > w_s > \left.\frac{dH}{du}\right|_{u_j^+} < 0\right) \end{cases}$$

where w_s is the shock velocity. This can be evaluated by the use of the Rankine-Hugoniot jump condition (coming from the integral form of conservation law 3.45) [56]:

$$w_s = \frac{H(u_-) - H(u_-)}{u_- - u_+} = \frac{[H(u)]}{[u]} \tag{J.8}$$

In the special case that $H(u) = h\left(u^2\right)$, it is possible to combine all the cited cases in a most straightforward form to be implemented in one algorithm. It is, hence, possible to write down the previous expressions in the elegant form[3] [79] [18] [69]:

$$\begin{cases} \text{if } \dfrac{dH}{d\left(u^2\right)} < 0 & \Longrightarrow \quad \tilde{H}_j^G = H\left(\min\left(\min\left(u_j^-, 0\right)^2, \max\left(u_j^+, 0\right)^2\right)\right) \\ \text{if } \dfrac{dH}{d\left(u^2\right)} > 0 & \Longrightarrow \quad \tilde{H}_j^G = H\left(\max\left(\max\left(u_j^-, 0\right)^2, \min\left(u_j^+, 0\right)^2\right)\right) \end{cases} \tag{J.9}$$

considering that the characteristic direction[4] is given by:

$$\frac{dH}{du} = \frac{dH}{d\left(u^2\right)}\frac{d\left(u^2\right)}{du} = 2u\frac{dH}{d\left(u^2\right)} \tag{J.10}$$

Engquist-Osher (EO) [18]

In the case of an "Hamiltonian-flux" function convex, it is possible of easily approximate the numerical Hamiltonian thought the Engquist Osher scheme. For that the flux is given by:

$$\begin{aligned} \tilde{H}_j^{EO}\left(u_j^+, u_j^-\right) &= H\left(u_j^-\right) + \int_{u_j^-}^{u_j^+} \min\left(\frac{dH}{du}, 0\right) du = \\ &= H\left(u_j^+\right) + \int_{u_j^-}^{u_j^+} \max\left(\frac{dH}{du}, 0\right) du = \\ &= \frac{H\left(u_j^-\right) + H\left(u_j^+\right)}{2} - \frac{1}{2}\int_{u_j^-}^{u_j^+} \left|\frac{dH}{du}\right| du \end{aligned} \tag{J.11}$$

considering all the possible cases rising from the expression J.11, we have:

(a) fully supersonic $\begin{cases} \left.\dfrac{dH}{du}\right|_{u_j^-} > 0 \\ \left.\dfrac{dH}{du}\right|_{u_j^+} > 0 \end{cases} \Longrightarrow \tilde{H}_j^{EO} = H\left(u_j^-\right)$

(b) fully subsonic $\begin{cases} \left.\dfrac{dH}{du}\right|_{u_j^-} < 0 \\ \left.\dfrac{dH}{du}\right|_{u_j^+} < 0 \end{cases} \Longrightarrow \tilde{H}_j^{EO} = H\left(u_j^+\right)$

(c) transonic expansion $\begin{cases} \left.\dfrac{dH}{du}\right|_{u_j^-} < 0 \\ \left.\dfrac{dH}{du}\right|_{u_j^+} > 0 \end{cases} \Longrightarrow \tilde{H}_j^{EO} = H\left(\left(\left.\dfrac{dH}{du}\right|_{u=0}\right)^{-1}\right)$

(d) transonic shock $\begin{cases} \left.\dfrac{dH}{du}\right|_{u_j^-} > 0 \\ \left.\dfrac{dH}{du}\right|_{u_j^+} < 0 \end{cases} \Longrightarrow \tilde{H}_j^{EO} = H\left(u_j^-\right) + H\left(u_j^+\right) - H\left(\left(\left.\dfrac{dH}{du}\right|_{u=0}\right)^{-1}\right)$

Note that the approximation of the scheme is only in the case of a transonic shock (case **(d)**). For this case, the exact solution is either $H\left(u_j^-\right)$ or $H\left(u_j^+\right)$, depending on the shock wave velocity sign (which comes out from the Rankine-Hugoniot condition J.8), and introducing some

3 that is particularly fitted to the level set equation (both in one-dimensional and in several dimensions versions of it).
4 in the shown relation between Hamilton-Jacobi and conservation law

diffusion. While for all the other cases, the scheme picks out the exact solution of the Riemann problem.

In the special case of an Hamiltonian such a function of u:

$$H(u) = h\left(u^2\right) \quad ; \quad H(u=0) = 0$$

the EO approximate Riemann solver can be also put in the elegant unique formulation [31] [59] [18]:

$$\begin{cases} \text{if } \dfrac{dH}{d\left(u^2\right)} < 0 & \Longrightarrow \quad \tilde{H}_j^{EO} = H\left(\min\left(u_j^-, 0\right)^2\right) + H\left(\max\left(u_j^+, 0\right)^2\right) \\ \text{if } \dfrac{dH}{d\left(u^2\right)} > 0 & \Longrightarrow \quad \tilde{H}_j^{EO} = H\left(\max\left(u_j^-, 0\right)^2\right) + H\left(\min\left(u_j^+, 0\right)^2\right) \end{cases} \tag{J.12}$$

Osher-Sethian (OS) [31]

If the Hamiltonian $H(u)$ is a quadratic function of u, so that $H(u) = H\left(u^2\right)$, over the EO exists another approximate Riemann solver due to Osher and Sethian. This is very similar to the first J.12, hence it is an upwind monotone scheme, given by the following expression of its numerical Hamiltonian:

$$\begin{cases} \text{if } \dfrac{dH}{d\left(u^2\right)} < 0 & \Longrightarrow \quad \tilde{H}_j^{OS} = H\left(\min\left(u_j^-, 0\right)^2 + \max\left(u_j^+, 0\right)^2\right) \\ \text{if } \dfrac{dH}{d\left(u^2\right)} > 0 & \Longrightarrow \quad \tilde{H}_j^{OS} = H\left(\max\left(u_j^-, 0\right)^2 + \min\left(u_j^+, 0\right)^2\right) \end{cases} \tag{J.13}$$

that is monotone with the CFL condition:

$$\Delta t \leqslant \frac{\Delta x}{2 \max\left|\dfrac{dH}{du}\right|}$$

From the equation J.13, it is possible to argue the strong relation between the OS and EO scheme. In particular, it is simple to see that in the case of *fully subsonic* and *supersonic flow* and *transonic expansion* the two numerical schemes gives both the exact Riemann solution. In the presence of a *transonic shock*, instead, there is a little difference expressed by the fact that:

$$H\left(u_j^{-2} + u_j^{+2}\right) \neq H\left(u_j^{-2}\right) + H\left(u_j^{+2}\right)$$

except from the case in which the Hamiltonian is a linear operator respect to u^2. The advantage of the use, respect to others, of the OS numerical scheme stands on that is easily generalizable to several space dimensions (see paragraph J.2, page n).

Now, it is possible to show, in a very simple manner, that the OS Riemann solver, in the case of the 1D Level Set equation, is even less dissipative than the EO. In fact, considering the case of transonic shock (in all the other cases the OS and the EO give the exact solution), we have that:

$$\text{transonic shock} \implies u_j^+ < 0\,,\ u_j^- > 0$$

$$\left(\tilde{H}_j^{EO}\right)_{LS} = \sqrt{\max\left(u_j^-,0\right)^2} + \sqrt{\min\left(u_j^+,0\right)^2} = \sqrt{\left(u_j^-\right)^2} + \sqrt{\left(u_j^+\right)^2} = \left|\left(u_j^-\right)\right| + \left|\left(u_j^+\right)\right|$$

$$\left(\tilde{H}_j^{OS}\right)_{LS} = \sqrt{\max\left(u_j^-,0\right)^2 + \min\left(u_j^+,0\right)^2} = \sqrt{\left(u_j^-\right)^2 + \left(u_j^+\right)^2}$$

$$\left(\tilde{H}_j^{G}\right)_{LS} = \begin{cases} \sqrt{\left(u_j^-\right)^2} = \left|u_j^-\right| & \text{if } w_s = \dfrac{\sqrt{\left(u_j^+\right)^2} - \sqrt{\left(u_j^-\right)^2}}{u_j^+ - u_j^-} > 0 \\ \sqrt{\left(u_j^-\right)^2} = \left|u_j^+\right| & \text{if } w_s = \dfrac{\sqrt{\left(u_j^+\right)^2} - \sqrt{\left(u_j^-\right)^2}}{u_j^+ - u_j^-} < 0 \end{cases}$$

by the chain rules of inequalities:

$$\left|u_j^-\right|, \left|u_j^+\right| \leqslant \sqrt{\left(u_j^-\right)^2 + \left(u_j^+\right)^2} \leqslant \left|\left(u_j^-\right)\right| + \left|\left(u_j^+\right)\right|$$

so it is proved what stated.

Since this point, in all the numerical schemes introduced, it is considered a *first order Euler forward time marching methods* and a *first order space upwind approximations for derivatives* ϕ_x^+ *and* ϕ_x^-. A way to improve the spatial numerical accuracy to high-order approximations is to use ENO or Weighted Essentially Non Oscillatory (WENO) methods (respectively third and fifth order for example), thought the essentially non oscillatory polynomial interpolation of the ϕ function and its weighted version. Unfortunately the ENO and WENO schemes are not TVD, but only Total Variation Bounded (TVB). However, this condition fortunately is sufficient to guarantee convergence of the overall numerical method.

Practical experience suggests that more efforts must be considered to develop numerical schemes with an accurate reconstruction of spatial derivatives. While less one attention is necessary for temporal discretization, because of its less impact on the solution degradation. If in some application it is necessary to an accurate time derivatives reconstruction, it is possible to consider Runge-Kutta method, especially TVD ones that ensure no-formation of spurious oscillations. TVD Runge-Kutta schemes are obtained simply taking convex combination of Euler steps, that are TVD by assumption.

J.2 Multi-D Hamiltonian Jacobi Equations

For the several dimensional Hamilton-Jacobi equations, the same techniques devised for the one dimensional type one can be used with some little complications due to multidimensional aspects (for simplicity will be valuated formulations only for the two dimensional case).

Lax-Friedrichs (LF) [21] [79]

For LF scheme, from the monodimensional form J.2, it is easy to write down the expression of the numerical Hamiltonian $\tilde{H}_{j\,k}^{LF}$:

$$\begin{aligned} \tilde{H}_{j\,k}^{LF}\left(u_{j\,k}^+, u_{j\,k}^-, v_{j\,k}^+, v_{j\,k}^-\right) \;=\; & H\left(\frac{u_{j\,k}^+ + u_{j\,k}^-}{2}, \frac{v_{j\,k}^+ + v_{j\,k}^-}{2}\right) + \\ & -\tfrac{1}{2}\,\alpha^x\left(u_{j\,k}^+ - u_{j\,k}^-\right)\tfrac{1}{2}\,\alpha^y\left(v_{j\,k}^+ - v_{j\,k}^-\right) \end{aligned} \tag{J.14}$$

where:

$$u^{\pm}_{j\,k} = D^{\pm}\phi_{j\,k} = \pm\frac{(\phi_{j\pm1\,k} - \phi_{j\,k})}{\Delta x} \quad ; \quad v^{\pm}_{j\,k} = D^{\pm}\phi_{j\,k} = \pm\frac{(\phi_{j\,k\pm1} - \phi_{j\,k})}{\Delta y}$$

$$\alpha^{x} = \max_{u\in[A;B]\ v\in[C;D]} \left|\frac{\partial H(\phi_x, \phi_y)}{\partial \phi_x}\right| = \max_{u\in[A;B]\ v\in[C;D]} \left|\frac{\partial H(u,v)}{\partial u}\right|$$

$$\alpha^{y} = \max_{u\in[A;B]\ v\in[C;D]} \left|\frac{\partial H(\phi_x, \phi_y)}{\partial \phi_y}\right| = \max_{u\in[A;B]\ v\in[C;D]} \left|\frac{\partial H(u,v)}{\partial v}\right|$$

This scheme is monotone for:

$$u^{\pm} \in [A;B] \quad ; \quad v^{\pm} \in [C;D]$$

For the same pointed out considerations made for one dimensional LF numerical method, it is preferable to use some modified versions of the original LF, in order to avoid too much smearing out of the solution where is not necessary:

- **Stencil Lax-Friedrichs (SLF)**
  The dissipation coefficients α^x, α^y are determined including only grid points in a neighbourhood of the generic point; for $\vec{x}_{j\,k}$, for example the stencil:

  $$\left[\vec{x}_{j-3\,k}, \vec{x}_{j+3\,k}\right] \quad \longrightarrow \quad \text{for } \alpha^{x}_{j\,k} \quad ; \quad \left[\vec{x}_{j\,k-3}, \vec{x}_{j\,k+3}\right] \quad \longrightarrow \quad \text{for } \alpha^{y}_{j\,k}$$

  that contains all the points necessary to build a WENO scheme. Or in alternative to the previous dimension by dimension evaluation of dissipation coefficients, it is possible to use the following form, that considers a rectangular grid points domain:

  $$\left[\vec{x}_{j\,k-3}, \vec{x}_{j\,k+3}\right] \times \left[\vec{x}_{j-3\,k}, \vec{x}_{j+3\,k}\right] \quad \longrightarrow \quad \text{for both } \alpha^{x}_{j\,k}\,;\, \alpha^{y}_{j\,k}$$

- **Local Lax-Friedrichs (LLF) [33]**
  Searching even more local values of the dissipation coefficients brings to:

  $$\begin{aligned}\tilde{H}^{LLF}_{j\,k}\left(u^{+}_{j\,k}, u^{-}_{j\,k}, v^{+}_{j\,k}, v^{-}_{j\,k}\right) \;=\; & H\left(\frac{u^{+}_{j\,k}+u^{-}_{j\,k}}{2}, \frac{v^{+}_{j\,k}+v^{-}_{j\,k}}{2}\right) + \\ & -\tfrac{1}{2}\,\alpha^{x}_{j\,k}\left(u^{+}_{j\,k}, u^{-}_{j\,k}\right)\left(u^{+}_{j\,k} - u^{-}_{j\,k}\right) + \\ & -\tfrac{1}{2}\,\alpha^{y}_{j\,k}\left(v^{+}_{j\,k}, v^{-}_{j\,k}\right)\left(v^{+}_{j\,k} - v^{-}_{j\,k}\right)\end{aligned} \tag{J.15}$$

  where, this time:

  $$\alpha^{x} = \max_{u\in I(u^-;u^+)\ v\in[C;D]} \left|\frac{\partial H(u,v)}{\partial u}\right|$$

  $$\alpha^{y} = \max_{u\in[A;B]\ v\in I(v^-;v^+)} \left|\frac{\partial H(u,v)}{\partial v}\right|$$

  and the interval I is given by the expression J.4. Similarly to the one-dimensional LLF, it is monotone for:

  $$u^{\pm} \in [A;B] \quad ; \quad v^{\pm} \in [C;D]$$

- **Local Local Lax-Friedrichs (LLLF) [35]** Even more local and so less dissipative is the Local Local LF, where the numerical Hamiltonian is formally given by the same expression J.15 of the Local LF:

  $$\begin{aligned}\tilde{H}^{LLLF}_{j\,k}\left(u^{+}_{j\,k}, u^{-}_{j\,k}, v^{+}_{j\,k}, v^{-}_{j\,k}\right) \;=\; & H\left(\frac{u^{+}_{j\,k}+u^{-}_{j\,k}}{2}, \frac{v^{+}_{j\,k}+v^{-}_{j\,k}}{2}\right) + \\ & -\tfrac{1}{2}\,\alpha^{x}_{j\,k}\left(u^{\pm}_{j\,k}, v^{\pm}_{j\,k}\right)\left(u^{+}_{j\,k} - u^{-}_{j\,k}\right) + \\ & -\tfrac{1}{2}\,\alpha^{y}_{j\,k}\left(u^{\pm}_{j\,k}, v^{\pm}_{j\,k}\right)\left(v^{+}_{j\,k} - v^{-}_{j\,k}\right)\end{aligned} \tag{J.16}$$

and with dissipation coefficients defined as:

$$\alpha^x = \max_{u\in I(u^-;u^+)\ v\in I(v^-;v^+)} \left|\frac{\partial H(u,v)}{\partial u}\right|$$

$$\alpha^y = \max_{u\in I(u^-;u^+)\ v\in I(v^-;v^+)} \left|\frac{\partial H(u,v)}{\partial v}\right|$$

Unfortunately that scheme is not monotone.

Note that when the Hamiltonian H is separable in the sense of:

$$H(\phi_x,\phi_y) = H^x(\phi_x) + H^y(\phi_y) \qquad \left(H(u,v) = H^1(u) + H^2(v)\right)$$

then the LLLF reduces to the LLF scheme.

Roe-Fix (RF) [33] [35]

The RF scheme uses the same building block of its one-dimensional version: Roe with LLF entropy correction near sonic points:

$$\tilde{H}\left(u^{\pm}_{j\,k}, v^{\pm}_{j\,k}\right) = \begin{cases} \text{case (a):} & H\left(u^*_{j\,k}, v^*_{j\,k}\right) \\ \text{case (b):} & H\left(\dfrac{u^+_{j\,k}+u^-_{j\,k}}{2}, v^*_{j\,k}\right) - \frac{1}{2}\,\alpha^x_{j\,k}\left(u^+_{j\,k}, u^-_{j\,k}\right)\left(u^+_{j\,k}-u^-_{j\,k}\right) \\ \text{case (c):} & H\left(u^*_{j\,k}, \dfrac{v^+_{j\,k}+v^-_{j\,k}}{2}\right) - \frac{1}{2}\,\alpha^y_{j\,k}\left(v^+_{j\,k}, v^-_{j\,k}\right)\left(v^+_{j\,k}-v^-_{j\,k}\right) \\ \text{case (d):} & \tilde{H}^{LLF}_{j\,k}\left(u^+_{j\,k}, u^-_{j\,k}, v^+_{j\,k}, v^-_{j\,k}\right) \end{cases} \tag{J.17}$$

where the four cases are defined as follow:

(a) if $\dfrac{\partial H(u,v)}{\partial u}$ and $\dfrac{\partial H(u,v)}{\partial v}$ do not change sign in $u \in I(u^-;u^+)$, $v \in I(v^-;v^+)$

(b) otherwise and if $\dfrac{\partial H(u,v)}{\partial v}$ does not change sign in $u \in [A;B]$, $v \in I(v^-;v^+)$

(c) otherwise and if $\dfrac{\partial H(u,v)}{\partial u}$ does not change sign in $u \in I(u^-;u^+)$, $v \in I[C;D]$

(d) otherwise

while $u^*_{j\,k}$ and $v^*_{j\,k}$ are given by:

$$u^*_{j\,k} = \begin{cases} u^+_{j\,k} & \text{if } \dfrac{\partial H(u,v)}{\partial u} \leqslant 0 \\ u^-_{j\,k} & \text{if } \dfrac{\partial H(u,v)}{\partial u} \geqslant 0 \end{cases} \quad ; \quad v^*_{j\,k} = \begin{cases} v^+_{j\,k} & \text{if } \dfrac{\partial H(u,v)}{\partial v} \leqslant 0 \\ v^-_{j\,k} & \text{if } \dfrac{\partial H(u,v)}{\partial v} \geqslant 0 \end{cases}$$

Similarly to the one-dimensional formulation, this scheme is monotone for:

$$u^{\pm} \in [A;B] \quad ; \quad v^{\pm} \in [C;D]$$

Godunov (G) [5] [34] [32]

The multidimensional Hamilton-Jacobi formulation of the Godunov exact Riemann solver, previously analyzed in its mono-dimensional form, is given by:

$$\tilde{H}^G_{j\,k}\left(u^+_{j\,k}, u^-_{j\,k}, v^+_{j\,k}, v^-_{j\,k}\right) = \operatorname*{ext}_{u\in I\left(u^-_{j\,k}, u^+_{j\,k}\right)} \operatorname*{ext}_{v\in I\left(v^-_{j\,k}, v^+_{j\,k}\right)} H(u,v) \tag{J.18}$$

in which the ext operator is given by expression J.7. This is a monotone scheme for:

$$\Delta t \leqslant \frac{1}{\dfrac{\max\left|\dfrac{\partial H}{\partial u}\right|}{\Delta x} + \dfrac{\max\left|\dfrac{\partial H}{\partial v}\right|}{\Delta y}}$$

An important remark is that, in general, the operators ext are not commutable in sense that[5]

$$\underset{u}{\text{ext}}\,\underset{v}{\text{ext}}\,H \neq \underset{v}{\text{ext}}\,\underset{u}{\text{ext}}\,H$$

So that, it is possible to obtain different versions of J.18, changing the operators order[6].

In the special case that the Hamiltonian H is a quadratic function in both its variables: $h\left(u^2\,;\,v^2\right)$, the following expression for the numerical Hamiltonian can be considered: [69]:

$$\tilde{H}^{G}_{j\,k}\left(u^{\pm}_{j\,k}, v^{\pm}_{j\,k}\right) = \begin{cases} \text{if} \quad \left(\dfrac{\partial H}{\partial\left(u^2\right)} > 0\,,\, \dfrac{\partial H}{\partial\left(v^2\right)} > 0\right) \\ \quad \Longrightarrow H\left(\left(\max\left(u^{-}_{j\,k}\right)^2_{+}, \left(u^{+}_{j\,k}\right)^2_{-}\right)\;;\; \max\left(\left(v^{-}_{j\,k}\right)^2_{+}, \left(v^{+}_{j\,k}\right)^2_{-}\right)\right) \\ \text{if} \quad \left(\dfrac{\partial H}{\partial\left(u^2\right)} > 0\,,\, \dfrac{\partial H}{\partial\left(v^2\right)} < 0\right) \\ \quad \Longrightarrow H\left(\max\left(\left(u^{-}_{j\,k}\right)^2_{+}, \left(u^{+}_{j\,k}\right)^2_{-}\right)\;;\; \min\left(\left(v^{-}_{j\,k}\right)^2_{-}, \left(v^{+}_{j\,k}\right)^2_{+}\right)\right) \\ \text{if} \quad \left(\dfrac{\partial H}{\partial\left(u^2\right)} < 0\,,\, \dfrac{\partial H}{\partial\left(v^2\right)} > 0\right) \\ \quad \Longrightarrow H\left(\min\left(\left(u^{-}_{j\,k}\right)^2_{-}, \left(u^{+}_{j\,k}\right)^2_{+}\right)\;;\; \max\left(\left(v^{-}_{j\,k}\right)^2_{+}, \left(v^{+}_{j\,k}\right)^2_{-}\right)\right) \\ \text{if} \quad \left(\dfrac{\partial H}{\partial\left(u^2\right)} < 0\,,\, \dfrac{\partial H}{\partial\left(v^2\right)} < 0\right) \\ \quad \Longrightarrow H\left(\min\left(\left(u^{-}_{j\,k}\right)^2_{-}, \left(u^{+}_{j\,k}\right)^2_{+}\right)\;;\; \min\left(\left(v^{-}_{j\,k}\right)^2_{-}, \left(v^{+}_{j\,k}\right)^2_{+}\right)\right) \end{cases} \tag{J.19}$$

Where the following notation has been used:

$$x_{-} = \min(x, 0) \quad ; \quad x_{+} = \max(x, 0)$$

Osher-Sethian (OS) [31]

In the special case of:

$$H(u, v) = h\left(u^2, v^2\right)$$

it is easy to extend, in a straightforward manner, the Osher Sethian approximate Riemann solver J.13 to several dimensions. Hence, the numerical Hamiltonian takes the form:

5 the notation used is:

$$\underset{u}{\text{ext}} = \underset{u\in I\left(u^{-}_{j\,k}, u^{+}_{j\,k}\right)}{\text{ext}} \quad ; \quad \underset{v}{\text{ext}} = \underset{v\in I\left(v^{-}_{j\,k}, v^{+}_{j\,k}\right)}{\text{ext}}$$

6 if the Hamiltonian is splittable, in the sense mentioned before, the commutative property of the operator ext stands.

$$\tilde{H}^{OS}_{j\,k}\left(u^{\pm}_{j\,k}, v^{\pm}_{j\,k}\right) = \begin{cases} \text{if } \left(\dfrac{\partial H}{\partial\left(u^2\right)} > 0\,,\ \dfrac{\partial H}{\partial\left(v^2\right)} > 0\right) \\ \quad \Longrightarrow H\left(\max\left(u^{-}_{j\,k}, 0\right)^2 + \min\left(u^{+}_{j\,k}, 0\right)^2, \max\left(v^{-}_{j\,k}, 0\right)^2 + \min\left(v^{+}_{j\,k}, 0\right)^2\right) \\ \text{if } \left(\dfrac{\partial H}{\partial\left(u^2\right)} > 0\,,\ \dfrac{\partial H}{\partial\left(v^2\right)} < 0\right) \\ \quad \Longrightarrow H\left(\max\left(u^{-}_{j\,k}, 0\right)^2 + \min\left(u^{+}_{j\,k}, 0\right)^2, \min\left(v^{-}_{j\,k}, 0\right)^2 + \max\left(v^{+}_{j\,k}, 0\right)^2\right) \\ \text{if } \left(\dfrac{\partial H}{\partial\left(u^2\right)} < 0\,,\ \dfrac{\partial H}{\partial\left(v^2\right)} > 0\right) \\ \quad \Longrightarrow H\left(\min\left(u^{-}_{j\,k}, 0\right)^2 + \max\left(u^{+}_{j\,k}, 0\right)^2, \max\left(v^{-}_{j\,k}, 0\right)^2 + \min\left(v^{+}_{j\,k}, 0\right)^2\right) \\ \text{if } \left(\dfrac{\partial H}{\partial\left(u^2\right)} < 0\,,\ \dfrac{\partial H}{\partial\left(v^2\right)} < 0\right) \\ \quad \Longrightarrow H\left(\min\left(u^{-}_{j\,k}, 0\right)^2 + \max\left(u^{+}_{j\,k}, 0\right)^2, \min\left(v^{-}_{j\,k}, 0\right)^2 + \max\left(v^{+}_{j\,k}, 0\right)^2\right) \end{cases} \tag{J.20}$$

which is monotone subjected to the CFL restriction:

$$\Delta t \leqslant \frac{1}{2\left(\dfrac{\max\left|\dfrac{\partial H}{\partial u}\right|}{\Delta x} + \dfrac{\max\left|\dfrac{\partial H}{\partial v}\right|}{\Delta y}\right)}$$

All the remarks made on the possibility, thought ENO or WENO and Runge-Kutta schemes, to built higher order accurate, in space and time, numerical schemes are still valid in multiple dimensions numerical techniques just shown.

K

Instability of central differences used in 1D-LS equation

In this section, the instability of the numerical scheme for the numerical solution the simple 1D Level equation, based on the use of central differences for the spatial derivative approximation is demonstrated [59].

Starting from the known 1D Level Set equation, with the initial condition:

$$\begin{cases} \frac{\partial \phi}{\partial t} + V\sqrt{1+\phi_x^2} = 0 \\ \phi(x, t=0) = \begin{cases} \frac{1}{2} - x & \text{for} \quad x \leqslant \frac{1}{2} \\ x - \frac{1}{2} & \text{for} \quad x > \frac{1}{2} \end{cases} \end{cases}$$

The solution of this problem is known, by the Huygens's principle, to remain a sharp "V" corner, located at $x = 1/2$.

Considering, now, a building-up of the numerical solution with the use of the central difference for the spatial derivatives and of the Euler's method for the time derivative (considering $V = -1$):

$$\phi|_j^{n+1} = \phi|_j^n + V\Delta t\sqrt{1+\left(\frac{\phi|_{j+1}^n - \phi|_{j-1}^n}{2\Delta x}\right)^2}$$

we have clearly a blowing up of the code for a finite number of timesteps, due to the spurious oscillations, induced just by the use of the central differences.

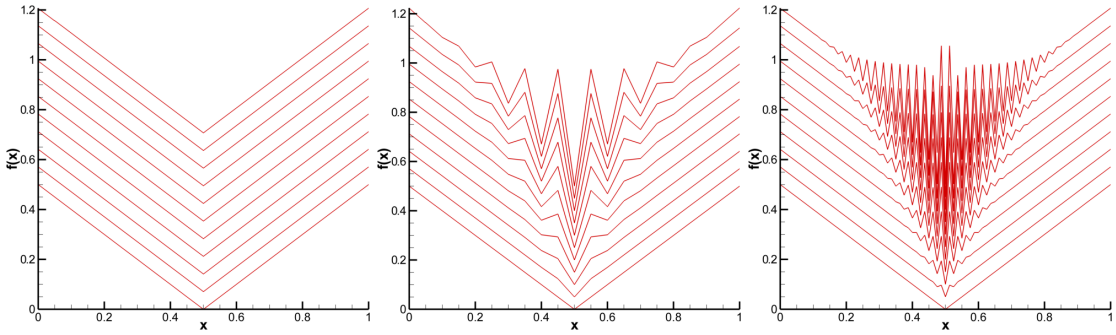

(a) Exact Solution (b) Central differences $\Delta t = 0.005$ (c) Central differences $\Delta t = 0.0005$

Figure K.1: Marker particles method

In fact, while for all nodes $x \neq 1/2$ the eikonal term is exactly evaluated as $1/2$; for the point at $x = 1/2$ for even points number, the calculation of the eikonal term is completely wrong, no matter how many computational points (see figure K.1), or how much small is the timestep

we consider. This is simply due to how the spatial derivative is evaluated. As a consequence of this wrong approach in approximating spatial derivatives, as the calculation progress, these miscalculations of the slope affect all the mesh points causing spurious oscillations (see figure K.1).

L

Smart LS method for a class of grains

We consider in this section, the particular case that the grain is described, for all its motion, by a monovalued function, respect one of the independent spatial variables (x,y,z for the rectangular Cartesian system coordinate; r,θ,z for the cylindrical one, where z represents the motor axis). In this case, the Level Set problem can be formulated in a simpler manner, with a one less dimension, saving consequently the computational time, re-sampling the Level Set function in an explicit fashion.

Starting from the Level Set equation in the general case (3.27), we consider without lack of generality that:

$$\phi\left(x\left(t\right),y\left(t\right),z\left(t\right),t\right)=\pm\left[z\left(t\right)-f\left(x\left(t\right),y\left(t\right)\right)\right] \tag{L.1}$$

We have, with simple calculations [31] the Level Set equation, considering along the dependent variable the use of the equation L.1:

$$z_t-V\sqrt{f_x^2+f_y^2+1}=0 \tag{L.2}$$

Hence, the problem can be computed in only two independent variables, not three, in a similar manner, as direct "Lagrangian" approaches, with the advantages of an Eulerian technique. This is, in particular, due to the fact that, as the surface itself can be written in an explicit fashion, the derivative along the z axis is know for all time to be $\phi_z=1$. In fact, this can be seen by the related PDE and initial condition (being z a dependent variable for the front, $V\left(z\right)=V\left(x,y\right)$):

$$\begin{cases}\left(\phi_z\right)_t+V\frac{\phi_z}{|\vec{\nabla}\phi|}\phi_{zz}=0\\ \phi_z\left(x,y,t=0\right)=1 \qquad \text{IC}\end{cases} \tag{L.3}$$

Since the initial condition is defined with the application of L.1 for the 3D Level Set problem.

The reduction of the problem, as stated even before, is restricted in its application to initial grain shapes that can be represented in a explicit fashion (analytically or numerically). Moreover, they must remain described by an explicit function during their motion, or in other words, the motion field velocity that leads their evolution, must leave them defined by an esplicit function. Hence, for example inhibited grains, difficultly can be treated with this technique. While finocyl grains, today commonly used in modern SRM can be efficiently computed with this reduction. Note that the numerical technique and the CFL condition are the one expressed in the equation 3.77, 3.79, with variations due to the problem simplification.

As matter of fact, in the case that the problem reduction is possible, for the given time and spatial varying motion field, no other difficulties are implied in applying the Level Set technique. In fact, the surface is discretely represented by the grid explicit function $f\left(x,y\right)$.

Moreover, the boundary in the grain surface motion defined by the case boundary is simply obtained. In the same time, the procedure for evaluating the grain geometrical properties are directly given by the discrete tessellation of the surface.

At last, the problem reduction is effectively recommended when the problem allows it. It is, in fact, a smart computationally efficient application of the Level Set technique to a class of not-inhibited grains, which can be represented by a surface in an explicit fashion form for one of the spatial variables (simply the motor axis). Its limitation can be viewed in the fact that difficulty the grain shape is represented numerically in a selection of points coordinate with the desired grid discretization. Hence, some efforts must be made to computerize the initialization procedure. We can use, for example, the banded SDF calculation, which the grain initial shape is extracted from and thus by means of an interpolation procedure, define in such a manner, the correspondent grid points of the reduced problem. But more efficient implementation can be made.

As sample of the illustrated technique, the figure L.1 shows the 3D evolution of an analytical finocyl grain, given by an Osher-Sethian star (see paragraph 5.2.2, page 92) with variable parameters along the motor axis, in cylindrical coordinates.

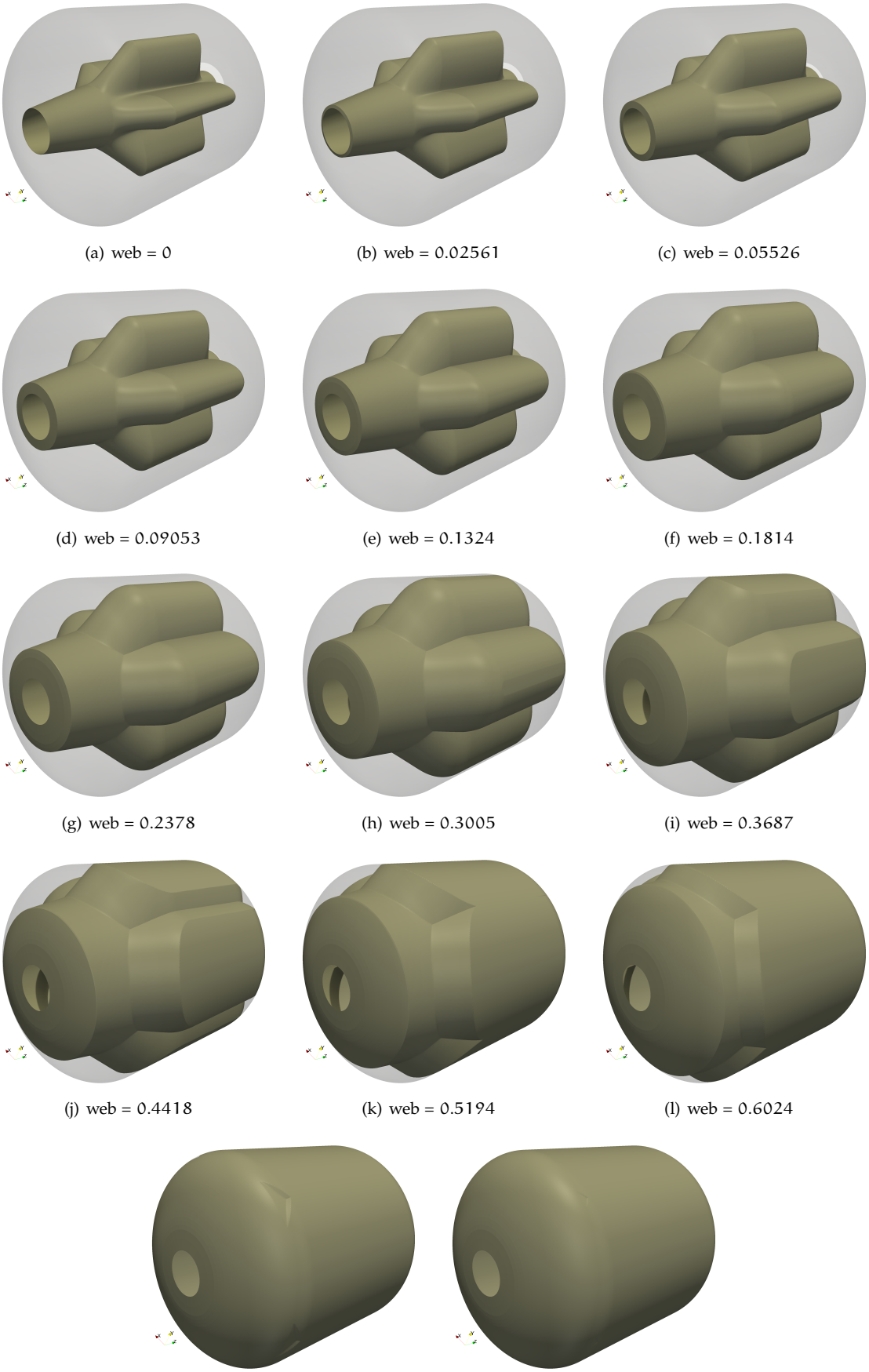

(a) web = 0 (b) web = 0.02561 (c) web = 0.05526

(d) web = 0.09053 (e) web = 0.1324 (f) web = 0.1814

(g) web = 0.2378 (h) web = 0.3005 (i) web = 0.3687

(j) web = 0.4418 (k) web = 0.5194 (l) web = 0.6024

(m) web = 0.6918 (n) web = 0.7156

Figure L.1: Finocyl grain 3D evolution

t

M

GREG Code Overview

The mathematical and numerical models presented in the chapter 3, page 32 have been implemented into the Grain REGression model model and code. GREG code is an "home-made" code entirely written by the author during this research work. In this chapter, some details of the GREG code are presented. GREG code is written in standard Fortran 95, with partial use Object Oriented Programming (OOP) style. The computational costs for each simulation are quite low and hence, at now, no parallelization of the code has been required. GREG is made up by 3 different softwares:

1. Mesh and Initial conditions Generator (GREGPreP)
2. Level Set Equation solver (GREG)
3. Post-processing Output Generator (GREGPP)

The workflow is the following: first the mesh and the initial conditions are generated using GREGPreP; then GREG loads the outputs of GREGPreP and the simulation starts; finally the GREG outputs are post-processed by GREGPP in order to obtain synthetic data like images, graphs and movies, more easy to understand (figure 3.11).

M.1 GREGPreP code

The GREGPreP code is able to deal directly with the CAD output, defined by the STL fileformat and/or with radius versus motor axis tabulated points values, for axisymmetric grains and TPs initial surface configurations. Also the inputs as predefined analytic functions are allowed, in order to make tests in rectangular meshes and/or in cylindrical meshes. After the STL (ascii or binary STL format are supported) and/or the tabulated axisymmetric points files of the grain propellant initial surface and the TP initial surface are loaded, the GREGPreP code generates the numerical mesh. As option of the code, this can be user defined: as bounds, number of cells along each coordinate direction, or fitted in terms of bounds to the SRM geometry, in order to avoid the use of point of the mesh where not necessary. In the code structure, the meshes can be only orthogonal meshes, stretched or not, even if at now, only uniform meshes have been used. In the future, it will be however possible to consider the stretching of the mesh in order to allocate more points where the geometrical features of the grain evolution want to be better represented.

The generation of the IC for the grain surface is made by means of the construction of the SDF for the grid. Typically the bounds are fitted to the grain and the Thermal Protections configuration, with the algorithm described in chapter 3.6.1, page 55.

The mesh output and the grain and TPs surface are saved into a GREG geometric binary standard file. This kind of file is loaded, as input, by GREG and GREGPP. In particular, the Level Set Method Initial Conditions are saved into a file identical to the solution output file of

the GREG solver: there is no distinction between an IC and a solution at a certain timestep. This choice makes easy to restart an interrupted simulation, if required.

M.2 GREG code

The GREG code is the main software, within the Level Set model is implemented with a Full Matrix approach. Thus, it make the numerical integration of the Hamilton-Jacobi equation with the first or second order numerical schemes presented in the chapter 3, paragraph 3.4.2 (page 51), in rectangular grids and paragraph 3.4.2 (page 52) for the cylindrical grids. Two different Riemann Solvers are supported: the exact one and the Osher-Sethian one (see paragraph J.2, page n). The one typically used in all the simulation made, as there is not a difference in the computational cost required, is the exact Riemann solver. The Object Oriented Programming style allows to integrate in a simple manner future developments of the code, as for example, an extension velocity module and Narrow Banding techniques. The grain and bore chamber geometrical properties can be evaluated directly with the techniques presented in the chapter 3, paragraph 3.11 (page 66), as option in the main code, without saving all the Level Set fields. A particular option, moreover, enables a specific output format to save the Q1D grain and bore geometrical parameters to be used in SPINBALL internal ballistics numerical simulations. The visualization can be made then using the post processing code GREGPP, in order to save the hard-disk space for the simulation. At now, the computational costs required for each simulation are quite bounded (at the most some hours on a single processor). Then a code parallelization is not required, but however possible for future needs. The workflow of the code is shown in the figure M.1.

M.3 GREGPP code

After the GREG code has completed the simulation, the Level Set fields are stored into a binary compressed files in order to limit the hard-disk space use (3D simulations can produce huge output files). This kind of files can be post-processed and converted into a more understandable file format, like images, graphs and movies. This task is made by the Post-processing Output Generator code: GREGPP. The GREGPP code loads as inputs, the output of GREGPreP and GREG and produces as output, the selected post-processing conversions. It evaluates also, if user requires it as input option, the grain and bore geometrical parameters from the Level Set representation of the front, as presented in the chapter 3, paragraph 3.11 (page 66).

The post-processing of the Level Set fields can be saved over the whole simulated volume, or over slice along one coordinate direction. These field outputs can be exported into 2 different visualization file formats:

1. Tecplot[1] file format.(ascii and binary formats are supported[2])
2. VTK[3] file format (ascii and binary formats are supported[2])

Although Tecplot is very powerfull, it is a commercial, closed software. So the better choice is VTK open source file format. In particular, the possibility of VTK-exporting allows the use of a powerfull open-source visualization software based on VTK: Paraview[4]. The most part of the 3D visualization of this dissertation are made with Paraview.

The grain and bore geometrical parameters, if evaluated as option, are saved for visualization in the Tecplot file format, for checking and visualizing the evaluated quantities and/or in the SPINBALL compatible file format.

1 Tecplot is commercial visualization software widely used into CFD engineering.
2 binary is preferred as limits the hard disk space required
3 The Visualization Toolkit (VTK) is an open source graphics toolkit. It is a platform independent graphics engine with parallel rendering support. VTK has an active development community that includes laboratories, institutions and universities from around the world. http://www.vtk.org/
4 ParaView is an open source, freely available program for parallel, interactive, scientific visualization. http://www.paraview.org

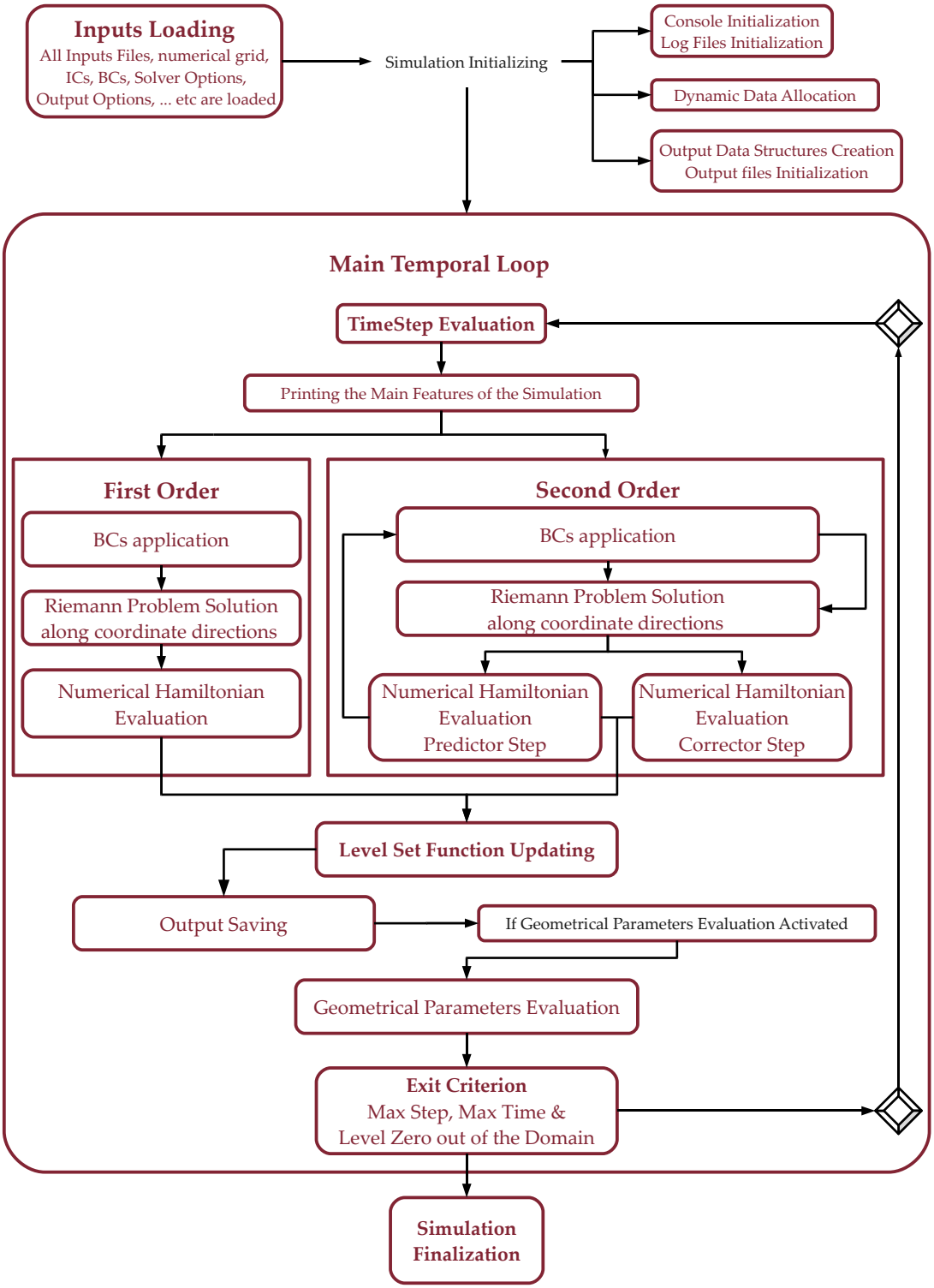

Figure M.1: GREG code Workflow

Bibliography

[1] C. Bruno and B. Favini. Studio e sviluppo di modelli di simulazione delle Grandi Scale (LLS) per flussi turbolenti con cinetica chimica reale semplificata. Università degli Studi Roma "La Sapienza" - Dipartimento di Meccanica e Aeronautica.

[2] J. Gibbs. The Scientific Papers of J. Willard Gibbs. Longmans, Green and co, N.Y. (1906).

[3] D. Bartz. A Simple Equation for Rapid Estimation of Rocket Nozzle Convective Heat Transfer Coefficients. Jet Propulsion (1957).

[4] J. M. Lenoir and G. Robillard. A Mathematical Method to Predict the Effects of the Erosive Burning in Solid Propellant Rockets. In Proc. of the Sixth Symposium on Combustion, pages 663–667 (1957). New York.

[5] S. Godunov. Finite Difference Method for Numerical Computation of Discontinuos Solution of the Equation of Fluid Dynamics. Matematicheskii Sbornik, volume 47 (89)(3):page p.271 (1959).

[6] D. Baker. Method of Predicting Chamber Pressure Transients during the Ignition of Solid Propellant Rocket Motor. UTC TM-14-62-Uz. United Tecnology Center,Sunnyvale, CA (March 1962).

[7] H. Bradley. Theory of a Homogeneus Model of Rocket Motor Ignition Transient. Solid Propellant Rocket Conference, Palo Alta, CA (January 1964). AIAA Paper n.64-127.

[8] G. Markstein. Nonsteady Flame Propagation. Pergamon Press, Oxford (1964).

[9] S. De Soto and A. Friedman. Flame Spreading and Ignition Transient in Solid Grain Propellant. AIAA, volume 3(3):pages 405–412 (1965). doi:10.2514/3.2879.

[10] W. Lawrence, D. Matthews, and L. Deverall. The Experimental and Theoretical Comparison of the Erosive Burning Characteristics of Composite Propellants. AIAA-Paper n. 68-531 (1968). Atlantic City, N.Y.

[11] Solid Rocket Motor Performances Analysis and Prediction. NASA SP-8039. NASA (May 1971).

[12] A. Peretz, K. Kuo, L. Caveney, and M. Summerfield. Starting transient of Solid Propellant Rocket Motor with High Internal Gas Velocities. AIAA Journal, volume 11(12):pages 1719–1727 (December 1973).

[13] W. Noh and P. Woodward. A Simple Line Interface Calculation. In Fifth International Conference on Fluid Dynamics (edited by A. vn de Vooran and P. Zandberg). Springer-Verlag (1976).

[14] S. Peskin. Numerical Analisys of Blood Flow in the Heart. Journal of Computational Physics, volume 23:pages 220–232 (1977).

[15] R. Beddini. Effects of Grain Port Flow on Solid Propellant Erosive Burning. AIAA Paper 78-977 (July 1978).

[16] A. Chorin. Flame Advection and Propagation Algorithms. Journal of Computational Physics, volume 35:pages 1–11 (1980).

[17] C. W. Hirt and B. D. Nicholls. Volume of Fluid (VOF) Method for Dynamics of Free Boundaries. Journal of Computational Physics, volume 39:pages 201–225 (1981).

[18] B. Van Leer. On the Relation between the Upwind-Differencing Schemes of Godunov, Enquist-Osher and Roe. Institute for Computer Application in Science Engineering, (Report n 81-11) (1981).

[19] J. Sethian. Ph.D. Dissertation. Ph.D. thesis, University of California, Berkeley, California (june 1982).

[20] G. Crandall and P. L. Lions. Viscosity Solutions of Hamilton-Jacobi Equations. Transactions of the American Mathematical Society, volume 277(1) (1983).

[21] G. Crandall and P. L. Lions. Two Approssimations of Solution of Hamilton-Jacobi Equations. Mathematics of Computation, volume 43(p. 167):pages 1–19 (1984).

[22] K. Kuo, J. Gore, and M. Summerfield. Transient Burning of Solid Propellants (1984).

[23] A. Mayo. The Fast Solution of Poisson's and the Biharmonic Equations on Irregular Regions. SIAM Journal of Numerical Analisys, volume 21(2):pages 285–299 (April 1984).

[24] M. Radzan and K. Kuo. Erosive Burning of Solid Propellant (1984).

[25] J. Salee. The Middle-Cut Triangulations of the N-Cube. SIAM Journal of Alg. Disc. Methods, volume 5(3):pages 407–419 (September 1984).

[26] J. Sethian. Turbulent Combustion in Open and Closed Vessels. Journal of Computational Physics, volume 54:pages 425–456 (1984).

[27] A. Chorin. Curvature and Solidification. Journal of Computational Physics, volume 57(3):pages 472–490 (1985).

[28] J. Sethian. Curvature and the Evolution of Fronts. Communication in Mathematical Physics, (101):pages 487–499 (1985).

[29] R. Hermsen, J. Lamberty, and R. McCormick. Volume V: User's Manual for the SPP Grain Design and Ballistics Modules (December 1987).

[30] W. Lorenson and H. Cline. Marching Cubes: A High Resolution 3D Surface Construction Algorithm. Computer Graphics, (21):pages 163–169 (1987).

[31] S. Osher and J. Sethian. Front Propagating with Curvature-Dependent Speed: Algorithms Based on Hamilton-Jacobi Formulation. Journal of Computational Physics, volume 79:pages 12–49 (1988).

[32] S. Osher. The Nonconvex Multi-dimensional Riemann Problem for Hamilton-Jacobi Equations. ICASE Report 89-53 (1989).

[33] C. Shu and S. Osher. Efficient Implementation of Essentially Nonoscillatory Shock Capturing Schemes II (two). Journal of Computational Physics, volume 83:pages 32–78 (1989).

[34] M. Bardi and S. Osher. The Non Convex Multi-Dimensional Riemann Problem for Hamilton-Jacobi Equations. SIAM Journal of Numerical Analisys, volume 22:pages 344–351 (1991).

[35] S. Osher and C. Shu. High-Order Essentially Nonoscillatory Schemes for Hamilton-Jacobi Equations. SIAM Journal of Numerical Analisys, volume 28(4):pages 907–922 (1991).

[36] E. G. Puckett. A Volume-of-Fluid Interface Tracking Algorithm with Applications to Computing Shock Wave Refraction. In Proceedings, 4th International Symposium on Computational Fluid Dynamics (1991). Davis, California.

[37] B. Novozhilov. Theory of Nonsteady Burning and Combustion Stability of Solid Propellants by Zeldovich-Novozhilov Method (1992).

[38] S. Gordon and B. McBride. Computer Program for Calculation of Complex Chemical Equilibrium Compositions and Applications. NASA Reference Publication 1311, part 1: analysis edition (October 1994).

[39] B. Lafuarie, C. Nardone, R. Scardovelli, S. Zaleski, and G. Zanetti. Modelling Merging and Fragmentation in Multiphase Flows with SURFER. Journal of Computational Physics, volume 113:pages 134–147 (1994).

[40] F. Milos and D. Rasky. Review of Numerical Procedures for Computational Surface Thermochemistry. Journal of Thermophysics and Heat Transfer, volume 8(1) (January-march 1994).

[41] M. Sussman, P. Smereka, and S. Osher. A Level Set Approach for Computing Solutions to Incompressible Two-Phase Flow. Journal of Computational Physics, volume 114:pages 146–159 (1994).

[42] D. Adalsteisson and J. Sethian. A Fast Level Set Method for Propagating Interfaces. Journal of Computational Physics, volume 118:pages 269–277 (1995).

[43] F. Vuillot. Vortex-Shedding Phenomena in Solid Rocket Motors. Journal of Propulsion and Power, volume 11(4):pages 626–639 (july-august 1995).

[44] S. Gordon and B. McBride. Computer Program for Calculation of Complex Chemical Equilibrium Compositions and Applications. NASA Reference Publication 1311, part 2: users manual and program description edition (june 1996).

[45] B. Novozhilov. Nonlinear Interaction between Acoustics and Propellant Combustion. Technical Report F61708-96-W-0281, European Office of Aerospace Research and Development, 223/231 Old Marylebone Road, London, NW1 5TH, UK (1996).

[46] J. Sethian. Theory, Algorithms, Applications of Level Set Methods for Propagating Interfaces. Acta Numerica (1996).

[47] F. Blomshield, J. Crump, H. Mathes, and R. Stalnaker. Stability Testing Full-Scale Tactical Motors. Journal of Propulsion and Power, volume 13(3):pages 349–355 (may-june 1997).

[48] H. Mukunda and P. Paul. Universal Behaviour in Erosive Burning of Solid Propellants. Combustion and Flame, volume 109:pages 224–236 (1997).

[49] H. Wenzel. Turbolent premixed combustion in the laminar flamelet and the thin reaction zone regime. Center for Turbolent Research Annual Research Briefs, pages 237–252 (1997).

[50] F. Blomshield and R. Stalnaker. Pulsed Motor Firings: Pulse Amplitude, Formulation, and Enhanced Instrumentation. AIAA 1998-3557 (July 1998). 34^{th} AIAA Joint Propulsion Conference and Exhibit, Cleveland, OH.

[51] M. Salita. Closed-Form Analitical Solution for Fluid Mechanical, Thermochemical and Thermal Processes in Solid Rocket Motors. 34^{th} Joint Propulsion Conference, Cleveland, Ohio (July 1998). AIAA Paper n.98-3965.

[52] M. Sussman, P. Smereka, E. Fatemi, and S. Osher. An Improved Level Set Method for Incompressible Two-Phase Flow. Computers and Fluids, volume 27:pages 663–680 (1998).

[53] M. Ward, S. Son, and M. Brewster. Role of Gas-and-Codensed-Phase Kinetics in Burning Rate Control of Energetic Solids. Combustion Theory and Modeling, volume 2(3):pages 293–312 (1998).

[54] D. Adalsteisson and J. Sethian. The Fast Construction of Extension Velocities in Level Set Methods. Journal of Computational Physics, volume 148:pages 2–22 (1999).

[55] C. Hirsch. Numerical Computation of Internal and Esternal Flows, volume 2. John Wiley & Sons, second edition (1999).

[56] R. J. LeVeque. Numerical Methods for Conservation Laws. Birkhauser, second edition (1999).

[57] D. Peng, B. Merriman, S. Osher, H. Zhao, and M. Kang. A PDE-Based Fast Local Level Set Method. Journal of Computational Physics, volume 155:pages 410–438 (1999).

[58] F. Sabetta. Gasdinamica. Edizini Ingegneria 2000 (1999).

[59] J. Sethian. Level Set Methods and Fast Marching Methods. Cambridge University Press, second edition (1999).

[60] M. Sussman and E. Fatemi. An Efficient Interface-Preserving Level Set Redistancing Algorithm and its Applications to Interfacial Incompressible Fluid Flow. SIAM Journal of Scientific Computing, volume 20:pages 1165–1191 (1999).

[61] M. Beckstead. Solid Propellant Chemistry, Combustion and Motor Internal Ballistic (2000). New York.

[62] F. Blomshield. Pulsed Motor Firings. Technical Report NAWCWD TP 8444, Naval Air Warfare Center Weapons Division, China Lake, CA 93555-6100 (August 2000).

[63] M. Brewster. Solid Propellant Combustion Response: Quasi Steady Theory Development and Validation (2000).

[64] J. French. Analytic Evaluation of a Tangential Mode Instability in a Solid Rocket Motor. AIAA 2000-3698 (July 2000). 36^{th} AIAA/ASME/SAE/ASEE Joint Propulsion Conference and Exhibit, Huntsville; Alabama.

[65] G. Russo and P. Smereka. A Remark on Computing Distance Functions. Journal of Computational Physics, volume 163:pages 51–67 (2000).

[66] M. Di Giacinto and F. Serraglia. Modeling of Solid Motor Start-up. AIAA Paper 2001-3448 (July 2001). 37^{th} AIAA/ASME/SAE/ASEE Joint Propulsion Conference, Salt Lake City, UT.

[67] M. Di Giacinto and F. Serraglia. Modeling of SRM Ignition Transient: Role of the Main Phenomena. AIDAA (September 2001). XVI Congresso Nazionale AIDAA, Palermo, Italy.

[68] L. Kobbelt, M. Botsch, U. Schwanecke, and H. Seidal. Feature Sensitive Surface Extraction from Volume Data. SIGGRAPH, pages 57–66 (2001).

[69] S. Osher and R. Fedkiw. Level Set Methods:An Overview and Some Recent Results. Journal of Computational Physics, (169):pages 463–502 (2001).

[70] M. Salita. Modern SRM Ignition Transient Modeling (Part1): Introduction and Physical Models. AIAA Paper 2001-3443 (July 2001). 37^{th} Joint Propulsion Conference, Salt Lake City, UT.

[71] K. Tang and M. Brewster. Dynamic combustion of AP composite propellants - Ignition pressure spike. AIAA 2001-4502 (July 2001). 37^{th} AIAA/ASME/SAE/ASEE Joint Propulsion Conference and Exhibit, Salt Lake City, UT.

[72] K. Tang and M. Brewster. Non Linear Dynamic Combustion in Solid Rockets:L^* Effects. Journal of Propulsion and Power, volume 17(4):pages 909–918 (July-August 2001).

[73] F. Dauch and D. Ribereau. A Software for SRM Grain Design and Internal Ballistics Evaluation, PIBAL. 38^{th} AIAA/ASME/SAE/ASEE Joint Propulsion Conference & Exhibit, Indianapolis, Indiana (July 2002). SNPE Propulsion, Saint Mèdard en Jalles, France.

[74] M. Di Giacinto. Numerical Simulation of Solid Motor Ignition Transient. 5-ISICP-027-8-pp-MDG. Begell House Inc., New York, 2001 (June 2002). 5^{th} International Symposium on Special Topics in Chemical Propulsion, Stresa, Italy.

[75] B. Favini, M. Di Giacinto, and F. Serraglia. Solid Rocket Motor Ignition Transient Revisited. In Proc. of the 8^{th} Int. Workshop on Combustion and Propulsion (June 2002). Pozzuoli, Italy.

[76] B. Favini, F. Serraglia, and M. Di Giacinto. Modeling of Flowfield Features During Ignition of Solid Rocket Motors. AIAA Paper 2002-3753 (July 2002). 38^{th} AIAA/ASME/SAE/ASEE Joint Propulsion Conference, Indianapolis, Indiana.

[77] D. Coats, J. French, S. Dunn, and D. Berker. Improvements to the Solid Performance Program (SPP). 39^{th} AIAA/ASME/SAE/ASEE Joint Propulsion Conference & Exhibit (2003). 20-23 July, Huntsville, AL.

[78] R. Hartfield, R. Jenkens, J. Burkhalter, and W. Foster. A Review of Analytical Methods for Solid Rocket Motor Grain Analysis. AIAA Paper 2003-4506 (July 2003).

[79] S. Osher and R. Fedkiw. Level Set Methods and Dynamic Implicit Surface. Springer, first edition (2003).

[80] F. Serraglia. Modeling and Numerical Simulation of Ignition Transient of Large Solid Rocket Motors. Ph.D. thesis, Università degli Studi di Roma La Sapienza (2003).

[81] A.-K. Tornberg and B. Engquist. Regularization Techniques for Numerical Approximation of PDEs with Singularities. Journal of Scientific Computing, volume 19(1–3):pages 527–552 (December 2003).

[82] D. Calhounn and P. Smereka. The Numerical Approximation of a Delta Function (2004). Manuscript.

[83] R. Hartfield, P. Jenkins, J. Burkhalter, and W. Foster. Analytical Methods for Predicting Grain Regression in Tactical Solid-Rocket Motors. Journal of Spacecraft and Rockets, volume 41(4):pages 689–693 (2004).

[84] F. Serraglia, B. Favini, M. Di Giacinto, and A. Neri. Gas Dynamic Features in Solid Rocket Motors with Finocyl Grain during Ingnition. ESA/DLR (November 2004). Cologne.

[85] A.-K. Tornberg and B. Engquist. Numerical Approximation of Singular Source Terms in Differential Equations. Journal of Computational Physics, volume 200:pages 462–488 (2004).

[86] M. Brandyberry, R. Fieldler, and C. McLay. Verification and Validation of Rocstar 3D Multi-physics Solid Rocket Motor Simulation Program (2005). 10-12 July, Tucson, Arizona.

[87] W. Dick, M. Heath, R. Fiedler, and M. Brandyberry. Advanced Simulation of Solid Propellant Rockets from First Principles (July 2005). 41^{st} Joint Propulsion Conference, Tucson, Arizona.

[88] B. Engquist, A. K. Tornberg, and R. Tsai. Discretization of Dirac delta function in level set methods. Journal of Computational Physics, volume 207:pages 28–51 (2005).

[89] B. Engquist, A.-K. Tornberg, and R. Tsai. Discretization of Dirac Delta Functions in Level Set Methods. Journal of Computational Physics, volume 207:pages 28–51 (2005).

[90] B. Favini, M. Di Giacinto, and F. Serraglia. Ignition Transient Pressure Oscillations in Solid Rocket Motors. AIAA (July 2005). 41^{st} AIAA/ASME/SAE/ASEE Joint Propulsion Conference, Tucson, Arizona.

[91] B. Favini, F. Serraglia, M. Di Giacinto, and A. Neri. Pressuring Gas Effects on Pressure Oscillations during the Ignition Transient of SRM. EUCASS (July 2005). 1^{st} European Conference for AeroSpace Sciences, Moscow.

[92] J. French and G. Flandro. Linked Solid Rocket Motor Combustion Stability and Internal Ballistics Analysis. AIAA 2005-3998 (July 2005). 41^{th} AIAA/ASME/SAE/ASEE Joint Propulsion Conference and Exhibit, Tucson, Arizona.

[93] X. Jiao, L. Massa, and K. Tang. Rocburn2D User's and Developer's Guide. Technical report, Center for Simulation of Advanced Rockets, University of Illinois at Urbana-Champaign 2260 Digital Computer Laboratory - Urbana, IL (March 2005).

[94] E. Landsbaum. Erosive Burning of Solid Rocket Propellants: A Revisit. Journal of Propulsion and Power, volume 21(3):pages 470–477 (2005).

[95] C. Yildirim and M. Aksel. Numerical Simulation of the Grain Burnback in Solid Propellant Rocket Motor. 41th AIAA/ASME/SAE/SEE Joint Propulsion Conference & Exhibit (2005). 10-13 July, Tucson, Arizona.

[96] B. Favini, M. Di Giacinto, A. Attili, D. Scoccimarro, M. Biagioni, R. De Amicis, A. Neri, P. Bellomi, S. Bianchi, F. Serraglia, and M. Bonnet. Ignition Transient Induced Loads Control Strategy for VEGA Launcher' Solid Rocket Motors: the Zefiro9 Static Firing Test Predictions and Post Firing Analysis. Zefiro9 Static Firing Test Predictions and Post-firing Analysis. AIAA Paper 2006-5277 (July 2006). 42^{nd} AIAA/ASME/SAE/ASEE Joint Propulsion Conference, Sacramento, California.

[97] B. Favini, S. Zaghi, F. Serraglia, and M. Di Giacinto. 3D Numerical Simulation of Ignition Transient in SRM. AIAA (July 2006). 42^{nd} AIAA/ASME/SAE/ASEE Joint Propulsion Conference, Sacramento, California.

[98] F. Qin, H. Guoqiang, L. Peijin, and L. Jiang. Algorithm Study on Burning Surface Calculation of Solid Rocket Motor with Complicated Grain Based on Level Set Methods. 42th AIAA/ASME/SAE/SEE Joint Propulsion Conference & Exhibit (2006). 9-12 July, Sacramento, California.

[99] P. Smereka. The Numerical Approximation of a Delta Function with Application to Level Set Method. Journal of Computational Physics, volume 211:pages 77–90 (2006).

[100] F. Blomshield. Lessons Learned in Solid Rocket Combustion Instability. AIAA 2007-5803 (July 2007). 43rd AIAA/ASME/SAE/ASEE Joint Propulsion Conference and Exhibit, Cincinnati, Ohio.

[101] M. Di Giacinto, B. Favini, A. Attili, F. Serraglia, D. Scoccimarro, and C. Di Trapani. Internal Ballistics and Dynamics of VEGA Launcher Solid Rocket Motors During Ignition Transient: Firing Test Predictions and Post Firing Analysis. AIAA (July 2007). 43rd AIAA/ASME/SAE/ASEE Joint Propulsion Conference, Cincinnati, Ohio.

[102] B. Favini, S. Zaghi, M. Di Giacinto, and F. Serraglia. A Fully Three Dimensional Analysis of Pre-Ignition Transient in Solid Rocket Motors. AIAA Paper 2007-5781 (July 2007). 43rd AIAA/ASME/SAE/ASEE Joint Propulsion Conference, Cincinnati, Ohio.

[103] B. Favini, S. Zaghi, M. Di Giacinto, and F. Serraglia. A Fully Three Dimensional Analysis of Pre-Ignition Transient in Solid Rocket Motors. AIAA (July 2007). 43rd AIAA/ASME/SAE/ASEE Joint Propulsion Conference, Cincinnati, Ohio.

[104] X. Jiao. Face offsetting: A unified approach for explicit moving interfaces. Journal of Computational Physics, volume 220:pages 612–625 (2007).

[105] R. Lafranconi and M. Lopez. The European Small Launcher. Technical Report Vega Programme Dept., ESA Directorate of Launchers - European Space Agency BR-257, ESA-ESTEC, ESTEC, PO Box 299 2200 AG Noordwijk,The Netherlands (april 2007). 2nd Imprint.

[106] C. Min and F. Gibou. Geometrical integration over irregular domains with apllication to level-set methods. Journal of Computational Physics, volume 226:pages 1432–1443 (2007).

[107] M. Willcox, M. Brewster, K. Tang, and D. Steward. Solid Propellant Grain Design and Burnback Simulation Using a Minimum Distance Function. Journal of Propulsion and Power, volume 23(2):pages 465–475 (march-april 2007).

[108] M. Willcox, M. Brewster, K. Tang, D. Steward, and I. Kuznetsov. Solid Rocket Motor Internal Ballistic Simulation Using Three-Dimensional Grain Burnback. Journal of Propulsion and Power, volume 23(3):pages 575–584 (may-june 2007).

[109] A. Attili. Numerical Simulation of Internal Ballistic of Solid Rocket Motors. Ph.D. thesis, Sapienza Università di Roma (2008).

[110] A. Attili, B. Favini, M. Di Giacinto, and F. Serraglia. Numerical Simulation of Multiphase Flow in Solid Rocket Motors. ESA-ONERA (November 2008). 6th European Symposium on Aerothermodynamics for Space Vehicles, 3-6 November 2008, Versailles, France.

[111] E. Cavallini, M. Di Giacinto, B. Favini, and F. Serraglia. An Ignition-to-Burn Out Analysis of Solid Rocket Motors Internal Ballistic. Space Propulsion 2008 - 2nd International Symposium on Propulsion for Space Transportation (May 2008). 5-8 May, Heraklion - Crete, Greece.

[112] E. Cavallini and B. Favini. Numerical Simulation of the SRM Combustion Surface Evolution with Time. Technical report, Internal Report for ESA-ESRIN, Fascati, Italy (January 2008).

[113] B. Favini, E. Cavallini, M. Di Giacinto, and F. Serraglia. An Ignition-to-Burn Out Analysis of SRM Internal Ballistic and Performances. 44th AIAA/ASME/SAE/SEE Joint Propulsion Conference & Exhibit (July 2008). , Hartford, Connecticut.

[114] C. Min and F. Gibou. Robust Second-Order Accurate Discretizations of the Multi-Dimensional Heaviside and Dirac Delta Functions. Journal of Computational Physics, volume 227:pages 9686–9695 (2008).

[115] S. Zaghi. Multidimensional Unsteady Gasdynamics. Ph.D. thesis, Sapienza Università di Roma (2008).

[116] S. Zaghi, B. Favini, M. Di Giacinto, and F. Serraglia. 3D Simulations of Pre-Ignition Transient of P80 SRM. AIAA Paper 2008-4606 (July 2008). 44^{th} AIAA/ASME/SAE/ASEE Joint Propulsion Conference & Exhibit, 21-23 July 2008, Hartford, Connecticut.

[117] S. Zaghi, B. Favini, M. Di Giacinto, and F. Serraglia. Ignition Transient of Vega Solid Rocket Motors. Space Propulsion 2008 (May 2008). 5^{th} International Spacecraft Propulsion Conference - 2^{nd} International Symposium on Propulsion for Space Transportation, 5-9 May 2008, Heraklion, Crete, Greece.

[118] A. Attili, B. Favini, M. Di Giacinto, and F. Serraglia. Numerical Simulation of Multiphase Flows in Solid Rocket Motors. AIAA 2009-5507 (August 2009). 45^{th} AIAA/ASME/SAE/ASEE Joint Propulsion Conference and Exhibit, Denver, Colorado.

[119] E. Cavallini, B. Favini, M. Di Giacinto, and F. Serraglia. SRM Internal Ballistic Numerical Simulation by SPINBALL Model. AIAA Paper 2009-5512 (August 2009). 45^{th} AIAA/ASME/SAE/ASEE Joint Propulsion Conference & Exhibit, 2-5 August 2009, Denver, Colorado.

[120] E. Toro. Riemann Solvers and Numerical Methods for Fluid Dynamics. Springer Edition, third edition (2009).